Solid-State Nuclear Magnetic Resonance of Exotic Quadrupolar Nuclei as a Direct Probe of Molecular Structure in Organic Ionic Solids

by

Kevin M. Burgess

B.Sc., University of Ottawa, 2010

A thesis submitted to the Faculty of Graduate and Postdoctoral Studies
in partial fulfillment of the requirements for the
Doctorate in Philosophy (Ph.D.) degree in Chemistry

Candidate

Kevin M. Burgess

Supervisor

Dr. David L. Bryce

Ottawa-Carleton Chemistry Institute
Department of Chemistry
University of Ottawa

Abstract

In the past decade, the field of NMR spectroscopy has seen the emergence of ever more powerful superconducting magnets, which has opened the door for the observation of many traditionally challenging or non-receptive nuclei. In this dissertation, a variety of ionic solids with organic coordination environments are investigated using quadrupolar solid-state NMR experiments with an ultrahigh-field magnet (21.1 T). Two general research directions are presented including a $^{79/81}$Br solid-state NMR study of a series of 6 triphenylphosphonium bromides for which single-crystal X-ray structures are reported herein. A second research direction is also presented wherein alkaline-earth metal (^{25}Mg, ^{43}Ca, and ^{87}Sr) solid-state NMR is used to characterize a systematic series of 16 aryl and alkyl carboxylates. In both studies, the quadrupolar nuclei studied are deemed "exotic" due to their unreceptive nature to NMR spectroscopic analysis including low natural abundances, large quadrupole moments, or low resonance frequencies. A variety of coordination modes to alkaline-earth metals, including N-atom coordination, are characterized herein for the first time using alkaline-earth metal solid-state NMR. In all cases, the electric field gradient (EFG) and chemical shift (CS) tensors are characterized and correlated to structural features such as interatomic distances measured from the crystal structure of the compound under study.

In all of the projects undertaken herein, the gauge-including projector-augmented-wave density functional theory (GIPAW DFT) method is used, which allows for the prediction and rationalization of the experimental EFG and CS tensor parameters based on the input crystal structure. In the case of ^{43}Ca solid-state NMR experiments reported in this

dissertation, a linear correlation between the calculated and experimental ^{43}Ca quadrupolar coupling constants, C_Q, is used as a calibration curve for GIPAW DFT calculations performed on the 18 structural models currently available for the vaterite polymorph of $CaCO_3$. Vaterite cannot be fully characterized by X-ray diffraction alone; therefore an NMR crystallography protocol is used in order to identify the model that best accounts for ^{43}Ca solid-state NMR experiments performed on vaterite. It is expected that the conclusions from this dissertation can be used for future studies involving structural refinement and elucidation of solid materials containing challenging quadrupolar nuclei.

Dedication

I dedicate this thesis to the loving memory of my dad,

Michael Burgess

October 25th 1953 – August 22nd 2013

Acknowledgments

There are many people over the past four years who have contributed directly as well as indirectly to the accomplishments reported herein and deserve recognition. The first person that merits my gratitude is of course my doctoral supervisor, Dr. David L. Bryce, who has been a great role model and friend over the course of my doctorate. Thank you for taking me on as a graduate student even with my synthetic organic chemistry background. You taught me how someone can be both a great group leader as well as a great person. I hope we can stay in touch in the future.

Secondly I thank the professors who are taking time to examine the current dissertation in more detail including Dr. Paul Mayer (uOttawa), Dr. Javier Giorgi (uOttawa), Dr. Jeff Smith (CarletonU), and Dr. Paul Hazendonk (Lethbridge). Professors Mayer and Giorgi are also acknowledged for their part in my Ph.D. committee over the past four years.

I also recognize the many NMR technicians that were integral for the implementation and success of the NMR experiments in this thesis. All of you were great teachers who taught me a great deal on the theoretical and experimental aspects of solid-state NMR. Thank you for always keeping the magnets fed with liquid N_2 and liquid He. At the University of Ottawa, I first thank Glenn Facey for his support and positive attitude. Glenn always has a solution to every problem and is an excellent teacher. I hope to see you around at Sam's for lunch. I thank also Eric Ye for his help and advice over the course of my Ph.D. At the National Ultrahigh-Field NMR Facility for Solids, Victor Terskikh is greatly acknowledged for his technical assistance and was indispensable for the acquisition of the nicest NMR spectra you could hope for! I also had a lot of fun going to M-21 for lunch

every day I was there. As for X-ray analysis, I would like to thank both Ilia Korobkov for his expertise and his contribution to the single-crystal X-ray data collection reported in this thesis, as well as Tara Kell for her assistance with powder X-ray diffraction experiments. I also thank Ron Hartree for his help and service for powder X-ray experiments at the beginning of my degree. I am grateful to the large number of administrative and support staff both at the Chemistry department and at the graduate studies office that made the process of graduate studies a lot smoother with their presence. In particular I thank Josée, Annette, and Linda for their assistance and smiles at the Chemistry department office and I thank Lorraine Houle for her support and concern for the success of my degree at the graduate studies office. It was always a pleasure to chat with you all when our paths crossed.

I would also like to thank the thousands of students I've had the pleasure to teach as both a TA and professor in the past 6 years. You have all reinforced my passion for teaching. I wish you all the best of luck with your endeavors. A large amount of gratitude goes out to the undergraduate students in the Bryce group who contributed to some of the work presented in this thesis; Yang Xu and Matthew Leclerc. Both of you were a great help for the synthesis of the alkaline-earth metal complexes. Yang, I wish you the best in your economics studies. As for "The" Matt, best of luck with the remainder of your Ph.D. in the Baker group. Maybe one day I will get around acquiring those ^{59}Co NMR spectra for you. I also thank the other undergraduate students I've had the pleasure of mentoring including Apurva and Arnaud.

My time in the Bryce group would not have been the same had it not been for the presence of the people that have worked alongside me in the Marion 05 office. As the first graduate students, Becky Chapman, Cory Widdifield, and Joey Weiss, are acknowledged for

sharing with me their expertise in all aspects of research in solid-state NMR at the beginning of my graduate studies. Becky, thank you for showing me the basics of halogen solid-state NMR as well as for your smile each morning. Cory, I always enjoyed your unique sense of humor and our "late night" contests. Thank you for sharing with me some of the ideas you didn't have time to complete. Joey, I was glad to have worked across from you in the old office. I wish you plenty of success with Bruker Canada. I also thank the new generation of graduate students including Pat, Sherif, and Scott. I thank Scott for being a great TA for CHM 1311F. I'm sure you will figure out the tetrel bond soon. I also thank Sherif for taking on the ^{17}O project as well as the CHM 3122 TA position. I thank Pat also for his friendship and our Tim Horton's and Elgin Street Diner trips. Thanks also for letting me shop at SZellers. Don't ever fall into a clap-trap. Thank you also to Colette for your great personality; I count you as an honorary graduate student. Finally, I thank Igor Moudrakovski who spent a few months in our group and was a great help for ^{43}Ca NMR experiments.

I also have to thank both Fred and Jas, whom I've had the pleasure to grow in friendship with over the course of the past 8 years. We were, all three of us, in the same physical chemistry course with Dave and are now going are separate ways. Fred, you've always had a passion for your research and I hope you will have fun in the Pruski lab. Thank you also for all of your help with DOR experiments. Jas, thank you for being a great friend throughout my university career. I will always cherish the memories we made together and look forward to more! Good luck with the remainder of your Ph.D. I thank as well all of the other Bryce group members that have come and gone over the course of my studies but are not mentioned above for conciseness. All of you contributed in some way to the positive atmosphere of the group and I hope to see you again someday.

Many other people made a difference over the course of my graduate studies. Nicolas Das Neves, thank you for being a great friend and for your sense of humor. We all miss you here in Canada. I hope to see you one day in Europe! Thank you also Jean-François Vincent-Rocan for your friendship over the years and for giving me organic chemistry advice and dry solvents. I also thank Justin Renaud, honorary Bryce lab member and sergeant-at-arms of the Chemistry Graduate Student Association, who is a great friend I've made over the course of my Ph.D. I wish you the best back home in southern Ontario. I thank Alex Gagné for his friendship and the good times we've had together in past years. Finally, thank you also to Justin Thibault for your support and friendship.

Outside of my university life, I thank the church family I was part of for the past 4 years at Notre-Dame Cathedral. Thank you everyone at the 7:30 pm Mass including Gwen, Lyn, Leslie, Ricardo, Fr. Geoff, and many more. I thank also Marie-Andrée, Jacques and Hélène for your prayers and support. I give thanks to God for this community.

Finally, I would like to thank my family for all of their love, prayers, and support. A very big thank you to my mom and dad, Linda and Michael, who made me the person I am today. Thank you also to my sister, Melanie, and Craig for all of the great times we've had together here in Ottawa. I also thank my sister, Christine, and Louis-Charles and Jeremy. I always enjoy our vacations together! I love you all.

Table of Contents

List of Figures

List of Tables

List of Abbreviations

1D, 2D, 3D	one, two, or three dimensional
acac	acetylacetonate
acq	acquire
ADF	Amsterdam Density Functional
a.u.	atomic units
B3LYP	Becke three-parameter Lee-Yang-Parr
ben	benzoate
Bu	butyl
CASTEP	Cambridge Serial Total Energy Package
CCDC	Cambridge Crystallographic Data Centre
CP	cross polarization
CS	chemical shift
CSA	chemical shift anisotropy
CT	central transition
CW	continuous wave
DE	dead time
DFS	double frequency sweeps
DFT	density functional theory
DNA	deoxyribonucleic acid
DOR	double rotation
EDTA	ethylenediaminetetracetate
EFG	electric field gradient
Et	ethyl
FID	free induction decay
FT	Fourier transformation
FWHM	full width at half maximum
GGA	generalized gradient approximation
GIPAW	gauge-including projector-augmented-wave
HRTEM	high-resolution transmission electron microscopy
HS	hyperbolic secant
Hz	hertz
IR	infrared
kHz	kilohertz
IUPAC	International Union of Pure and Applied Chemistry
MAS	magic-angle spinning
Me	methyl
MHz	megahertz
mb	millibarn ($1\ mb = 1 \times 10^{-31}\ m^2$)
MOF	metal organic framework
MRI	magnetic resonance imaging

MS	magnetic shielding
MQMAS	multiple quantum magic-angle spinning
n/a	not available
NMR	nuclear magnetic resonance
NOE	nuclear Overhauser effect
OAc	acetate
o.d.	outer diameter
PAS	principal axis system
PBE	Perdew Burke Ernzerhof
pams	*para*-aminosalicylate
*p*Cl	*para*-chlorobenzoate
*p*F	*para*-fluorobenzoate
Ph	phenyl
pNO_2	*para*-nitrobenzoate
POV	persistence of vision
Pr	propyl
ppm	parts per million
PXRD	powder X-ray diffraction
QCPMG	quadrupolar Carr-Purcell-Meiboom-Gill
QI	quadrupolar interaction
QIS	quadrupole induced shift
QZ4P	quadruple zeta quadruple-polarized
RAPT	rotor assisted population transfer
ref.	reference
RF	radio frequency
RMSD	root-mean-square deviation
sal	salicylate
SIMPSON	a simulation program for NMR experiments
SN	signal to noise
SQC	single quantum coherence
SSNMR	solid-state nuclear magnetic resonance
ST	satellite transition
TPP	triphenylphosphonium
TPPM	two pulse phase modulation
TQC	triple quantum coherence
TRAPDOR	transfer of population in double resonance
VOCS	variable offset cumulative spectrum
WURST	wideband uniform-rate and smooth truncation
XC	exchange-correlation
XRD	X-ray diffraction
ZORA	zeroth-order regular approximation

List of Symbols

a_c, b_c, c_c	unit cell dimensions
Å	Angstrom (1.0×10^{-10} m)
B_0	magnetic field strength
$\mathbf{B_0}$	external magnetic field vector
B_1	transverse magnetic field strength
$\mathbf{B_1}$	transverse magnetic field vector
B_{eff}	effective magnetic field strength
$\mathbf{B_{eff}}$	effective magnetic field vector
B_{loc}	local magnetic field strength
$\mathbf{B_{loc}}$	local magnetic field vector
C_Q	quadrupolar coupling constant
$d_{A\text{-}B}$	distance between atom A and atom B
e	fundamental charge (1.60×10^{-19} C)
E_{cut}	kinetic energy cut-off
h	Planck's constant (6.626×10^{-34} J · s)
$\hbar$	reduced Planck's constant (1.055×10^{-34} J · s)
$\widehat{\mathcal{H}}_D$	dipolar Hamiltonian
$\widehat{\mathcal{H}}_J$	*J*-coupling Hamiltonian
$\widehat{\mathcal{H}}_{MS}$	magnetic shielding Hamiltonian
$\widehat{\mathcal{H}}_Q$	quadrupolar Hamiltonian
$\widehat{\mathcal{H}}_{RF}(t)$	radiofrequency Hamiltonian
$\widehat{\mathcal{H}}_{SPIN}$	total spin Hamiltonian
$\widehat{\mathcal{H}}_Z$	Zeeman Hamiltonian
$\hat{I}_Z$	*z* component of the spin angular momentum operator
I	spin quantum number
$\hat{\mathbf{I}}$	spin angular momentum operator vector
K	Kelvin

l_i	true bond length
l_0	ideal bond length
L	generic ligand
L and S	generic spins
m	magnetic quantum number
$\mathbf{M}$	bulk magnetization vector
$\mathbf{M_{XY}}$	bulk magnetization in xy plane
$\mathbf{M_Z}$	bulk magnetization in z-direction
N	arbitrary number
P_Q	quadrupolar product
q	largest component of the EFG tensor, $V_{33} = eq$
Q	quadrupole moment
$\mathbf{r}$	spatial coordinates (x,y,z)
R or R^2	correlation coefficient
R_D	dipolar coupling constant
R_1	reliability factor (crystallography)
s	second
t	time
t_P	pulse duration
T	Tesla
T_1	spin lattice or longitudinal relaxation time
T_2	spin-spin or transverse relaxation time constant
$\overline{\mathrm{V}}$	EFG tensor
$\overline{\mathrm{V}}_{\mathrm{PAS}}$	EFG tensor in its principal axis system
$V(\mathbf{r})$	electric potential
V_α	electric field (first derivative of the electric potential, $\alpha = x, y,$ z)
$V_{\alpha\beta}$	electric field gradient tensor coordinates ($\alpha,\beta = x, y,$ z)
V_{ii}	electric field gradient tensor principal components (ii = 11, 22, 33)
wR_2	reliability factor calculated with squared structure factors (crystallography)
W	water molecule ligand
$\mathbf{x}$	spatial and spin components of a wave function

x/a_c, y/b_c, z/c_c	unit cell parameters
${}^{A}Z$	mass number "A" with associated atom symbol, X
$\|\alpha\|$	longitudinal strain parameter
α, β, γ	Euler angles
α_c, β_c, γ_c	unit cell angles
δ_{ii}	chemical shift tensor principal components (ii = 11, 22, 33)
δ_{DOR}	chemical shift in a double rotation NMR spectrum
δ_{iso}	isotropic chemical shift
δ_{ISO}	chemical shift in the indirect dimension of an MQMAS spectrum
δ_{QIS}	quadrupole induced shift
$\mathbf{\Delta B}$	residual magnetic field vector
ΔC_Q	difference between calculated and experimental C_Q
$\Delta\delta_{iso}$	difference between calculated and experimental δ_{iso}
ΔE	difference in energy
$\Delta\nu_{CT}$	breadth of central transition resonance
ϕ	phase of a radiofrequency pulse
γ	magnetogyric ratio
γ_∞	Sternheimer antishielding factor
Γ	pulse flip angle
η_Q	asymmetry parameter for the electric field gradient tensor
φ	electron spin component of a wave function
κ	asymmetry parameter for the chemical shift tensor (skew)
λ	wavelength
μ_0	permeability of free space ($4\pi \times 10^{-7}$ $T^2 \cdot J^{-1} \cdot m^3$)
$\boldsymbol{\mu}$	magnetic moment vector
μs	microsecond
ν	frequency
ν_L	Larmor frequency
ν_{ref}	reference sample frequency

ν_{rot}	frequency of magic-angle spinning rotation
$\pi/2$	90 degrees in radians
θ	general angle
θ_{rot}	angle of rotation for magic-angle spinning
2θ	diffraction angle in a powder X-ray diffraction experiment
ρ or $\rho(\mathbf{r})$	electron density
σ	shielding constant
$\bar{\sigma}$	magnetic shielding tensor
$\bar{\sigma}_{PAS}$	magnetic shielding tensor in its principal axis system
σ_{ij}	magnetic shielding tensor components ($ij = x, y,$ z)
σ_{ii}	magnetic shielding tensor principal components (ii = 11, 22, 33)
σ_{dia}	diamagnetic shielding constant
σ_{iso}	isotropic magnetic shielding
σ_{para}	paramagnetic shielding constant
σ_{ref}	reference sample shielding constant
$\sigma_{iso,ref}$	isotropic shielding for a reference sample
τ_1 and τ_2	delays during an echo experiment
Ψ or Ψ_{elec}	electronic wave function
Ψ_{nuc}	nuclear wave function
ω_L	angular Larmor frequency
$\omega_{rot.\ frame}$	angular frequency of the rotating frame of reference
ω_{RF}	angular frequency of applied radiofrequency pulse
Ω	chemical shift tensor span
°	degree
$\angle$	angle

Statement of Originality

I certify that the results presented in this dissertation are my own work. Any reference to publications or the work of others is fully acknowledged using proper scientific guidelines. I thank my supervisor, Dr. David L. Bryce, for guidance in the research projects. I acknowledge Mr. Yang Xu and Mr. Matthew C. Leclerc for assistance with the synthesis of some alkaline-earth metal complexes as well as the acquisition of ^{13}C NMR spectra. Dr. Ilia Korobkov is acknowledged for solving single-crystal X-ray diffraction structures. With permission from the publishers, the following Chapters are based on published work in peer-reviewed journals:

Chapter 3: Burgess, K. M. N.; Korobkov, I.; Bryce, D. L. A Combined Solid-State NMR and X-ray Crystallography Study of the Bromide Anion Environments in Triphenylphosphonium Bromides, *Chem. Eur. J.* **2012**, *18*, 5748.

Chapter 4: Burgess, K. M. N.; Xu, Y.; Leclerc, M. C.; Bryce, D. L. Insight into Magnesium Coordination Environments in Benzoate and Salicylate Complexes through ^{25}Mg Solid-State NMR Spectroscopy, *J. Phys. Chem. A* **2013**, *117*, 6561.

Chapter 5: Burgess, K. M. N.; Xu, Y.; Leclerc, M. C.; Bryce, D. L. Alkaline-Earth Metal Carboxylates Characterized by ^{43}Ca and ^{87}Sr Solid-State NMR: Impact of Metal-Amine Bonding, *Inorg. Chem.* **2014**, *53*, 552.

Chapter 6: Burgess, K. M. N.; Bryce, D. L. On the Crystal Structure of the Vaterite Polymorph of $CaCO_3$. A Calcium-43 Solid-State NMR and Computational Assessment, *Solid State Nucl. Magn. Reson.* **2014**, DOI: 10.1016/j.ssnmr.2014.08.003

1 Introduction and Objectives

In the mid XXth century, the emergence of nuclear magnetic resonance (NMR) spectroscopy created a revolution in the way problems in molecular structural characterization were approached. The NMR method is now the gold standard in small molecule structure elucidation in academic and industrial settings and has become a powerful tool in the characterization of the secondary structures in biomolecules such as enzymes and other proteins.[1,2,3] One would be hard pressed to find a scientific research institution without an NMR facility that contains multiple NMR spectrometers capable of various applications in solution state and solid state materials characterization.[4] One particularly important application of NMR is for *in vivo* imaging of various tissues and matter within the human body known as magnetic resonance imaging (MRI),[5,6,7,8] a diagnostic technique used on a routine basis in medical institutions and hospitals around the world.

1.1 A Sample NMR Spectrum

An example of a one-dimensional (1D) NMR spectrum is found in Figure 1.1 for the proton nuclei of a cobalt catalyst in solution. An assignment of the different resonances (or peaks) in the spectrum is also provided with respect to the molecular structure of the

compound. One will notice that the power of the NMR technique lies in its ability to distinguish between different molecular environments within the studied system. The *x*-axis of the spectrum is conventionally known as the chemical shift axis and has units of frequency (in Hz) represented in parts per million (or ppm). This refers to the level at which a resonance frequency of a certain spin is shifted compared to an established reference (see section 1.6). Other information available from this spectrum is the splitting of some resonances caused by *J*-coupling resulting in the observation of distinct multiplicities, which allow for an elucidation of the structure, based on how the nuclei are coupled to each other through the chemical bonds of the molecule. Further into this Chapter, the theory of the various interactions that can affect an NMR spectrum will be discussed in much greater detail. In Chapter 2, experimental considerations for the acquisition and interpretation of NMR spectra in the solid state will be discussed. The important point here is to acknowledge the site-specific resolving power of NMR as well as its ability to establish atomic connectivities within a molecule (from *J*-coupling) compared to other spectroscopic techniques such as infrared (IR) spectroscopy. In an IR spectrum of the same compound, one will only be able to distinguish between the various functional groups that comprise the molecule and not necessarily the arrangement of the atoms of the molecule.[3] Another important feature of the NMR spectrum in Figure 1.1 is that the area below each peak may be integrated allowing for a quantitative assessment of each of the different ^{1}H sites in the molecule. Furthermore, every atom in the cobalt catalyst of Figure 1.1 can be observed by NMR spectroscopy with varying degrees of difficulty since ^{1}H, ^{13}C, ^{17}O, and ^{59}Co are "NMR-active" nuclei.

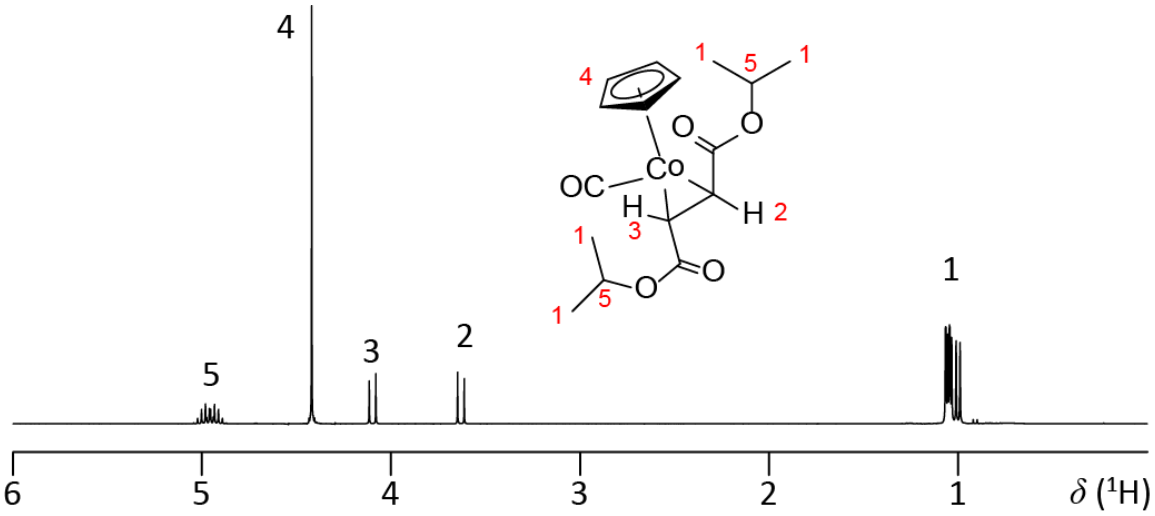

Figure 1.1: Sample ^{1}H NMR spectrum of a Co(I) catalyst in the solution state. The spectrum was a acquired at a ^{1}H frequency of 300 MHz in a C_6D_6 solvent. It is possible to assign each proton resonance to a specific site in the molecule based on the chemical shift, δ, and the *J*-coupling between the nuclei.

1.2 The Basics of NMR – The Zeeman Interaction

In order to be observable using NMR spectroscopy, a nucleus must possess a non-zero value for its nuclear spin quantum number, *I*. Spin is defined as the intrinsic angular momentum of the nucleus and is determined by the ground state configuration of the protons and neutrons (each with $I = 1/2$) in the nucleus. If the nucleus of an atom has a non-zero value for *I*, the nucleus inherently has a magnetic moment (represented by the vector $\boldsymbol{\mu}$) since the nuclear spin vector, **I**, and $\boldsymbol{\mu}$ are related by the magnetogyric ratio, γ, of the nucleus ($\boldsymbol{\mu} = \gamma \mathbf{I}$).[9] The magnetic moment can interact with a constant and homogeneous magnetic field represented by the vector $\mathbf{B_0}$ in units of Tesla. The value of *I* indicates the number of energy states that will appear once the nucleus is placed in a static and homogeneous magnetic field

(i.e., $2I + 1$) with magnetic quantum numbers, m, of $-I$, $-I + 1$, $-I + 2$, …, $I - 2$, $I - 1$, I (see Figure 1.2). In the case of a spin-1/2 nucleus, there are two eigenstates labeled $m = +1/2$ and $m = -1/2$. In the case of the quadrupolar spin-3/2 case, there are four eigenstates labeled, $m =$ +3/2, +1,2, –1/2, and –3/2. The splitting of the eigenstates in the presence of $\mathbf{B_0}$ is caused by the Zeeman interaction[10] and is the main mechanism for allowing the observation of an NMR spectrum. The difference in energy between each of the states is given by equation 1.1:[9]

(1.1) $\Delta E = \gamma \hbar B_0$

The value of γ is a constant for each individual NMR-active isotope in the periodic table and B_0 is the magnitude of the magnetic field. As a result, each NMR-active nucleus resonates at a characteristic frequency at every applied magnetic field strength and can be studied independently. Conventionally, the resonance frequency is known as the frequency of precession, ω_L (in rad s^{-1}), and is defined by the product between the magnetogyric ratio and the magnetic field strength (i.e., $\omega_L = -\gamma B_0$). The negative sign is a convention used to indicate the direction of precession. It is more convenient to express ω_L in units of Hz (or MHz) and so dividing ω_L by 2π yields equation (1.2) for the Larmor frequency, ν_L.

(1.2) $$\nu_L = -\frac{\gamma B_0}{2\pi}$$

The relative spin populations of the upper and lower energy levels at thermal equilibrium depend on the Boltzmann distribution. Hence, a larger population difference, and NMR signal, is observable at higher magnetic field strengths and for nuclei with larger γ values. It will be shown later that nuclear spin populations can be manipulated causing a polarization of the states and increasing the sensitivity of the NMR experiment.

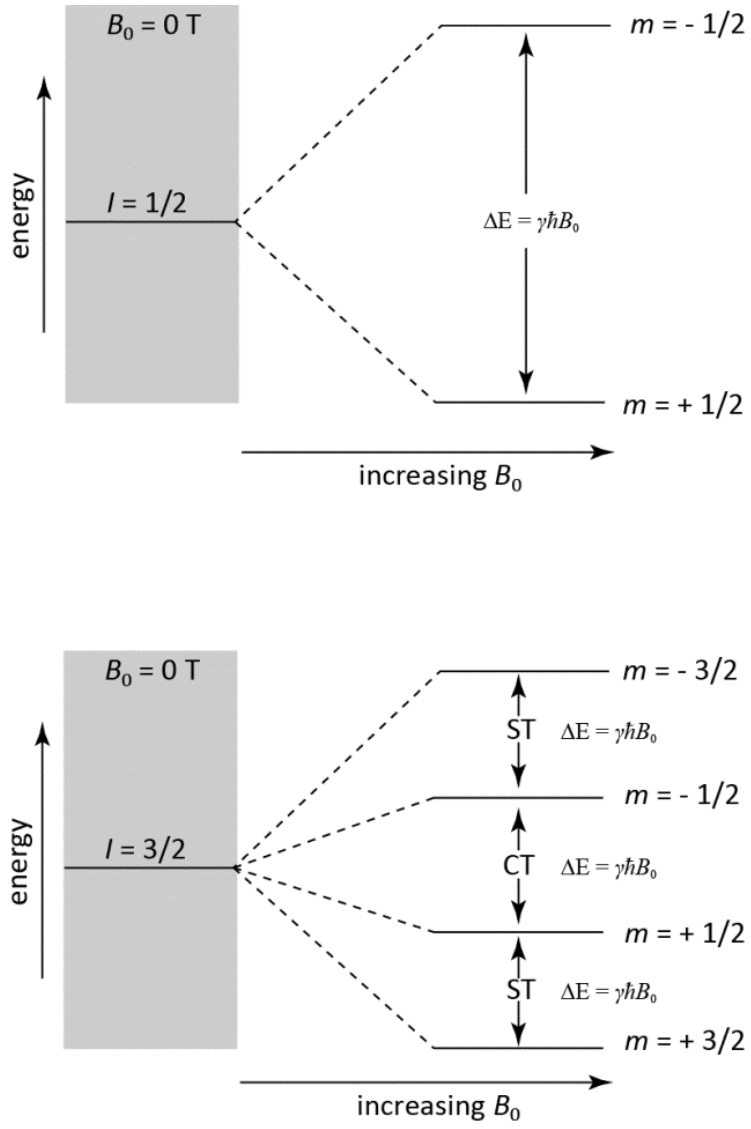

Figure 1.2: Energy level diagram for a nuclear spin in the presence of a magnetic field of strength B_0. The top diagram is for an arbitrary spin-1/2 nucleus whereas the bottom diagram is for an arbitrary spin-3/2 nucleus. In the absence of a magnetic field, all nuclear spin states are degenerate in the case of the spin-1/2 nucleus. The labels ST and CT refer to satellite and central transitions respectively.

1.3 NMR-active Nuclei in Solution and in Solids

Nearly all elements in the periodic table possess at least one naturally occurring NMR-active isotope. Some have a nuclear spin of 1/2 (e.g., ^{1}H, ^{13}C, ^{15}N, ^{31}P, etc.), which means that the charge distribution in the nucleus is spherical. However, nearly 3/4 of the NMR-active nuclei are quadrupolar, in that the charge distribution about the nucleus is non-spherical, resulting in a prolate ($Q > 0$) or oblate ($Q < 0$) shaped nucleus. Quadrupolar nuclei have nuclear spin quantum numbers greater than 1/2 and can take integer values (up to 7 for ^{176}Lu for example) as well as half-integer values (up to 9/2 for ^{87}Sr for example).[11]

Applications of NMR spectroscopy in solution are much more developed in comparison to NMR studies on solid samples. The reasons for this are because nuclear spins interact with their surroundings (i.e., the magnetic field, the electrons, and other nuclei) causing a broadening of the resonances in the NMR spectrum. In solution, most of this broadening can be averaged due to the isotropic tumbling of the molecules resulting in sharp lines such as those observed in Figure 1.1. In a crystalline powdered solid sample, however, the various crystallites are oriented in all directions with respect to that of the magnetic field causing a distinct and anisotropic broadening of the resonance that depends on the magnitude of the interaction between the nucleus and its surroundings. Hence, the spectrometer hardware and data interpretation are quite different for solid-state NMR (or SSNMR) applications compared to its solution-state counterpart. There are, however, many structural problems and applications in solid-state chemistry that would benefit from the site specific characterization only NMR can provide; these include the identification of polymorphs and solvates in active pharmaceutical ingredients,[12,13,14] porous materials such as zeolites[15,16] and

metal organic frameworks,[17,18] ion dynamics in electrochemical cells,[1920] glass materials,[21] and large biomolecules to name just a few examples.[22]

1.4 The Observation of an NMR Signal

Individual spins precess in the presence of a magnetic field and the frequency of precession is the Larmor frequency. This precession can be grossly visualized by the nuclei spinning about the magnetic field's axis at the Larmor frequency. When there are multiple spins in the sample (i.e., always) in the presence of a constant external magnetic field which defines the laboratory's *z*-direction, there begins a net alignment of the nuclear spins with the *z* axis. When equilibrium is reached, net bulk magnetization is induced and can be symbolized by a vector, **M**, in Figure 1.3. It is convenient to introduce at this time the spin-lattice time constant, T_1, which is analogous to the concept of a half-life. One typically waits five times the value of T_1 to reach thermal equilibrium for **M**, which is the amount of time required for equilibrium bulk magnetization to be reached.[23]

The sample is placed in a coil, which is usually positioned in the transverse *xy* plane (i.e., 90° with respect to the orientation of $\mathbf{B_0}$) of the spectrometer in what is called an NMR probe. As will be discussed in Chapter 2, many different NMR probes exist for various applications. A basic NMR experiment is performed by re-orienting **M** in the *xy* plane (i.e., 90° with respect to the *z*-axis) by what is known as a 90° or $\pi/2$ radiofrequency (RF) pulse via the coil.[24] When current is passed through a coil, a magnetic field is generated inside the coil. The RF pulse thus generates an oscillating magnetic field of frequency equal to the ν_L of the observe nucleus. After the 90° RF pulse has been applied, **M** preceses about *z* in the

xy plane (see Figure 1.3). As there is no constant magnetic field oriented in the *xy* plane, the individual spin magnetization vectors comprising the bulk magnetization, $\mathbf{M}_{xy}$, dephase, and the resulting $\mathbf{M}_{xy}$ vector decays to zero. The time elapsed for *xy*-magnetization to decay to zero is known as spin-spin (or transverse) relaxation and is defined by a time constant, T_2. The profile of this decay can by monitored since the coil acts as a detector for the decay. The signal as a function of time is a decaying exponential function, which is modulated by a sinusoidal function, known as the free induction decay (FID). In order to observe the NMR spectrum, the real and imaginary time domain functions of the FID are subjected to a mathematical transformation known as a Fourier transformation (FT), which produces the desired real and an imaginary frequency domain spectra.[23]

1.5 The Nuclear Spin Hamiltonian

If the information from an NMR spectrum was solely dependent upon the Zeeman interaction, this thesis would not be very long. As stated previously, nuclear spins interact with their surroundings and these effects can be quantified by NMR spectroscopy. Each individual effect acts as a perturbation to the Zeeman interaction and slightly alters the energy of the eigenstates in Figure 1.2. The pertinent NMR interactions for solids will now be presented in more detail. The vector operator $\hat{\mathbf{I}}$ is used to describe the nuclear spin angular momentum operator. The total nuclear spin Hamiltonian, $\widehat{\mathcal{H}}_{\mathrm{spin}}$, can be expressed as the sum of each of the different Hamiltonians for the individual NMR interactions under consideration.[11]

$$\widehat{\mathcal{H}}_{\mathrm{spin}} = \widehat{\mathcal{H}}_{\mathrm{Z}} + \widehat{\mathcal{H}}_{\mathrm{RF}} + \widehat{\mathcal{H}}_{\mathrm{Q}} + \widehat{\mathcal{H}}_{\mathrm{MS}} + \widehat{\mathcal{H}}_{\mathrm{OTHER}} \quad (1.3)$$

The Hamiltonian, $\widehat{\mathcal{H}}_{\mathrm{Z}}$, describes the Zeeman interaction already discussed:

(1.4) $\widehat{\mathcal{H}}_{\mathrm{Z}} = -\gamma\hbar B_0 \hat{I}_{\mathrm{Z}}$

As discussed in the previous section, RF pulses are required in order to observe an NMR signal. Quantum mechanically, the RF Hamiltonian, $\widehat{\mathcal{H}}_{\mathrm{RF}}$, is dependent on time and is represented by equation 1.5.

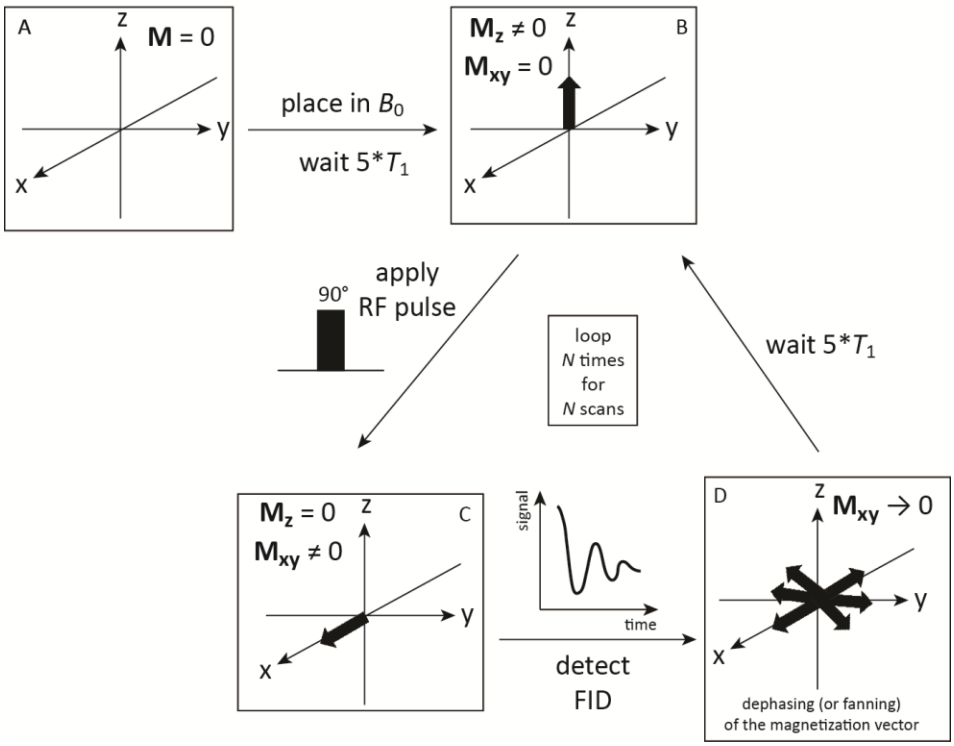

Figure 1.3: The pathway of the bulk magnetization vector, **M**, over the course of a single pulse NMR experiment. The sample outside B_0 (A) is placed inside the magnet and thermal equilibrium of **M** is reached after time 5*T_1 (B). A RF pulse is applied and **M** is rotated onto the *xy* plane (C) in order to observe the dephasing signal (D). Over the course of an NMR experiment, this loop is repeated *N* times. The static magnetic field is in the +*z* direction.

$$(1.5)\ \widehat{\mathcal{H}}_{\mathrm{RF}}(t) = -\gamma\hbar B_1\left[\hat{I}_x\cos(\omega_{RF}t - \phi) \pm \hat{I}_y\sin(\omega_{RF}t - \phi)\right]$$

In equation 1.5, B_1 is the magnitude of the oscillating magnetic field in the *xy* plane, ω_{RF} is the angular frequency (or transmitter frequency) of the RF pulse, and ϕ is the phase of the RF pulse.

It is noted at this point that all NMR experiments are observed in the rotating frame of reference with respect to the Larmor frequency of the observed nucleus.[24] In the rotating frame of reference, a coordinate system is chosen such that the transverse *xy* plane is rotating about the *z* axis at a certain frequency, $\omega_{\text{rot. frame}}$, which is close to that of ω_{L}. Therefore, the frequency of precession will appear to be at $\omega_{\mathrm{L}} - \omega_{\text{rot. frame}}$ thereby replacing $\mathbf{B_0}$ by a reduced magnetic field, $\mathbf{\Delta B}$. If the magnitude of $\omega_{\text{rot. frame}}$ is set to ω_{RF} the $\mathbf{B_1}$ field generated by the application of the RF pulse, appears as a static magnetic field. During the application of the RF pulse, the bulk magnetization vector, **M**, will precess about an effective magnetic field, $\mathbf{B_{eff}}$, which results from the vector sum of $\mathbf{B_1}$ and $\mathbf{\Delta B}$. Since $\mathbf{\Delta B} < \mathbf{B_1}$, **M** will effectively precess about $\mathbf{B_1}$, which is applied either along the *x* or *y* axis for a 90° pulse. The use of the rotating frame of reference greatly simplifies the interpretation of NMR spectra as the $\widehat{\mathcal{H}}_{\mathrm{Z}}$ term in equation 1.3 can be ignored. The resulting frequency domain NMR spectrum is a result of the subtle changes in the Larmor frequencies caused by the magnetic shielding interaction (MS), and other interactions, which will now be introduced.

1.6 The Magnetic Shielding Interaction

The MS interaction is first expressed using the MS Hamiltonian, $\widehat{\mathcal{H}}_{\mathrm{MS}}$, given by equation 1.6:[25]

(1.6) $\widehat{\mathcal{H}}_{MS} = -\gamma\hbar\,\hat{\mathbf{I}}\cdot\bar{\sigma}\cdot\mathbf{B_0}$

In equation 1.6, $\bar{\sigma}$ is the nuclear shielding tensor (*vide infra*). Since electrons are charged particles and continuously in motion, they create their own local magnetic fields, $\mathbf{B_{loc}}$. These additional local fields add to the existing magnetic field, $\mathbf{B_0}$, resulting in a localized change of the magnetic field observed by the nucleus (i.e., a shielding from the true $\mathbf{B_0}$ value) as shown in equation 1.7.[2]

(1.7) $\mathbf{B_{loc}} = (1-\sigma)\mathbf{B_0}$

In equation 1.7, σ is the shielding constant and is extremely sensitive to the chemical environment of the different spins in a sample. Under isotropic conditions (in solution for example), the value of σ is either positive or negative depending on the chemical environment and is typically reported in parts per million (ppm) of B_0. Unfortunately, it is not possible to measure the value of σ directly in an NMR experiment, thus it is reported with respect to the shielding constant of a reference sample. The chemical shift, δ, is expressed in equation 1.8 as a function of the shielding constant of the sample under study, σ, and the shielding constant of a reference, σ_{ref}.[23]

(1.8) $\delta = \dfrac{\sigma_{ref} - \sigma}{1 - \sigma_{ref}}$

In a typical NMR experiment, δ is measured by identifying the resonance frequencies of the sample, ν, and that of a reference, ν_{ref}. Similarly to equation 1.8, equation 1.9 is the δ value of a particular resonance in an NMR spectrum in terms of frequency:

$$(1.9)\quad \delta = \frac{\nu - \nu_{ref}}{\nu_{ref}}$$

The International Union of Pure and Applied Chemistry (IUPAC) has established reference standards for each individual NMR-active nucleus. For example, for ^{1}H NMR, the reference standard is the methyl protons in tetramethylsilane ($Si(CH_3)_4$). A shielded resonance with respect to TMS has a negative value for δ and a deshielded resonance with respect to TMS will have a positive value for δ.[26,27]

In the solid state, the value of σ is orientationally dependent with respect to the magnetic field and is expressed as a second-rank tensor (or 3 × 3 matrix) known as the magnetic shielding (MS) tensor. The symmetric part of the MS tensor (which affects the NMR spectrum), is written in equation 1.10.

$$(1.10)\quad \overline{\sigma} = \begin{bmatrix} \sigma_{xx} & \sigma_{xy} & \sigma_{xz} \\ \sigma_{yx} & \sigma_{yy} & \sigma_{yz} \\ \sigma_{zx} & \sigma_{zy} & \sigma_{zz} \end{bmatrix} \xrightarrow{\text{diagonalize}} \begin{bmatrix} \sigma_{11} & 0 & 0 \\ 0 & \sigma_{22} & 0 \\ 0 & 0 & \sigma_{33} \end{bmatrix} = \overline{\sigma}_{\text{PAS}}$$

In principle, the nucleus experiences a shielding value in all different orientations in three dimensions with respect to $\mathbf{B_0}$. It is then convenient to diagonalize the magnetic shielding tensor into its principal axis system (PAS, see equation 1.10). This orientation dependence of the MS tensor results in anisotropic inhomogeneous broadening of the observed resonance line in the NMR spectrum under solid-state conditions. This anisotropic broadening leads to

the appearance of an envelope referred to as a powder pattern. Recall that the shielding scale is interchangeable with the chemical shift scale, which is experimentally observable (see equations 1.8 and 1.9). As shown in Figure 1.4, the values of δ_{11}, δ_{22}, and δ_{33} indicate discontinuities (or singularities) in the shape of the signal of a spin-1/2 nucleus. The intensities at various discontinuities are a measure of the probability of finding a crystallite at this orientation of the PAS with respect to the magnetic field. The numerical values of the principal components of the CS tensor are ordered herein such that $\delta_{11} > \delta_{22} > \delta_{33}$. Also, the Maryland convention is used exclusively in this thesis to report the CS tensor in its PAS: the isotropic chemical shift, δ_{iso} (equation 1.11), the span, Ω (equation 1.12), and the skew, κ (equation 1.13).[28,29]

(1.11) $$\delta_{iso} = \frac{1}{3}\left(\delta_{11} + \delta_{22} + \delta_{33}\right)$$

(1.12) $$\Omega = \sigma_{33} - \sigma_{11} \approx \delta_{11} - \delta_{33}$$

(1.13) $$\kappa = \frac{3\left(\sigma_{iso} - \sigma_{22}\right)}{\Omega} = \frac{3\left(\delta_{22} - \delta_{iso}\right)}{\Omega}$$

The value of Ω is always positive and represents the breadth of the powder pattern. Any system with non-zero values for Ω is said to have chemical shift anisotropy (CSA). The numerical value of κ is dimensionless and ranges between –1 and +1. The CS tensor is axially symmetric if the value of κ is –1 or +1, which occurs when the molecule possesses an axis of rotational symmetry that passes through the nucleus.

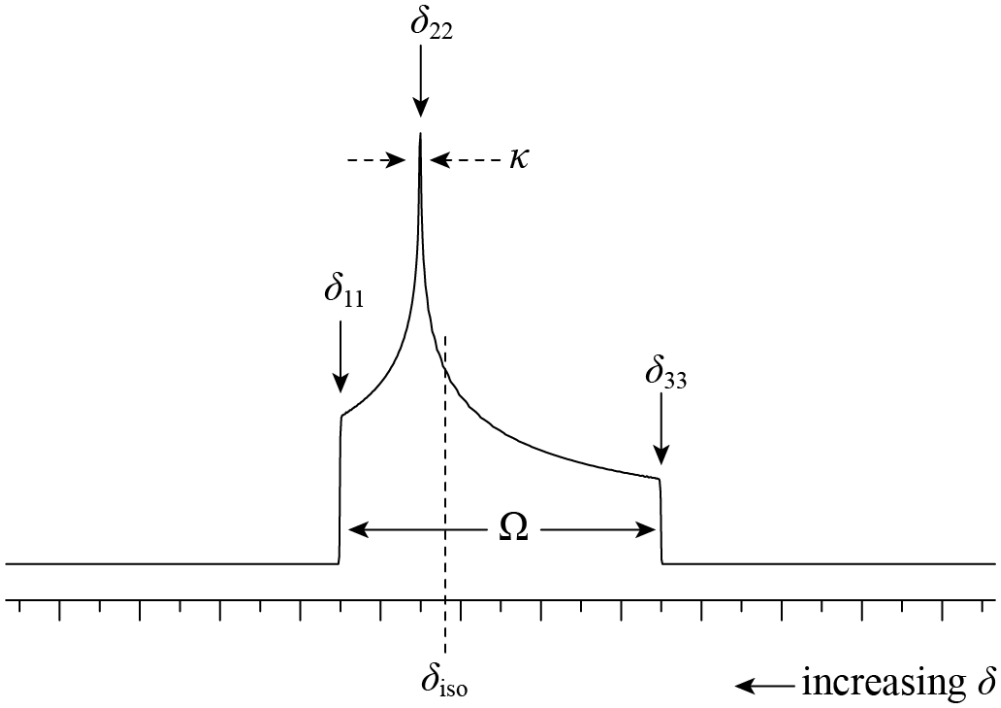

Figure 1.4: A typical powder line shape for any spin-1/2 nucleus with illustrated CS tensor parameters.

1.7 The Quadrupolar Interaction

In classical physics, the energy of the interaction between a charge distribution of density, ρ, with a potential V is given by equation 1.14.

$$E = \int \rho(\mathbf{r})V(\mathbf{r})\mathrm{d}r \quad (1.14)$$

Upon expansion of $V(\mathbf{r})$, equation 1.15 can be derived:[30]

$$E = V(0)\int \rho\, \mathrm{d}\tau + \sum_{\alpha} V_{\alpha}\int x_a\, \rho\, \mathrm{d}\tau + \frac{1}{2}\sum_{\alpha\beta} V_{\alpha\beta}\int x_a x_\beta\, \rho\, \mathrm{d}\tau \quad (1.15)$$

Where α and β refer to x, y, or z coordinates. The first term in equation 1.15 is the monopole term and refers to the electrostatic energy of the nucleus as a point charge. The second term is the dipole term where V_α is the first derivative of the potential (the electric field). The dipole term is zero by definition since nuclei do not possess a dipole moment. The third term refers to the nuclear electric quadrupole term where $V_{\alpha\beta}$ is the second derivative of the electric potential (the electric field gradient, EFG). This term is non-zero for nuclei with I values greater than 1/2. The distribution of nuclear charge in a quadrupolar nucleus is characterized by the quadrupole moment, Q, of the nucleus, which can couple with the electric field gradient (EFG) present at the nucleus resulting in the quadrupolar interaction (QI). Rather than a magnetic interaction such as for MS, the QI is an electrostatic interaction between quadrupolar nuclei and the surrounding charges (i.e., electrons and other nuclei) and is the major source of line broadening observed in the solution and solid state. The quadrupolar Hamiltonian, $\hat{\mathcal{H}}_{\mathrm{Q}}$, is shown in written in 1.16.[11]

$$(1.16)\quad \hat{\mathcal{H}}_{\mathrm{Q}} = \frac{eQ}{6I(2I-1)h}\,\hat{\mathbf{I}}\cdot\overline{\mathrm{V}}\cdot\hat{\mathbf{I}}$$

The EFG tensor in the above equation is represented by $\overline{\mathrm{V}}$, a 3 × 3 matrix that can be diagonalized (see equation 1.17) into its PAS just like the MS interaction.

$$(1.17)\quad \overline{\mathrm{V}} = \begin{bmatrix} V_{xx} & V_{xy} & V_{xz} \\ V_{yx} & V_{yy} & V_{yz} \\ V_{zx} & V_{zy} & V_{zz} \end{bmatrix} \xrightarrow{\text{diagonalize}} \begin{bmatrix} V_{11} & 0 & 0 \\ 0 & V_{22} & 0 \\ 0 & 0 & V_{33} \end{bmatrix} = \overline{\mathrm{V}}_{\mathrm{PAS}}$$

The individual $V_{\alpha\beta}$ matrix elements can be calculated using a point-charge model and equation 1.18:[30]

(1.18) $V_{\alpha\beta} = \frac{e}{r^3}\left(\frac{3x_\alpha x_\beta}{r^2} - \delta_{\alpha\beta}\right)$

where r is the distance between the nucleus and a charged particle.

The EFG tensor is traceless (equation 1.19) and is described numerically by two parameters; the quadrupolar coupling constant (C_Q, equation 1.20) and the asymmetry parameter of the tensor (η_Q, equation 1.21). The C_Q value is most often reported in units of MHz and the η_Q value ranges between 0 and 1. The EFG tensor's principal components are ordered such that $|V_{33}| > |V_{22}| > |V_{11}|$. Thus, the measurement of C_Q is a direct measurement of the largest component of the EFG tensor.

(1.19) $V_{11} + V_{22} + V_{11} = 0$

(1.20) $C_Q = \frac{eQV_{33}}{h}$

(1.21) $\eta_Q = \frac{V_{11} - V_{22}}{V_{33}}$

A distinct application of SSNMR spectroscopy as opposed to NMR experiments in solution is its ability to readily study quadrupolar nuclei. Due to fast relaxation of quadrupolar nuclei and isotropic tumbling in solution, their resonance lines are simply broadened to such an extent that they cannot be observed. In SSNMR spectroscopy however, molecular motions are hindered, thus relaxation is slower, which results in the observation of distinct resonance line shapes that are rich in information regarding the QI (*vide infra*).

1.8 The Central Transition NMR Spectrum

Both the CS interaction and the QI are treated as perturbations to the Zeeman interaction meaning that the Zeeman eigenstates are only slightly altered by the presence of these additional interactions. The CS interaction commutes with the Zeeman interaction and so first-order perturbation theory is the exact solution to the characterization of the CS tensor, which typically has a small effect on the NMR spectrum (on the order of Hz or kHz). The QI on the other hand must be treated up to second-order since its effect on the NMR spectrum is much more extensive (on the order of MHz). To first-order and in the case of an axially symmetric EFG tensor ($\eta_Q = 0$), the nuclear eigenstates labeled m have the following energy:

$$(1.22)\ E_m^{(1)} = -\gamma\hbar B_0 m + \frac{e^2qQ}{4I(2I-1)}\left(\frac{3\cos^2\theta - 1}{2}\right)(3m^2 - I(I+1))$$

In equation 1.22, θ is the angle between the spin quantization axes of the pure Zeeman and the quadrupolar-perturbed Zeeman eigenstates. In Figure 1.5 is shown an energy level diagram of an arbitrary spin-3/2 nucleus perturbed by the first and second-order QI with labels for the central transition (CT, m = +1/2 ↔ –1/2) and the satellite transitions (ST, m = +3/2 ↔ +1/2 and m = –1/2 ↔ –3/2).[31] As can be inferred by equation 1.22, the first-order QI does not affect the energy difference, ΔE, of the CT. Thus, the CT does not exhibit additional broadening from the first-order QI whereas the broadening is observed for the STs. The CT of a quadrupolar nucleus is thus only affected by the second-order QI and as a result, is much narrower in frequency units than the STs. Therefore, the CT in the SSNMR spectra for half-integer quadrupolar nuclei is the easiest to detect. The correction to the energy levels from the 2nd order QI is given by equation 1.23 when $\eta_Q = 0$:[25]

$$(1.23)\quad E_m^{(2)} = -\left\{\left(\frac{e^2qQ}{4I(2I-1)}\right)^2\left(\frac{m}{\omega_L}\right)\left(-\frac{3}{5}(I(I+1)-3m^2\right)\right\}$$
$$-\left\{\frac{3}{28}(8I(I+1)-12m^2-3)(3\cos^2\theta-1)\right\}$$
$$+\left\{\frac{1}{18}(18I(I+1)-34m^2-5)\left[\frac{18}{140}(35\cos^2\theta-30\cos\theta+3)\right]\right\}$$

Equation 1.23 can be abbreviated by equation 1.24:

$$(1.24)\quad E_m^{(2)} = C_0 + C_2P_2(\cos\theta) + C_4P_4(\cos\theta)$$

Hence, there exists an orientation independent term, C_0, that displaces the isotropic chemical shift in the spectrum by a factor known as the quadrupole induced shift (QIS). The other two terms depend on the 2nd order ($P_2(\cos\theta) = 1/2[3\cos^2\theta - 1]$) and the 4th order ($P_4(\cos\theta) = 1/8[35\cos^2\theta - 30\cos\theta + 3]$) Legendre polynomials. From equation 1.23, the breadth of the CT resonance of half-integer quadrupolar nuclei is given by equation 1.25 for any η_Q value.[32]

$$(1.25)\quad \Delta\nu_{CT} = \left(\frac{25+22\eta_Q+\eta_Q^2}{144}\right)\left(\frac{3C_Q}{(2I)(2I-1)}\right)^2\left(\frac{I(I+1)-\frac{3}{4}}{\nu_L}\right)$$

Therefore, as depicted in Figure 1.6, the breadth of the CT powder pattern is proportional to the square of the value of C_Q. It is also important to note that the breadth of the CT is inversely proportional to the value of ν_L. In the acquisition of SSNMR spectra of quadrupolar nuclei, it is advantageous to use the highest possible B_0 strength in order to reduce the broadening of the CT line shape. Furthermore, when comparing different nuclei with similar EFG tensor parameters, the CT will be narrower for nuclei with larger values of *I*. The asymmetry of the EFG tensor, η_Q, also has an effect on the appearance of the CT line

shape as it describes the relative position of both horn singularities in the SSNMR spectrum (see Figure 1.6).

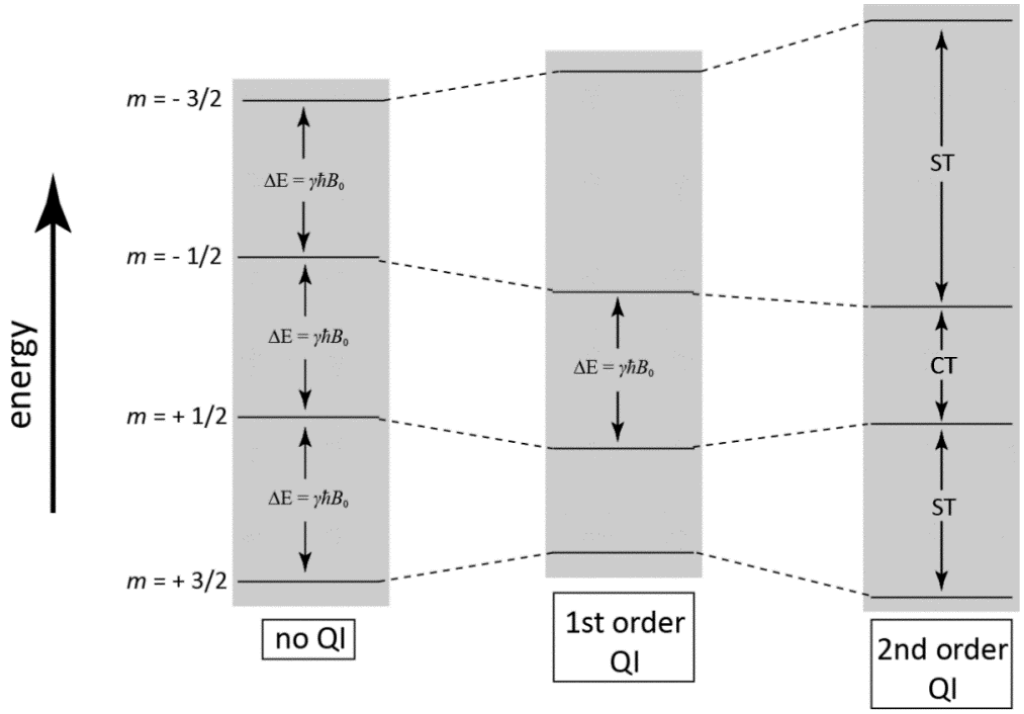

Figure 1.5: Illustration of the effects of the of the 1st and 2nd order QI on the pure Zeeman energy levels of a spin-3/2 nucleus. The first-order QI affects the STs but not the CTs. The resonance frequency of the CT is only shifted by the second-order QI.

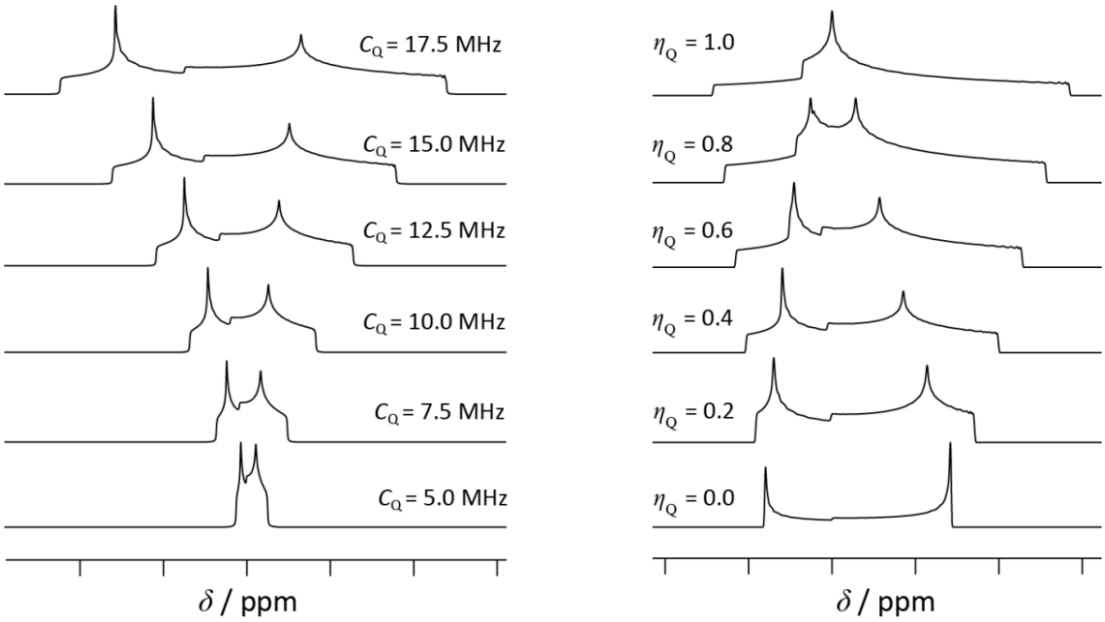

Figure 1.6: Appearence of the CT powder pattern of a half-integer quadrupolar nucleus under stationary conditions as a function of varying C_Q and η_Q. Simulations are for the ^{81}Br nucleus (I = 3/2) at B_0 = 9.4 T. When varying C_Q, the η_Q value was set to 0.40. When varying η_Q, the C_Q value was set to 5.0 MHz.

1.9 Tensor Orientations

Most of the SSNMR spectra presented in this thesis are affected by both the CS interaction and the QI. In the previous sections, only the principal components of the CS and EFG tensors were discussed. In theory, each of these components has a distinct orientation with respect to the molecular frame of reference. For the CS tensor, there are a maximum of three possible such angles and for the EFG tensor, there are also 3 possible Euler angles relating it to the molecular frame of reference.

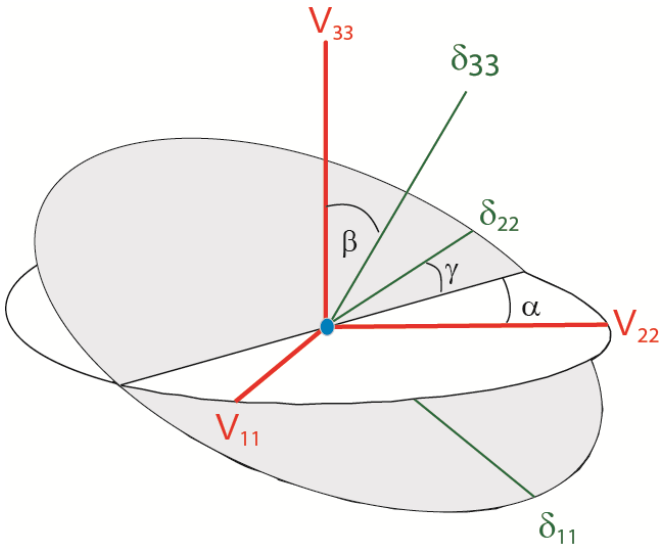

Figure 1.7: Representation of the Euler angles (α, β, and γ) that relate the CS tensor PAS to the EFG tensor PAS.

It is not possible to characterize all six EFG and CS tensor component orientations simply by acquiring a SSNMR spectrum on a powdered sample. This type of information can be extracted by performing NMR experiments on multiple known orientations of a single crystal on the sample of interest.[33] However, most SSNMR experiments under stationary conditions are performed on powdered samples. The result is that it is only possible to extract the *relative* orientations between the principal components of the EFG and the CS tensors in their respective PASs. In Figure 1.7 is shown a pictorial representation of the three Euler angles (α, β, and γ) that relate the EFG and CS tensor principal components using the "ZYZ" convention.[34] The Euler angles describe how one would rotate the principal components of the CS tensor so that they are coincident with the principal components of the EFG tensor using the z, y, and z axes. The values of α and γ can take any value between 0° and 360° whereas the value of β is between 0° and 180°.

1.10 Other NMR Interactions

The final term in equation 1.3 for the total spin Hamiltonian is reserved for the other possible NMR interactions that can affect the appearance of a SSNMR spectrum, $\widehat{\mathcal{H}}_{\mathrm{OTHER}}$. Firstly, we consider the Dipolar Hamiltonian, $\widehat{\mathcal{H}}_{\mathrm{D}}$, where two spins can be visualized as two magnetic dipoles ($\boldsymbol{\mu_1}$ and $\boldsymbol{\mu_2}$) coupling to one another through space. The energy of this interaction is proportional to the distance between the two spins such that $\widehat{\mathcal{H}}_{\mathrm{D}}$ can be written:[30]

$$(1.26)\quad \widehat{\mathcal{H}}_{\mathrm{D}} = hR_{\mathrm{D}}\,\hat{\mathbf{I}}_{\mathbf{1}} \cdot \begin{bmatrix} 1 & 0 & 0 \\ 0 & 1 & 0 \\ 0 & 0 & -2 \end{bmatrix} \cdot \hat{\mathbf{I}}_{\mathbf{2}} \quad \text{where} \quad R_{\mathrm{D}} = \left(\frac{\gamma_1\gamma_2}{r^3}\right)\left(\frac{\hbar}{2\pi}\right)\left(\frac{\mu_0}{4\pi}\right)$$

In favorable circumstances for solid samples, the dipolar coupling constant, R_{D}, can be measured, which is a direct measurement of the distance between two spins. This method is often used in NMR studies of biological samples in order to measure distances between various parts of biomolecules.[35] The through space interactions of spins are also a major source of relaxation (T_2 relaxation) and are the main mechanism in the observation of the Nuclear Overhauser Effect (NOE).[2,36] Finally, indirect nuclear spin-spin coupling or *J*-coupling is considered. The *J*-coupling Hamiltonian, $\widehat{\mathcal{H}}_{\mathrm{J}}$, causes very small perturbations to the total spin Hamiltonian and is only visible in the most favorable cases with SSNMR experiments since there is generally a lower level of resolution in solids than in solution. As an example, the ^{81}Br CT SSNMR powder pattern can span several hundreds of kilohertz (kHz) whereas its isotropic *J*-coupling may be only a few Hz, a negligible effect. In the solution state however, the indirect spin-spin coupling interaction is quite informative for the identification of neighboring spins as *J*-couplings are often described as the "through-bond

coupling" interaction.[11] Since $\hat{\mathcal{H}}_D$ and $\hat{\mathcal{H}}_J$ have negligible effects on the broad CT SSNMR spectra such as those presented in this thesis, these interactions will not be considered further.

1.11 Research Objectives and Motivations

1.11.1 Initial Motivations

There are currently some well-established characterization tools available to the chemist in order to determine the solid-state or 3D structure of ionic and molecular systems. One such method is single-crystal X-ray diffraction (XRD), wherein a rather large crystal must be grown without defects in order to obtain an unambiguous structural model of the sample of interest. In many instances however, it is not possible to obtain that perfect single crystal for single-crystal XRD analysis due to the presence of some kind of disorder or an amorphous state of the solid. In this dissertation, we wish to move past the conventional XRD analysis towards the 3D structural elucidation of ionic solids with SSNMR. Given the CS and EFG tensors introduced above and their relationship to the local electronic configuration about the nucleus, SSNMR should be quite capable of providing site specific information on the probed nuclei within the crystalline lattice. In general terms, it is necessary to establish such correlations between SSNMR parameters (i.e., C_Q, δ_{iso}, Ω to name a few) and critical structural features such as interatomic distances and bond angles. In the cases of ^{1}H and ^{13}C NMR of organic molecules for example, such widely accepted trends are taught at the undergraduate level (i.e., aromatic benzene ring protons always have a chemical shift ranging between 7 and 8 ppm with respect to TMS; carbonyl ^{13}C nuclei have chemical shifts ranging from 170 to 200 ppm with respect to TMS). These trends might be

well established for spin-1/2 nuclei in solution, but this is far from the case in solids, particularly in cases where exotic quadrupolar nuclei are the focus of study such as the case in this dissertation.

1.11.2 Exotic Quadrupolar SSNMR

In Table 1.1 are presented some pertinent nuclear properties for the exotic quadrupolar nuclei under study herein, in comparison with those more familiar to the general chemist, ^{1}H and ^{13}C, which are both spin-1/2 nuclei. In the case of the NMR-active nuclei for bromine (^{79}Br and ^{81}Br), both have relatively large Q values of 313 and 262 mbarn respectively, resulting in relatively broad CT SSNMR spectra spanning from several hundred kHz to MHz in certain cases for small values for $|C_Q(^{81}\text{Br})|$. Typically, experiments are performed on the ^{81}Br nucleus rather than the ^{79}Br nucleus, given the smaller Q value of the former. Therefore systematic studies involving this nucleus present in non-symmetric bromide environments are rare.[37] As for the alkaline-earth metals, each of them has only one NMR-active nucleus: ^{25}Mg for magnesium, ^{43}Ca for calcium, and ^{87}Sr for strontium. All three nuclei are considered "low-gamma" nuclei given their γ values below that of ^{15}N. Therefore, their ν_L values are all at low-frequency (24.5, 26.9, 17.3 MHz for ^{25}Mg, ^{43}Ca, and ^{87}Sr respectively) in comparison to ^{13}C (100.61 MHz) when B_0 = 9.4 T. In fact, on the 400 MHz spectrometer dedicated for solids at the University of Ottawa, a frequency of 17.3 MHz for ^{87}Sr is not even tunable within our infrastructure. The quadrupole moments for ^{25}Mg and ^{87}Sr (199.4 and 305 mbarn respectively) also make the acquisition of those SSNMR spectra quite challenging. As for ^{43}Ca, its main pitfall is its natural abundance of 0.135 % making the observation of even an NMR signal a time consuming task. Each of the quadrupolar

nuclei in Table 1.1 have at least one nuclear property that deem them "exotic"; however, it is still possible that meaningful structural information may be gained by performing SSNMR experiments on these nuclei.

Table 1.1: Table of nuclear properties for the studied exotic quadrupolar nuclei in this thesis.

nucleus	^{1}H	^{13}C	^{79}Br	^{81}Br	^{25}Mg	^{43}Ca	^{87}Sr
nuclear spin, I	1/2	1/2	3/2	3/2	5/2	7/2	9/2
natural abundance /%	99.99	1.07	50.69	49.31	10.00	0.135	7.00
$\gamma/10^7$ rad s^{-1} T^{-1}	26.75	6.73	6.73	7.25	–1.64	–1.80	–1.16
ν_L (B_0 = 9.4 T) /MHz	400.13	100.61	100.25	108.06	24.49	26.93	17.34
Q /mbarn[a]	-	-	313	262	199.4	–40.8[b]	305

[a]The Q values are those tabulated by Pyykkö in ref. 38
[b]The value of Q(^{43}Ca) was updated as part of the work presented in Chapter 5

For an added level of difficulty in the systems studied herein, most of them are indeed ionic but are in organic coordination environments. Therefore, the counter ion or ligand will typically be a bulky organic moiety containing phenyl rings. This will result in a more dilute amount of the probed nucleus per unit of volume in comparison to inorganic systems. This will be particularly challenging for the alkaline-earth metals given their lower natural abundances (^{43}Ca in particular) and Larmor frequencies. These systems were chosen as only a handful of previous literature exists for the study of these exotic quadrupolar nuclei in organic ionic solids. The main motivation is that virtually no meaningful and unambiguous correlations between SSNMR parameters and the crystal structures have been determined for these exotic quadrupolar nuclei when only organic ionic systems are considered. The establishment of such correlations will allow for the study of non-crystalline samples containing these exotic quadrupolar nuclei.

1.11.3 Direct Structural Information from the CS Tensor in Exotic Quadrupolar Nuclei

Firstly, the CS tensor is very sensitive to subtle chemical differences about the probed nucleus; however, it is often lost or forgotten in the analytical simulation of SSNMR spectra that are most often dominated by the QI. It is therefore desirable to measure the manifestations of CSA from the probed exotic, half-integer, quadrupolar nucleus in the studied organic ionic solids. As the magnitude of the CSA is more affected by the immediate electronic distribution about the nucleus, CSA will correlate with very specific and immediate structural features such as bond lengths. With accurate measurements of CSA, a specific CS tensor parameter can be correlated to a particular structural feature from the available crystal structures of the compounds under study.

It is more facile to measure CSA at higher magnetic field strengths. Therefore, in all of the research projects presented in this thesis, the use of the Ultrahigh-Field NMR Facility for Solids in Ottawa equipped with a B_0 = 21.1 T ($\nu_L(^1H)$ = 900.13 MHz) magnet was indispensable. For quadrupolar SSNMR applications, ultrahigh-field (B_0 > 18.8 T) NMR has many advantages. Firstly, there is a gain in sensitivity of the NMR experiments performed at 21.1 T compared to standard magnetic field strengths as the spin population difference (Boltzmann distribution) between the NMR energy levels is much larger. Furthermore, recalling equation 1.25, where $\Delta\nu_{CT}$ was inversely proportional to the Larmor frequency, experiments performed at B_0 = 21.1 T result in a significant amount of narrowing in Hz for the CT NMR spectra of quadrupolar nuclei. Narrowing of the CT powder pattern allows for a great amount of resolution between the different crystallographically unique sites in the crystal structure using techniques such as magic-angle spinning (MAS, see Chapter 2).

Another advantage of ultrahigh-field NMR is its ability to accentuate the features resulting from the CSA in the CT powder patterns when there is less broadening from the QI. For the same shift values at 9.4 T and at 21.1 T, the difference in frequency is much greater, thus fine features are more apparent at higher magnetic field strengths. Hence, ultrahigh-field NMR will be essential for the characterization of the CS in the organic ionic solids presented in this dissertation, but more importantly in allowing for the identification of structural correlations with the CS interaction.

1.11.4 Application to Structural Refinements and NMR Crystallography

Along a second, but similar vein, our systematic studies of exotic quadrupolar nuclei with SSNMR will permit the elucidation of the 3D structures of ionic solid materials. On the one hand, bromine and/or alkaline-earth metal SSNMR could be used as a tool for structural refinement where the reported crystal structure is not in agreement with NMR experiments. On the other hand, we wish to apply this new knowledge to the emerging field of NMR crystallography, where the correlations established herein between NMR observables and known crystal structures are used as constraints in order to solve the solid-state structures of more challenging, weakly crystalline or non-crystalline systems. So far in the literature, most NMR crystallography studies have involved only spin-1/2 nuclei.[39,40,41,42]

Hence, a main task herein is to accurately characterize both the EFG and CS tensor parameters using state-of-the-art quadrupolar SSNMR methods presented in Chapter 2. These include the acquisition of CT SSNMR spectra of the aforementioned exotic quadrupolar nuclei under stationary conditions as well as under sample spinning in order to observe high-resolution SSNMR spectra. In general the EFG and CS tensors can be

extracted by simulating the CT powder patterns analytically at multiple magnetic field strengths using software that accounts for QI under the high-field approximation (i.e., the QI is treated only to second-order). We then desire to correlate these NMR parameters with a particular structural feature from the available crystal structures of the compounds under study. In order for this endeavor to be successful, the use of computational chemistry is essential as it will i) allow for the visualization of the EFG and CS tensor components with respect to the molecular frame of reference and; ii) allow for the corroboration of a proposed crystal structure (either from XRD or *ab inito*) with SSNMR observables. The computational methods used throughout this thesis will be discussed in Chapter 2.

1.12 Overview of the Research Projects Undertaken

The general theme of this thesis is the determination of molecular structural parameters of exotic quadrupolar nuclei by using SSNMR spectroscopy, specifically when coordinated by organic coordination ligands. The various materials investigated find a wide range of applications in materials sciences, which will be discussed in their respective chapters within this thesis.

In order to achieve the objectives outlined above, two main areas of research were envisioned and are reported in this thesis. The first study will be presented in Chapter 3 and is a $^{79/81}$Br investigation of the bromide anion environments in triphenylphosphonium (TPP) bromides. In that study, it will be necessary to acquire X-ray crystal structures of the studied compounds in order to relate the $^{79/81}$Br CS and EFG tensor parameters to a particular structural feature. In Chapters 4 and 5, the focus is moved towards alkaline-earth metal

cations in organic coordination environments. Our main motivation for those studies was due to the paucity of previous work on alkaline-earth metal SSNMR specifically when the metal is involved in coordination to organic ligands. The results therein will be exciting as this study opens the door for the characterization of coordination environments (specifically N-coordination) to alkaline-earth metals by SSNMR. With a greater understanding of how some NMR parameters can be related to structural features in the known crystal structures, it will then be possible to apply this knowledge in the field of NMR crystallography. In Chapter 6, ^{43}Ca SSNMR experiments will be used in attempts to identify the correct structural model of the vaterite polymorph of $CaCO_3$. In that Chapter, an NMR crystallography approach is used in order to retain or refute a possible structural model of vaterite by comparing experimental ^{43}Ca SSNMR spectra with those of proposed models by diffraction or *ab inito* methods. It is anticipated that through this work, high-resolution ^{43}Ca SSNMR experiments (see Chapter 2) may become indispensable when attempting to elucidate the structure of calcium-containing materials.

1.13 References for Chapter 1

1. Ikura, M.; Kay, L. E. Bax, A. *Biochemistry*, **1990**, *29*, 4659.
2. Silversetin, R. M.; Webster, F. X.; Kiemle, D. J.; Bryce, D. L. Spectrometric Identification of Organic compounds, 8th Edition, Wiley, Hoboken NJ, **2015**.
3. Pavia, D.; Lampman, G. Kriz, G.; Vyvyan, J. Introductions to Spectroscopy, 4th Edition, Brooks/Cole, Belmont CA, **2009**.
4. The University of Ottawa NMR Facility's website; URL: www.nmr.uottawa.ca, consulted October 26th, 2014.
5. Lauterbur, P. C. *Nature* **1973**, *242*, 190.
6. Damadian, R. *Science* **1971**, *171*, 1151.
7. Lauffer, R. B. *Chem. Rev.* **1987**, *87*, 901.
8. Madelin, Lee, J.-S.; Regatte, R. R.; Jerschow, A. *Prog. Nucl. Magn. Reson. Spectrosc.* **2014**, *79*, 14.
9. Hore, P. J. Nuclear Magnetic Resonance (Oxford chemistry primers 32), Oxford University Press, Oxford NY, **1995**.
10. Zeeman, P. *Nature* **1897**, *55*, 347.
11. Levitt, M. H. Spin Dynamics, Wiley, Hoboken NJ, **2008**.
12. Harris, R. K.; Ghi, P. Y.; Puschmann, H.; Apperley, D. C.; Griesser, U. J. Hammond R. B.; Ma, C.; Roberts, K. J. Pearce, G. J.; Yates, J. R.; Pickard C. J. *Org. Process Res. Dev.* **2005**, *9*, 902.
13. Burgess, K. M. N.; Perras, F. A.; Lebrun, A.; Messner-Henning, E.; Korobkov, I.; Bryce D. L. *J. Pharm. Sci.* **2012**, *101*, 2930

14. Hamaed, H.; Pawlowski, J. M.; Cooper B. F. T.; Fu, R. Eichhorn, S. H.; Schurko, R. W. *J. Am. Chem. Soc.* **2008**, *130*, 11056.

15. Fyfe, C. A.; Thomas, J. M.; Klinowski, J.; Gobbi, G. C. *Angew Chem. Int. Ed. Engl.* **1983**, *22*, 259.

16. Deng, F.; Yue, Y.; Ye, C. *Solid State Nucl. Magn. Reson.* **1998**, *10*, 151.

17. Sutrisno, A.; Huang, Y. Solid State *Nucl. Magn. Reson.* **2013**, *49-50*, 1.

18. Fracaroli, A. M.; Furukawa, H.; Suzuki, M.; Dodd. M.; Okajima, S.; Gandara, F.; Reimer, J. A.; Yaghi, O. M. *J. Am. Chem. Soc.* **2014**, *136*, 8863.

19. He, X. J.; Davis, L. J. M.; Bain, A. D. Goward, G. R. *Solid State Nucl. Magn. Reson.* **2012**, *42*, 26.

20. Ilott, A. J.; Trease, N. M.; Grey, C. P.; Jerschow, A. *Nature Communications* **2014**, *5*, 4536.

21. Aguiar, P. M.; Michaelis, V. K.; McKinley, C. M.; Kroeker, S. *J Non-Cryst. Solids* **2013**, *363*, 50.

22. Mcdermott, A. *Annu. Rev. Biophys.* **2009**, *38*, 385.

23. Keeler, J. Understanding NMR Spectroscopy, 2nd Edition, Wiley, Hoboken NJ, **2010**.

24. Hore, P. J.; Jones, J. A.; Wimperis, S. NMR: The Toolkit (Oxford chemistry primers 92), Oxford University Press, Oxford NY, **2000**.

25. Duer, M. J. Introduction to Solid-State NMR Spectroscopy, Blackwell, Oxford UK, **2004**.

26. Harris, R. K.; Becker, E. D.; Cabral de Menezes, S. M.; Goodfellow, R.; Granger, P. *Pure Appl. Chem.* **2001**, *73*, 1795.

27. Gottlieb, H. E.; Kotlyar, V.; Nudelman, A. *J. Org. Chem.* **1997**, *62*, 7512.

28. Herzfeld, J.; Berger, A. E. *J. Chem. Phys.* **1980**, *73*, 6021.

29. Mason, J. *Solid State Nucl. Magn. Reson.* **1993**, *2*, 285.

30. Slichter, C. P. Principles of Magnetic Resonance, 3rd Edition, Springer-Verlag, New York Berlin Heidelberg, **1990**.

31. Ashbrook, S. E. Wimperis, S. Nuclear Quadrupole Coupling: An Introduction & Crystallographic Aspects, in "NMR Crystallography", R. K. Harris, R. E. Wasylishen and M. J. Duer (editors); Wiley, Hoboken NJ, **2009**.

32. MacKenzie, K. J. D.; Smith, M. E. Multinuclear Solid-State NMR of Inorganic Materials; Pergamon, Amsterdam, **2002**.

33. Eichele, K.; Chan, J. C. C.; Wasylishen, R. E.; Britten, J. F. *J. Phys. Chem. A* **1997**, *101*, 5423.

34. Power, W. P.; Wasylishen, R. E.; Mooibroek, S.; Pettitt, B. A.; Danchura, W. *J. Phys. Chem.* **1990**, *94*, 591.

35. Chen, K.; Tjandra, N. *Top. Curr. Chem.* **2012**, *326*, 47.

36. Neuhaus, D.; Williamson, M. P. The Nuclear Overhauser Effect in Structural and Conformational Analysis, 2nd edition, Wiley, New York NY, **2009**.

37. Bryce, D. L.; Widdifield, C. M.; Chapman, R. R.; Attrell, R. J. Chlorine, Bromine, and Iodine Solid-State NMR, in "NMR of Quadrupolar Nuclei in Solid Materials", R. E. Wasylishen, S. E. Ashbrook, and S. Wimperis (editors); Wiley, Chichester UK, **2012.**

38. Pyykkö, P. *Mol. Phys.* **2008**, *106*, 1965.

39. Harris, R. K. *Solid State Sciences* **2004**, *6*, 1025.

40. Pickard, C. J.; Salager, E.; Pintacuda, G.; Elena, B.; Emsley, L. *J. Am. Chem. Soc.* **2007**, *129*, 8932.

41. Brower, D. H. *J. Magn. Reson.* **2008**, *194*, 136.

42. Harris, R. K.; Wasylishen, R. E.; Duer, M. J. (editors), NMR Crystallography, Wiley, Hoboken NJ, **2009.**

2 Experimental and Theoretical Methods

The simplest method used to acquire an NMR spectrum is by performing a single pulse experiment as discussed in Chapter 1. In this Chapter are presented the more complex data acquisition methods and pulse sequences used in the various research projects presented as part of this thesis.

2.1 Pulse Calibrations and Chemical Shift Referencing

In order to acquire an NMR spectrum with an optimal signal to noise (SN) ratio, it is important to calibrate the optimal 90° pulse duration described by equation 2.1.[1]

(2.1) $\Gamma = \gamma B_1 t_P$

The flip angle, Γ, describes the value (in degrees) of the rotation of **M** (see section 1.4) onto the *xy* plane and is proportional to the amplitude of the applied transverse magnetic field strength, B_1 (or pulse power), and the duration of the pulse, t_P. Typically, concentrated aqueous solutions or cubic solids are used as setup standards in order to optimize the duration and power of the 90° pulse. Specific details for the various nuclei presented in this thesis are reported in their respective chapters. Optimal pulse lengths and powers are particularly

important when multiple pulses are applied over the course of a pulse sequence. Inaccuracy in their calibration will affect the excitation profile of the pulse and therefore, the appearance of the NMR spectrum possibly rendering the acquired data unusable. Because of the absence of a QI in solution, or in cubic solids, the calibrated 90° t_p is non-selective and both CT and STs can be excited at once. In non-cubic solids, however, it is generally only possible to observe the CT selectively, as the magnitude of the RF field typically is much smaller than the QI, thus scaling the 90° pulse durations from a cubic solid or a solution by a factor of $1/(I + 1/2)$ (i.e., 1/2, 1/3, 1/4, and 1/5 for $I = 3/2$, 5/2, 7/2, and 9/2 respectively) is necessary.[2] For very small C_Q values such as in near cubic solids, the RF pulse is non-selective for the CT, whereas, in the case of environments with large C_Q values, the STs are very far off resonance from the Larmor frequency since they are affected by the first-order QI. Thus, the CT can be excited selectively in non-cubic solids.[3]

As stated Chapter 1.6, chemical shifts are always reported with respect to an agreed upon external chemical shift reference. Chemical shift references are typically aqueous solutions with specific concentrations of a solute (ex., 85% H_3PO_4 for ^{31}P NMR) containing the studied NMR-active nucleus. In certain circumstances, a secondary cubic solid reference can be used (ex., ammonium dihydrogen phosphate for ^{31}P NMR).[2] Chemical shift referencing must be done quite regularly when performing SSNMR experiments specifically when days or weeks elapse between experiments. The absolute frequency of the standard sample can change over a small period of time as the magnitude of B_0 can drift on the order of μT due to some external factors such as metal objects close to the magnetic field or vibrations. The specific chemical shift references that were used as part of this thesis will be presented as needed in each individual chapter. It is worth noting here however that, in the

case of the ^{43}Ca chemical shift reference solution (saturated $CaCl_2$ in H_2O) the δ_{iso} value of the observed resonance is highly dependent on the concentration of $CaCl_2$. Varying degrees of $CaCl_2$ saturation in the literature have resulted in discrepancies for reported ^{43}Ca chemical shifts for solid samples.[4,5] Thus, in this thesis, the concentrations of the $CaCl_2$ reference solutions were less than 2 M as recommended previously.[5]

.

2.2 The Echo Experiment for Quadrupolar Nuclei[6]

The spin echo experiment is one of the most important NMR experiments. The pulse sequence shown in Figure 2.1 consists of a 90° pulse followed by a delay τ_1. Subsequently to the initial delay τ_1, a 180° refocusing pulse is applied. Over the course of the initial delay, the transverse magnetization, $\mathbf{M}_{xy}$, dephases into a distribution of multiple frequencies for different nuclear environments (or crystallite orientations). The 180° pulse refocuses these frequencies (brings them back together) during the second delay, τ_2, where the FID signal reaches a maximum (theoretically when $\tau_1 = \tau_2$). After the second pulse, the receiver (or detector) is turned on and the signal is acquired. Typically signal from the first half of the echo is removed by throwing away the respective data points prior to FT by "left shifting" the echo (see red part of FID in Figure 2.1). A FT can be performed to yield the spectrum. Due to the broad nature (kHz to MHz in width) of the CT spectra of quadrupolar nuclei, the FID is attenuated rather quickly compared to the case of solutions. The spin echo sequence allows for a delay in the observation of the signal after the second RF pulse, thereby avoiding any interference with the acoustic ringing caused by the NMR probe.

In its simplest form, a single-channel NMR probe is comprised of a tank circuit,[7] which contains both a tuning and matching capacitor as well as an inductor coil. The tuning capacitor allows for adjustments of the circuit to produce the correct frequency (the Larmor frequency) and the matching capacitor is used to adjust for the quality factor of the circuit. The inductance of the coil is also important in obtaining the desired range of tunable frequencies for the probe, for transmitting RF power, and receiving the NMR signal. Due to some inherent resistance from the coil, it is not possible to acquire an NMR signal immediately after a pulse, hence there is always a probe dead time (DE), where the acoustic ringing from the probe is allowed to relax before signal acquisition (see Figure 2.1). The best hardware can handle a setting of 5 μs for the DE, which would result in a significant loss of signal for a quadrupolar nucleus and significant line shape distortions. Probe acoustic ringing is particularly a problem at low frequencies, such as for low-γ nuclei like the alkaline-earth metals presented in this thesis. The echo experiments allow for the delay in the acquisition of the FID by a time τ_1, hence no signal loss is observed due to probe ringing.

The 90°/180° echo is typically referred to as the Hahn echo.[8] For qudrupolar nuclei, another type of echo, called to the solid (or Solomon) echo is used frequently where both pulses have a flip angle of 90°.[9,10] For particularly broad CT powder line shapes, the solid echo yields a more quantitative line shape since it allows for a more uniform excitation profile in the frequency domain. It was observed by Bodart *et al*. that crystallites behave differently after the 180° refocusing pulse depending on their orientation with respect to the magnetic field causing line shape distortions. A good compromise between minimizing line shape distortions and signal intensity was found by shortening the refocusing pulse to a 90° pulse.[11] Since the signal is not being entirely refocused (90° pulse instead of a 180° degree

pulse), there is a usual associated loss in signal by a factor of nearly 2 when compared to the Hahn echo experiment. This is due to the dependence of the signal intensity on a $[\sin(\Gamma_1)\cdot\sin^2(\Gamma_2/2)]$ factor, where Γ_1 and Γ_2 are the flip angles of the pulses.[8] In this thesis, both experiments are used interchangeably. Due to its typically higher quality line shapes, the solid echo was most often utilized. In certain cases, specifically for the alkaline-earth metals, the Hahn echo was used for the improved SN ratio.

2.3 Experiments on Stationary Samples

The most intuitive method to acquire an NMR spectrum on a solid (or liquid) sample is by simply placing it in the spectrometer and leaving it stationary. If there are ^{1}H nuclei in close proximity to the quadrupolar nucleus, there is the possibility for additional broadening caused by the dipolar coupling interaction that is not averaged under stationary conditions. These effects can be removed (or decoupled) by irradiating the ^{1}H nuclei with a high power RF (between 60 and 100 kHz) at their Larmor frequency while the NMR signal is being acquired for the quadrupolar nucleus (see Figure 2.1).[2] The resulting spectrum will have an increased signal-to-noise compared to a spectrum acquired without ^{1}H decoupling. In most cases in this work, continuous wave (CW)[12] ^{1}H decoupling was used however other decoupling schemes exist.[13]

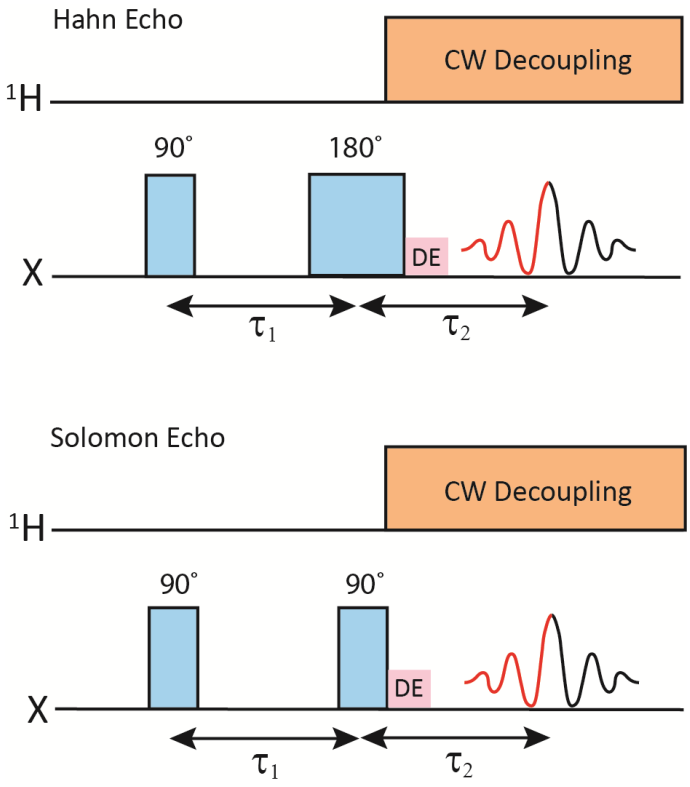

Figure 2.1: Hahn and Solomon echo pulse sequences used for the acquisition of SSNMR spectra of quadrupolar nuclei. When processing the data, the points in the red part of the FID are thrown away by performing a left shift of the data points. Under stationary conditions, ^{1}H decoupling is usually applied during signal acquisition.

Due to technological limits and the excitation profile of RF pulses over which excitation is uniform, the spread of frequencies that can be excited during one experiment, for ^{81}Br experiments for example, is typically a range of 200 kHz at one frequency transmitter offset setting (i.e., a 0 kHz setting for example corresponds to a transmitter positioned exactly at the Larmor frequency). For most spectra acquired as part of this thesis, one transmitter offset setting was sufficient to observe a uniformly excited CT NMR spectrum. In some specific cases for $^{79/81}$Br, ^{25}Mg, and ^{87}Sr SSNMR, one transmitter offset setting positioned at the center of the line shape was not adequate in yielding uniformly

excited powder patterns since their CT breadths exceeded the profile of frequencies that could be excited uniformly at once. In those specific cases, the variable-offset cumulative spectrum (VOCS) method[14] was used to acquire meaningful SSNMR data. With VOCS, many NMR spectra of the same compound are acquired at different transmitter offset settings with identical acquisition parameters such as the pulse durations, delays, and number of scans. In order to get the proper shape of the full NMR spectrum, the individual transmitter offset frequency settings of each NMR spectrum must be uniformly spaced (see Figure 2.2 for an example with 5 offset settings separated by 150 kHz). Each subspectrum, or "piece", is processed on its own (i.e., left shifting, FT) and the individual spectra sum together in the frequency domain to yield the full spectrum that appears to be uniformly excited.[15] The offset value in kHz is typically measured experimentally by identifying the quantity in kHz of uniform excitation in the first subspectrum. There are some limitations when using the VOCS method especially when large C_Q values are observed. The full spectrum can become so broad that the optimal pulse duration and/or the Boltzmann population at the high frequency end of the CT powder pattern is different from that of the low frequency end.[16] In those cases, distortions may be observed in the fully co-added spectrum. In this thesis however, the characterized QIs are not strong enough to need to account for these affects.

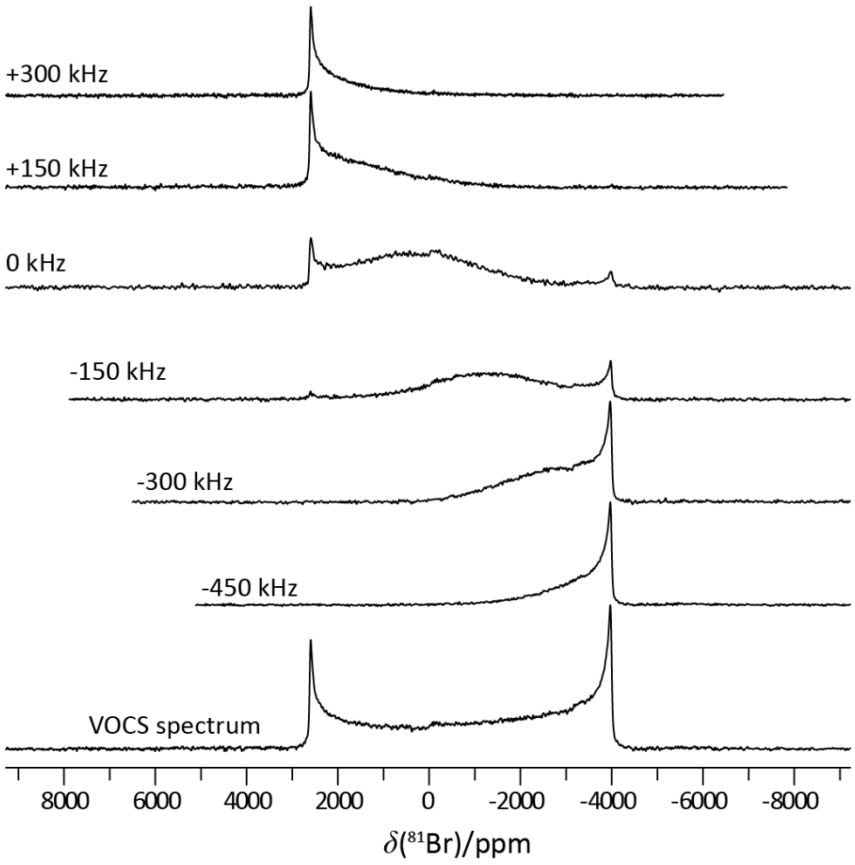

Figure 2.2: Bromine-81 SSNMR spectrum of triethylammonium bromide ($HNEt_3Br$) acquired using the VOCS method and a Solomon echo pulse sequence. Five transmitter offset settings were necessary in order to observe a uniformly excited line shape.

2.4 Magic-Angle Spinning[17,18]

It is possible to significantly narrow the breadth of the powder patterns of SSNMR spectra by mechanically spinning the sample at a specific angle with respect to the magnetic field and at high spinning rates, ν_{rot}, relative to the breadth of the powder pattern in kHz. In the Zeeman frame, the anisotropy of certain NMR interactions such as the dipolar interaction and the CS interaction, have an orientational dependence with respect to the magnetic field

direction as a function of $(3\cos^2\theta_{rot} - 1)$.[19] If θ_{rot} is precisely set to 54.74°, the additional broadening caused by those particular interactions can be averaged to zero resulting in a significant narrowing of the resonance. Hence a specialized probe, known as a magic-angle spinning (MAS) probe can be designed where the sample of interest is positioned at the magic angle of 54.74° with respect to the external magnetic field.[20] For spin-1/2 nuclei such as ^{1}H, ^{13}C, ^{15}N, and ^{31}P, their powder patterns are broadened only by CSA; a MAS experiment with a sufficiently large spinning rate yields a spectrum with a solution-like appearance (see Figure 2.3). If the spinning rate is smaller than the breadth of the powder pattern, the line shape is split into sharp resonances known as spinning sidebands. If multiple experiments are performed at various spinning frequencies, one peak remains independent of ν_{rot}. This isotropic peak is a direct measurement of the δ_{iso} value.

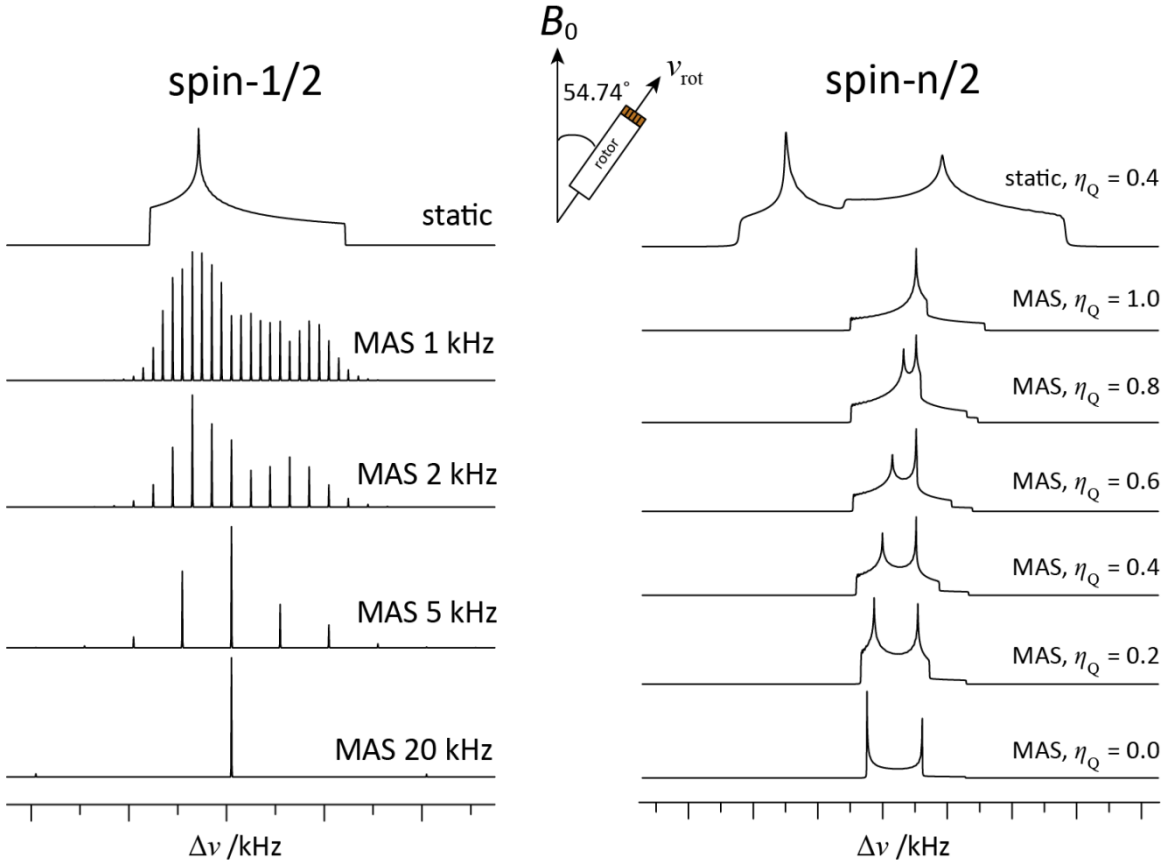

Figure 2.3: Powder patterns for spin-1/2 and half-integer quadrupolar nuclei (spin-n/2) under MAS conditions. For spin-1/2 nuclei, the spectra have a solution-like appearence at sufficiently high spinning frequencies. Residual broadening still remains for half-integer quadrupolar nuclei due to the second-order quadrupolar interaction.

For a half-integer quadrupolar nucleus, MAS experiments are possible but only partially narrow the CT powder patterns (by a factor of 3 or 4).[21] As discussed previously, the CT is broadened by the second-order QI, where the anisotropic broadening is dependent upon the 2nd order ($P_2(\cos\theta) = 1/2[3\cos^2\theta - 1]$) and the 4th order ($P_4(\cos\theta) = 1/8[35\cos^4\theta - 30\cos^2\theta + 3]$) Legendre polynomials, meaning that the magic angle of 54.74° is not adequate in averaging the powder pattern.[22,23] In Figure 2.3 is presented the appearance of the CT

SSNMR spectrum of a half-integer quadrupolar nucleus under stationary conditions in comparison to that under MAS conditions. In most cases in this thesis, with the exception of ^{87}Sr SSNMR, it was possible to perform experiments under both stationary conditions and MAS conditions. If both the CS interaction and QI are considered as the major factors affecting the appearance of the CT SSNMR line shapes, a total of up to eight individual NMR parameters can be extracted from a spectrum acquired under stationary conditions: C_Q, η_Q, δ_{iso}, Ω, κ, Euler angles (α, β, and γ). Since the CS interaction is averaged under MAS conditions, only three parameters affect the MAS spectrum: C_Q, η_Q, δ_{iso}. This fact provides a high level of certainty for the latter three parameters which are assumed to be identical for the simulation of the static CT line shape. Currently at the 21.1 T facility, it is possible attain ν_{rot} values up 62.5 kHz, which was indispensable for the acquisition of ^{81}Br NMR spectra in this work.

2.5 High-Resolution SSNMR of Half-Integer Quadrupolar Nuclei

2.5.1 Double Rotation

Since the CT resonance of a half-integer quadrupolar nucleas is broadened only by the second-order quadrupolar interaction, the anisotropic broadening cannot be completely removed by a conventional 1D MAS experiment. The broadening is modulated by both the 4th order Legendre polynomial (see equation 1.24; $P_4(\cos\theta)$ has magic angles of 30.56° and 70.12°) as well as $P_2(\cos\theta)$.[24] The second-order QI can be completely averaged by spinning at two angles simultaneously known as the double rotation (DOR) NMR technique. In DOR

experiments, a small rotor, called the inner rotor, is placed inside are large outer rotor positioned at an angle of 54.74° with respect to the direction of the external magnetic field.[25,26,27] The inner rotor is oriented at an angle of 30.56° with respect to the axis of rotation of the large rotor. The result is a solution-like NMR spectrum for a half-integer quadrupolar nucleus in solids in the presence of spinning sidebands separated by the spinning rate of the outer rotor. Due to the obvious engineering challenges of having one rotor simultaneously spinning quickly inside another spinning rotor, the applicability of DOR has been so far used for quadrupolar nuclei with relatively small Q values such as ^{11}B, ^{17}O, and ^{23}Na.[28,29,30] In this thesis, DOR NMR is applied to the ^{43}Ca nucleus in Chapter 6. The Q value of the ^{43}Ca nucleus (see Table 1.1) seems to make it an ideal candidate for DOR NMR studies.

2.5.2 Multiple Quantum Magic-Angle-Spinning

DOR NMR experiments require specialized DOR NMR probes, hence it has not received as much attention in the scientific literature as the Multiple Quantum (MQ) MAS experiment. The MQMAS technique was first proposed by Frydman *et al*. in 1995[31,32] and has since revolutionized the field of high-resolution SSNMR for half-integer quadrupolar nuclei because it is possible to utilize a conventional MAS probe.[33] The only constraint for the MQMAS experiment is to obtain a 1D MAS NMR spectrum in a reasonable amount of time due to the sensitivity issues of the 2D method of acquisition for the MQMAS technique. This can be challenging especially when low-γ and low natural abundance nuclei such as ^{43}Ca are studied.

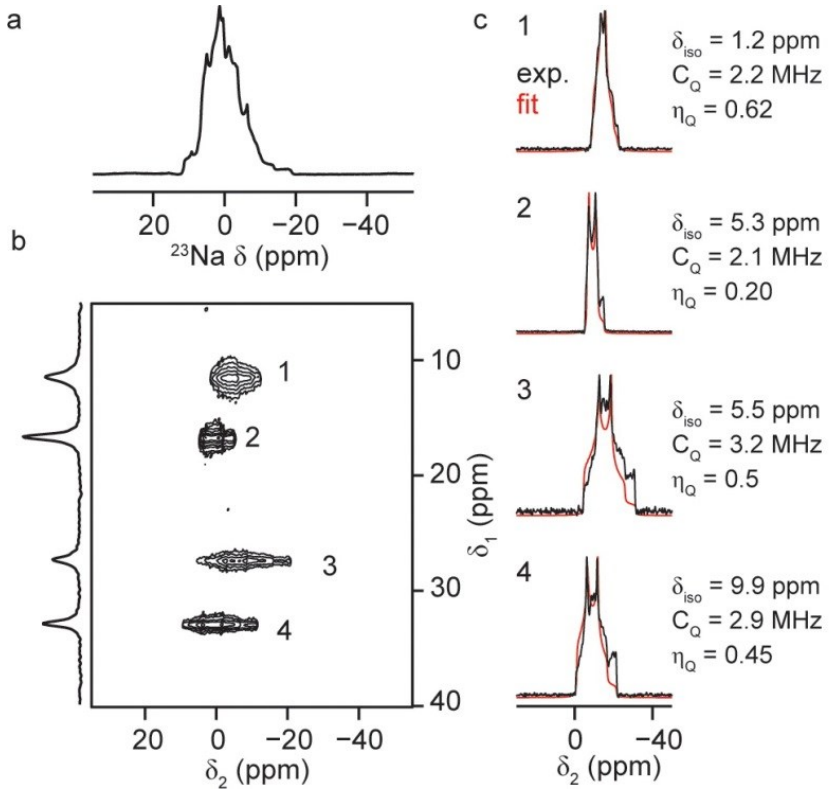

Figure 2.4: Example ^{23}Na MQMAS experiment (B_0 = 14.1 T, ν_{rot} = 14 kHz) on $Na_4P_2O_7$ (b) reproduced with permission from reference 33. The horizontal (δ_2) axis in (b) is that of the 1D ^{23}Na NMR spectrum in (a). The vertical axis (δ_1) is the isotropic dimension, where there are clearly 4 crystallographically unique Na sites. It is possible to extract horizontal slices in the case of each resolved ^{23}Na site and simulate them individually whith their respective quadrupolar and δ_{iso} parameters (c).

In its simplest form, the MQMAS technique involves excitation of triple quantum coherences (TQC, m = 3/2 ↔ –3/2) with an RF pulse followed by an evolution time and a subsequent conversion of the TQCs to the observable single quantum coherence (SQC) of the CT. Like the CT, the TQC is only affected by the second-order QI. Under MAS conditions, the $C_2P_2(\cos\theta)$ term from equation 1.24 can be averaged. Knowing that the second-order QI

of the CT and the TQC is affected differently depending on the coherence order, the $C_4P_4(\cos\theta)$ term from equation 1.24 can still be averaged even without the use of the magic angles of $P_4(\cos\theta)$, thereby leaving behind only isotropic interactions after data manipulation.[34] In other words, the spins are permitted to evolve for various amounts of time in the CT coherence and in the TQC.[35] Like an echo experiment, the QI is refocused to yield an isotropic echo. The MQMAS technique, when appropriately processed using a shearing transformation, yields the usual 1D MAS spectrum in the direct (horizontal) dimension and isotropic resonances for each of the crystallographically unique sites in the indirect (vertical) dimension. In a shearing transformation, the anisotropic axis of the 2D spectrum, which contains all of the anisotropic broadening caused by the second-order QI, is placed parallel to the F_2 axis of the spectrum thereby creating a new dimension called δ_{ISO}. The δ_{ISO} axis does not contain any anisotropic broadening from the QI, thus isotropic peaks are observed. In Figure 2.4, a sample ^{23}Na MQMAS spectrum of $Na_4P_2O_7$ is presented where the 4 crystallographically unique sodium sites are resolved. When taking horizontal slices (or cross sections) at each of the isotropic resonances, the individual 1D MAS spectra can be visualized and simulated with the appropriate NMR parameters. The MQMAS technique, however, is quite an insensitive technique because TQCs are forbidden transitions meaning that they cannot be directly observed. To get around this complication, one must convert the excited TQCs to observable SQCs and use a 2D method of acquisition, yet it remains the method of choice due to the relatively straightforward implementation compared to other methods that currently exist.

2.6 Signal Enhancement Methods for SSNMR

2.6.1 Cross Polarization

The cross polarization technique (CP) is routinely used for spin-1/2 nuclei such as ^{13}C, ^{15}N, and ^{31}P under MAS spinning conditions (CP/MAS).[36] CP is a signal enhancement technique where spin magnetization from an abundant spin, *L* (usually ^{1}H), is transferred to a more dilute spin, *S*, in order to observe an increased SN ratio of the *S* spin.[37] In a typical CP experiment, an RF spin-locking pulse, known also as a contact pulse, is applied simultaneously to both the *L* and *S* spins in order to match their respective nutation frequencies under what is called the Hartman-Hahn matching conditions resulting in a polarization transfer from *L* to *S*.[38] For example, since ^{1}H (*L* spin) has a higher magnetogyric ratio than ^{13}C (*S* spin), the difference in Boltzmann population between the two energy levels of the ^{13}C will be greater during the contact pulse thereby increasing the SN ratio of the spectrum compared to direct detection of the ^{13}C nucleus. The efficiency of CP is mediated by the dipolar coupling between the *L* and the *S* spins, therefore both spins need to be in close proximity to one another in order to observe any significant signal enhancements. One advantage of CP over direct excitation of the *S* spin is that it is only necessary to wait for the T_1 relaxation of the ^{1}H (*L*) nuclei before each scan. In the case of ^{13}C (*S*) for example, the T_1 value in certain chemical environments can be on the order of minutes whereas the T_1 for ^{1}H is typically on the order of seconds, resulting in a significant sensitivity enhancement over a fixed amount of time. In the case of ^{1}H nuclei, the dipolar mechanism for relaxation significantly increases the relaxation rates compared to ^{13}C nuclei given their differences in magnetogyric ratios.[7] It is possible to perform CP experiments between ^{1}H and half-integer

quadrupolar nuclei under stationary conditions,[39,40] however spin-locking is rather inefficient under MAS conditions of a quadrupolar nucleus since a time dependence is introduced to the energy states of the quadrupolar nucleus during the contact pulse and rotor period.[41,42,43] CP under static conditions has been reported on low-γ nuclei such as ^{43}Ca (ref. 44) and others.[45,46] CP/MAS experiments are used herein for high-resolution ^{13}C and ^{31}P experiments (see Figure 2.5).

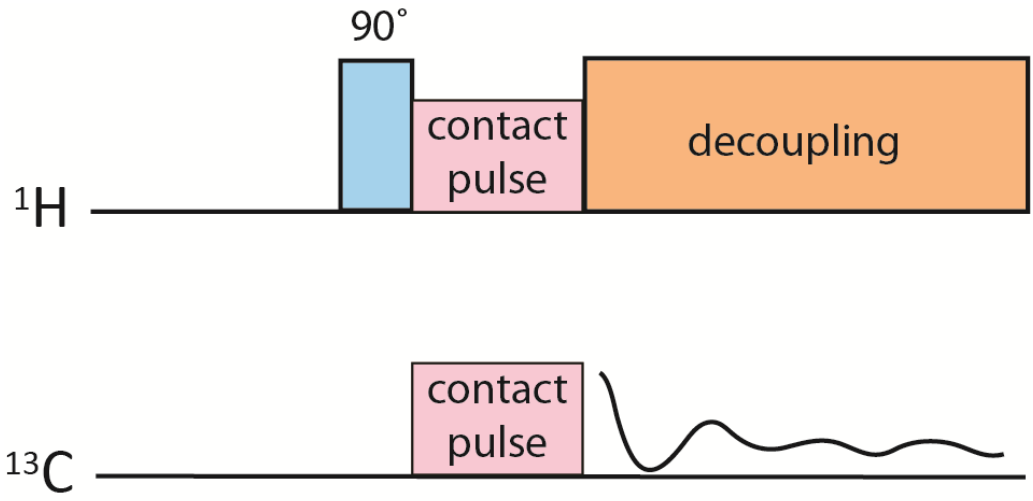

Figure 2.5: Pulse sequence for the acquisition of a ^{13}C CP/MAS experiment. Note that a 90° pulse is performed on the ^{1}H channel and the ^{13}C signal is detected after the contact pulse.

2.6.2 The Quadrupolar Carr-Purcell-Meiboom-Gill Sequence

In order to improve the sensitivity of the NMR experiments in certain cases over the course of this research, the quadrupolar Carr-Purcell-Meiboom-Gill (QCPMG) pulse sequence, as shown in Figure 2.6, was used.[47] The first part of the sequence is identical to

the echo sequence presented in section 2.2 as an initial echo signal is generated by a 90° pulse followed by a 180° degree pulse. After the creation and acquisition of the first echo, the signal is repeatedly refocused N times by a series of N 180° pulses until the signal has completely decayed in the time domain. Over the course of the pulse sequence, only ±1 quantum coherences are generated and these can be selected using a simple two-step phase cycle.[48] The resulting FID is a train of repeating echoes with decaying intensity as a function of time T_2. Upon applying a FT to the train of echoes, the NMR spectrum in the frequency domain is a series of sharp spikelets separated by the CPMG repetition rate (in Hz). This is analogous to the FT of rotational echoes in the FID of a spin-1/2 nucleus under MAS conditions. The outline from the maximum intensities of the spikelets takes the shape of the stationary powder line shape. The QCPMG method is advantageous as a signal enhancement technique since it allows for the concentration of the signal in the entire powder pattern into a set number of spikelts and multiple echoes are acquired as part of each scan.[49] For a given CT line shape, largely separated spikelets might yield higher intensity but at the expense of spectral resolution of the line shape. A compromise must be found by the experimentalist for both an adequate SN ratio and the accuracy of the observed line shape.

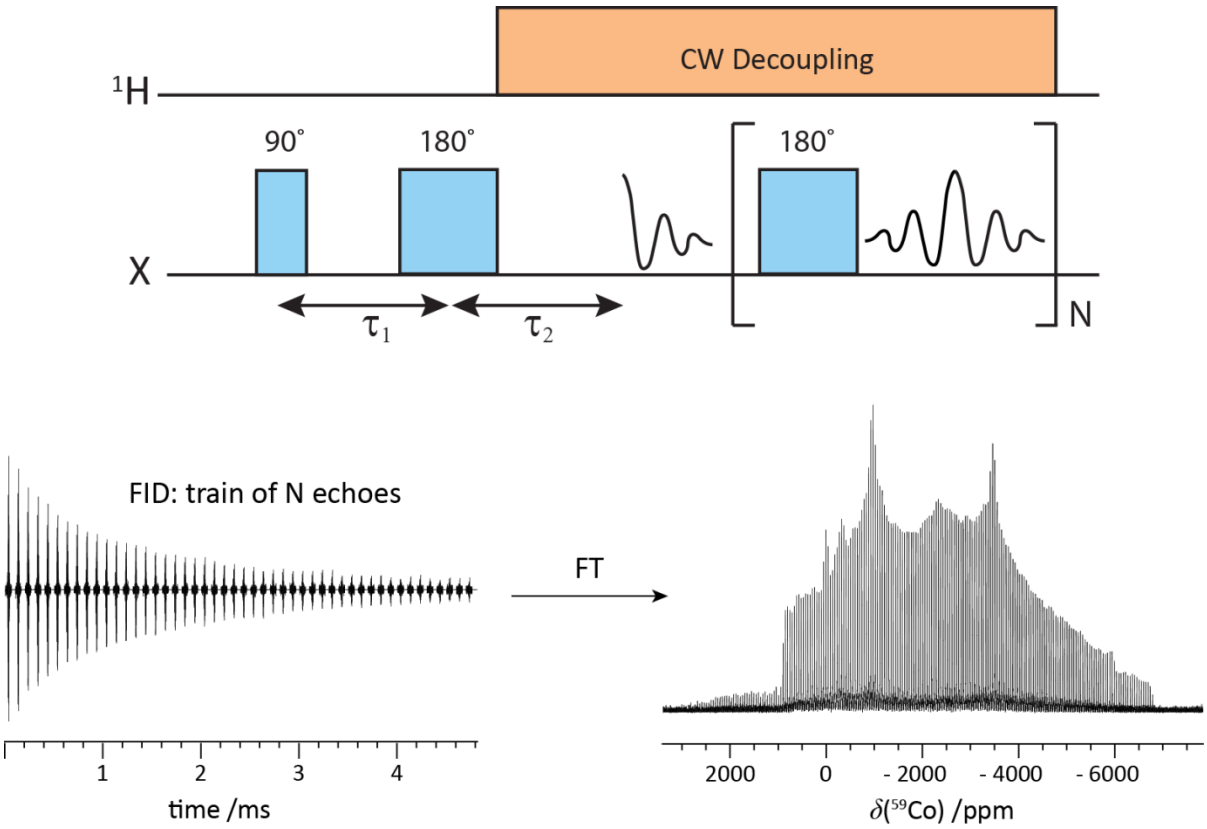

Figure 2.6: Pulse sequence diagram for the QCPMG experiment with ^{1}H decoupling. The signal is refocused N times with the application of N 180° pulses resulting in a train of N echoes. The train of echoes can be Fourier transformed to yield the QCPMG spectrum where the powder pattern is broken into spikelets.

In order for the QCPMG method to yield accurate results, the 90° and 180° pulses must be accurately known (not trivial at times) and the application of a train of 180° pulses typically results in a narrower range of pulse bandwidths (i.e., uniformly excitable frequencies). In those cases, it is necessary to couple the QCPMG method with the VOCS method, see section 2.2, in order to observe the full CT powder pattern.[48] In 2008, O'Dell and Schurko[50] proposed the use of the frequency and amplitude-modulated wideband

uniform rate smooth truncation (WURST) shaped pulses rather than the conventional pulses in a QCPMG experiment. Over the course of a WURST pulse, an effective magnetic field, $\mathbf{B_{eff}}$, is created, which acts as the axis of precession for the bulk magnetization vector **M**. Initially, the frequency of the pulse is far off resonance and $\mathbf{B_{eff}}$ colinear with $\mathbf{B_0}$. The frequency is then swept closer to resonance and $\mathbf{B_{eff}}$ is eventually tilted onto the *xy* plane. In order for the WURST pulse to be effective, the sweep rate must be slow enough such that **M** continues to precess about $\mathbf{B_{eff}}$ over the course of the pulse, thereby satisfying the condition of the adiabatic passage.[50] The result of the WURST pulse is that a much larger and uniform excitation profile of frequencies is attainable, which results in the need for fewer transmitter offset settings when acquiring ultra-wideline CT SSNMR spectra.[15] In many cases (such as the ^{87}Sr NMR experiments performed herein), the WURST-QCPMG method could be used to acquire powder patterns at only one transmitter offset setting. This method has facilitated the acquisition of particularly broad CT spectra (on the order of several MHz broad) in recent years.[51,52]

2.6.3 Population Transfer Methods from the Satellite Transitions

Because of our interest mostly in the CT spectrum of a half-integer quadrupolar nucleus, the STs are often ignored. If the Boltzmann distribution is considered for an arbitrary spin-5/2 nucleus (see Figure 2.7), the population difference between the two lower ST states is much larger than that of the CT. In principle, one would desire to use the excess of population from the STs to polarize that of the CT.[53,54] In Figure 2.7 are presented both methods by which the CT can be polarized from adjacent STs: saturation or inversion of the STs. Both methods provide a larger difference in population between the CT energy levels

than from thermal equilibrium and signal enhancement is accessible by applying a scheme of known signal enhancement pulses prior to an echo or QCPMG sequence.

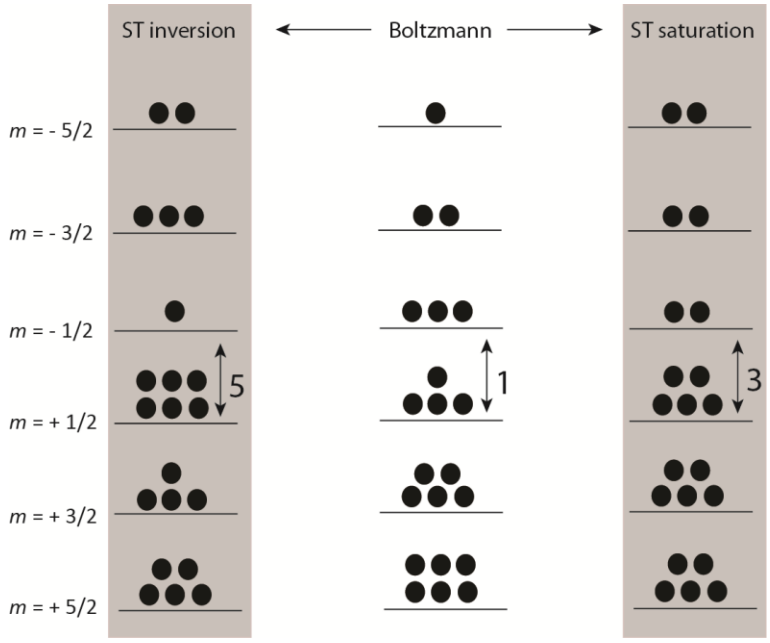

Figure 2.7: Illustration of the ST inversion and ST saturation methods for the enhancement of the CT population difference in an arbitrary spin-5/2 nucleus. Theoretically, ST inversion is more efficient at creating a larger population difference accross the CT. For the ST inversions, the outer transitions (m = ±5/2 are inverted with the inner satellites (m = ±3/2) followed by inversion of the inner satellites with the central states (m = ±1/2). For the ST saturation, the three lower energy states are equalized and the three upper states are equalized.

For the saturation of STs, these can be a double frequency sweeps (DFS)[55] shaped pulse or a series of pulses with alternating phases known as the rotor assisted population transfer (RAPT)[56] sequence under MAS conditions. In the DFS experiment, the ST

frequencies are adiabatically swept in order to saturate the ST populations and to allow for enhanced polarization across the CT. Saturation of the STs has a theoretical enhancement level of $I + 1/2$ (or 2, 3, 4, or 5 for $I = 3/2$, 5/2, 7/2, or 9/2 respectively).[54] As for the inversion of the STs, this can be achieved using the family of selective offset-independent adiabatic[57] inversion pulses such as the hyperbolic secant (HS)[58] pulses with theoretical maximum enhancements of $2I$ (or 3, 5, 7, or 9 for $I = 3/2$, 5/2, 7/2, or 9/2 respectively). It is advantageous when using HS pulses to have prior knowledge of the magnitude of the QI in the system of interest. Therefore, in all the cases in this thesis, the DFS signal enhancement method was used as its implementation is a lot more uniformly sensitive to systems containing a distribution of C_Q values.

2.7 Computational Methods

As stated in the Objectives (Chapter 1.11) of this thesis, computational methods will be used in this thesis as a complementary technique to the SSNMR experiments performed herein. The computational techniques that will be discussed allow for the prediction of the experimental NMR parameters as well as the visualization of the EFG and CS tensors of the nucleus under study. These methods are used in general to corroborate experimental findings by NMR and to identify the underlying structural mechanism that affects a certain NMR parameter.

2.7.1 DFT Calculations

In general, to theoretically model some property of a molecule in its ground state, one must solve the Schrödinger equation (equation 2.2). The Hamiltonian, $\hat{H}$, is the sum of

kinetic and potential energy operators of the collection of electrons and nuclei, Ψ is an eigenfunction of $\hat{H}$ describing the wave function of that state, and E is the total energy of the state referring to Ψ.

(2.2) $\hat{H}\Psi = E\Psi$

Under the Born-Oppenheimer approximation, the total wave function, Ψ, can be split into electronic and nuclear components ($\Psi = \Psi_{elec}\Psi_{nuc}$) because electrons move a lot more quickly than nuclei due to the smaller mass of electrons. Hence, the interest here is to solve Schrödinger's equation using only Ψ_{elec} since electrons are responsible for most chemical properties. The electronic wave function, henceforth referred to as simply Ψ for conciseness, has four coordinates: the spatial coordinates (x, y, and z) and a spin coordinate (φ).

(2.3) $\Psi(x,y,z,\varphi) = \Psi(\mathbf{r},\varphi) = \Psi(\mathbf{x})$

For a system containing N electrons, Ψ will be a function of space and spin coordinates for N electrons (i.e. $\Psi(\mathbf{x_1},\mathbf{x_2},\mathbf{x_3},\mathbf{x_4},\ldots,\mathbf{x_N})$). In practice, the wavefunction is constructed with the use of molecular orbitals. In density functional theory (DFT), the square of the complicated N-electron and 4-coordinate wavefunction is approximated as the electron density, $\rho(\mathbf{r})$, thus allowing for the use of a 3D function to describe the system (equation 2.4).[59]

(2.4) $|\Psi(\mathbf{x_1},\mathbf{x_2},\mathbf{x_3},\mathbf{x_4},\ldots,\mathbf{x_N})|^2 = \rho(\mathbf{r})$

From the Hohenberg-Kohn theorem, there exists a functional of density $\rho(\mathbf{r})$, that will allow for the determination of the energy E according to equation 2.5:[60]

(2.5) $E = E[\rho(\mathbf{r})]$

The exact nature of $\rho(\mathbf{r})$ is unknown; therefore the calculations must resort to the use of orbitals using the Kohn-Sham approach.[61] The Kohn-Sham orbitals are not the conventional molecular orbitals but express $\rho(\mathbf{r})$ in terms of the number of spin-up (N^{α}) and spin-down (N^{β}) orbitals according to equation 2.6.

$$(2.6)\quad \rho(\mathbf{r}) = \sum_{a=1}^{N^{\alpha}} |\Psi_a^{\alpha}(\mathbf{r})|^2 + \sum_{b=1}^{N^{\beta}} |\Psi_b^{\beta}(\mathbf{r})|^2$$

In the Kohn-Sham approach, the total energy is decomposed into an electronic kinetic energy component, T, a Coulombic term, U, as well as term E_{xc} that factors in electronic exchange and correlation such that:

$$(2.7)\quad E[\rho(\mathbf{r})] = T[\rho(\mathbf{r})] + U[\rho(\mathbf{r})] + E_{xc}[\rho(\mathbf{r})]$$

From the geometry of the molecule, the T and U terms can easily be calculated. The final component is the exchange and correlation (XC) functional which is an unknown functional that remains an active area of research in computational chemistry.[62] Many XC functionals have been proposed; those important for the calculations in the present dissertation are mentioned below.

Multiple software packages are currently available for the calculations of NMR parameters. In this thesis, some calculations were performed using the Gaussian '09 program[63] for cluster model based calculations. For a cluster model, a structural model based on the experimentally determined X-ray crystal structure is built around the nucleus of interest. For NMR parameter calculations, the model can usually be truncated to contain atoms located within 3 – 4 Å away from the nucleus in order to reduce computational time

and cost. In most circumstances, electrons and nuclei located outside this distance radius do not affect the accuracy of the calculated NMR parameters. In the case of this thesis, all Gaussian calculations used the DFT method described above. Many DFT methods exist but for the Gaussian cluster model calculations shown herein, the popular hybrid Becke three-parameter Lee-Yang-Parr (B3LYP) functional[64] was chosen. The B3LYP hybrid functional has been shown previously to accurately reproduce experimental SSNMR parameters in ionic solids.[65]

2.7.2 ZORA DFT

Another cluster-based model program used was the Amsterdam Density Functional (ADF) program specifically for the calculation of some $^{79/81}$Br SSNMR parameters in Chapter 3. The ADF program[66,67,68] allows for the inclusion of relativistic effects in the calculations under the zeroth-order regular approximation (ZORA) formulism.[69] The electrons closest to the nucleus (i.e., the core electrons) in heavy elements begin to travel close to the speed of light, and so it becomes important to incorporate the effects of relativity into the calculations. In the ZORA DFT method, the kinetic energy functional, $T[\rho(\mathbf{r})]$, is expressed using the Dirac formulism in order to account for relativity in the kinetic energy of the electrons closest to the nucleus. The kinetic energy functional is further split into a one-component (scalar relativity) term and the so-called spin-orbit terms, which factors in the splitting of the orbital energy levels via the coupling of the electron spin and the angular momentum caused by orbital motions.[70] Scalar as well as spin-orbit relativistic effects are the most important factors when explaining certain behaviors of heavy elements. One application where including relativistic effects are important is in the calculation of CS tensors for heavy elements such as ^{199}Hg and ^{207}Pb.[71] For bromine and iodine for example,

including relativistic effects has been shown to be of importance in the calculation of ^{1}H chemical shifts in HBr and HI.[72]

2.7.3 GIPAW DFT

Most of the calculations performed in this thesis used the gauge-including projector-augmented-wave (GIPAW) DFT method, where, rather than constructing an isolated cluster model, the experimentally determined 3D X-ray crystal structure is used as input for the DFT calculation. In the case of ionic solids such as those studied in this work, cluster models are often in poor agreement with experiment because of the repetitive nature of the unit cell (smallest repetitive unit in a solid). For example, long-range effects such as packing of the unit cell can effect on EFG tensor parameters given their $1/r^3$ distance dependence to the surrounding charges (see equation 1.18). Thus, atoms located in an adjacent unit cell might affect the EFG about the nucleus of interest. In any crystal, there exist too many electrons in order to perform any meaningful calculation using the cluster-model approach explained above. Since the unit cell is repeated an infinite number of times in a crystal, the GIPAW DFT approach uses periodic boundary conditions that modulates the wave function by a periodic function, $u_{\mathrm{N},\mathbf{k}}(\mathbf{r})$:[73]

$$\Psi_{\mathrm{N},\mathbf{k}}(\mathbf{r}) = e^{i\mathbf{k}.\mathbf{r}} u_{\mathrm{N},\mathbf{k}}(\mathbf{r}) \quad (2.8)$$

Since $u_{\mathrm{N},\mathbf{k}}(\mathbf{r})$ is periodic, the wave function at the same lattice position in an adjacent unit cell (related to $\mathbf{r}$ by a lattice vector $\mathbf{R}$) must be identical to $u_{\mathrm{N},\mathbf{k}}(\mathbf{r})$ such that $u_{\mathrm{N},\mathbf{k}}(\mathbf{r}) = u_{\mathrm{N},\mathbf{k}}(\mathbf{r} + \mathbf{R})$. In equation 2.8, the value of $\mathbf{k}$ is defined as the number of *k*-points used in the calculations, which is the number of sampling points determined in reciprocal lattice space within the Brillouin zone.[74,75] In the GIPAW DFT method, plane waves are used as the basis functions

for the $\Psi_{N,\mathbf{k}}(\mathbf{r})$ function, because they are simple mathematically and, due to their complex exponential form (e^{ix}), they incorporate the necessary periodic boundary condition with respect to the lattice symmetry.[73,76] The core region of the total electronic wave density of an atom has high kinetic energy from the faster moving electrons in close proximity the nucleus due to the decrease in potential energy of the core electrons. As a result, the wave function describing the core electrons is described by a large number of oscillations, which become increasingly more difficult to model with plane waves. In order to increase the speed of the calculations, smooth functions known as pseudopotentials are used to approximate the core electron wave function up to a certain critical radius from the nucleus. After that critical distance, the pseudopotential accurately depicts the smooth nature of total wave function of the outer shell electrons. The pseudopotentials available within the Cambridge Serial Total Energy Package (CASTEP) code,[77,78,79] (i.e., the software packaged used for GIPAW DFT computations in this thesis), have been previously optimized for NMR calculations on some known systems. When setting up a GIPAW DFT calculation, a kinetic energy cut-off, E_{cut}, and *k*-point grid are specified. The E_{cut} is a representation of the quality of the chosen ensemble of plane wave functions and the number of *k*-point sampling points used to perform the calculation. The value of E_{cut} becomes the main adjustable parameter for the desired accuracy and convergence level of the calculation.[76] Lower E_{cut} values may result in a lower accuracy of the calculated NMR parameters but higher E_{cut} values will result in more computational time and expense. The volume of the crystal structure's unit cell will dictate the value of E_{cut} permissible to obtain a convergence in the calculation. Hence, both the E_{cut} and *k*-point settings are a measurement of the accuracy of the plane wave basis functions used to approximate the periodic wave function of the crystal.

2.7.4 Other Important Points

As will be discussed in the pertinent chapters, it is most often essential to optimize the hydrogen atom positions of an X-ray crystal structure or of a cluster model prior to the calculation of NMR parameters. Most structures solved as part of this thesis, as well as those used from the literature, were acquired using single-crystal X-ray diffraction, which does not position the hydrogen atoms accurately. Since X-ray diffraction measures electron densities, it is difficult to detect the presence of hydrogen atoms using this method because hydrogen only has one valence electron. Hydrogen atoms are only inferred during the structure solving process but often have fixed bond lengths that are not representative of the system under study. If a neutron diffraction structure exists, however, geometry optimization of the hydrogen positions is not necessary as these are known from experiment. All three computational programs referred to above (Gaussian, ADF, and CASTEP) allow for the positional optimization of hydrogen atoms.

Finally, it is possible to extract the MS and EFG tensor parameters from a DFT calculation using a data parsing program written in the Bryce group, known as the EFGShield program.[80] It is noted here that the MS tensor data must be converted into CS tensor data using equation 1.8. Currently, EFGShield has a graphical user interface and can extract NMR parameters as well as the relative MS and EFG tensor orientations from Gaussian, ADF, and CASTEP calculations. The MS and EFG tensor orientations can be visualized using a third party software such as Diamond (Crystal Impact) or Mercury (CCDC).

2.8 References for Chapter 2

1. Ernst, R. R.; Anderson, W. A. *Rev. Sci. Instrum.* **1966**, *37*, 93.
2. Bryce, D. L.; Bernard, G. M.; Gee, M.; Lumsden, M. D.; Eichele, K.; Wasylishen, R. E. *Can J. Anal. Sci. Spect.* **2001**, *46*, 46-82.
3. Duer, M. J. Introduction to Solid-State NMR Spectroscopy, Blackwell, Oxford UK, **2004**.
4. Farmer, R. M.; Popov, A. I. *Inorg. Nucl. Chem. Lett.* **1981**, *17*, 51.
5. Bryce, D. L. *Dalton Trans.* **2010**, **39**, 8577.
6. Chan, J. C. C. *Concepts Magn. Reson.* **1999**, *11*, 363.
7. Keeler, J. Understanding NMR Spectroscopy, 2nd Edition, Wiley, Hoboken NJ, **2010**.
8. Hahn, E. L. *Phys. Rev.* **1950**, *80*, 580.
9. Solomon, I. *Phys. Rev.* **1958**, *100*, 61.
10. Weisman, I. D.; Bennett, L. H. *Phys. Rev.* **1969**, *181*, 1343.
11. Bodart, P. R.; Amoureux, J.-P.; Dumazy, Y.; Lefort, R. *Mol. Phys.* **2000**, *98*, 1545.
12. A. L. Bloom, J. N. Shoolery, *Phys. Rev.* **1955**, *97*, 1261.
13. Ernst, M. *J. Magn. Reson*. **2003**, *162*, 1.
14. Massiot, D.; Farnan, I.; Gautier, N.; Trumeau, D.; Trokiner, A.; Coutures, J. P. *Solid State Nucl. Magn. Reson. Spectrosc.* **1995**, *4*, 241.
15. Schurko, R. W. *Acc. Chem. Res.* **2013**, *46*, 1985.
16. Perras, F. A.; Widdifield, C. M.; Bryce, D. L. *Solid State Nucl. Magn. Reson*. **2012**, *45–46*, 36.
17. Andrew, E. R.; Bradbury, A.; Eades, R. G. *Nature* **1958**, *182*, 1659.

18. Lowe, I. J. *Phys. Rev. Lett.* **1959**, *2*, 285.

19. Andrew, E. R. *Prog. Nucl. Magn. Reson. Spectrosc.* **1971**, *8*, 1.

20. MAS probes are commercially available. URL: http://www.bruker.com/products/mr/nmr/probes/probes/solids/hx-cp-mas/overview.html, consulted October 27 2014.

21. Samoson, A.; Kunkla, E.; Lippmaa, E. *J. Magn. Reson.* **1982**, *49*, 350.

22. Freude, D.; Haase, J.; Klinowski, J.; Carpenter, T. A.; Ronikier, G. *Chem. Phys. Lett.* **1985**, *119*, 365.

23. Kundla, E.; Samoson, A.; Lippmaa, E. *Chem. Phys. Lett.* **1981**, *83*, 229.

24. Dupree, R. Double Rotation NMR in "Encyclopedia of Magnetic Resonance", Wiley, **2011**.

25. Samoson, A.; Lippmaa, E.; Pines, A. *Mol. Phys.* **1988**, *65*, 1013–1018.

26. Chmelka, B. F.; Mueller, K. T.; Pines, A.; Stebbins, J.; Wu, Y.; Zwanziger, J. W. *Nature* **1989**, *339*, 42–43.

27. Wu, Y.; Sun, B. Q.; Pines, A.; Samoson, A.; Lippmaa, E. *J. Magn. Reson.* **1990**, *89*, 297.

28. Wong, A.; Howes, A. P.; Yates, J. R.; Watts, A.; Anupold, T.; Past, J.; Samoson, A.; Dupree, R.; Smith, M. E. *Phys. Chem. Chem. Phys.* **2011**, *13*, 12213.

29. Perras, F. A.; Bryce, D. L. *J. Magn. Reson.* **2011**, *213*, 82.

30. Howes, A. P.; Vedishcheva, N. M.; Samoson, A.; Hanna, J. V.; Smith, M. E.; Holland, D.; Dupree, R. *Phys. Chem. Chem. Phys.* **2011**, *13*, 11919.

31. Frydman, L.; Harwood, J. S. *J. Am. Chem. Soc.* **1995**, *117*, 5367.

32. Medek, A.; Harwood, J. S.; Frydman, L. *J. Am. Chem. Soc.* **1995**, *117*, 12779.

33. Ashbrook, S. E.; Sneddon, S. *J. Am. Chem. Soc.* **2014**, *136*, 15440.

34. Jerschow, A. *Prog. Nucl. Magn. Reson.* **2005**, *46*, 63.

35. Amoureux, J.-P.; Pruski, M. MQMAS Advances, in "Encyclopedia of Magnetic Resonance", Wiley, **2007**.

36. Stejskal, E. O.; Schaefer, J.; Waugh, J. S. *J. Magn. Reson.* **1977**, *28*, 105.

37. Pines, A.; Gibby, M. G.; Waugh, J. S. *J. Chem. Phys.* **1972**, *56*, 1776.

38. Hartmann, S. R.; Hahn, E. L. *Phys. Rev.* **1962**, *128*, 2042.

39. Vega, A. J. *Solid State Nucl. Magn. Reson.* **1992**, *1*, 17.

40. Fernandez, C.; Pruski, M. *Topics Curr. Chem.* **2012**, *306*, 119.

41. Perras, F. A.; Viger-Gravel, J.; Burgess, K. M. N.; Bryce, D. L. *Solid State Nucl. Magn. Reson.* **2013**, *51-52*, 1.

42. Ashbrook, S. E.; Duer, M. J. *Concepts Magn. Reson. Part A* **2006**, *28A*, 183.

43. Ashbrook, S. E.; Wimperis, S. *J. Chem. Phys.* **2009**, *131*, 194509.

44. Widdifield, C. M.; Moudrakovski, I.; Bryce, D. L. *Phys. Chem. Chem. Phys.* **2014**, *16*, 13340.

45. Lipton, A. S.; Heck, R.W.; Hernick, M.; Fierke, C. A.; Ellis, P. D. *J. Am. Chem. Soc.* **2008**, *130*, 12671.

46. Lipton, A.S.; Heck R.W.; de Jong, W.A.; Gao, A.R.; Wu, X.; Roehrich, A.; Harbison, G.S.; Ellis, P.D. *J. Am. Chem. Soc.* **2009**, *131*, 13992.

47. Cheng, J. T.; Ellis, P. D. *J. Phys. Chem.* **1989**, *93*, 2549

48. Hung, I.; Gan, Z. *J. Magn. Reson.* **2010**, *204*, 256.

49. Larsen, F. H.; Jakobsen, H. J.; Ellis, P. D.; Nielsen, N. C. *J. Phys. Chem. A* **1997**, *101*, 8597.

50. O'Dell, L. A.; Schurko, R. W. *Chem. Phys. Lett.* **2008**, *464*, 97.

51. Hamaed, H.; Laschuk, M. W.; Terskikh, V. V.; Schurko, R. W. *J. Am. Chem. Soc.* **2009**, *131*, 8271.

52. Perras, F. A.; Bryce, D. L. *Angew. Chem. Int. Ed.* **2012**, *51*, 4227.

53. Siegel, R.; Nakashima, T. T.; Wasylishen, R. E. *Concepts Magn. Reson. A*, **2005**, *26*, 47.

54. Perras, F. A.; Viger-Gravel, J.; Burgess, K. M. N.; Bryce, D. L. *Solid State Nucl. Magn. Reson.* **2013**, *51*-52, 1.

55. Kentgens, A. P. M.; Verhagen, R. *Chem. Phys. Lett.* **1999**, *300*, 435–443.

56. Yao, Z.; Kwak, H.-T.; Sakellariou, D.; Emsley, L.; Grandinetti, P. J. *Chem. Phys. Lett.* **2000**, *327*, 85.

57. Tannús, A.; Garwood, M. *NMR Biomed.* **1997**, *10*, 423.

58. Siegel, R.; Nakashima, T. T.; Wasylishen, R. E. *Chem. Phys. Lett.* **2004**, *388*, 441.

59. Callaway, J.; March, N. H. *Solid State Physics* **1984**, *38*, 135.

60. Hohenburg, P.; Kohn, W. *Phys. Rev. B* **1964**, *136*, 864.

61. Kohn, S.; Sham, L. J. *Phys. Rev.* **1965**, *140*, A1133.

62. Scuseria, G. E.; Staroverov, V. N. Progress in the Development of Exchange-Correlation Functionals, in "Theory and Applications of Computational Chemistry: The First Forty Years", 1st Edition, Elsevier Science, Amsterdam, **2005**, Chapter 24, p. 663-724.

63. Gaussian 09, Revision A.02, Frisch, M. J.; Trucks, G. W.; Schlegel, H. B.; Scuseria, G. E.; Robb, M. A.; Cheeseman, J. R.; Scalmani, G.; Barone, V.; Mennucci, B.; Petersson, G. A.; Nakatsuji, H.; Caricato, M.; Li, X.; Hratchian, H. P.; Izmaylov, A.

F.; Bloino, J.; Zheng, G.; Sonnenberg, J. L.; Hada, M.; Ehara, M.; Toyota, K.; Fukuda, R.; Hasegawa, J.; Ishida, M.; Nakajima, T.; Honda, Y.; Kitao, O.; Nakai, H.; Vreven, T.; Montgomery, J. A., Jr.; Peralta, J. E.; Ogliaro, F.; Bearpark, M.; Heyd, J. J.; Brothers, E.; Kudin, K. N.; Staroverov, V. N.; Kobayashi, R.; Normand, J.; Raghavachari, K.; Rendell, A.; Burant, J. C.; Iyengar, S. S.; Tomasi, J.; Cossi, M.; Rega, N.; Millam, N. J.; Klene, M.; Knox, J. E.; Cross, J. B.; Bakken, V.; Adamo, C.; Jaramillo, J.; Gomperts, R.; Stratmann, R. E.; Yazyev, O.; Austin, A. J.; Cammi, R.; Pomelli, C.; Ochterski, J. W.; Martin, R. L.; Morokuma, K.; Zakrzewski, V. G.; Voth, G. A.; Salvador, P.; Dannenberg, J. J.; Dapprich, S.; Daniels, A. D.; Farkas, Ö.; Foresman, J. B.; Ortiz, J. V.; Cioslowski, J.; Fox, D. J. Gaussian, Inc., Wallingford CT, **2009**

64. Becke, A. D. *J. Chem. Phys.* **1993**, *98*, 5648.

65. Bryce, D. L.; Sward, G. D.; Adiga, S. *J. Am. Chem. Soc.* **2006**, *128*, 2121.

66. ADF2013, SCM, Theoretical Chemistry, Vrije Universiteit, Amsterdam, The Netherlands, http://www.scm.com

67. Te Velde, G.; Bickelhaupt, F. M.; van Gisbergen, S. J. A.; Fonseca Guerra, C.; Baerends, E. J.; Snijders, J. G.; Zieger, T. *J. Comput. Chem.* **2001**, *22*, 931.

68. Fonseca Guerra, C.; Snijders, J. G.; te Velde, G.; Baerends, E. J. *Theor. Chem. Acc.* **1998**, *99*, 391.

69. van Lenthe, E.; Snijders, J. G.; Baerends, E. J. *J. Chem. Phys.* **1996**, *105*, 6505.

70. Autschbach, J. *J. Chem. Phys.* **2012**, *136*, 150902.

71. Autschbach, J.; Ziegler, T. Relativistic Computation of NMR Shieldings and Spin-Spin Coupling Constants in “Encyclopedia of Magnetic Resonance”, Wiley, **2007**.

72. Autschbach, J. Calculation of NMR and EPR Parameters (M. Kaupp, M. Bühl, and V. B. Malkin, editors), Wiley, **2004**.

73. Yates, J. R.; Pickard, C. J. Computations of Magnetic Resonance Parameters for Crystalline Samples in "Encyclopedia of Magnetic Resonance", Wiley, **2008**.

74. Chadi, D. J.; Cohen, M. L. *Phys. Rev. B* **1973**, 8, 5747.

75. Yates, J. R.; Pickard, C. J.; Mauri, F. *Phys. Rev. B* **2007**, 76, 024401.

76. Charpentier, T. *Solid State Nucl. Magn. Reson.* **2011**, *40*, 1.

77. Segall, M. D.; Lindan, P. J. D.; Probert, M. J.; Pickard, C. J.; Hasnip, P. J.; Clark, S. J.; Payne, M. C. *J. Phys. Condens. Matter* **2002**, *14*, 2717.

78. Pickard, C. J.; Mauri, F. *Phys. Rev. B* **2001**, *63*, 245101.

79. Profeta, M.; Mauri, F.; Pickard, C. J. *J. Am. Chem. Soc.* **2003**, *125*, 541.

80. Adiga, S.; Aebi, D.; Bryce, D. L. *Can. J. Chem.* **2007**, *85*, 496.

3 A Combined $^{79/81}$Br SSNMR and X-ray Crystallography Study of Triphenylphosphonium Bromides

3.1 Introduction and Objectives

Phosphonium halides are a class of compounds which contain a tetrahedral phosphorus cation with a halide counter ion. They have garnered much interest in the literature because of their applications in various fields of chemistry. For instance, many of them are ionic liquids and are considered to have an advantage over the more common ammonium and imidazolium analogues because they are less expensive and more thermally stable (i.e., higher melting points).[1] They are also usually less hygroscopic, and lack an acidic proton[2] making them ideal candidates for solvents in "green" cross-coupling reactions involving basic additives.[3] Furthermore, phosphonium halides are phase-transfer catalysts[4,5] and reagents[6,7] in the synthesis of natural products (i.e., the Wittig reaction).[8,9] Importantly, it was shown that the counter ion plays a key role in the kinetics of these reactions.[10] Phosphonium halides bearing the alkyl triphenylphosphonium (TPP) cation have been employed as fertilizers,[11] anion receptors,[12] and are known to inhibit mitochondrial function specifically in cancerous cells.[13,14,15] Recently, their role as surfactants in polymer-cellulose[16] and polymer-clay nanocomposites[17,18] has been explored. In light of the

importance of this class of compounds, it is desirable to fully characterize the different components of phosphonium halides including the local electronic environment surrounding the phosphorus and halogen nuclei, and how these relate to crystal packing. SSNMR is a versatile tool amenable to this type of analysis.

In this Chapter, is reported a multinuclear (i.e., ^{31}P and $^{79/81}$Br) SSNMR study of phosphonium bromides containing the TPP moiety, with an emphasis on characterizing the ^{31}P and $^{79/81}$Br CS tensors. One account in the literature on the evaluation of ^{31}P CS tensor components by Ackermann *et al.* describes the effects of systematically replacing phenyl groups with furyl rings in ethyltriphenylphosphonium iodide.[19] They concluded that the smallest component of the CS tensor, δ_{33}, lies along the P–C(ethyl) bond as this would be consistent with Ramsey's theory of shielding (*vide infra*) as replacing phenyl rings with furyl rings results in a decrease in σ_{para} as electron density is withdraw from the phosphorus p orbitals.[19,20] Since ^{79}Br and ^{81}Br are quadrupolar nuclei with I = 3/2, additional information may be obtained by measuring the EFG tensor at the bromine nuclei. Because of the large quadrupole moments associated with bromine (see Chapter 1: $Q(^{81}\text{Br})$ = 262 mb and $Q(^{79}\text{Br})$ = 313 mb), CT lineshapes are often quite broad and NMR studies in the past have been limited to relatively symmetric systems.[21,22] Prior halogen NMR studies on the analogous ammonium and imidazolium halides exist.[23,24] For bromine examples, Alonso *et al.* report on the study of polycrystalline $C_xH_{2x+1}(CH_3)_3NBr$ samples and have shown that variations in the value of the ^{81}Br C_Q were due to small changes in the N–Br distance as the alkyl chain length is increased.[25] Other noteworthy examples are that of Ripmeester and co-workers where they studied the halogen (^{35}Cl, ^{79}Br, and ^{127}I) counter ion *via* solid and liquid state NMR in quaternary ammonium salts of room temperature ionic liquids in an effort to observe

residual order as the sample melted.[26] Bromine SSNMR experiments performed on TPP-based phosphonium halides will contribute to the general understanding of the relationship between the NMR parameters and the bromine local environment; we note in particular that data on bromine CS tensors are particularly sparse. Therefore, as part of this Chapter, it will be exciting to see how in particular the CS tensor parameters, could be used as a measurement of a specific structural feature of the TPP bromides. In order to achieve this, single crystal X-ray diffraction will first be employed in order to fully elucidate the solid-state structure of these systems.

In this Chapter, GIPAW DFT calculations will also be used in order to accurately model the infinite crystalline lattice of these ionic phosphonium halides. This method has been used by our group in the past for other systems containing bromine nuclei.[27,28] The aim here is that these computations will prove to be useful alongside the experimental NMR parameters when discussing the environment of the bromine nucleus in phosphonium halides.

3.2 Experimental section

3.2.1 Sample preparation

All phosphonium halides were purchased from commercial sources. Butyltriphenylphosphonium bromide ($BuPPh_3Br$), propyltriphenylphosphonium bromide ($PrPPh_3Br$), ethyltriphenylphosphonium bromide ($EtPPh_3Br$), methyltriphenylphosphonium bromide ($MePPh_3Br$) and tetraphenylphosphonium bromide (PPh_4Br) were purchased from Sigma-Aldrich while triphenylphosphonium hydrobromide $HPPh_3Br$), cyclopentyltriphenylphosphonium bromide ($C_5H_9PPh_3Br$) and butyltriphenylphosphonium

chloride ($BuPPh_3Cl$) were purchased from Alfa Aesar. All were used without further purification with the exception of PPh_4Br and $MePPh_3Br$, which were recrystallized from ethanol. All samples were ground into fine powders in air and packed into appropriately sized Bruker MAS zirconia rotors.

Appropriately sized single crystals for PPh_4Br, $EtPPh_3Br$, $MePPh_3Br$, and $C_5H_9PPh_3Br$ were grown in ethanol with the slow evaporation method. Approximately 0.5 g of powder was dissolved in a minimum of ethanol. In order to remove any undissolved material, the solution was filtered through a glass pipette plugged with a tissue into a separate vial. The desired crystals were formed upon standing in air overnight. Crystals of $PPh_4Br{\cdot}H_2O$ were grown from MeCN by slow diffusion of *n*-hexanes overnight. As for $BuPPh_3Cl$, a single crystal of suitable size was taken from the bottle sent by the manufacturer.

3.2.2 Single crystal X-ray diffraction

Suitable crystals were selected, mounted on a thin glass fibre using paraffin oil, and cooled to the data collection temperature of 200 K for all six samples. Data were collected on a Bruker AXS SMART single crystal diffractometer equipped with a sealed Mo tube source (wavelength = 0.71073 Å), and an APEX II CCD detector. Raw data collection and processing were performed with the APEX II software package from BRUKER AXS.[29] Diffraction data for the samples were collected with a sequence of 0.3° ω scans at 0° (650 frames), 120° (650 frames), and 240° (650 frames) in φ for all samples with the exception of PPh_4Br and $PPh_4Br{\cdot}H_2O$, which were collected with 0.3° ω scans at 0° (600 frames), 90° (600 frames), 180° (600 frames), 270° (600 frames), and an additional 50 frames at 0° in φ.

Initial unit cell parameters were determined from 60 data frames collected at different sections of the Ewald sphere. Semi-empirical absorption corrections based on equivalent reflections were applied.[30] The systematic absences and unit cell parameters were consistent with the space group $C2/c$ for $EtPPh_3Br$, $P2_1/n$ for $MePPh_3Br$, $Pnma$ for $C_5H_9PPh_3Br$, $P\bar{1}$ for PPh_4Br, $P\bar{1}$ for $PPh_4Br{\cdot}H_2O$, and $P2_1/c$ for $BuPPh_3Cl$. Solutions in the non-centrosymmetric space groups yielded chemically reasonable and computationally stable results of refinement. The structures were solved by direct methods, completed with difference Fourier syntheses, and refined with full-matrix least-squares procedures based on F^2. Positions of all the hydrogen atoms were obtained from the Fourier map analysis; however, all hydrogen atoms were treated isotropically. All scattering factors are contained in several versions of the SHELXTL program library, with the latest version used being v.6.12.[31] Crystallographic data are reported in Table 3.1 in the main text as well as in Table 3.4 for $PPh_4Br{\cdot}H_2O$. The crystallographic information files (.cif) for all new crystal structures can be found in Appendix B3.

3.2.3 Solid-state NMR Spectroscopy

3.2.3.1 Experiments at 4.7 T

Phosphorus-31 NMR experiments were performed on a Bruker AVANCE III NMR spectrometer (B_0 = 9.4 T, $\nu_L(^{31}P)$ = 80.998 MHz) using a Bruker 7 mm HXY triple-resonance MAS probe. Experimental setup and pulse calibration were performed with solid ammonium dihydrogen phosphate (ADP; δ_{iso} = 0.81 ppm with respect to 85% H_3PO_4 in D_2O) at room temperature.[32] Spectra were collected under MAS (ν_{rot} = 4.5 kHz; the number of scans were 32 and 16 for $MePPh_3Br$ and $BuPPh_3Cl$ respectively) as well as under stationary conditions

(the number of scans was 256 for both $MePPh_3Br$ and $BuPPh_3Cl$) using CP along with CW proton decoupling during the acquisition time.[33] The measured $\pi/2$ ^1H pulse lengths varied between 3.3 and 3.5 μs, the contact time was 2.0 ms, and the recycle delay used was of 2.0 s as it provided the maximum amount of signal.

3.2.3.2 Experiments at 9.4 T

Phosphorus-31, chlorine-35/37, and bromine-79/81 NMR experiments were performed on a Bruker AVANCE III NMR spectrometer (B_0 = 9.4 T, $\nu_L(^{31}P)$ = 161.976 MHz, $\nu_L(^{35}Cl)$ = 39.204 MHz, $\nu_L(^{37}Cl)$ = 32.634 MHz, $\nu_L(^{79}Br)$ = 100.248 MHz, and $\nu_L(^{81}Br)$ = 108.061 MHz) using a Bruker 4 mm HXY triple-resonance MAS probe. For phosphorus experiments, pulse calibrations were carried out with solid ADP at room temperature. Spectra were collected under MAS (ν_{rot} = 8 kHz; the number of scans were 16, 64, and 128 for $EtPPh_3Br$, $PrPPh_3Br$, and $BuPPh_3Br$ respectively) as well as under stationary conditions using CP along with two-pulse-phase-modulation (TPPM) proton decoupling during the acquisition time.[34] The measured $\pi/2$ ^1H pulse lengths were between 3.1 and 3.3 μs, the contact time was 5.0 ms, and the recycle delay used was of 2.0 s. For chlorine NMR experiments, experimental setup and pulse calibrations were carried out with solid NH_4Cl (δ_{iso} = 121.1 ppm with respect to solid NaCl)[35] at room temperature. The CT-selective pulse, used for $BuPPh_3Cl$ was that of NH_4Cl scaled by a factor of $1/(I + 1/2) = 1/2$ for both isotopes as this salt packs in a cubic lattice. The measured pulse lengths for $BuPPh_3Cl$ were 5.0 μs for both ^{35}Cl and ^{37}Cl respectively and the recycle delay used was of 2.0 s. See Table A3.1 for more specific details. Spectra were collected under MAS (ν_{rot} = 8 kHz) conditions using a rotor-synchronized Solomon echo with CW proton decoupling. For bromine experiments,

experimental setup and pulse calibrations were carried out with solid KBr (δ_{iso} = 54.31 and 54.51 ppm for ^{79}Br and ^{81}Br respectively with respect to 0.03 M NaBr in D_2O)[36] at room temperature. The CT-selective pulse used for the phosphonium bromides was that KBr scaled by a factor of $1/(I + 1/2) = 1/2$ for both isotopes since this salt packs in a cubic lattice. Typical measured pulse lengths were between 1.5 and 1.6 μs for ^{79}Br and between 1.0 and 1.3 μs for ^{81}Br for the compounds studied. The recycle delays used ranged from 0.2 to 0.5 s. Spectra were collected under stationary conditions using the Solomon echo sequence with CW proton decoupling. See Table A3.1 for more specific details on each compound.

3.2.3.3 Experiments at 11.75 T

Bromine-79/81 NMR experiments were performed on a Bruker AVANCE NMR spectrometer (B_0 = 11.75 T ($\nu_L(^{79}Br)$ = 125.302 MHz and $\nu_L(^{81}Br)$ = 135.068 MHz)) using a Bruker 4 mm HXY triple-resonance MAS probe. Experimental setup and pulse calibrations were carried out with solid KBr at room temperature. The CT-selective pulses were used as denoted earlier. Typical measured pulse lengths were between 2.0 and 2.2 μs for ^{79}Br and between 1.5 and 2.0 μs for ^{81}Br. The recycle delays used ranged from 0.2 to 0.5 s. See Table A3.1 for more specific details on each compound. Spectra were collected under stationary conditions using the Solomon echo sequence with CW proton decoupling. For some samples, it was necessary to use the VOCS data acquisition method.

3.2.3.4 Experiments at 21.1 T

Chlorine-35 and bromine-81 SSNMR data were also acquired at the National Ultrahigh-Field NMR Facility for Solids in Ottawa with a Bruker AVANCE II spectrometer

operating at B_0 = 21.1 T ($\nu_L(^{35}Cl)$ = 88.194 MHz and $\nu_L(^{81}Br)$ = 243.094 MHz). Chlorine experiments used a Bruker 4 mm HX MAS probe and experimental setup and pulse calibrations were referenced to solid NaCl as 0.00 ppm at room temperature. Since NaCl has a cubic ion lattice, the same statement as mentioned above for CT-selective pulses applies. Spectra were collected under MAS (ν_{rot} = 5 kHz) conditions with a pulse length of 2.0 μs and a recycle delay of 2.0 s using a rotor synchronized Solomon echo sequence with CW proton decoupling. For bromine experiments, stationary samples used a home-built HX static probe with a 5 mm coil while MAS experiments were carried out on a Bruker 2.5 mm HX probe (ν_{rot} = 31.25 kHz) and a Bruker 1.3 mm HX probe (ν_{rot} = 62.5 kHz). Experimental setup and calibrations were done with solid KBr. A rotor synchronized Solomon echo pulse sequence with CW proton decoupling (except at ν_{rot} = 62.5 kHz) with a pulse length of 1.0 μs and recycle delays between 0.5 and 1.0 s was used for all bromine samples. See Table A3.1 in Appendix A for more specific details.

3.2.4 Data processing and simulations

All NMR spectra were processed with Bruker's TopSpin 3.0 software. The FIDs acquired with Solomon echo sequences were left-shifted an appropriate number of points to the top of the CT echo signal. The NMR spectra were then simulated in the frequency domain in order to extract the experimental EFG and CS tensor parameters using the WSolids[37] software package, which incoroporates the high-field approximation[38,39] wherein the QI is treated as a perturbation the Zeeman Hamiltonian. Thus the quadrupolar interactions are treated using second-order perturbation theory. The simulations assumed one

or two (see main text) crystallographically distinct sites, consistent with the single crystal XRD data. Stack plots for figures were generated with DMFit (v. 2010).[40]

3.2.5 GIPAW DFT Computations

GIPAW DFT computations were performed with version 4.1 of CASTEP–NMR and input files were generated using the available crystal structure data *via* Materials Studio version 3.2. The X-ray structures of $BuPPh_3Br$[41] and $HPPh_3Br$[42] were used as reported in the literature. On-the-fly generated ultrasoft pseudopotentials were used for all atoms in the lattice and were obtained directly from Accelrys Inc. (San Diego, CA). All calculations used the Perdew, Burke, and Ernzerhof (PBE) XC functional under the generalized gradient approximation (GGA)[43] with an ultra-fine E_{cut}, and *k*-point grid settings (see Table A3.2 in Appendix A). Attempts at optimizing any atomic positions or unit cell dimensions from the X-ray crystal structures was not feasible in these systems since the unit cells were too large even at very low E_{cut} values. Therefore, NMR calculations were performed directly on the structures generated by XRD. Phosphorus MS as well as the bromine and chlorine EFG and MS tensors were then extracted from the output files using a modified version of the EFGShield program.

For ^{35}Cl, the shielding value for the reference is 974 ppm, which corresponds to an infinitely dilute solution of NaCl[44] and for ^{31}P, the shielding value is 328.35 ppm, which corresponds to an aqueous solution of H_3PO_4.[45] In the case of ^{81}Br, the computed absolute bromine shielding constant for KBr was used along with the added factor of 54.51 ppm, which is the chemical shift of solid $K^{81}Br$ (*vide supra*). This was done using the crystal structure of KBr as measured by Athee[46] again with ultra-fine E_{cut} and *k*-point values. In order to view tensor orientations with respect to the local environment of the phosphorus and

halogen nuclei, the output files from the calculations were rewritten in a way to view the molecular structure of the phosphonium halides and principal CS and EFG tensor components in the Diamond 3.2 program.

3.3 Results and Discussion

3.3.1 Single Crystal X-ray Diffraction Studies

In order to relate the NMR parameters to the molecular structures of the solids studied, we first set out to acquire all the necessary X-ray crystal structures *via* single crystal XRD. In this section, we report briefly on six crystal structures, i.e., those of $EtPPh_3Br$, $MePPh_3Br$, $C_5H_9PPh_3Br$, $BuPPh_3Cl$, $PPh_4Br{\cdot}H_2O$, and an updated structure for PPh_4Br which was reported earlier by Schweizer *et al*.[47] In their structure, disorder in the bromine position was assigned to two different bromine sites in the lattice, whereas we found that the unit cell parameters in fact match those of $PPh_4Br{\cdot}H_2O$ (see Table 3.4). The results from our NMR investigations therefore prompted us to re-investigate the solid-state structure of this compound (*vide infra*). The unit cell parameters for each of the structures are shown in Table 3.1. For $MePPh_3Br$, Curnow *et al.*[48] have reported a crystal structure that is a chloroform hemisolvate, which would not be desirable to complement our findings here since the presence of solvates in the lattice are known to alter the experimental and calculated NMR parameters.[49] As for $PrPPh_3Br$, the crystal structure isolated as part of this study matched what was reported by Czerwinski.[50] Our crystal structure was used for our calculations. The interpretations of the results from our crystallography studies will be discussed below in the context of the NMR parameters of the various compounds

Table 3.1: Crystallographic data for new X-ray crystal structures of phosphonium halides.

compound	$EtPPh_3Br$	$MePPh_3Br$	$C_5H_9PPh_3Br$	PPh_4Br	$BuPPh_3Cl$
crystal system	monoclinic	monoclinic	orthorhombic	triclinic	monoclinic
space group	$C2/c$	$P2_1/n$	$Pnma$	$P\bar{1}$	$P2_1/c$
a_c /Å	14.2027(2)	9.0887(2)	15.958(2)	9.3969(8)	11.1419(3)
b_c /Å	12.5625(2)	18.6129(4)	13.259(2)	10.2884(9)	9.9882(3)
c_c /Å	19.7600(3)	10.5950(2)	9.2250(14)	11.2664(10)	17.2512(5)
α_c / º	90.00	90.00	90.00	75.616(4)	90.00
β_c / º	92.991(1)	108.030(1)	90.00	71.910(4)	103.460(1)
γ_c / º	90.00	90.00	90.00	78.421(4)	90.00
volume /Å^3	3520.80(9)	1704.31(6)	1951.9(5)	993.81(15)	1867.11(9)
R_1	0.0201	0.0233	0.0214	0.0232	0.0290
wR_2	0.0558	0.0632	0.0611	0.0669	0.0866

3.3.2 Phosphorus-31 SSNMR of *n*-alkyltriphenylphosphonium bromides

To fully characterize the phosphonium halides studied here, ^{31}P SSNMR studies were carried out, and the ^{31}P CS tensor parameters are reported in Table 3.2. Figure 3.1 shows the spectrum of a stationary sample along with its analytical simulation and CP/MAS spectrum for powdered $BuPPh_3Br$ at 9.4 T. Phosphorus-31 CP/MAS and CP/static spectra were obtained for all of the other compounds considered here and are found in Figure 3.2. The value of δ_{iso} ranges between 21.0 and 28.1 ppm while the value of the span ($\Omega = \delta_{11} - \delta_{33}$) varies slightly between 34 and 39 ppm. These values are consistent with those reported by Ackermann *et al.*[19] for the analogous ethyltriphenylphosphonium iodides as well as those presented by Percharsky and coworkers on phosphonium salts containing the TPP moiety.[51] The CS tensor skews are all identical within experimental error. This result is not surprising, as the local electronic environment about the phosphorus does not change significantly, as only the length of the alkyl chain is being increased. In all five compounds discussed here,

the number of phosphorus sites present in the MAS spectra is consistent with the solid state structure elucidated by single crystal XRD data.

Table 3.2: Experimental and calculated ^{31}P chemical shift tensor parameters of *n*-alkyl triphenylphosphonium halides[a]

compound	expt. δ_{iso} /ppm	calc. δ_{iso} /ppm[b]	exp. Ω /ppm	calc. Ω /ppm	expt. κ	calc. κ
$BuPPh_3Br$	25.5(0.2)	70.9	36(1)	39.0	0.10(0.05)	-0.16
$PrPPh_3Br$	26.0(0.3)	69.1	39(2)	40.2	0.15(0.05)	0.04
$EtPPh_3Br$	28.1(0.4)	71.9	34(1)	36.6	0.20(0.05)	0.49
$MePPh_3Br$	21.0(0.5)	65.9	36(3)	39.9	0.15(0.05)	0.21
$BuPPh_3Cl$	25.0(0.2)	69.4	36(2)	39.6	0.15(0.05)	-0.04

[a] Error bounds are in parentheses.
[b] $\delta_{iso}(calc.) = \sigma_{iso}(H_3PO_4) - \sigma_{iso}(calc.) + \delta_{iso}(ADP) = 328.35$ ppm $- \sigma_{iso}(calc.) + 0.81$ ppm.

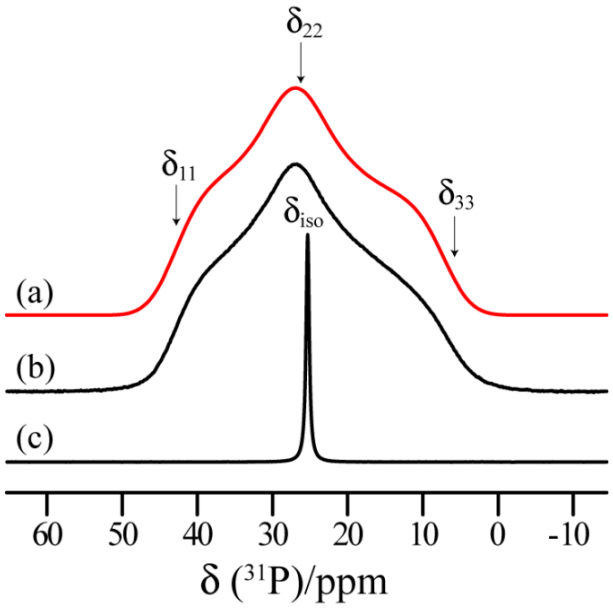

Figure 3.1: ^{31}P experimental CP/MAS (ν_{rot} = 8 kHz) (c), and CP/static (b) SSNMR spectra and simulation (a) for powdered $BuPPh_3Br$ acquired at B_0 = 9.4 T. 10 Hz of apodization was applied to the experimental spectrum.

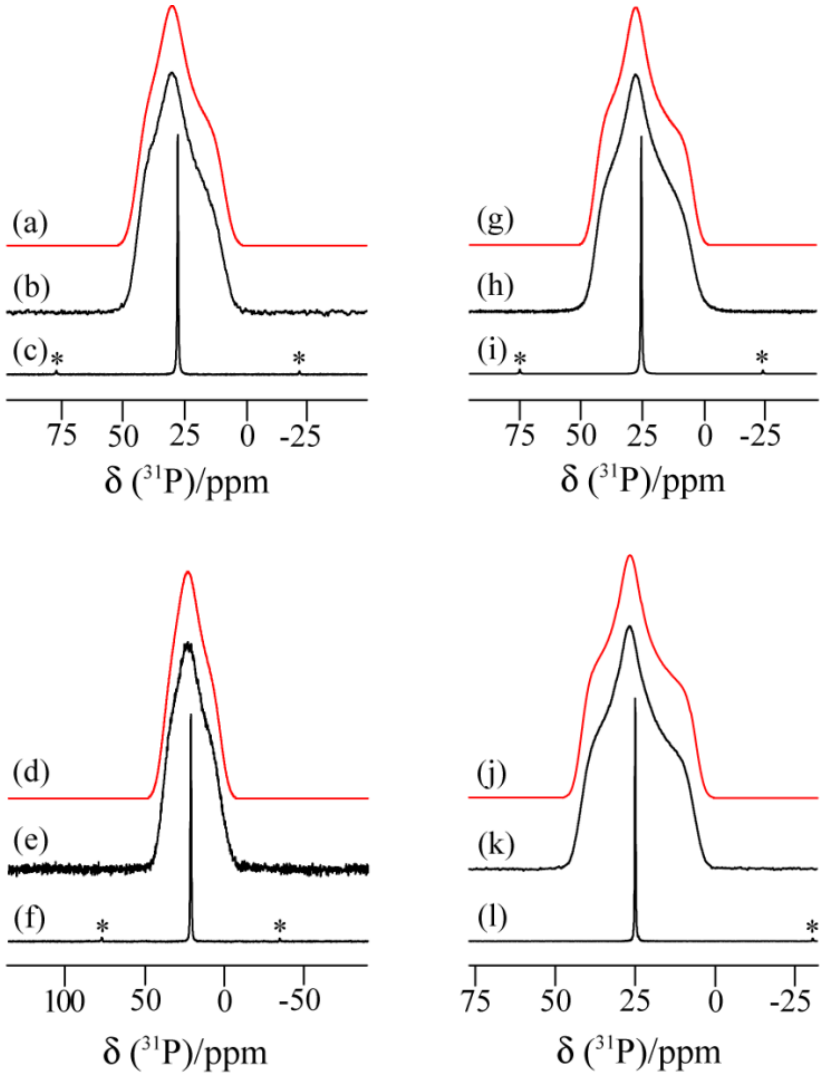

Figure 3.2: ^{31}P CP NMR experiments on a powdered stationary sample of $EtPPh_3Br$ (b), and $PrPPh_3Br$ (h), and CP/MAS, ν_{rot} = 8 kHz, on $EtPPh_3Br$ (c) and $PrPPh_3Br$ (i) acquired at B_0 = 9.4 T. ^{31}P CP experiments on a powdered stationary sample of $MePPh_3Br$ (e), and $BuPPh_3Cl$ (k), and CP/MAS, ν_{rot} = 4.5 kHz, on $MePPh_3Br$ (f) and $BuPPh_3Cl$ (l) acquired at B_0 = 4.7 T. All analytical simulations (a, d, g, and j) were performed using WSolids (data in Table 3.2). The asterisks (*) indicate spinning sidebands.

3.3.3 Bromine-79/81 SSNMR of triphenylphosphonium bromides.

The experimental bromine NMR parameters for each compound considered in this work are summarized in Table 3.3. These were obtained by simultaneous analytical simulations of each experimental $^{79/81}$Br spectrum collected at different magnetic fields. First, ^{81}Br MAS NMR spectra were fit in order to extract the EFG tensor parameters (i.e., C_Q and the η_Q) as well as the isotropic chemical shift, δ_{iso}, as the NMR line shape broadening caused by CSA is eliminated under these conditions. The collection of MAS NMR spectra for all compounds was only possible at 21.1 T because the second-order quadrupolar broadening, present in powder line shapes of half-integer quadrupolar nuclei, scales inversely with B_0 (or ν_L). After proper simulation of the MAS line shape, it was then possible to extract the remaining NMR parameters (i.e., the Ω, the κ, and the three Euler angles that relate the EFG and CS tensor principal axis systems (PAS)) by simulating the NMR spectra of stationary samples obtained at different B_0 strengths. In all cases, the ^{79}Br and ^{81}Br NMR spectra of stationary samples were collected at 11.75 T (as well as 9.4 T for select cases; see Figure 3.11). At high magnetic fields, it is possible to extract more accurately the CSA since this effect is more pronounced and visible in the spectrum. It is also advantageous to observe both isotopes of bromine since, to a very good approximation, their NMR parameters are identical with the exception of the C_Q, which scales directly by the ratio of the two quadrupole moments (for bromine, $C_Q(^{79}Br)/C_Q(^{81}Br) = (Q(^{79}Br)/Q(^{81}Br) = 1.19$).

Table 3.3: Experimental ^{81}Br EFG and CS tensor parameters of phosphonium bromides[a]

compound	$\lvert C_Q(^{81}Br)\rvert$[b] /MHz	η_Q	δ_{iso} /ppm	Ω /ppm	κ	α / º	β / º	γ / º
$BuPPh_3Br$	9.48(0.10)	0.54(0.07)	130.5(5)	99(5)	0(0.05)	31(1)	72(3)	102(3)
$PrPPh_3Br$	8.48(0.20)	0.56(0.03)	121(2)	105(5)	-0.35(0.10)	43(5)	82(3)	98(2)
$EtPPh_3Br$	14.00(0.10)	0.52(0.02)	151(1)	160(10)	-0.80(0.10)	5(5)	25(2)	0(3)
$MePPh_3Br$	9.80(0.15)	0.26(0.01)	155(2)	98(3)	0.60(0.05)	59(1)	57(2)	12(10)
$C_5H_9PPh_3Br$	12.80(0.10)	0.62(0.01)	82(1)	140(10)	0.50(0.20)	90(5)	24(2)	90(5)
$HPPh_3Br$	14.35(0.10)	< 0.01	228(5)	305(10)	0.55(0.05)	0[c]	20(1)	90(10)
PPh_4Br/site A	10.50(0.05)	0.48(0.02)	3(1)	[d]	[d]	[d]	[d]	[d]
PPh_4Br/site B	8.55(0.05)	0.57(0.02)	46(1)	[d]	[d]	[d]	[d]	[d]

[a] Error bounds are in parentheses.
[b] One typically measures the absolute value, $|C_Q|$. $|C_Q(^{79}Br)|$ is found by scaling $|C_Q(^{81}Br)|$ by the ratio of the quadrupole moments of both bromine isotopes (i.e., by a factor of 1.19). Both ^{79}Br and ^{81}Br experiments were performed to determine all values in this table.
[c] This is inferred from the calculations and is consistent with an axially symmetric EFG tensor.
[d] It was not possible to unambiguously measure CS tensor information for this compound due to the presence of overlapping powder patterns for the two sites and the lack of any symmetry restrictions on the NMR parameters.

The magnitude of $C_Q(^{81}Br)$ for the phosphonium halides considered here varies between 8.48 MHz ($PrPPh_3Br$) and 14.35 MHz ($HPPh_3Br$), which is in the range of those observed for the imidazolium and ammonium solid ionic liquids studied by Ripmeester and coworkers,[26] but are on the larger end of the values reported by Alonso *et al.*[25] for the *n*-alkyltrimethylammonium bromides, which range from 6.03 to 8.08 MHz. In terms of the isotropic chemical shifts, these are similar to those measured for the ionic liquids[26] but varied more from compound to compound (ranging from 3 to 228 ppm) than in the previous studies. As for the CS tensor span, the values obtained are larger by roughly 30 ppm compared to the ionic liquids while the *n*-alkyltrimethylammonium bromides spans are consistent with the low end of values determined in this study. The range is from 98 ppm for $MePPh_3Br$ to 305

ppm for $HPPh_3Br$, which are comparable to the values obtained by Widdifield and Bryce for alkaline earth metal bromides.[27] Specific results and highlights are addressed below for each of the individual compounds considered in this work.

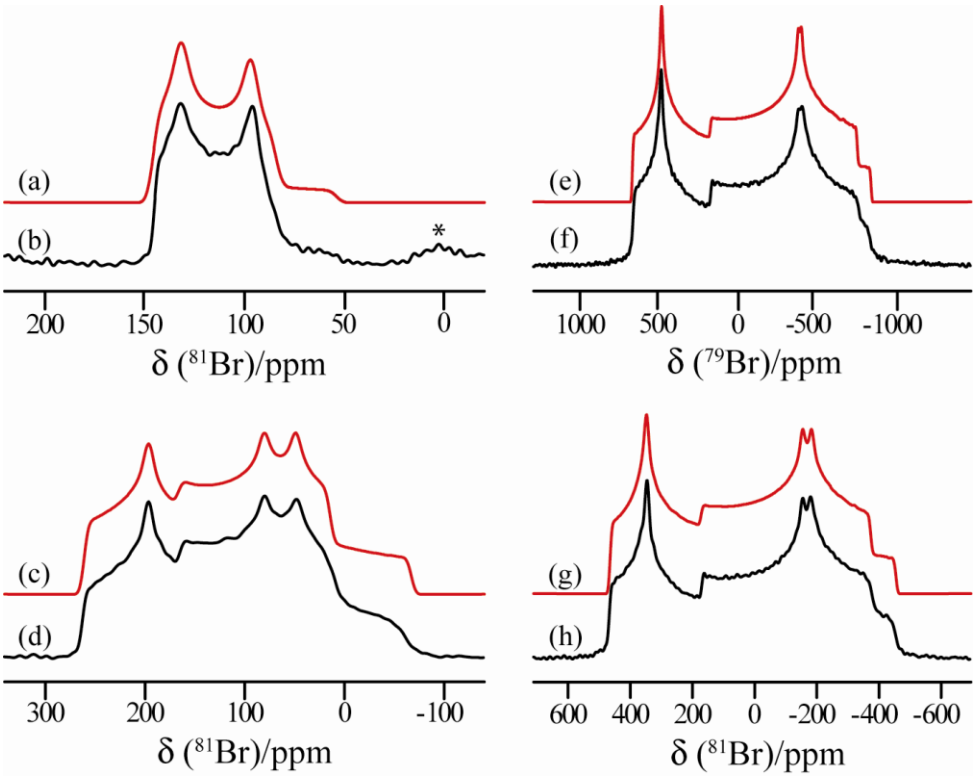

Figure 3.3: $^{79/81}$Br solid-state NMR spectra of powdered $MePPh_3Br$. An experimental ^{81}Br MAS NMR spectrum, ν_{rot} = 31.25 kHz (b), was acquired at B_0 = 21.1 T (the visible spinning sideband is marked '*'). A ^{79}Br NMR spectrum was acquired at B_0 = 11.75 T (f) and ^{81}Br NMR spectra were acquired at B_0 = 21.1 T (d) and 11.75 T (h), all under stationary conditions. All analytical simulations (a, c, e, and g) were performed using WSolids (data in Table 3.3). Complementary $^{79/81}$Br NMR data at B_0 = 9.4 T along with their analytical simulations may be found in Figure 3.11.

$MePPh_3Br$ crystallizes in the $P2_1/n$ space group, whereas both $PrPPh_3Br$ and $BuPPh_3Br$ share a slightly different one of $P2_1/c$. The single crystal XRD data for all three

compounds show that there is one bromine site in the asymmetric unit and that it does not sit on a rotation axis or mirror plane. This indicates that neither the CS nor EFG tensors need to have axial symmetry and no particular orientation of their PASs with respect to the molecular frame is required by the lattice symmetry. Experimental SSNMR spectra of $MePPh_3Br$ are shown in Figure 3.3. The value of $C_Q(^{81}Br)$, 9.80 ± 0.15 MHz, determined by the MAS experiment is confirmed by simulating the stationary spectra. The CS tensor span for this sample was found to be 98 ± 3 ppm. Observing Figure 2 more closely reveals the power and the utility of performing these experiments at many different magnetic field strengths. The splitting between the two singularities observed on the right hand side of the powder pattern at 11.75 T (Figure 3.3h for ^{81}Br) increases at 21.1 T (Figure 3.3d). Furthermore, this splitting is greatly reduced for the stationary ^{79}Br NMR spectrum at 11.75 T (Figure 3.3f). These distinct spectral features are attributed to the more important role of CSA in the higher magnetic field. The same observations can be made for $PrPPh_3Br$ (Figure 3.4), where the span of 105 ± 5 ppm is close to that of $MePPh_3Br$. The value of $C_Q(^{81}Br)$ determined for the two samples however, differ by approximately 1 MHz. For $BuPPh_3Br$ (Figure 3.5), the experimentally extracted Euler angles are close to the values for $PrPPh_3Br$ and, as is the case with all of the *n*-alkyl TPP bromides, the asymmetry parameters of both the CS and EFG tensors are representative of a bromine ion not positioned on any particular symmetry axis or plane, consistent with the reported X-ray crystal structures. As for the value of Ω, 99 ± 5 ppm, this is very close to the values for the propyl and methyl analogues.

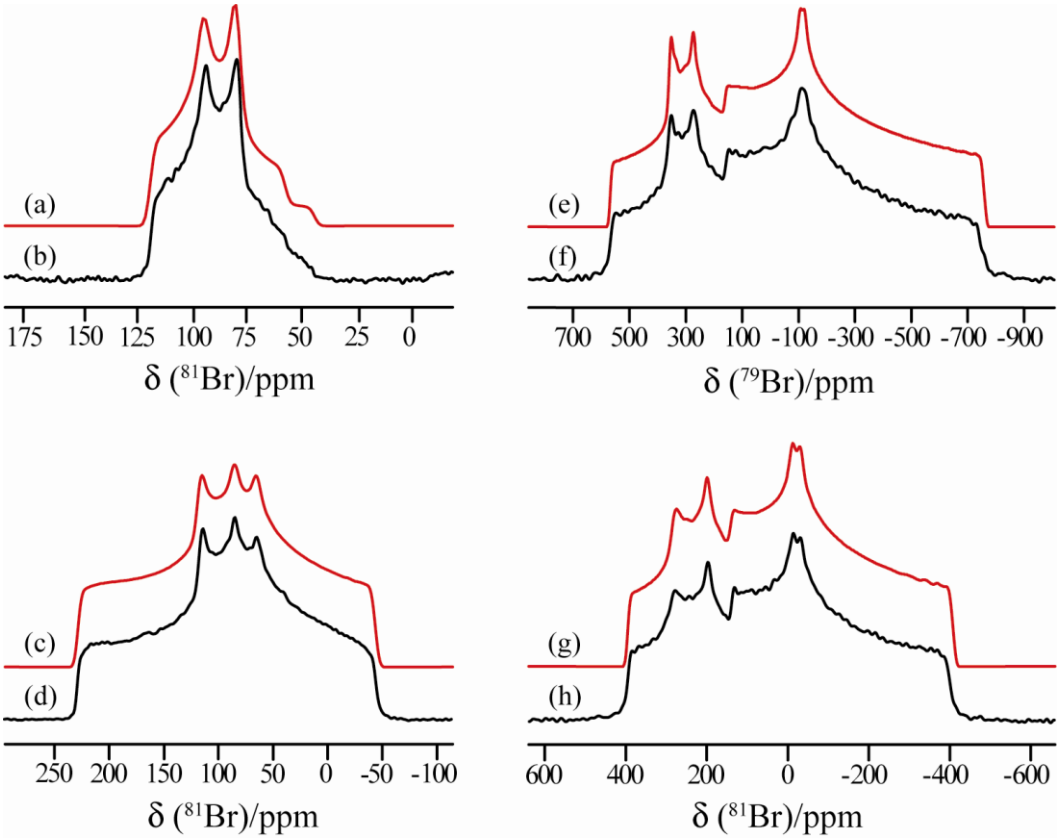

Figure 3.4: $^{79/81}$Br solid-state NMR spectra of powdered $PrPPh_3Br$. An experimental ^{81}Br MAS NMR spectrum, ν_{rot} = 31.25 kHz (b), was acquired at B_0 = 21.1 T. A ^{79}Br NMR spectrum was acquired at B_0 = 11.75 T (f) and ^{81}Br NMR spectra were acquired at B_0 = 21.1 T (d) and 11.75 T (h), all under stationary conditions. All analytical simulations (a, c, e, and g) were performed using WSolids (data in Table 3.3). Complementary $^{79/81}$Br NMR data at B_0 = 9.4 T along with their analytical simulations may be found in Figure 3.11.

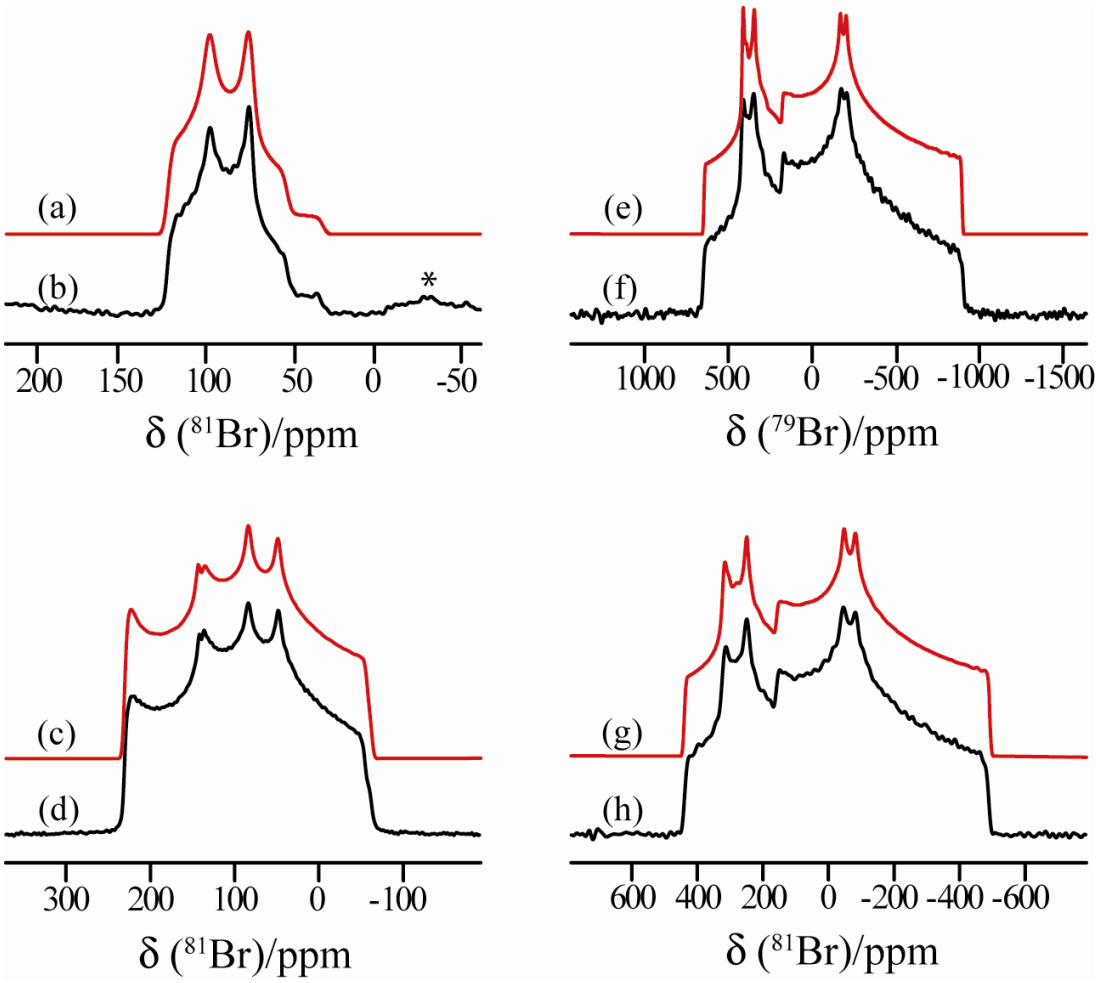

Figure 3.5: $^{79/81}$Br solid-state NMR spectra of powdered $BuPPh_3Br$. An experimental ^{81}Br MAS NMR spectrum, ν_{rot} = 31.25 kHz (b), was acquired at B_0 = 21.1 T (the visible spinning sideband is marked with '*'). A ^{79}Br NMR spectrum was acquired at B_0 = 11.75 T (f) and ^{81}Br NMR spectra were acquired at B_0 = 21.1 T (d) and 11.75 T (h), all under stationary conditions. All analytical simulations (a, c, e, and g) were performed using WSolids (data in Table 3.3). Complementary $^{79/81}$Br NMR data at B_0 = 9.4 T along with their analytical simulations may be found in Figure 3.11.

Recently, Wu and Terskikh[52] have shown that C_Q is related linearly to the quantity $Q(1 - \gamma_\infty)/V$, where γ_∞ is the Sternheimer antishielding factor unique to each atomic type and

where V is the unit cell volume from XRD experiments, for a series of isostructural compounds. This type of relationship has also been discussed and demonstrated for many group two metal halides and their hydrates,[27,49,53] and we attempt here to further extend this trend to halogen nuclei in phosphonium halides. This knowledge would be useful in order to estimate and confirm experimental C_Q values within a series of analogous compounds, which finds applicability in the field of NMR crystallography. $BuPPh_3Br$ and $BuPPh_3Cl$ should be nominally isostructural ($P2_1/c$ space group), which suggests that the $C_Q(^{81}Br)/C_Q(^{35}Cl)$ and $[Q_{81Br}(1 - \gamma_{\infty(81Br)})/V]/[Q_{35Cl}(1 - \gamma_{\infty(35Cl)})/V]$ ratios should be close. To accurately determine the value of $C_Q(^{35}Cl)$ for $BuPPh_3Cl$, SSNMR experiments under MAS conditions were performed at 9.4 T (Figure 3.6d and Figure 3.6f for ^{35}Cl and ^{37}Cl respectively) and at 21.1 T (Figure 3.6b). The experimental value of $C_Q(^{35}Cl)$ is 1.13 ± 0.01 MHz, whereas the value of $C_Q(^{37}Cl)$, 0.88 ± 0.01 MHz, is in perfect agreement with the value expected by evaluating the product between the ratio of both quadrupole moments (i.e., $Q(^{37}Cl)/Q(^{35}Cl)$) and the value of $C_Q(^{35}Cl)$. Using the experimental SSNMR data, the value of $C_Q(^{81}Br)/C_Q(^{35}Cl)$ is 8.39. From the crystallographic data, the ratio $[Q_{81Br}(1 - \gamma_{\infty(81Br)})/V]/[Q_{35Cl}(1 - \gamma_{\infty(35Cl)})/V]$ is calculated to be 6.11, a 37 % difference, consistent with previous studies on the group 2 metal chlorides and bromides.[27,49] A key contribution to this error lies in the fact that $BuPPh_3Cl$ and $BuPPh_3Br$ are not precisely isostructural even if they belong to the same space group. The position of the halide ion in each crystal structure is slightly different; for $BuPPh_3Br$, $x/a_c = 0.37978(2)$, $y/b_c = 0.1368(3)$, $z/c_c = 0.83347(1)$[41] and for $BuPPh_3Cl$, $x/a_c = 0.37565(3)$, $y/b_c = 0.12066(3)$, $z/c_c = 0.83537(2)$. We note here that the most significant change in the anion position is with respect to y/b_c and that this is a similar difference in that observed with the $CaBr_2/CaCl_2$ pair.[49] It has been shown in previous studies that changing

the bromide position by a very small increment (< 0.05 Å) can substantially affect the value of $C_Q(^{81}Br)$.[28]

The final compound studied in the *n*-alkyl TPP bromide family is $EtPPh_3Br$, for which the experimental SSNMR spectra may be found in Figure 3.7. The spectral line shapes associated with this compound were some of the broadest acquired in this study and required VOCS data acquisition at 11.75 T. In contrast to the methyl, propyl, and butyl adducts, $EtPPh_3Br$ is characterized by a notably larger $C_Q(^{81}Br)$ value of 14.00 ± 0.10 MHz. This type of observation may also be made for the value of Ω as well, which is on average 100 ppm for the other *n*-alkyl TPP bromides and 160 ppm for $EtPPh_3Br$. This suggests that $EtPPh_3Br$ does not crystallize in the same fashion as the analogous compounds. This NMR finding prompted us to seek independent confirmation by X-ray diffraction, which indeed shows that $EtPPh_3Br$ crystallizes in the *C*2/c space group, thereby demonstrating the power of SSNMR in detecting small structural changes among a set of chemically similar compounds.

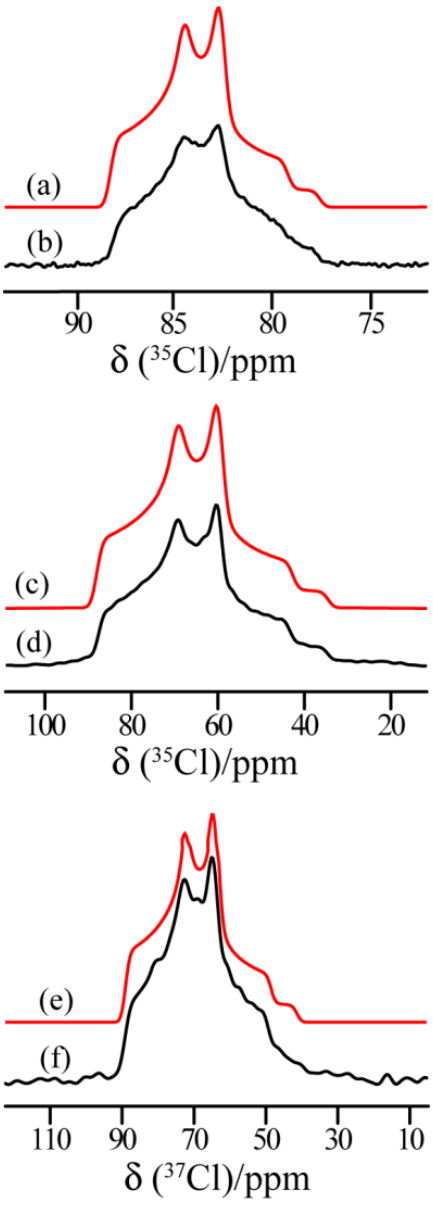

Figure 3.6: $^{35/37}$Cl solid-state NMR spectra of powdered $BuPPh_3Cl$. Experimental MAS NMR spectra were acquired for ^{35}Cl at 21.1 T (b) and 9.4 T (d) and for ^{37}Cl at 9.4 T (f). Analytical simulations (a, c and e) resulted in the following NMR parameters: $C_Q(^{35}Cl)$ = 1.13 ± 0.01 MHz, $C_Q(^{37}Cl)$ = 0.88 ± 0.01 MHz, η_Q = 0.65 ± 0.01 and δ_{iso} = 88.5 ± 0.5 ppm.

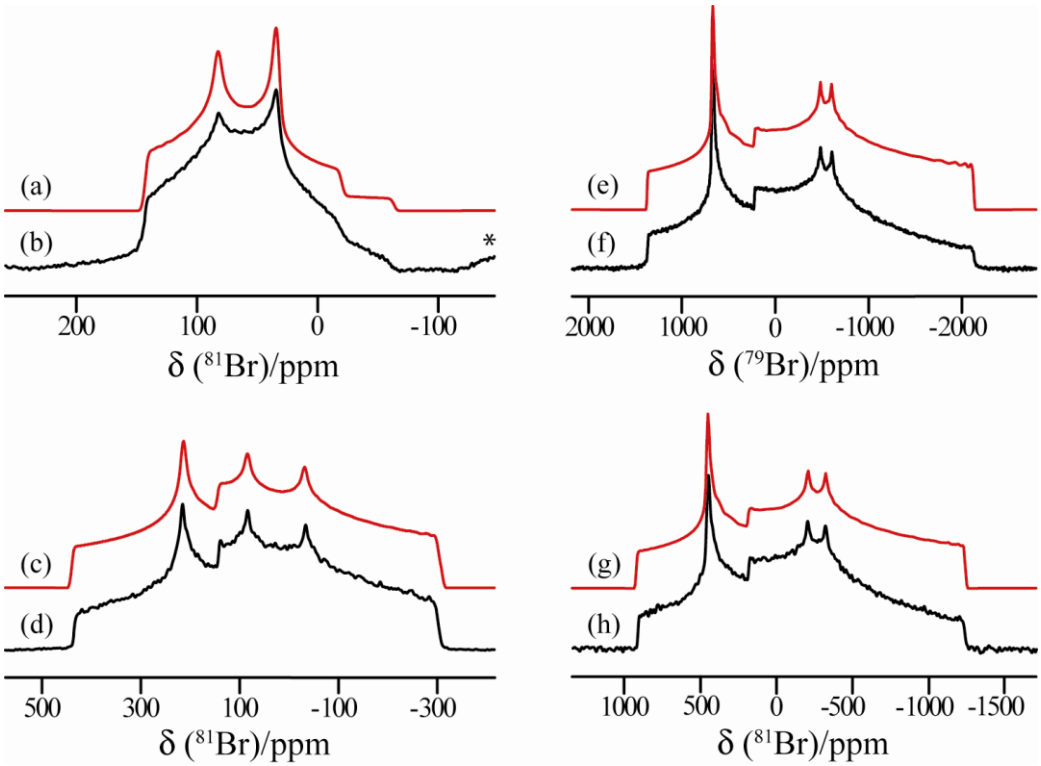

Figure 3.7: $^{79/81}$Br solid-state NMR spectra of powdered $EtPPh_3Br$. An experimental ^{81}Br MAS NMR spectrum, ν_{rot} = 62.5 kHz (b), was acquired at B_0 = 21.1 T (the visible spinning sideband is marked with '*'). A ^{79}Br NMR spectrum was acquired at B_0 = 11.75 T (f) and ^{81}Br NMR spectra were acquired at B_0 = 21.1 T (d) and 11.75 T (h), all under stationary conditions. All analytical simulations (a, c, e, and g) were performed using WSolids (data in Table 3.3). Complementary $^{79/81}$Br NMR data at B_0 = 9.4 T along with their analytical simulations may be found in Figure 3.11.

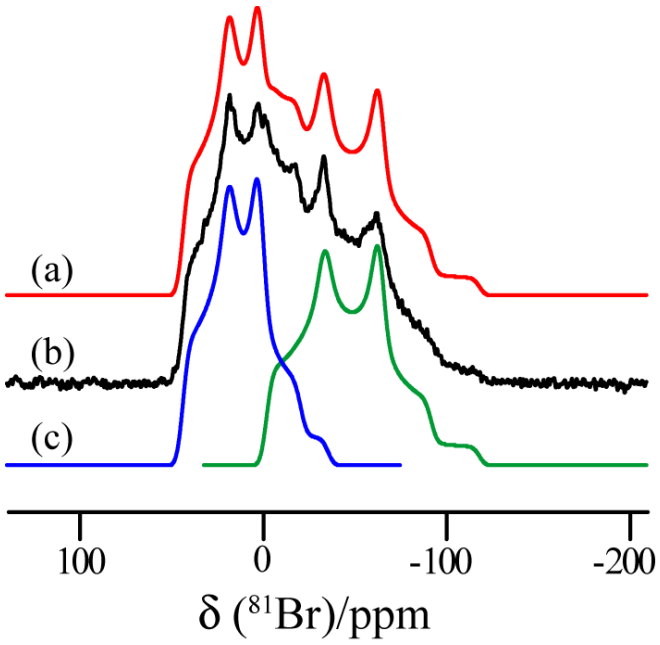

Figure 3.8: Experimental ^{81}Br MAS NMR spectrum of powdered PPh_4Br, ν_{rot} = 62.5 kHz (b), acquired at B_0 = 21.1 T. The analytical simulation (a) required two bromine sites to properly fit the spectrum with the parameters shown in Table 3.3. The deconvolution of this simulation is shown in (c).

Shown in Figure 3.8 is the ^{81}Br MAS NMR spectrum acquired at 21.1 T along with analytical simulations (including a deconvolution of the individual line shapes) associated with what is clearly two distinct bromine sites for PPh_4Br. Spectra of the stationary sample (not shown) have been acquired at multiple fields, but a unique and accurate analytical simulation including all of the CSA and EFG tensor parameters, along with their relative orientations for the two sites, proved to be quite difficult due to the large number of adjustable parameters. As shown in Figure 3.8c, both powder patterns exhibit similar quadrupolar asymmetry parameters, 0.48 ± 0.02 and 0.57 ± 0.02 for sites A and B

respectively. The major differences lay in the values of δ_{iso}, 3 ± 1 and 46 ± 1 ppm for sites A and B, as well as the width of the two powder patterns which are directly related to the quadrupolar coupling constants. The most shielded resonance (site A) is broader and is characterized by a $C_Q(^{81}Br)$ of 10.50 ± 0.05 MHz, whereas the narrower site B has a smaller $C_Q(^{81}Br)$ of 8.55 ± 0.05 MHz. The previously reported crystal structure by Schweizer *et al.*[47] is not consistent with the aforementioned results since the NMR line shape does not exhibit any form of disorder or fractional occupancy, as would be expected from their proposed structure. Our revised crystal structure packs in the $P\bar{1}$ space group and now has two crystallographically distinct bromine sites (each with 100% occupancy) that both sit on inversion centres, which is in full agreement with our NMR experiments. We are confident that our structure is an improvement over the latter as we obtained an R_1 of 2.60% (see Table 3.3) compared to 5.75% obtained previously (see Table 3.4). It is believed that the previously characterized structure was the monohydrate form, $PPh_4Br{\cdot}H_2O$, as we've obtained its crystal structure as part of this study and the crystallographic data for $PPh_4Br{\cdot}H_2O$ (see Table 3.4) match the unit cell parameters of the anhydrous form reported by Schweizer *et al*.[47] This result further demonstrates how SSNMR spectra can corroborate or refute X-ray crystallographic data, and that SSNMR can distinguish between what are seemingly chemically identical bromine sites in organic materials specifically when differentiating between the various hydrates and solvates that exist for a compound.

Table 3.4: Select Crystallographic data for $PPh_4Br{\cdot}H_2O$

structure	$PPh_4Br{\cdot}H_2O$	previous PPh_4Br[47]
space group	$P\bar{1}$	$P\bar{1}$
a_c /Å	9.954(3)	10.031(3)
b_c /Å	10.573(4)	10.688(3)
c_c /Å	10.647(3)	10.678(3)
α_c /deg	77.282(16)	77.45(2)
β_c /deg	83.514(16)	83.27(2)
γ_c /deg	71.942(17)	71.87(2)
volume /Å^3	1038.1(6)	1060.5(5)
R_1	0.0260	0.0575
wR_2	0.0730	0.0833

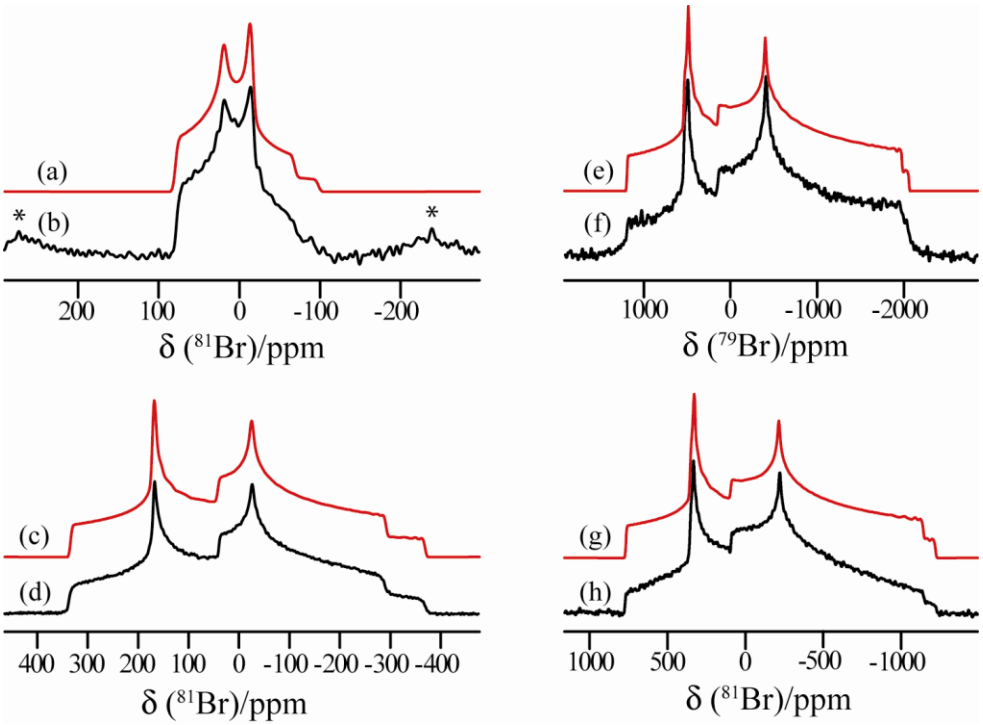

Figure 3.9: $^{79/81}$Br solid-state NMR spectra of powdered $C_5H_9PPh_3Br$. An experimental ^{81}Br MAS NMR spectrum, ν_{rot} = 62.5 kHz (b), was acquired at B_0 = 21.1 T (the visible spinning sidebands are marked with '*'). A ^{79}Br NMR spectrum was acquired at B_0 = 11.75 T (f) and ^{81}Br NMR spectra were acquired at B_0 = 21.1 T (d) and 11.75 T (h), all under stationary conditions. All analytical simulations (a, c, e, and g) were performed using WSolids (data in Table 3.3).

$C_5H_9PPh_3Br$ (Figure 3.9) and $HPPh_3Br$ (Figure 3.10) both crystallize in the *Pnma* space group and each has a single bromine site that sits on a mirror plane. This dictates that one of the principal components of the EFG tensor and another from the CS tensor must be collinear and perpendicular to the plane. For $C_5H_9PPh_3Br$, the experimental Euler angles (α = 90, β = 24, γ = 90°) indicate geometrically that both the smallest component of the EFG tensor, V_{11}, and the largest component of the CS tensor, δ_{11} are coincident whereas in the case of $HPPh_3Br$, V_{22} and δ_{11} are collinear. It is clear from the ^{81}Br MAS spectrum at 21.1 T for $HPPh_3Br$ (Figure 3.10) that the EFG tensor is axially symmetric (i.e., $\eta_Q < 0.01$), in contrast to that observed for $C_5H_9PPh_3Br$ where $\eta_Q = 0.62 \pm 0.01$, a value similar to those of the *n*-alkyl TPP bromides (see Table 3.3). Although both compounds share identical space groups, $HPPh_3Br$ has the largest $C_Q(^{81}Br)$ of the compounds characterized by SSNMR in this study, 14.35 ± 0.10 MHz, as well as the largest CS tensor span of 305 ± 10 ppm and isotropic chemical shift, 228 ± 5 ppm, in this study.

It is noted here that it was possible to obtain as part of this study accurate measurements of the CS tensor Ω values. This is in part due to the acquisition of bromine SSNMR spectra for both NMR-active isotopes at multiple magnetic field strengths and under MAS conditions. The additional SSNMR experiments performed at B_0 = 9.4 T are presented in Figure 3.11. Data at 11.75 T was emphasized more than the 9.4 T data as the CT line shapes were narrower at the higher magnetic field resulting in fewer transmitter offset settings for the VOCS acquisition method.

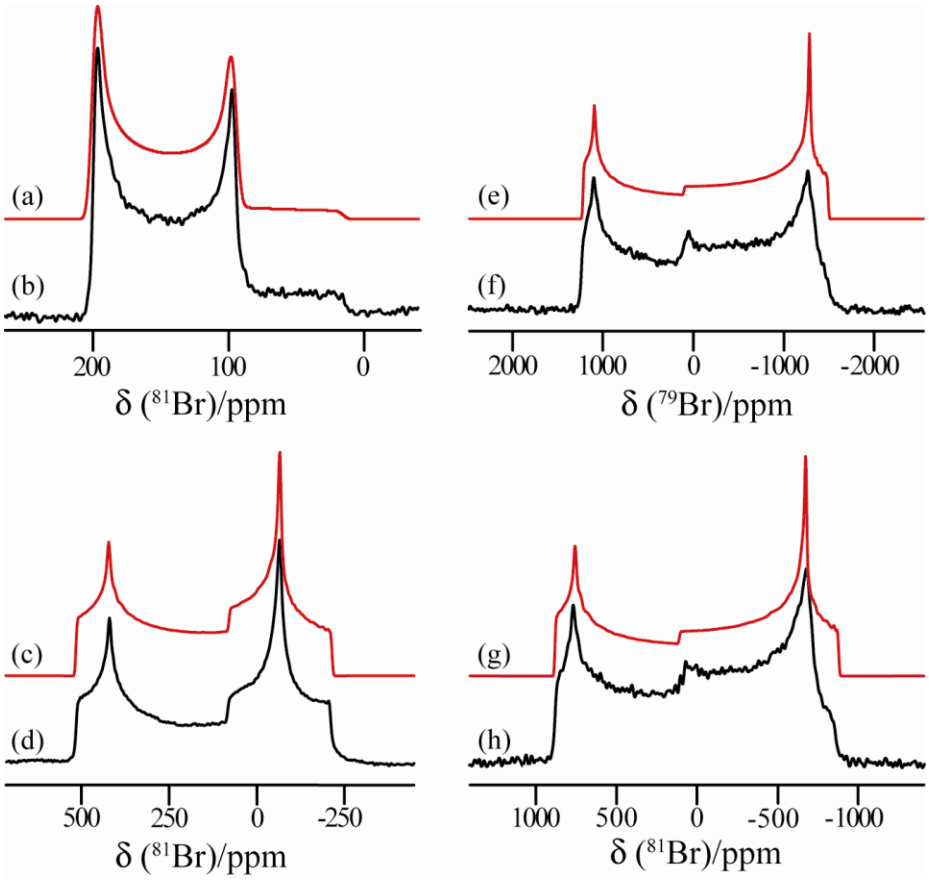

Figure 3.10: $^{79/81}$Br solid-state NMR spectra of powdered $HPPh_3Br$. An experimental ^{81}Br MAS NMR spectrum, ν_{rot} = 62.5 kHz (b), was acquired at B_0 = 21.1 T (the spinning sidebands were added into the centre band to ensure a more accurate simulation). A ^{79}Br NMR spectrum was acquired at B_0 = 11.75 T (f) and ^{81}Br NMR spectra were acquired at B_0 = 21.1 T (d) and 11.75 T (h), all under stationary conditions. All analytical simulations (a, c, e, and g) were performed using WSolids (data in Table 3.3).

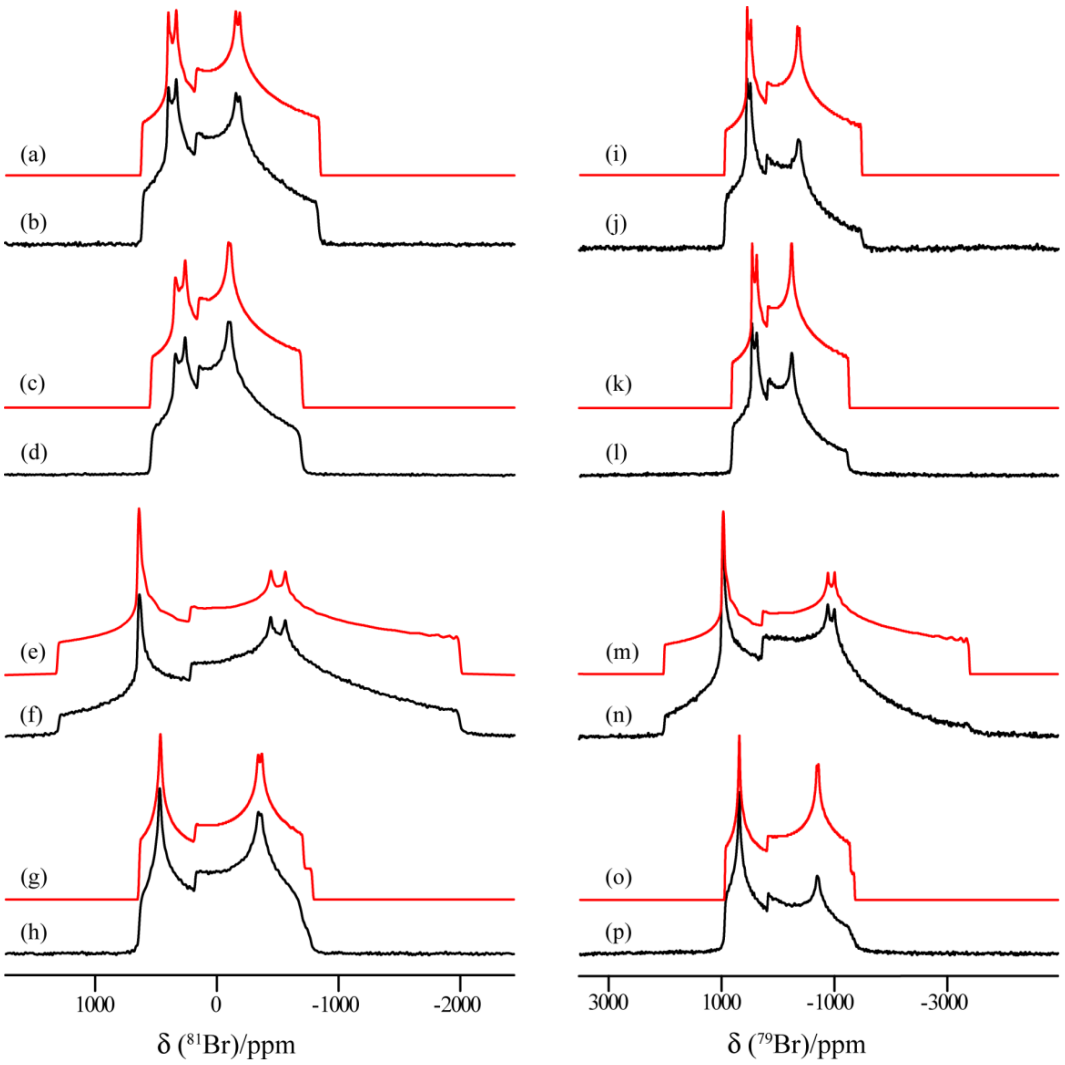

Figure 3.11: Complementary $^{79/81}$Br solid-state NMR spectra acquired at B_0 = 9.4 T. ^{81}Br spectra were acquired for $BuPPh_3Br$ (b), $PrPPh_3Br$ (d), $EtPPh_3Br$ (f), and $MePPh_3Br$ (h) under stationary conditions. ^{79}Br spectra were acquired for $BuPPh_3Br$ (j), $PrPPh_3Br$ (l), $EtPPh_3Br$ (n), and $MePPh_3Br$ (p) under stationary conditions. All analytical simulations (a, c, e, g, i, k, m, and o) were performed using WSolids (data in Table 3). Some spectra (j, l, n, and p) require more pieces; however we are confident with our simulations as we performed experiments at multiple fields.

3.3.4 Experimental Data Interpretation

We next sought to address the origins of the large range in the values of Ω (98 to 305 ppm) that characterizes the TPP bromides studied, which was not observed in the studies on long chain *n*-alkyltrimethylammonium bromides where the span ranged between 105 and 117 ppm (standard deviation of 6 ppm).[25] We find that in all the TPP bromides studied here, the bromine CS tensor span for a given compound correlates with the shortest bromine–phosphorus distance measured by single crystal XRD. The correlation is such that larger spans are observed when this distance is shorter (Figure 3.12a). Since this parameter is representative of the difference between the largest and the smallest components of the CS tensor (i.e., $\Omega \approx \delta_{11} - \delta_{33}$), there should be a correlation between either δ_{11} or δ_{33} and the Br–P distance. A better correlation between δ_{11} and the shortest Br–P distance is noted (Figure 3.12b) as the *R* value changes from 0.950 (for Ω) to 0.973 (for δ_{11}). This type of observation demonstrates how one can relate the crystal structure of a compound to the NMR parameters as distinct structural differences manifest themselves in the NMR spectrum, which has applicability in NMR crystallography. The use of computational methods is therefore expected to greatly aid in determining the reasons behind this experimentally observed trend. Likewise, computations make it possible to assign the EFG and CS tensor orientations in the molecular frame.

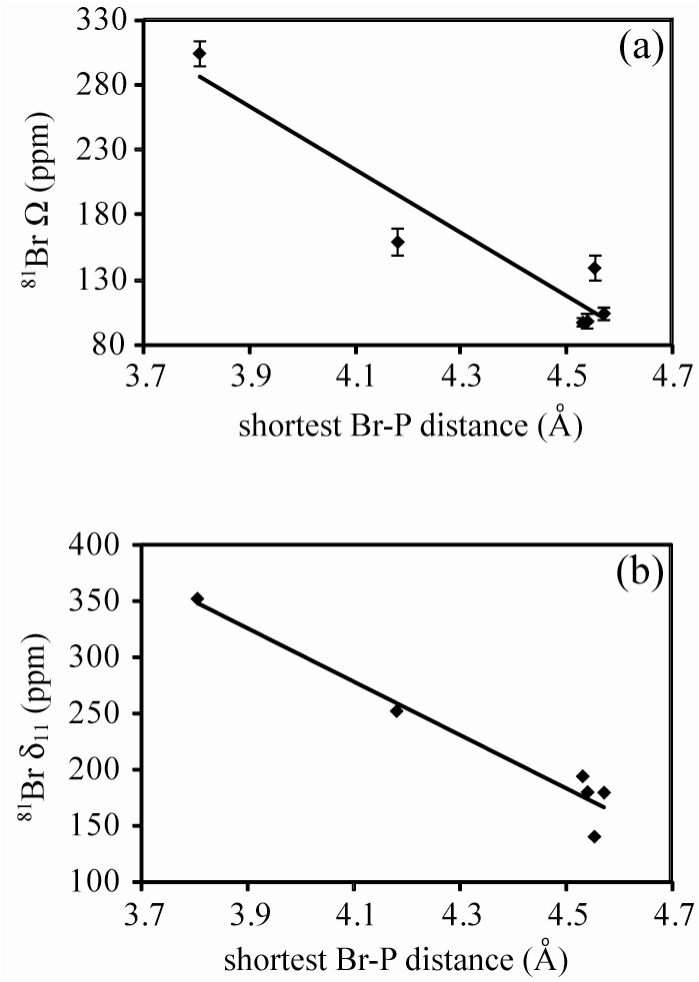

Figure 3.12: Plots of the experimental CS tensor parameters Ω (a) and δ_{11} (b) as a function of the shortest Br–P ($d_{Br\text{-}P}$) distance in the crystal structures of compounds studied. The lines of best fit are as follows: (a) $\Omega(^{81}\text{Br, expt. /ppm}) = -242.81(d_{Br\text{-}P}\text{ /Å}) + 1210.6$, $R = 0.950$; (b) $\delta_{11}(^{81}\text{Br, expt.}) = -237.55(d_{Br\text{-}P}) + 1253$, $R = 0.973$.

3.3.5 GIPAW DFT Calculations

We briefly comment on the GIPAW-DFT calculated ^{31}P MS tensor parameters for the *n*-alkyl TPP halide compounds. First of all, the magnitudes of the span are very well predicted as is evidenced in Table 3.2 for all samples considered. For the skew, the

agreement is quite good with the exception of $EtPPh_3Br$, whereas the isotropic chemical shift is overestimated in all cases by approximately 40 ppm when using the absolute shielding scale for ^{31}P. GIPAW DFT calculations have previously been performed on the ^{31}P nucleus in aluminophosphates by Ashbrook *et al*.[54] Their values, however, were not interpreted in terms of an absolute shielding scale but rather with respect to an optimal experimentally-determined value within their studied systems. Using this method, they get poor agreement between the relative experimental and calculated isotropic chemical shifts. In contrast to their study, the relative chemical shifts computed here for the phosphonium halides agree fairly well with experiment. For example, the lowest experimental δ_{iso} (21.0 ± 0.5 ppm for $MePPh_3Br$) has the lowest calculated shift of 65.9 ppm while the highest experimental δ_{iso} (28.1 ± 0.4 ppm for $EtPPh_3Br$) has the highest calculated isotropic chemical shift of 71.9 ppm. We investigated whether the overestimation in the ^{31}P chemical shifts could stem in part from spin-orbit relativistic effects associated with the nearby bromine ion.[55,56] ADF calculations under ZORA were performed to address this hypothesis since spin-orbit and scalar relativistic effects can be considered. The calculated isotropic shielding for a crude model of $BuPPh_3Br$ increases by about 9 ppm (3 %) when compared to a calculation without considering relativistic effects (see Table A3.3 in Appendix A). The GIPAW DFT calculations also provide insight into the orientations of the MS eigenvectors with respect to the molecular frame. It was found that σ_{33} is oriented approximately 35° away from the P–CH_2 bond in all of the *n*-alkyl TPP halides. In $BuPPh_3Br$ this angle is 36.0° and in $BuPPh_3Cl$ it is 37.4° (see Figure 3.13). This is consistent with the conclusions made by Ackermann *et al.* for ethyltriphenylphosphonium iodide where the angle between σ_{33} and the P–C(ethyl) bond vector was 39.3° (calculated with the B3LYP hybrid DFT functional).[19] Although

relatively good agreement (root-mean-square deviation (RMSD) of 4.2 ppm) between the experimental and calculated magnitudes of the Ω and the δ_{iso} was obtained when using the phosphoric acid absolute shielding scale, their models did not include the halide anions, whereas these are included in our GIPAW DFT calculations. Therefore, we performed these calculations on our structures while excluding the halogen ions and accounting for the resulting charge of the unit cell. Although the value of span is still well predicted, we observe a change in the orientation of the σ_{33} eigenvector with respect to the P–CH_2 bond vector. In the case of $BuPPh_3Br$ and $BuPPh_3Cl$, this angle changes to 48.7° and 48.5° respectively (see Figure 3.13). This is in disagreement with the models used by Ackermann *et al*. and suggests that it is important to always include the halogen anion in the calculation of these ^{31}P MS tensors when performing GIPAW DFT calculations on these systems. We note in passing that B3LYP calculations using a cluster model were attempted on the phosphonium bromides and these did not yield results consistent with those of Ackerman *et al*.

Table 3.5: Calculated $^{79/81}Br$ EFG and CS tensor parameters for phosphonium bromides using GIPAW DFT

compound	$C_Q(^{81}Br)$ /MHz	η_Q	δ_{iso} /ppm	Ω /ppm	κ	α /°	β /°	γ /°
$BuPPh_3Br$	-9.35	0.79	54.6	151	0.06	47	89	68
$PrPPh_3Br$	-8.98	0.59	25.4	162	-0.01	61	71	116
$EtPPh_3Br$	-10.78	0.84	87.9	292	-0.78	74	89	52
$MePPh_3Br$	6.74	0.34	47.3	156	-0.534	65	44	140
$C_5H_9PPh_3Br$	-65.52	0.24	3.4	314	-0.42	90	15	90
$HPPh_3Br$	-74.85	0.00	359.8	726	0.85	0	9	90
PPh_4Br/site 1	13.20	0.279	-88.3	257	0.19	45	74	123
PPh_4Br/site 2	12.50	0.34	16.0	365	0.32	67	77	4

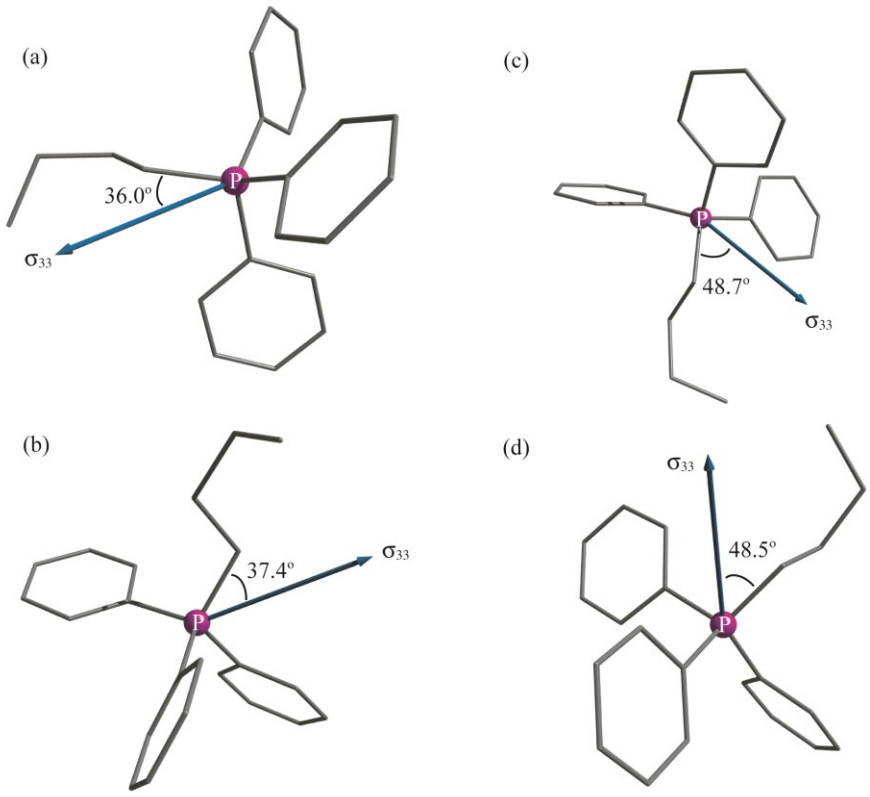

Figure 3.13: POV-ray image of the computed phosphorus magnetic shielding tensors from GIPAW DFT calculations on $BuPPh_3Br$ with (a) and without (c) the bromine atom, and on $BuPPh_3Cl$ with (b) and without (d) the chlorine atom. The halogen atoms were simply omitted from the input files, thus leaving empty spaces between the cations for calculations without the bromine or chlorine atoms. The orientation of σ_{33} with respect to the P–CH_2 bond changes upon the absence of the anions in the calculations. The carbon frameworks are represented by grey wires while the hydrogen atoms have been omitted for clarity. The halogen atoms have also been omitted in (a) and b).

In Table 3.5 the GIPAW DFT calculated ^{81}Br EFG and CS tensor parameters for the phosphonium halides are shown. It is evident that $C_Q(^{81}Br)$ is well predicted with an RMSD of 2.24 MHz (up to 31 % error for $MePPh_3Br$ and as low as 1% for $BuPPh_3Br$) for the *n*-alkyl

TPP bromides, whereas for $C_5H_9PPh_3Br$ and $HPPh_3Br$, this is not the case. It has been shown before that in this type of calculation, any inaccuracy in the position of the halogen or the surrounding atoms may result in very large errors in the predicted $C_Q(^{81}Br)$.[28] As the solid state structures input into the calculations were generated from X-ray diffraction data, the positions of the hydrogen atoms are not known exactly, and thus their positional optimization is desirable. Unfortunately, as the unit cell volumes of the structures considered here were too large (i.e., V > 1500 Å^3), it was not computationally feasible with our infrastructure as was the case with some of the amino acid hydrochlorides reported by Chapman *et al.*[57] If one compares the crystal structure of $BuPPh_3Br$ (where the calculated $C_Q(^{81}Br)$ is predicted within 1 % of the experimental value) and that of $HPPh_3Br$ (where this is 5 times greater than the experimental value determined by MAS), it can be shown that the closest hydrogen atom in the lattice is much closer to the bromide anion (2.25 Å) than in $BuPPh_3Br$ (2.84 Å). Granted in $C_5H_9PPh_3Br$, the closest hydrogen atom is at an unoptimized position of 2.54 Å (i.e., farther than in $HPPh_3Br$) but a wagging disorder in the cyclopentyl ring adjacent to the bromine atom may contribute to the large inaccuracy of its predicted $C_Q(^{81}Br)$. These effects on the $C_Q(^{81}Br)$ due to the proximity of the closest hydrogen atoms have been observed before in the case of glycyl-L-alanine $HBr{\cdot}H_2O$ where V_{33} for bromine was oriented towards the nearest hydrogen atom.[58] As for PPh_4Br, the two different crystallographic sites yield different calculated values for their $C_Q(^{81}Br)$s, which was observed experimentally. The ratio of $C_Q(^{81}Br)_{site1}/C_Q(^{81}Br)_{site2}$ of 1.06 is close to the observed ratio of 1.23 for $C_Q(^{81}Br)_{siteA}/C_Q(^{81}Br)_{siteB}$, which corresponds to a difference of nearly 14 %.

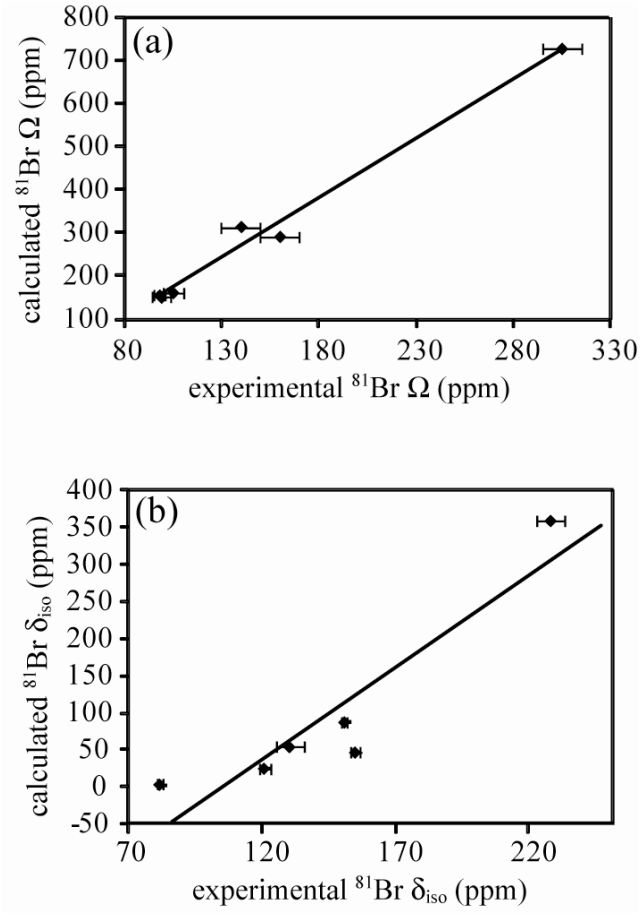

Figure 3.14: The GIPAW DFT calculated Ω (a) and δ_{iso} (b) plotted versus their experimental values for TPP bromides. The lines of best fit are as follows: (a) Ω(^{81}Br, calc.) = 2.763(Ω (^{81}Br, expt.)) – 117.36, R = 0.993; (b) δ_{iso}(^{81}Br, calc.) = 2.502(δ_{iso} (^{81}Br, expt.)) – 265.2, R = 0.919.

Shown in Figure 3.14b is a plot of the GIPAW DFT calculated vs. experimental values of δ_{iso}. The computed isotropic chemical shift is significantly overestimated in the calculations by approximately the same amount in all of the compounds studied; thus, there is a good correlation overall (Pearson's correlation coefficient R = 0.919). In the case of PPh_4Br, these calculations permit us to tentatively assign each bromine site in the crystal

structure of that compound. Site A has a slightly higher experimental $C_Q(^{81}Br)$ but a smaller η_Q and δ_{iso}, which is consistent with site 1 in the calculations. This site corresponds to the bromide ion lying further from the phosphorus cation ($d_{Br\text{-}P}$ = 6.24 Å). Site 2, which corresponds to the shortest Br–P distance (5.50 Å), is therefore assigned to site B.

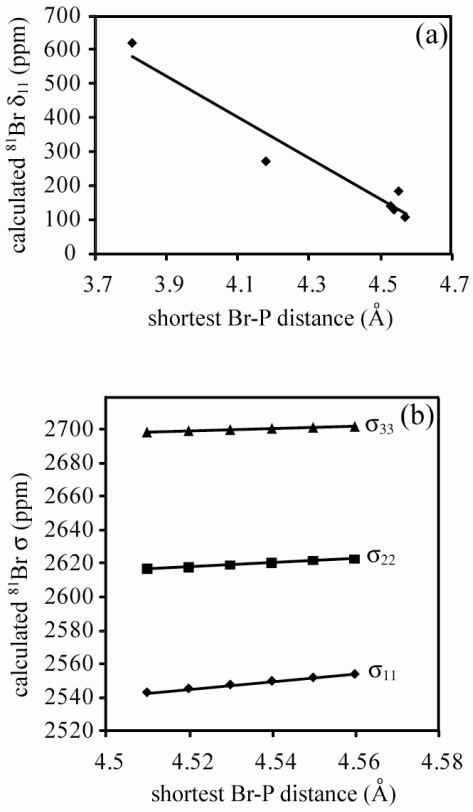

Figure 3.15: The GIPAW DFT calculated δ_{11} for all phosphonium halides (a) and σ_{ii} (i = 1, 2, 3) of $BuPPh_3Br$ (b) as a function of the shortest Br–P distance present in the crystal structure. The lines of best fit are as follows: (a) $\delta_{11}(^{81}Br, calc.) = -606.04(\delta_{11}\ (^{81}Br, expt.)) + 2885.9$, R = 0.969; (b) $\sigma_{11}(^{81}Br, calc.) = 220.6\ (d_{Br\text{-}P}) + 1548$, R = 1.000 and $\sigma_{22}(^{81}Br, calc.) = 122.6(d_{Br\text{-}P}) + 2064$, R = 0.999 and $\sigma_{33}(^{81}Br, calc.) = 63.3(d_{Br\text{-}P}) + 2413$, R = 0.998.

Unlike the δ_{iso} values, it is observed that the calculated spans are overestimated compared with the experimental values, but possess a relatively improved R value of 0.993 (Figure 3.14a). Because of this strong correlation, along with the relatively small error margins deduced experimentally for the CS tensor spans, we sought to investigate the experimental correlation between δ_{11} and the smallest Br–P distance in the crystal structure. Figure 3.15a shows that the experimental trend is corroborated by GIPAW DFT calculations, where the largest component of the calculated CS tensor in its PAS is inversely related to the shortest Br–P distance (R value of 0.969). When visualizing the calculated orientations of the different eigenvectors of the MS tensor PAS in the molecular frame, it is evident that, in all cases, σ_{11} is oriented approximately 90° from the internuclear vector corresponding to the smallest Br–P distance in the crystal structure (see Figure 3.16). This result may be interpreted by considering the effects of paramagnetic shielding on the bromine nucleus. According to Ramsey,[20] MS may be described using diamagnetic and paramagnetic terms (i.e., $\sigma = \sigma_{dia} + \sigma_{para}$), where the latter is an indication of the degree of mixing between occupied and virtual wave functions, which contribute to a particular shielding component. To probe the effects on the individual components of the MS tensor as the Br–P distance is systematically changed in the crystal structure, we performed multiple GIPAW DFT calculations on $BuPPh_3Br$, where the bromine atom is displaced along the direction of the Br–P internuclear vector. It is clear from Figure 3.15b that the most sensitive MS tensor component to this action is σ_{11} since the slope of this curve is 221 ppm/Å vs 123 ppm/Å for σ_{22} and 63 ppm/Å for σ_{33}. This is consistent with Ramsey's theory which, in this case, makes σ_{11} (or δ_{11}) the axis of rotation about which one of the bromide ion's p-type molecular orbitals will rotate 90° in order to favorably overlap with a virtual one, resulting in a

paramagnetic contribution to shielding. In fact, a decrease in the Br–P distance results in a decrease of $\sigma_{11,para}$ and because this term is negative, this results in an overall smaller σ_{11}. A smaller value of σ_{11} corresponds to a larger δ_{11}, which is consistent with the experimentally observed trend shown in Figure 3.12. We additionally performed ADF calculations with the PBE functional in order to validate our hypothesis. Although this method is cluster model based, these computations allow one to relate molecular orbitals to the diamagnetic and paramagnetic contributions to the overall shielding of the nucleus. Here, we used a model of $BuPPh_3Br$ and displaced the bromine nucleus along the Br–P internuclear vector. The results indicate an occupied molecular orbital with *p* character centered on Br^- that, when rotated 90° about the direction of σ_{11}, overlaps with a similar virtual orbital, thereby generating a paramagnetic contribution to shielding which changes most significantly upon varying the Br–P distance, which is in full agreement with Ramsey's theory.

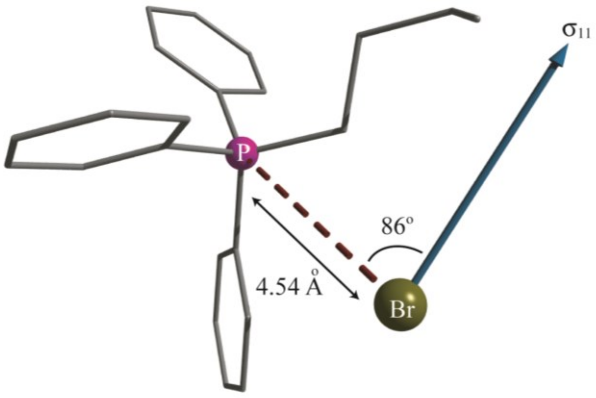

Figure 3.16: POV-ray image of the computed bromine magnetic shielding tensor from a GIPAW DFT calculation of $BuPPh_3Br$. It is clear that the σ_{11} (or δ_{11}) vector is nearly perpendicular to the Br–P internuclear vector as reported in the main text. The carbon frameworks are represented by grey wires while the hydrogen atoms have been omitted for clarity.

3.4 Conclusions

In summary, solid-state NMR techniques including challenging $^{79/81}$Br experiments have been employed with a range of applied magnetic field strengths, and the $^{79/81}$Br EFG and CS tensors for six TPP-cation-bearing phosphonium bromides of broad interest and application have been characterized. In order to relate these parameters to the molecular and crystal structure of these compounds, six new crystal structures were solved by single crystal XRD, including an updated structure for PPh_4Br, as the experimental SSNMR data extracted for this particular compound were not consistent with the reported crystal structure in the literature. It was found that small structural changes, which included the presence or absence of site symmetry elements, between each compound can manifest themselves in the NMR parameters as seen in the large ranges (hundreds of ppm) in the bromine CS tensor span and in the isotropic chemical shifts. These findings are non-trivial for nuclides where large quadrupolar interactions typically dominate the NMR spectra, such as $^{79/81}$Br, and demonstrate the power of SSNMR of nuclei which are typically thought of as "exotic" in detecting changes in crystal packing between nearly identical compounds.

Valuable information was also extracted from the results of GIPAW DFT calculations which employed the crystal structure data of the studied compounds. These have an advantage over cluster-based calculations, as they account for the periodicity of the structure and thus are well suited for predicting the NMR parameters of the ionic phosphonium halides. For the calculation of ^{31}P shielding tensors, the span is well predicted within experimental error while the isotropic chemical shifts are systematically overestimated using the ^{31}P absolute shielding scale. In addition, it was deemed important to include the halide ion in the calculations as its exclusion results in errors of the CS tensor's orientation with

respect to the molecular frame. It was possible to relate important structural features of the molecules and their crystal structures to the NMR parameters. For instance, the calculations substantiate the experimentally-determined strong dependence of the largest component of the bromine CS tensor, δ_{11}, on the shortest Br–P distance in the crystal structure, an exciting finding which shows that CS tensors (not just quadrupolar interactions) for exotic nuclei such as $^{79/81}$Br can be used to provide insight into structure, and therefore has possible application in the field of NMR crystallography. These calculations also permitted us to distinguish between the two chemically similar bromine sites in PPh_4Br, further demonstrating how halogen NMR can detect finite changes in the crystal structure.

3.5 References for Chapter 3

1. Neves, C. M. S. S.; Granjo J. F. O.; Freire, M. G.; Robertson, A.; Oliveira, N. M. C.; Coutinho, J. A. P. *Green Chem.* **2011**, *13*, 1517.
2. Bradaric, C. J.; Downard, A.; Kennedy, D.; Robertson, A. J.; Zhou, Y. *Green Chem.* **2003**, *5*, 143.
3. Gerritsma, D. A.; Robertson, A.; McNulty, J.; Capretta, A. *Tetrahedron Lett.* **2004**, *45*, 7629.
4. He, R.; Ding, C.; Maruoka, K. *Angew. Chem. Int. Ed.* **2009**, *48*, 4559.
5. Zhu, C.-L.; Zhang, F.-G.; Meng, W.; Nie, J.; Cahard, D.; Ma, J.-A. *Angew. Chem. Int. Ed.* **2011**, *50*, 5869.
6. Sun, J.; Wang, L.; Zhang, S.; Li, Z.; Zhang, X.; Dai, W.; Mori, R. *J. Mol. Catal. A-Chem.* **2006**, *256*, 295.

7. Cristiano, R.; Walls, A. D.; Weiss, R. G. *J. Phys. Org. Chem.* **2010**, *23*, 904.

8. Wittig, G.; Schöllkopf, U. *Ber.* **1954**, *87*, 1318.

9. Corey, E. J.; Yamamoto, H. *J. Am. Chem. Soc.* **1970**, *92*, 226.

10. Hon, Y.-S.; Lee, C.-F. *Tetrahedron* **2000**, *56*, 7893.

11. Sukman, E. L.; Montclair, N. J. (M&T Chemicals Inc. Woodbridge, N.J.). Tris(aryl)alkyl phosphonium halides and pesticidal compositions thereof. US Patent 4,264,593, April 28, **1981**.

12. Pomecko, R.; Asfari, Z.; Hubscher-Bruder, V.; Bochenska, M.; Armaud-Neu, F. *Supramol. Chem.* **2007**, *19*, 459.

13. Rideout, D. *Cancer Invest.* **1994**, *12*, 189.

14. Rideout, D.; Bustamante, A.; Patel, J. *Int. J. Cancer* **1994**, *57*, 247.

15. Cooper, W. A.; Bartier, W. A.; Rideout, D. C.; Delikatny, E. J. *Magn. Reson. Med.* **2001**, *45*, 1001.

16. Doiron, M.; Moulins, J.; Dean, R.; Palepu, R. M. *Phys. Chem. Liq.* **2008**, *46*, 212.

17. Mirau, P. A.; Serres, J. L.; Jacobs, D.; Garrett, P. H.; Vaia, R. A. *J. Phys. Chem. B* **2008**, *112*, 10544.

18. Bourgigot, S.; Vanderhart, D. L.; Gilman, J. W.; Awad, W. H.; Davis, R. D.; Morgan, A. B.; Wilkie, C. A. *J. Polym. Sci. Pol. Phys.* **2003**, *41*, 3188.

19. Ackermann, M.; Pascariu, A.; Höcher, T.; Siehl, H.-U.; Berger, S. *J. Am. Chem. Soc.* **2006**, *128*, 8434.

20. Ramsey, N. F. *Phys. Rev.* **1950**, *78*, 699.

21. Trill, H.; Eckert, H.; Srdanov, V. I. *J. Am. Chem. Soc.* **2002**, *124*, 8361.

22. Trill, H.; Eckert, H.; Srdanov, V. I. *J. Phys. Chem. B* **2003**, *107*, 8779.

23. Remsing, R. C.; Wildin, J. L.; Rapp, A. L.; Moyna, G. *J. Phys. Chem. B* **2007**, *111*, 11619.

24. Gordon, P. G.; Brouwer, D. H.; Ripmeester, J. A. *J. Phys. Chem. A* **2008**, *112*, 12527.

25. Alonso, B.; Massiot, D.; Florian, P.; Paradies, H. H.; Gaveau, P.; Mineva, T. *J. Phys. Chem. B* **2009**, *113*, 11906.

26. Gordon, P. G.; Brouwer, D. H.; Ripmeester, J. A. *ChemPhysChem* **2010**, *11*, 260.

27. Widdifield, C. M.; Bryce, D. L. *J. Phys. Chem. A* **2010**, *114*, 2102.

28. Widdifield, C. M.; Bryce, D. L. *Phys. Chem. Chem. Phys.* **2009**, *11*, 7120.

29. APEX Software Suite v.2010; Bruker AXS: Madison, WI, **2005**.

30. R. Blessing, *Acta Cryst.* **1995**, *A51*, 33.

31. G. M. Sheldrick, *Acta Cryst.* **2008**, *A64*, 112.

32. D. L. Bryce, G. M. Bernard, M. Gee, M. D. Lumsden, K. Eichele, R. E. Wasylishen, *Can. J. Anal. Sci. Spectrosc.* **2001**, *46*, 46.

33. A. L. Bloom, J. N. Shoolery, *Phys. Rev.* **1955**, *97*, 1261.

34. A. E. Bennett, C. M. Rienstra, M. Auger, K. V. Lakshmi, R. G. Griffin, *J. Chem. Phys.* **1995**, *103*, 6951.

35. T. L. Weeding, W. S. Veeman, *J. Chem. Soc. Chem. Commun.* **1989**, 946.

36. R. P. Chapman, C. M. Widdifield, D. L. Bryce, *Prog. Nucl. Magn. Reson. Spectrosc.* **2009**, *55*, 215.

37. K. Eichele, R. E. Wasylishen, *WSOLIDS NMR Simulation Software Version 1.17.30*, Universitat Tübingen, Tübingen (Germany), **2001**.

38. D. W. Alderman, M. S. Solum, D. M. Grant, *J. Chem. Phys.* **1986**, *84*, 3717.

39. W. P. Power, R. E. Wasylishen, S. Mooibroek, B. A. Pettitt, W. Danchura, *J. Phys. Chem.* **1990**, *94*, 591.

40. D. Massiot, F. Fayon, M. Capron, I. King, S. Le Calvé, B. Alonso, J.-O. Durand, B. Bujoli, Z. Gan, G. Hoatson, *Magn. Reson. Chem.* **2002**, *40*, 70.

41. Czerwinski, E. W. *Acta Cryst.* **2005**, *E61*, o2272.

42. Bricklebank, N.; Godfrey, S. M.; McAuliffe, C. A.; Pritchard, R. G. *Acta Cryst.* **1993**, *C49*, 1017.

43. a) Perdew, J. P.; Burke, K.; Ernzerhof, M. *Phys. Rev. Lett.* **1996**, *77*, 3865; b) Perdew, J. P.; Burke, K.; Ernzerhof, M. *Phys. Rev. Lett.* **1997**, *78*, 1396.

44. M. Gee, R. E. Wasylishen, A. Laaksonen, *J. Phys. Chem. A* **1999**, *103*, 10805.

45. C. J. Jameson, A. de Dios, A. K. Jameson, *Chem. Phys. Lett.* **1990**, *167*, 575.

46. M. Athee, *Ann. Acad. Sci. Fenn. A6* **1969**, *313*, 1.

47. Schweizer, E. E.; Baldacchini, C. J.; Rheingold, A. L. *Acta Cryst.* **1989**, *C45*, 1236.

48. Curnow, O. J.; Robinson, W. T.; Shang, *Acta Cryst.* **2007**, *E63*, o3951.

49. Widdifield, C. M.; Bryce, D. L. *Can. J. Chem.* **2011**, *89*, 754.

50. Czerwinski, E. W. *Acta Cryst.* **2004**, *E60*, o1442.

51. Balema, V. P.; Wiench, J. W.; Pruski, M.; Percharsky, V. K. *Chem. Commun.* **2002**, 724.

52. Wu, G.; Terskikh, V. *J. Phys. Chem. A* **2008**, *112*, 10359.

53. Widdifield, C. M.; Bryce, D. L. *J. Phys. Chem. A* **2010**, *114*, 10810.

54. Ashbrook, S. E.; Cutajar, M.; Pickard, C. J.; Walton, R, I.; Wimperis, S. *Phys. Chem.Chem. Phys.* **2008**, *10*, 5754.

55. F. Aquino, R. Govind, J. Autschbach, *J. Chem. Theory Comput.* **2011**, *7*, 3278.

56. M. Kaupp, M. Bühl, V. G. Malkin, Eds., Calculation of NMR and EPR Parameters. Theory and Applications. Wiley-VCH: Weinheim, Germany, 2004, p. 237.

57. Chapman, R. P.; Hiscock, J. R.; Gale, P. A.; Bryce, D. L. *Can J. Chem.* **2011**, *89*, 822.

58. Kehrer, A.; Weiden, N.; Weiss, A. *Z. Phys. Chem.* **1992**, *178*, 1.

4 Magnesium Aryl Carboxylates Characterized with ^{25}Mg SSNMR Spectroscopy

In Chapter 3 was presented a comprehensive $^{79/81}$Br SSNMR study of bromide anion when crystallized with organic TPP cations. One of the main conclusions was that the $^{79/81}$Br CS tensor could be correlated to the Br–P distance measured in the crystal structures. The following two Chapters will focus rather on the exotic alkaline-earth metal quadrupolar nuclei crystallized once again in organic coordination environments. In this Chapter, it will be shown that ^{25}Mg EFG and CS tensor parameters can be correlated to the coordination geometry of the magnesium cation.

4.1 Introduction

The divalent magnesium cation (Mg^{2+}) plays an essential role in many biochemical processes as well as in materials science.[1,2] Very recently, there has been substantial interest in the synthesis and characterization of metal organic frameworks (MOFs) comprising affordable metals such as the alkaline-earth metals, including magnesium.[3,4,5,6] Insight into the local structure and coordination environment surrounding the Mg^{2+} cation is important if we wish to understand how magnesium can play a role in future materials science

applications in general. Analytical methods currently available to gain site-specific information on the coordination polyhedra about Mg^{2+} in the solid state are rare.[7] However, it is known that SSNMR parameters are sensitive to small structural changes about the probed nucleus.[8,9,10] This has opened the door to the possibility of NMR crystallography,[11] where crystal structures can be refined[12,13,14,15] or fully solved with both SSNMR and powder X-ray diffraction (PXRD).[16,17,18,19,20,21,22,23,24]

As presented in Table 1.1, the nuclear properties of the only NMR-active nucleus for magnesium, ^{25}Mg, make it a particularly unattractive nucleus for NMR studies. Advances in NMR technology have allowed for the development of ultrahigh-field magnets thus making the study of the challenging ^{25}Mg nucleus increasingly feasible. However, studies to date have been mainly focused on inorganic materials such as oxides, silicates, and phosphates.[25] For example, Laurencin and co-workers[26] recently recorded high-quality ^{25}Mg SSNMR spectra for a series of magnesium phosphates in magnetic fields of 17.6 and 20.0 T and have attempted to use their benchmark ^{25}Mg SSNMR data to aid in the characterization of magnesium-doped hydroxyapatite [$Ca_{9.1}Mg_{0.9}(PO_4)_6(OH)_2$], a material found in bone and teeth. However, it is apparent that there is a dearth of ^{25}Mg SSNMR studies of Mg^{2+} in organic molecular environments as highlighted by Smith and co-workers in a recent review;[25] they state that "the accumulation of a larger number of reliable NMR data in Mg-containing organic materials is certainly required for the establishment of meaningful and useful correlations between the ^{25}Mg NMR parameters and structural aspects of the bonding involving Mg^{2+}". In addition to the difficulties associated with all ^{25}Mg NMR studies noted above, one of the main reasons for the lack of ^{25}Mg SSNMR data of organic systems is the low mass-percentage of magnesium present in them, resulting in challenges in obtaining

spectra with acceptable signal-to-noise ratios. Such difficulties have led to the use of somewhat costly ^{25}Mg isotopic enrichment schemes[27] such as in the cases of Mg(TTP)·Py_2 (TTP = 5,10,15,20-tetraphenylporphyrinato) [28] and magnesium phthalocyanine (MgPc·H_2O·Py).[29] Lipton et al.[30] have used isotopic enrichment along with $^{1}H \rightarrow ^{25}Mg$ CP at very low temperatures (10 K) in order to investigate the binding modes of Mg^{2+} (0.07% by weight) in the DNA repair protein apurinic/apyrimidic endonuclease 1 (AEP1). Simultaneously, sensitivity enhancement methods that manipulate nuclear satellite populations in favor of enhancing the CT population difference such as HS or DFS[31] or the QCPMG pulse sequence have enabled the characterization of a handful of octahedral 'MgO_6' environments such as those found in magnesium acetate, acetylacetonate, and formate.[32,33] With an eye to application in characterizing magnesium-based MOFs and other Mg^{2+}-binding organic and biochemical compounds, it is therefore desirable to acquire reliable ^{25}Mg SSNMR data for a larger set of organic complexes with known structure to establish useful relationships between the ^{25}Mg NMR parameters and the immediate coordination environment surrounding Mg^{2+} in such systems.[25]

In this study we have synthesized six magnesium benzoates and salicylates where the structures of the ligands are found in Figure 4.1, and for which crystal structures are known from XRD.[34] These are an important class of ligands given the utility of benzoates as common backbones in many MOFs used, for example, for the adsorption of gases such as CO_2.[35] Very recently, Huang and co-workers probed Mg^{2+} centers *via* ultrahigh-field ^{25}Mg SSNMR in the CPO-27-Mg[36] and α-$Mg_3(HCOO)_6$[37] MOFs upon the adsorption of solvent vapors such as water, acetonitrile, acetone, dimethylformamide, and benzene. In both of these studies, it was not obvious how the NMR parameters (i.e., a range of 0.9 to 6.4 MHz in

the $|C_Q(^{25}Mg)|$ values) are related to the fine details of the coordination environment about Mg. Although the complexes in the present work lack the extended three-dimensional network structures needed to be considered MOFs, they are nonetheless representative of various Mg MOFs both chemically, i.e., the nature of the Mg^{2+} coordination environments, and from a technical NMR standpoint, i.e., the number of ^{25}Mg nuclei per nm^3 of the solid (0.45 for CPO-27-Mg, 0.73 for α-$Mg_3(HCOO)_6$, and only 0.12 for Mg(pams) in this work). This systematic investigation will allow for more meaningful correlations regarding the relationship between ^{25}Mg NMR parameters and octahedral MgO_6 coordination environments in organic systems such as MOFs. Our interpretation of the NMR data will be aided by the use of the GIPAW DFT method, which has found wide-spread usage for the calculation of NMR parameters in solids.[38]

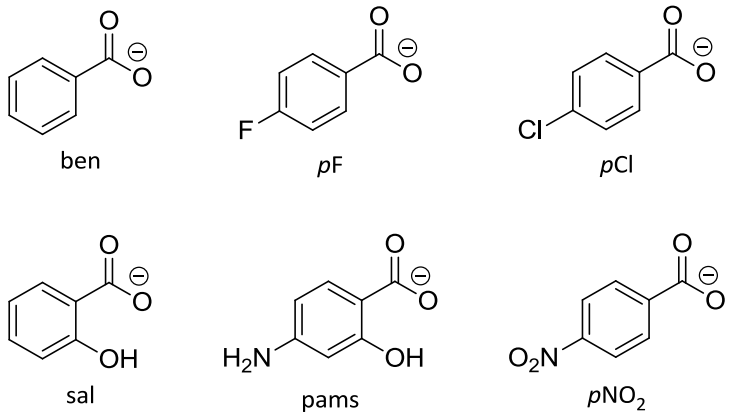

Figure 4.1 Benzoate and salicylate ligands used in this study: ben (benzoate), *p*F (*p*-fluorobenzoate), *p*Cl (*p*-chlorobenzoate), sal (salicylate), pams (*p*-aminosalicylate), and *p*NO_2 (*p*-nitrobenzoate).

4.2 Experimental Details

4.2.1 Sample Preparation and Synthesis

The materials necessary for the synthesis of the magnesium carboxylates in Figure 4.1 (*p*-fluorobenzoic acid (*p*F), *p*-chlorobenzoic acid (*p*Cl), *p*-nitrobenzoic acid (*p*NO_2), sodium benzoate (Na(ben)), sodium salicylate (Na(sal)), sodium *p*-aminosalicylate (Na(pams)), magnesium carbonate ($MgCO_3$), and magnesium chloride ($MgCl_2$)) were all purchased from Sigma-Aldrich. All samples were prepared with ^{25}Mg at natural abundance.

Mg(*p*Cl) and Mg(*p*NO_2) were synthesized *via* a variation of a previously reported method by Arlin *et al*.[34] whereby a 1:1 stoichiometric mixture of 1 g of *p*Cl or *p*NO_2 and the appropriate amount of $MgCO_3$ are first dissolved in 20 mL of distilled water. The solution is stirred overnight after which the non-dissolved starting material is filtered over a pad of Celite. The collected colorless mother liquor is slowly evaporated at room temperature for several days until crystals of the appropriate Mg salt are obtained.

For Mg(ben), Mg(sal), and Mg(pams), 1 g of the apposite sodium salt was dissolved in a minimum of water to which the appropriate amount of $MgCl_2$ is added to form a 1:1 stoichiometric ratio. The mixture was stirred for several minutes and then filtered through cotton. The resulting homogeneous solution was allowed to slowly evaporate over several days until transparent crystals appeared in the flask. A new crystal structure for Mg(ben) was acquired in the course of this study, which can be found in Appendix B4.

Mg(*p*F) cannot be synthesized in pure form in the same way as Mg(*p*Cl) or Mg(*p*NO_2). Thus, 1 g of (*p*F) was dissolved in 20 mL of EtOH to which 1 equivalent of

NaOH was added and the mixture was refluxed for 1 hour. The solvent was then evaporated and 1 g of the resulting sodium salt was dissolved in a minimum of water to which the appropriate amount of $MgCl_2$ was added for a 2:1 stoichiometric ratio of Na(*p*F) to $MgCl_2$. This solution was filtered over cotton and the collected mixture was allowed to evaporate slowly at room temperature where crystals of pure Mg(*p*F) formed within a few days.

All samples were ground into fine powders with a mortar and pestle for PXRD experiments and subsequently packed into 4 or 7 mm ZrO_2 rotors for solid-state NMR experiments.

4.2.2 Single Crystal X-Ray Diffraction

Suitable crystals of Mg(ben) were selected, mounted on a thin glass fibre using paraffin oil, and cooled to the data collection temperature of 200 K. Data were collected on a Bruker AXS SMART single crystal diffractometer equipped with a sealed Mo tube source (wavelength = 0.71073 Å), and an APEX II CCD detector. Raw data collection and processing were performed with the APEX II software package from Bruker AXS.[39] Diffraction data were collected with a sequence of 0.3° ω scans at 0°, 120°, and 240° each with 650 frames in φ. Initial unit cell parameters were determined from 60 data frames and correspond to different sections of the Ewald sphere. Semi-empirical absorption corrections based on equivalent reflections were applied.[40] The systematic absences and unit cell parameters were consistent with the *C*2/*c* space group. Solutions yielded chemically reasonable and computationally stable results of refinement. The structure was solved by direct methods, completed with difference Fourier syntheses, and refined with full-matrix least-squares procedures based on F^2. Positions of all the hydrogen atoms were obtained

from the Fourier map analysis; however, all hydrogen atoms were added into idealized positions in order to satisfy the formula. All scattering factors are contained in several versions of the SHELXTL program library, with the latest version used being 6.12.[41] The complete crystallographic information file (.cif) is found in Appendix B4.

4.2.3 Solid-State NMR Experiments

For ^{13}C solid-state NMR experiments, spectra were recorded at B_0 = 4.7 (Bruker AVANCE III, $\nu_L(^1H)$ = 200.13 MHz and $\nu_L(^{13}C)$ = 50.31 MHz) and 9.4 T (Bruker AVANCE III, $\nu_L(^1H)$ = 400.13 MHz and $\nu_L(^{13}C)$ = 100.62 MHz) using Bruker 4 mm (9.4 T) and 7 mm (4.7 T) triple-resonance (HXY) probes at the University of Ottawa under CP/MAS conditions. Individual experimental parameters along with chemical shift assignments for Mg aryl carboxylates can be found below. Dipolar dephasing experiments[42] at B_0 = 4.7 T used a 40 μs delay between the pulse and the signal acquisition. Specific experimental parameters and ^{13}C chemical shift assignments are as follows:

Mg(*p*F). ^{13}C CP/MAS NMR at B_0 = 9.4 T, ν_{rot} = 8 kHz, ^1H $\pi/2$ = 3 μs, contact time = 2.5 ms, recycle delay = 5 s, number of scans = 1368, δ (ppm): 176.9 (C=O), 170.0–157.7 (C–F), 133.3 (CH), 129.4 (C), 116.1 (CH), 114.7 (CH).

Mg(*p*Cl). ^{13}C CP/MAS NMR at B_0 = 9.4 T, ν_{rot} = 8 kHz, ^1H $\pi/2$ = 3 μs, contact time = 2.5 ms, recycle delay = 5 s, number of scans = 1368, δ (ppm): 176.8 (C=O), 172.6 (C=O), 142.1–137.9 (C–Cl), 132.7 (C), 131.7 (C), 129.2 (CH).

Mg(pNO$_2$). ^{13}C CP/MAS NMR at B_0 = 9.4 T, ν_{rot} = 8 kHz, ^{1}H $\pi/2$ = 3 μs, contact time = 2.5 ms, recycle delay = 5 s, number of scans = 880, δ (ppm): 170.4 (C=O), 147.2 (C–NO$_2$), 140.1 (C), 130.7 (CH), 124.5 (CH).

Mg(sal). ^{13}C CP/MAS NMR at B_0 = 4.7 T, ν_{rot} = 4.5 kHz, ^{1}H $\pi/2$ = 3.4 μs, contact time = 2 ms, recycle delay = 2 s, number of scans = 208, δ (ppm): 173.1 (C=O), 161.1 (C–OH), 136.3 (CH), 131.5 (CH), 119.4 (CH), 117.3 (C).

Mg(ben). ^{13}C CP/MAS NMR at B_0 = 4.7 T, ν_{rot} = 4 kHz, ^{1}H $\pi/2$ = 3.4 μs, contact time = 2 ms, recycle delay = 5 s, number of scans = 11744, δ (ppm): 177.8 (C=O), 172.7 (C=O), 136.2 (C), 135.2 (C), 132.7 (CH), 131.2 (CH), 129.1 (CH), 128.3 (CH).

Mg(pams). ^{13}C CP/MAS NMR at B_0 = 9.4 T, ν_{rot} = 8 kHz, ^{1}H $\pi/2$ = 3 μs, contact time = 2.5 ms, recycle delay = 5 s, number of scans = 1704, δ (ppm): 173.9 (C=O), 160.9 (C–OH), 151.5 (C–NH$_2$) 133.6 (CH), 110.7 (C), 110.1 (CH), 102.4 (CH).

^{25}Mg solid-state NMR spectra were recorded at 9.4 T (Bruker AVANCE III, $\nu_L(^1H)$ = 400.13 MHz and $\nu_L(^{25}Mg)$ = 24.49 MHz) at the University of Ottawa and at 21.1 T (Bruker AVANCE II, $\nu_L(^1H)$ = 900.13 MHz and $\nu_L(^{25}Mg)$ = 55.10 MHz) at the National Ultrahigh-Field NMR Facility for Solids in Ottawa. At B_0 = 9.4 T, Bruker 7 mm static and MAS low-frequency double-resonance (HX) probes were used. At B_0 = 21.1 T, a Bruker 4 mm MAS low-frequency double-resonance (HX) probe, a Bruker 7 mm MAS low-frequency single-channel probe, and a 7 mm static home-built low-frequency double-resonance (HX) static probe was used. Chemical shifts were referenced to a saturated aqueous solution of $MgCl_2$ at

0.0 ppm;[32] this solution was also used for pulse calibration. The CT–selective $\pi/2$ pulse for Mg aryl carboxylates was that of $MgCl_2$(aq) scaled by a factor of $1/(I+1/2) = 1/3$ for ^{25}Mg. Spectra were acquired using either a solid echo (i.e., $\pi/2-\tau_1-\pi/2-\tau_2$–acq.) or Hahn-echo (i.e., $\pi/2-\tau_1-\pi-\tau_2$–acq.) sequence. At 9.4 T it was sometimes necessary to use the DFS polarization method in order to enhance the signal of the CT. In those cases, the DFS pulse swept from 800 to 80 kHz for a duration of 5 ms. In the case of Mg(sal), an enhancement of 2.5 was observed compared to the spectrum acquired without DFS. For Mg(sal), the QCPMG pulse sequence was used in order to increase the signal-to-noise ratio of the spectrum. In this case, and in that of Mg(pams), the VOCS method was needed in order to observe a uniform excitation profile. Specific experimental details for each compound are found in Table A4.1 in Appendix A.

4.2.4 Data Processing and Simulations

All spectra were processed using the Bruker TopSpin software (ver. 3.0). Echoes were left shifted whenever necessary, then Fourier transformed. ^{25}Mg NMR spectra were simulated with the WSolids[43] software package or, in the case of Mg(*p*Cl), SIMPSON (with the zcw17710 crystallite file for powder averaging).[44] Some figures were generated with graphics produced by DMFit (version 2011).[45]

4.2.5 GIPAW DFT Calculations

GIPAW DFT computations were performed using version 4.1 of CASTEP-NMR (Accelrys Inc. San Diego, California). Input files were generated via the Materials Studio version 3.2 software package (Accelrys Inc.)[46] with the available crystallographic information files (i.e., ref. 34 for Mg(*p*F), Mg(*p*Cl), and Mg(pNO$_2$); ref. 48 for Mg(sal); ref.

47 for Mg(pams). The PBE XC functional was used under the GGA along with on-the-fly generated pseudopotentials. All hydrogen positions were optimized prior to NMR calculations and so it was sometimes necessary to use the "coarse" setting for the energy cut-off, E_{cut}, and *k*-point grid settings for certain calculations due to the large unit cell volumes. Specific computational details for each compound discussed in this work can be found in Table A4.2 in Appendix A. ^{25}Mg MS and EFG tensor information can be obtained from the generated .magres output files with a modified version of the EFGShield program. The calculated δ_{iso} is calculated from the available absolute shielding constant ($\sigma_{iso,ref}$ = 566.1 ± 1.0 ppm) for ^{25}Mg.[33] Because of a doubly-disordered water molecule in the lattices of Mg(ben) and Mg(*p*Cl), two separate calculations were performed for each compound to examine the effects of the disorder on the MS and EFG tensor parameters.

4.3 Results and Discussion

4.3.1 Synthesis and Initial Characterization

The X-ray crystal structures of Mg(*pF*), Mg(*p*Cl), Mg(ben), and Mg(*p*NO_2) have been previously reported by Arlin et al.[34] and slightly older structures are available for Mg(pams)[47] and Mg(sal).[48] Since our ^{25}Mg NMR data were not consistent with the reported structure for Mg(ben), we have acquired a new crystal structure for this compound (*vide infra*). In order to verify the purity of the synthesized magnesium aryl carboxylates, we performed PXRD on each of the samples (see Figure 4.2) to compare with the powder pattern predicted from the available crystal structures. As for Mg(*p*F), the proposed synthetic route[34] (1:1 $MgCO_3$ and *p*–fluorobenzoic acid) yielded the correct product but with the presence of an impurity that

was later identified by PXRD as nesquehonite ($MgCO_3 \cdot 3H_2O$).[49] Attempts at characterizing this byproduct by ^{25}Mg SSNMR were unsuccessful as it is known to release CO_2 upon contact with air.[50] Instead, we have synthesized pure Mg(*p*F) via the reaction of the sodium salt and $MgCl_2$ in a stoichiometric ratio of 1:2 (see Experimental section for more details).

4.3.2 Carbon-13 CP/MAS NMR Spectra

Our ^{13}C CP/MAS experiments were consistent with the reported diffraction structures. These spectra, along with those of the pure ligands, may be found in Figure 4.3 and were acquired at 4.7 or 9.4 T. ^{13}C resonance assignments were aided by field-dependent broadening of some of the resonances due to residual dipolar coupling with quadrupolar nuclei from various functionalities on the aryl ring (i.e., $^{13}C–^{14}N$, $^{13}C–^{35/37}Cl$, $^{13}C–^{19}F$) and by dipolar dephasing experiments at 4.7 T in order to identify *ipso*–^{13}C resonances.[42] In all cases, the number of ^{13}C carboxyl resonances is consistent with the expected number of magnetically unique carboxylate functionalities present in the crystal structure. Mg(ben) and Mg(*p*Cl) show two carbonyl resonances (for Mg(*p*Cl), $\delta_{iso}(^{13}C{=}O)$ = 176.8 and 172.6 ppm) whereas the other four compounds show only one. This highlights the possibility of differentiating between bridging (Mg–O–C–O–Mg, 176.8 ppm < $\delta_{iso}(^{13}C{=}O)$ < 177.8 ppm) and terminal (Mg–O–C–O, 172.6 ppm < $\delta_{iso}(^{13}C{=}O)$ < 173.9 ppm) carboxylates (see Figure 4.4) *via* ^{13}C CP/MAS NMR. Mg(*p*Cl) and Mg(ben) each form one-dimensional polymeric chains with bridging carboxylates and each Mg^{2+} site is bound to a terminal carboxylate. In Mg(sal) and Mg(pams), only the terminal type of carboxylate anion is present so one carbonyl resonance is observed in each spectrum. For Mg(*p*F), only one type of carboxylate group exists again but it is of the bridging type in a two-dimensional coordination polymer.

This would explain why its chemical shift resembles more closely that of the less shielded carbonyl resonance in Mg(*p*Cl) and Mg(ben) rather than that observed for Mg(sal), for example. The bridging carboxylate moieties tend to have more deshielded ^{13}C resonances than the terminal ones. As for Mg(pNO$_2$), the *p*–nitrobenzoate ligands are not bound to the magnesium centre thus an even lower chemical shift is observed for the ^{13}C resonance (170.4 ppm; see Figure 4.4). It is not possible, however, to distinguish in this case between the chemically equivalent but crystallographically inequivalent "floating" ligands present in the lattice. Such differentiations between different carboxylate binding modes have been observed previously by ^{13}C CP/MAS NMR for zinc clusters.[51,52]

Table 4.1: Experimental ^{25}Mg EFG Tensor Parameters and Chemical Shifts for Mg Aryl Carboxylates.[a]

compound	$\lvert C_Q(^{25}Mg)\rvert$[b] /MHz	η_Q	δ_{iso} /ppm
Mg(*p*F)	2.70(0.05)	0.47(0.03)	-5(1)
Mg(*p*Cl)	4.42(0.03)	0.50(0.03)	-4(1)
Mg(ben)	4.45(0.05)	0.35(0.05)	-5(1)
Mg(sal)	4.55(0.05)	0.50(0.05)	3(2)
Mg(pams)	6.15(0.05)	0.58(0.02)	3(2)
Mg(pNO$_2$)[c]	2.05(0.05)	0.85(0.05)	-2(2)

[a] Experimental errors are in parentheses.
[b] One measures the absolute value of the quadrupolar coupling constant under the present experimental conditions.
[c] These values represent the dominant site observed in the ^{25}Mg NMR spectra. It was not possible to unambiguously assign parameters for all three Mg sites in this compound. See the discussion for further details.

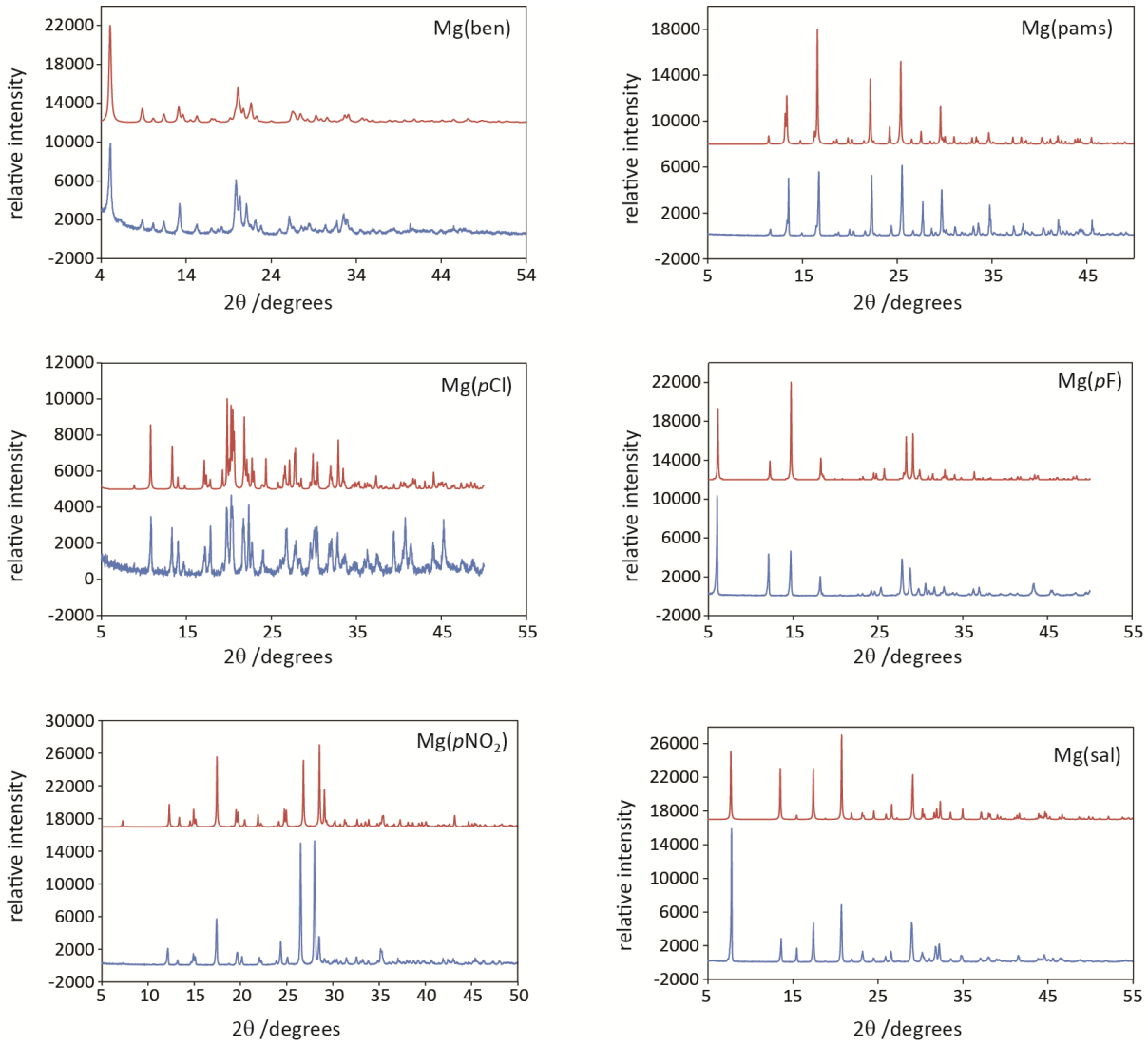

Figure 4.2: Experimental powder X-ray diffraction patterns for all magnesium compounds (experimental traces are in blue) along with simulations in red based on the existing X-ray crystal structure data. All experiments were carried out using a Rigaku Ultima IV instrument with 2θ ranging between 5 and 50 (or 55)° in increments of 0.02° at a rate of 2° per minute. Simulations were generated using the Mercury software available from the Cambridge Crystallographic Data Centre.

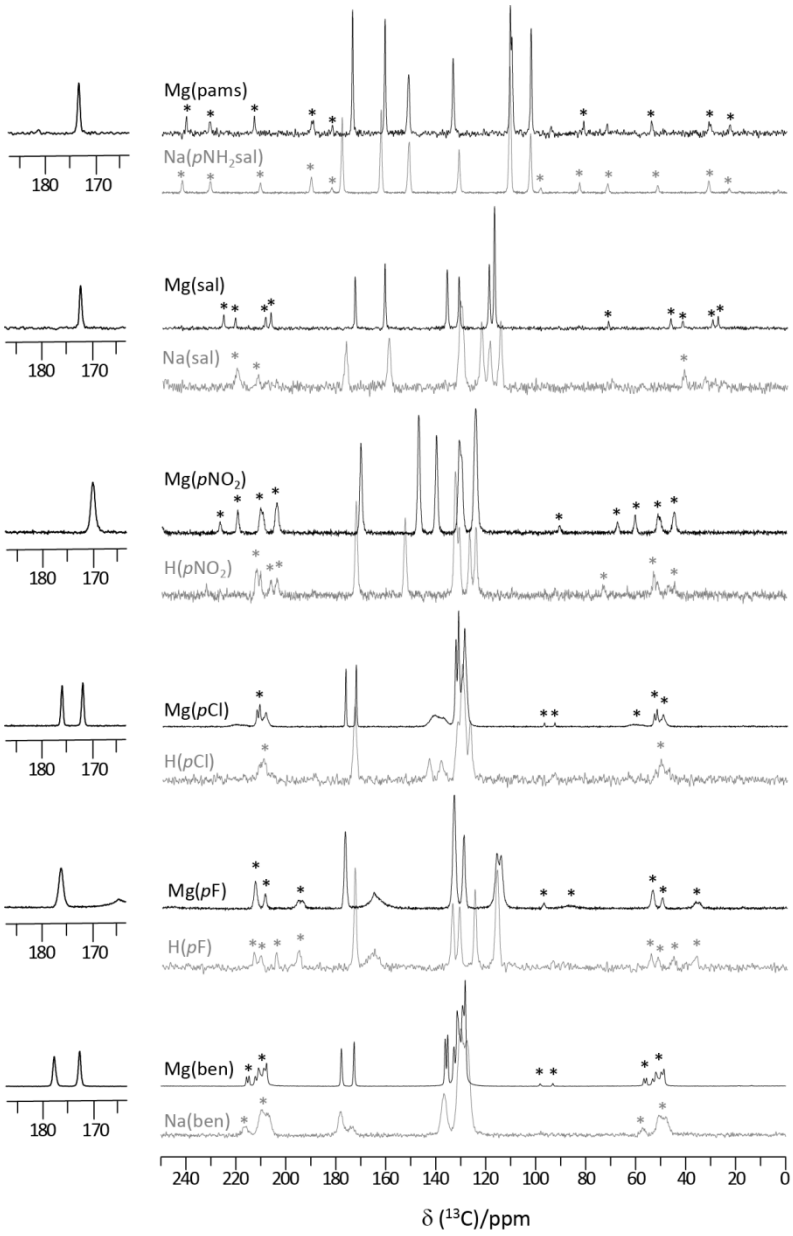

Figure 4.3: ^{13}C CP/MAS NMR spectra acquired at 4.7 or 9.4 T for all Mg salts (black) characterized in this work along with the spectra of the pure ligands in acid (HL) or sodium salt (NaL) form (grey). Zoom-in of the carbonyl region in the ^{13}C CP/MAS NMR spectra acquired are to the left of the full NMR spectra.

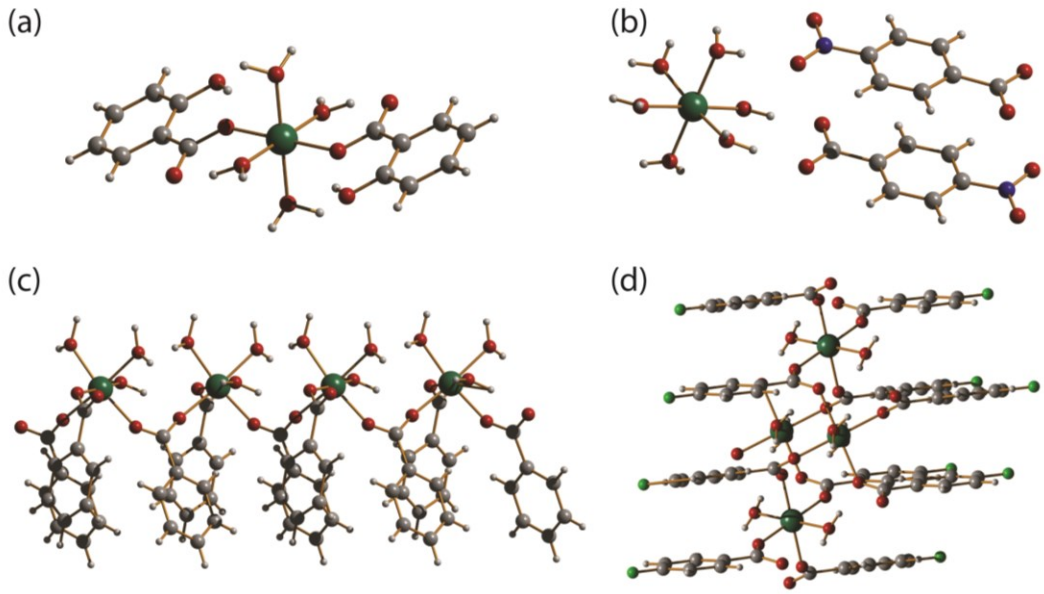

Figure 4.4: Local crystallographic structures for the magnesium benzoates and salicylates studied in this work. Mg(sal) and Mg(pams) crystallize similarly in isolated "molecular" coordination units with solely terminal carboxylate ligands as shown in (a) for Mg(sal). Mg(*p*NO_2) has a $[Mg(H_2O)_6]^{2+}$ dication and floating *p*-nitrobenzoate ligands as shown in (b). Mg(ben) and Mg(*p*Cl) crystallize similarly and feature bridging and terminal carboxylate ligands forming a 1D chain as shown for Mg(ben) in (c). Mg(*p*F) features solely bridging carboxylate ligands, forming a 2D coordination network in (d).

4.3.3 Experimental ^{25}Mg SSNMR of magnesium aryl carboxylates

Presented in Figure 4.5 are the ^{25}Mg MAS NMR spectra of the magnesium aryl carboxylates considered in this work. All spectra were acquired at B_0 = 21.1 T. These MAS spectra allow for an accurate determination of the ^{25}Mg quadrupolar parameters, C_Q and η_Q, as well as the isotropic chemical shifts, δ_{iso}, in the absence of broadening caused by CSA.

Complementary NMR spectra acquired under stationary conditions at B_0 = 21.1 T are illustrated in Figure 4.6. Spectra acquired at B_0 = 9.4 T are shown in Figure 4.7). We note that at the lower magnetic field strength, we sometimes employed the DFS method in order to enhance the CT signal *via* population transfer from the satellite transitions and/or the QCPMG pulse sequence to increase the signal-to-noise ratio. In Table 4.1 are listed the ^{25}Mg quadrupolar and chemical shift parameters extracted by analytical simulations of the observed line shapes. It was not possible to determine ^{25}Mg CSA at a useful level of precision, as, although its effects on the spectral line shapes are accentuated at higher magnetic field strengths, these are not expected to be larger than ~20 ppm from our calculations (*vide infra*). This is not surprising given that there are few reported CSA measurements from ^{25}Mg NMR experiments.[33] The observed range in the quadrupolar coupling constant for ^{25}Mg is from 2.70 MHz for Mg(*p*F) to 6.15 MHz for Mg(pams), which is consistent with other near-octahedral MgO_6 environments in the handful of reliable data (three compounds) that exist for Mg^{2+} in organic small-molecule environments (i.e., from 2.3 MHz in $Mg(HCOO)_2{\cdot}2H_2O$ to 7.1 MHz in $Mg(acac)_2{\cdot}2H_2O$).[32,33] Specific observations made for each compound reported in this work with respect to their individual structures are discussed below.

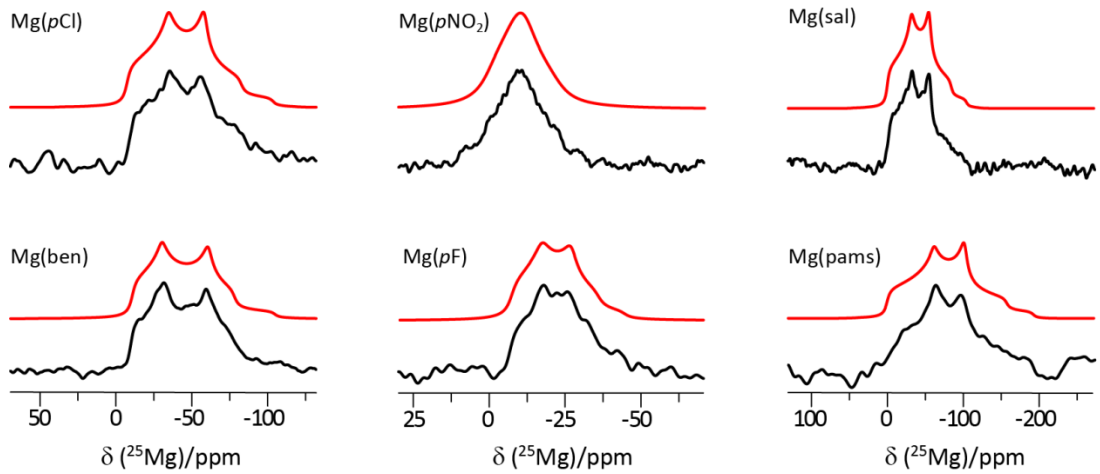

Figure 4.5: ^{25}Mg MAS NMR spectra acquired at B_0 = 21.1 T. Experimental spectra are in black and analytical simulations are in red. Spinning frequencies varied from 7 kHz to 12.5 kHz (see Experimental Details for more details).

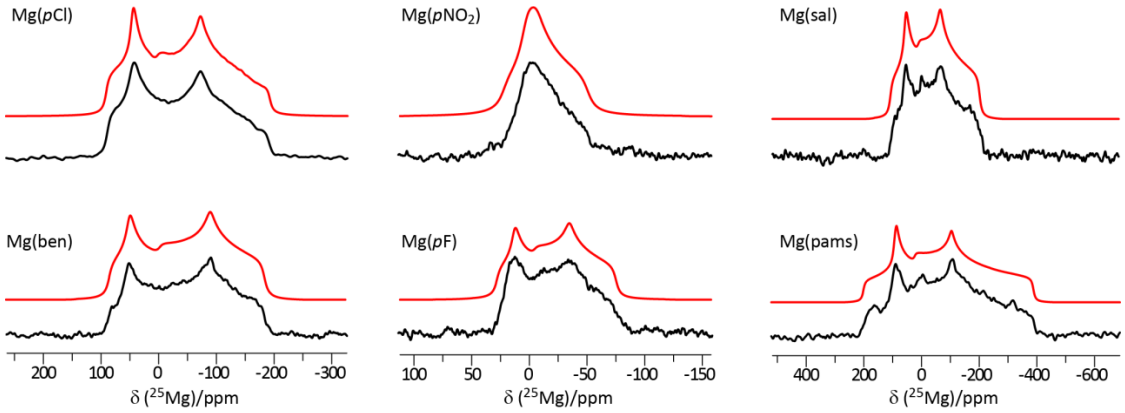

Figure 4.6: ^{25}Mg NMR spectra acquired at B_0 = 21.1 T under stationary conditions. Experimental spectra are in black and simulations are in red. Experiments were performed using a Hahn or solid echo sequence and ^{1}H decoupling (see Experimental Details for more details).

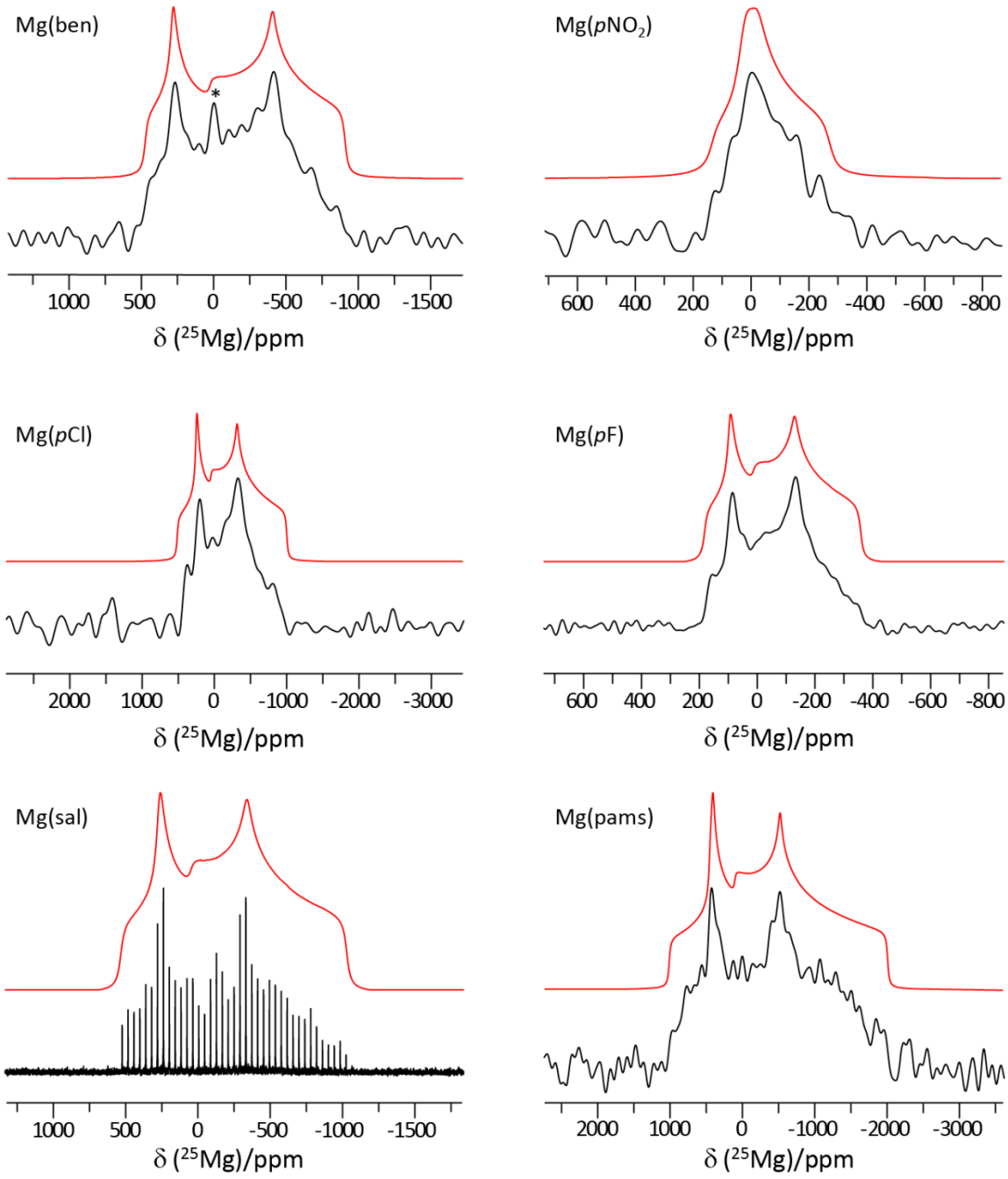

Figure 4.7: ^{25}Mg NMR spectra acquired at B_0 = 9.4 T under stationary conditions. Experimental spectra are in black and analytical simulations from WSolids are in red. All experiments used ^{1}H decoupling. QCPMG was used for Mg(sal). In some cases DFS was also used. See Appendix A4.1 for specific experimental conditions.

4.3.3.1 The structures of Mg benzoate and Mg p-chlorobenzoate

According to the crystal structure, Mg(ben) crystallizes in the $P2_1/n$ space group and contains two crystallographically distinct Mg^{2+} sites.[34] This is in apparent disagreement with our ^{25}Mg NMR data as only one site is resolved under MAS and stationary conditions (see Figures 4.5 and 4.6) with a $|C_Q(^{25}Mg)|$ of 4.45 MHz and a δ_{iso} of -5 ppm. Although it is conceivable that the two non-equivalent Mg sites could have fortuitously identical ^{25}Mg NMR parameters, this prompted us to re-determine the single-crystal X-ray structure for this compound and we find that Mg(ben) is better described in the $C2/c$ space group. Table 4.2 contains the relevant unit cell parameters from both structures. It is apparent that the unit cell parameters are very similar to those reported previously, with the main difference being simply the space group used to refine the structure. The new crystal structure has only one unique Mg^{2+} site, consistent with our ^{25}Mg NMR data. Furthermore, we would expect the presence of two terminal as well as two bridging carboxylate resonances in the ^{13}C CP/MAS NMR spectrum if the $P2_1/n$ structure were accurate; instead the spectrum clearly shows only two peaks total in the carboxylate region. The simulated PXRD diffractograms from both crystal structures are indistinguishable. This shows that ^{25}Mg SSNMR experiments can be useful in providing constraints for the refinement of diffraction-based crystallographic information. Figure 4.8 demonstrates this nicely with the aid of GIPAW DFT calculations. Computed parameters based on the $C2/c$ structure provide better agreement with the experimental MAS spectrum at 21.1 T than do computed parameters based on the $P2_1/n$ model. Further evidence for the validity of the $C2/c$ structure of Mg(ben) comes in the form of a comparison with that of Mg(*p*Cl). The structure of the latter is similar to that of Mg(ben) in that both form the same type of 1D coordination chains linked by carboxylate

anions in the solid state along with three Mg-bound H_2O molecules in a *fac* geometry and a disordered water molecule in the lattice (see Figure 4.4). Both compounds crystallize in the same space group, *C*2/*c*, and this is further corroborated by their identical $|C_Q(^{25}Mg)|$ and δ_{iso} values within experimental error.

Table 4.2: Select Crystallographic Information for Mg(ben) Compared to a Previously Reported Structure (ref. 34).[a]

parameter	previous work	this work
space group	$P2_1/n$	$C2/c$
a_c /Å	8.8802(16)	8.9061(9)
b_c /Å	10.4210(18)	10.4274(10)
c_c /Å	35.019(6)	35.226(4)
α_c /°	90.000	90.000
β_c /°	97.228(3)	97.477(8)
γ_c /°	90.000	90.000
volume /Å^3	3214.9(10)	3243.5(6)
R_1 parameter	0.1163	0.0878

[a] Experimental errors are in parentheses

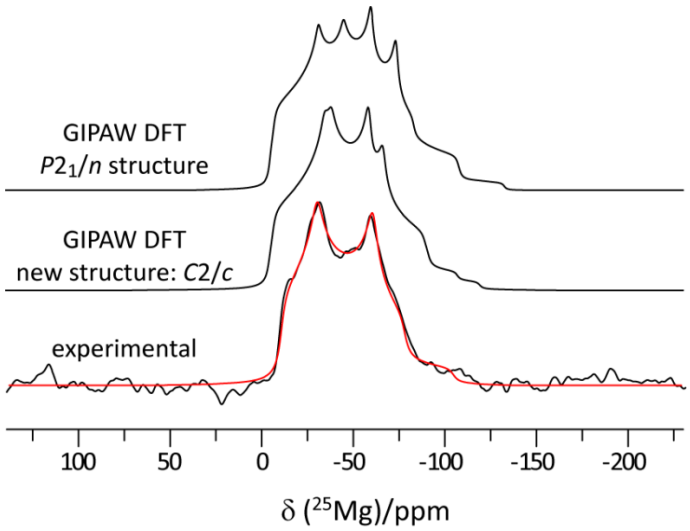

Figure 4.8: Comparison between the experimental MAS NMR spectrum (B_0 = 21.1 T, bottom trace with WSolids simulation in red) and simulations based on the GIPAW DFT-calculated NMR parameters of Mg(ben). The simulation based on the $C2/c$ structure is the sum of two separate calculations that account for a disordered water molecule in the lattice. The $P2_1/n$ structure has two distinct Mg sites. The results from the $C2/c$ structure provide a better fit to the experimental data. Experimental NMR parameters are reported in Table 4.1 for Mg(ben). Calculated NMR parameters for the $C2/c$ structure are in Table 4.3. For the $P2_1/n$ structure, the calculated NMR parameters for site 1 are $|C_Q(^{25}Mg)|$ = 5.00 MHz, η_Q = 0.54, δ_{iso} = –2 ppm; for site 2, they are $|C_Q(^{25}Mg)|$ = 4.61 MHz, η_Q = 0.44, δ_{iso} = 1 ppm.

4.3.3.2 ^{25}Mg chemical shifts and the binding motifs of aryl carboxylates

The single-crystal X-ray diffraction structure for Mg(*p*F) has one unique Mg^{2+} site and this is supported by the observation of a single resonance in the ^{25}Mg NMR spectra with a distinct second-order quadrupolar line shape at 21.1 T (see Figures 4.5 and 4.6) and at 9.4 T (see Figure 4.7). It is not immediately clear why one of the lowest $|C_Q(^{25}Mg)|$ values (2.70

MHz) is observed for this compound and we note that Mg(*p*F) also has one of the lowest δ_{iso} values of -5 ppm in this study. It has been suggested previously by Smith and co-workers[32] that in general, more strongly hydrated Mg^{2+} ions will tend to have smaller δ_{iso} values. There is an apparent incongruity in our work between Mg(*p*F), which has two H_2O molecules bound to Mg^{2+} and Mg(sal) for example, which has four water molecules coordinated to Mg^{2+} and a larger δ_{iso} of 3 ppm. Furthermore, Mg(*p*NO_2), in which the magnesium dications are present entirely as $[Mg(H_2O)_6]^{2+}$ units, has a more intermediate isotropic chemical shift of –2 ppm. From our data alone, we can speculate that in general, for near-octahedral MgO_6 units with carboxylate ligands, Mg^{2+} centres that are involved in coordination networks (i.e., 1D chains or 2D sheets) such as Mg(*p*F), Mg(*p*Cl), and Mg(ben) have lower δ_{iso} values than compounds where Mg^{2+} is not part of a coordination network such as in Mg(*p*NO_2), Mg(sal), and Mg(pams). In other words, the isotropic chemical shift for Mg^{2+} in organic molecular environments cannot be related to the hydration state of the compound. Our observations agree with data reported for $Mg(OAc)_2{\cdot}4H_2O$ and $Mg(acac)_2{\cdot}2H_2O$,[33] which form a discrete molecular magnesium complex and have δ_{iso} values of 4.1(0.3) and 2.7(4.0) ppm respectively. Magnesium formate dihydrate ($Mg(HCOO)_2{\cdot}2H_2O$) is not considered here as different research groups have reported very different experimental values of δ_{iso}.[25]

4.3.3.3 Significant range of ^{25}Mg quadrupolar coupling constants

Mg(sal) and Mg(pams) both crystallize with discrete magnesium coordination units comprised of four water molecules and two carboxylate ligands, which are *trans* with respect to each other (see Figure 4.4a). They crystallize in similar space groups (i.e., $P2_1/n$ and $P2_1/a$ for Mg(sal) and Mg(pams) respectively). It was somewhat unexpected then that their

respective $|C_Q(^{25}Mg)|$ values differ by 35%: 4.55 MHz for Mg(sal) and 6.15 MHz for Mg(pams). In order to investigate this more thoroughly, the inner sphere coordination environments surrounding each Mg^{2+} centre were examined and it is seen that more significant Mg–O distance distortions relative to a perfect octahedron are present in the Mg(pams) structure than in Mg(sal) in the form of an elongated octahedron. Despite the structural differences in the organic ligands used in this study, it is therefore possible that the relatively large range in the $|C_Q(^{25}Mg)|$ values may be chiefly attributed to the degree of distortion of the inner sphere MgO_6 octahedra in all of the aryl carboxylate structures. Previous ^{25}Mg studies[26,32] have already postulated such a correlation with respect to the longitudinal strain as proposed by Ghose and Tsang for ^{27}Al studies.[53] They defined this parameter as follows:

$$(4.1)\quad |\alpha| = \sum_i \left| \ln\left({}^{l_i}\!/\!_{l_0} \right) \right|$$

where l_i are the experimental Mg–O bond lengths of the octahedron and l_0 is the Mg–O bond length of a perfect octahedron of identical volume as the distorted polyhedron. Very recently, this correlation was *not* observed for inorganic magnesium phosphates,[26] but a reasonable correlation between $|C_Q(^{25}Mg)|$ and $|\alpha|$ was noted for a limited dataset comprised of only $Mg(HCOO)_2{\cdot}2H_2O$, $Mg(OAc)_2{\cdot}4H_2O$, and $Mg(acac)_2{\cdot}2H_2O$.[32] In Figure 4.9 is plotted our correlation between the C_Q and the longitudinal strains (filled diamonds) for the magnesium aryl carboxylates. Literature data for organic magnesium complexes are also included in the linear regression (white diamonds). This work has doubled the amount of available NMR data for near-octahedral 'MgO_6' environments with organic ligands. A clear linear correlation is observed indicating that the NMR parameters can reflect the geometry in

the first coordination sphere of Mg^{2+}. However, more information is necessary if we are to understand why the $|C_Q(^{25}Mg)|$ values in organic complexes correlate with the first coordination sphere structure whereas the values in inorganic compounds cannot be correlated with structure in this fashion. Insights from GIPAW DFT computations, which account for longer-range interactions between Mg^{2+} and its surroundings, will be useful in answering this question.

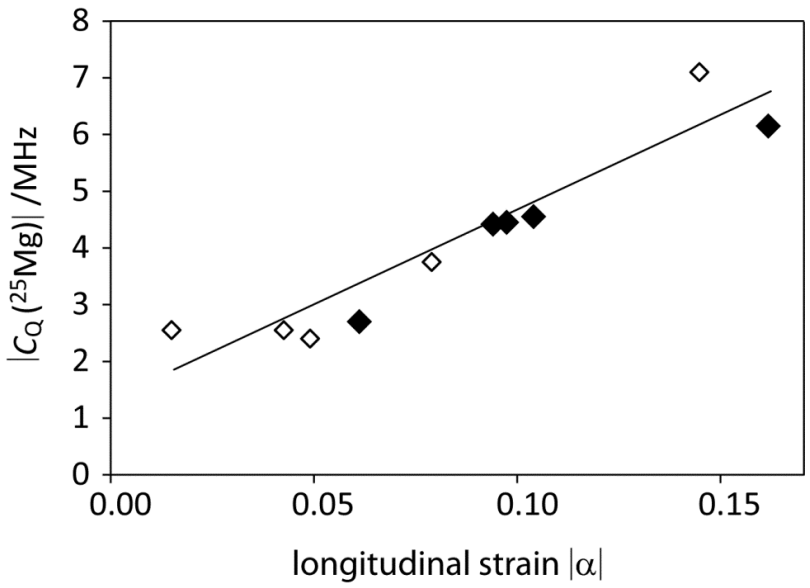

Figure 4.9: Linear correlation between the experimental $|C_Q(^{25}Mg)|$ values and the longitudinal strain, $|\alpha|$. The filled black diamonds represent data for the magnesium aryl carboxylates in this work and the empty diamonds represent data for $Mg(HCOO)_2{\cdot}2H_2O$, $Mg(OAc)_2{\cdot}4H_2O$, and $Mg(acac)_2{\cdot}2H_2O$ from previous studies. Experimental data for $Mg(pNO_2)$ were excluded from the plot because while the crystal structure shows three non-equivalent sites (and longitudinal strains), only a single set of quadrupolar parameters were resolved with ^{25}Mg NMR. Error bars do not exceed the size of the data points. The correlation is $|C_Q(^{25}Mg)| = 33.4|\alpha| + 1.2$ with a correlation coefficient, R, of 0.9435.

4.3.4 GIPAW DFT computations

The GIPAW DFT method has been used to complement experimental measurements of ^{25}Mg EFG and CS tensor parameters in crystalline inorganic and organic solids containing magnesium cations.[32,33,54] For instance, these have been used previously for spectral assignment[26] as well as for structure refinement purposes.[55] The GIPAW DFT calculated EFG and CS tensor parameters for the present work are reported in Table 4.3. The data show that it would be difficult to observe experimentally the effects of CSA on the ^{25}Mg NMR spectra given that the largest calculated span is only 35 ppm, for Mg(pams).

Table 4.3: Calculated ^{25}Mg EFG and CS Tensor Parameters for Mg Aryl Carboxylates

compound	$C_Q(^{25}Mg)$ /MHz	η_Q	δ_{iso} /ppm[a]	Ω /ppm	κ
Mg(*p*F)	-3.04	0.98	-1	21	0.16
Mg(*p*Cl) – 1[b]	-5.50	0.43	-2	19	0.45
Mg(*p*Cl) – 2[b]	-5.06	0.69	-1	21	0.17
Mg(ben) – 1[b]	-4.82	0.43	-1	16	0.50
Mg(ben) – 2[b]	-4.48	0.60	-2	18	0.21
Mg(sal)	-4.60	0.85	7	19	-0.27
Mg(pams)	-7.58	0.50	6	35	0.43
Mg(*p*NO_2) – 1[c]	2.58	0.82	7	11	-0.42
Mg(*p*NO_2) – 2[c]	3.66	0.70	6	14	-0.28
Mg(*p*NO_2) – 3[c]	1.95	0.74	7	6	0.06

[a] Chemical shifts were calculated using the absolute shielding constant of Pallister *et al*. (ref. 33). δ_{iso} = (566(1) ppm – σ_{iso}) / (1-566(1) ppm)

[b] There is a disordered floating water molecule in the lattice so two separate calculations were performed for each compound in order to assess its effect on the calculated NMR parameters.

[c] Three crystallographically distinct sites are present in the unit cell of this compound and it was not possible to resolve them experimentally. For more details, see the main text.

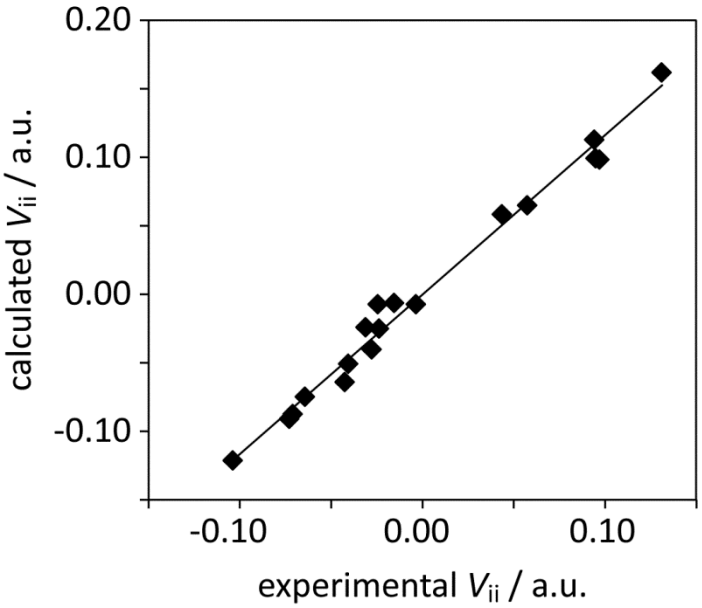

Figure 4.10: Relationship between the calculated and experimental EFG tensor principal components, V_{ii} (ii = 11, 22, and 33), for all Mg aryl carboxylates reported in this work. The average calculated values for Mg(*p*Cl), Mg(ben), and Mg(*p*NO_2) are represented in this plot (see Table 3). The correlation is described by V_{ii}(calc.) = 1.16V_{ii}(exp.) with a correlation coefficient, *R*, of 0.9923 and a *y* intercept of 0.00.

In terms of the reproducibility of experimental NMR parameters with GIPAW DFT computations, the quadrupolar parameters are very well estimated (see Figure 4.10) for the Mg aryl carboxylates as shown by the slope of 1.16 and correlation coefficient of 0.9923. Across all classes of Mg compounds, an overestimation of the C_Q(^{25}Mg) has been observed.[25] For Mg(*p*Cl) and Mg(ben), two different calculations were performed on each compound due to disorder of the unbound water molecule in each of the lattices. For Mg(*p*Cl) and Mg(ben), the calculated C_Q(^{25}Mg) values for different water molecule orientations were within ~9 % of each other. One outlier in our study, however, is evidently Mg(*p*NO_2), where three chemically distinct Mg sites are present in the lattice with calculated quadrupolar coupling

constants of 2.58, 3.66, and 1.95 MHz; only one site is unambiguously distinguishable in the experimental stationary ^{25}Mg NMR spectrum acquired at B_0 = 21.1 T. This can be interpreted initially by the possibility of an average $[Mg(H_2O)_6]^{2+}$ unit that could represent our structure under the current experimental conditions at room temperature since thermal motions of the water molecules are a possibility; the crystal structure was acquired at a temperature of 123 K and GIPAW DFT computations are typically performed at 0 K. However, after simulating the low-field ^{25}Mg MAS spectrum at 9.4 T (see Figure 4.7) with the NMR parameters determined from the 21.1 T data, we concluded that it could be difficult to unambiguously observe all three sites experimentally. Natural abundance ^{25}Mg MQMAS NMR spectroscopy could possibly be used to resolve these sites, as has been demonstrated recently in magnesium-containing MOFs.[37] Shown in Figure 4.11 are comparisons of the analytical simulations of the experimental and GIPAW DFT calculated NMR spectra. Given the observed line shape of the calculated spectra at both 9.4 T and 21.1 T, it is not surprising that the subtle singularities expected at low-field strengths are not present given the low sensitivity of the ^{25}Mg nuclide. As for the 21.1 T simulations, low-intensity singularities are expected for the broader Mg site because of the high calculated quadrupolar asymmetry parameters (see Table 4.3). Unfortunately, these seem to be too low in intensity to observe unambiguously, even at 21.1 T. This point highlights the advantages of this experimental-theoretical approach when attempting to corroborate or refine crystal structures, especially when the probe nuclide is as dilute in the samples as in the case of Mg aryl carboxylates.

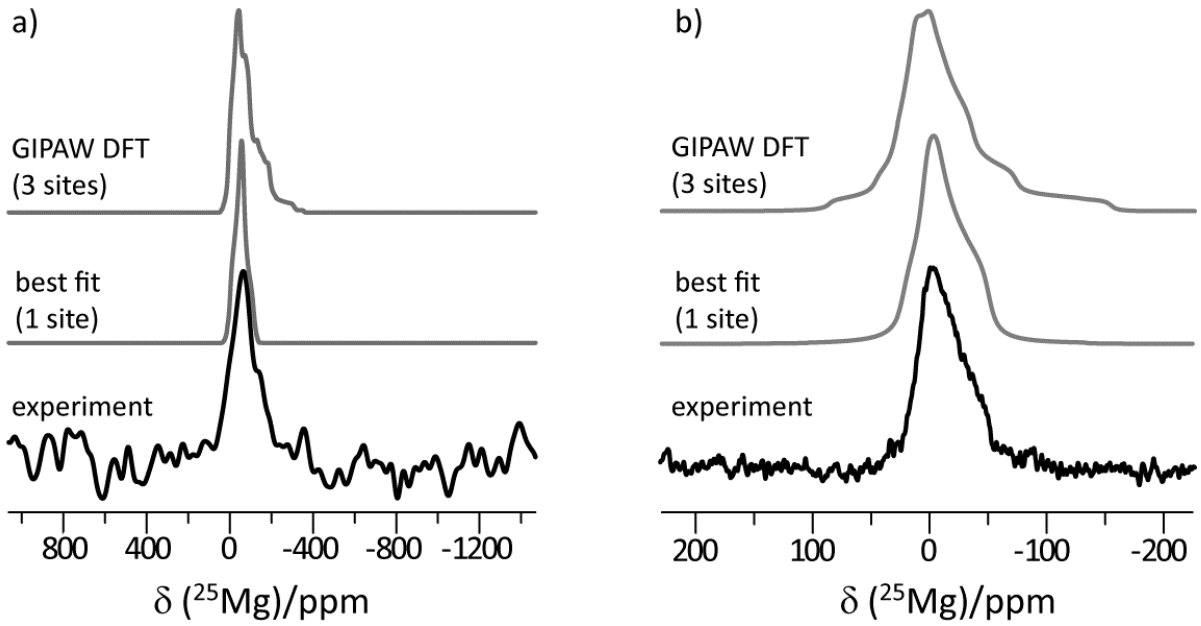

Figure 4.11: ^{25}Mg MAS (ν_{rot} = 5 kHz) NMR spectrum of Mg(pNO$_2$) at 9.4 T (a) and stationary ^{25}Mg NMR spectrum at 21.1 T (b). The "best fit" simulation is based on the spectrum acquired at 21.1 T. From the 9.4 T experiment, it is clear that one crystallographically unique Mg site does not adequately describe Mg(pNO$_2$). A better description of this system comes from a simulation using the GIPAW DFT calculated EFG tensor parameters (top traces).

Another benefit to complementing experimental NMR data with quantum chemical calculations is that theoretical EFG and CS tensor orientations with respect to the crystalline lattice can be obtained. This type of analysis can be advantageous in explaining certain experimental trends in the NMR parameters.[56,57,58,59,60] For ^{25}Mg, the visualization of the EFG tensor with respect to the molecular structure has not been done in a systematic way. In zirconium silicates for instance,[61] the largest component of the Zr EFG tensor, V_{33}, was calculated by DFT to be oriented along the shortest Zr–O bond in octahedral ZrO$_6$ units and

the presence of atoms in the 2nd or 3rd coordination sphere of Zr were shown to affect both the magnitudes and directions of the principal components of the EFG tensor. In Table 4.4, we report the calculated values of $C_Q(^{25}Mg)$ along with the orientation of V_{33} with respect to the shortest or longest (i.e., pseudo-unique) Mg–O bonds in the Mg aryl carboxylates. We note that when the value of $C_Q(^{25}Mg)$ is negative, V_{33} is oriented along the shortest Mg–O bond; when this is positive, V_{33} is along the longest Mg–O bond. An example for Mg(*p*F) is shown in Figure 4.12. This type of information is often only obtainable *via* quantum chemical calculations as it is not possible to evaluate the sign of C_Q experimentally in these systems in any straightforward manner.

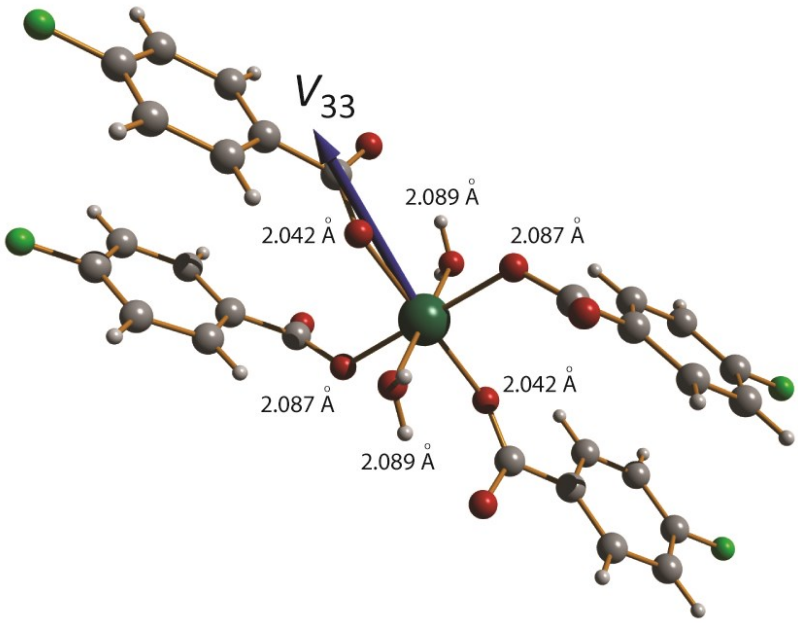

Figure 4.12: Calculated ^{25}Mg EFG tensor orientation for Mg(*p*F). For the compounds studied in this work, V_{33} is typically oriented along a unique Mg-O bond vector. For Mg(*p*F) this is along the shortest Mg-O bond. The V_{33}-Mg-O angle is 7.9°.

Table 4.4: Mg–O Distances, Calculated EFG Tensor Parameters, and the Orientation of V_{33} with Respect to a Unique Mg–O bond for Mg Aryl Carboxylates.

compound	$d_{Mg\text{-}O}$ /Å (L=ligand, W=water)		$C_Q(^{25}Mg)$ /MHz	η_Q	$\angle V_{33}$-Mg-O / °	V_{33} along
Mg(*p*F)	2.042(L)	2.042(L)	-3.30	0.98	7.9	2.042(L)
	2.087(L)	2.087(L)				
	2.089(W)	2.089(W)				
Mg(*p*Cl) with H_2O 1[a]	2.034(L)	2.041(L)	-5.50	0.43	5.3	2.046(W)
	2.046(L)	2.067(L)				
	2.104(W)	2.142(W)				
Mg(*p*Cl) with H_2O 2[a]	2.034(L)	2.041(L)	-5.06	0.69	3.5	2.046(W)
	2.067(L)	2.046(W)				
	2.104(W)	2.142(W)				
Mg(ben) with H_2O 1[a]	2.031(L)	2.033(L)	-4.82	0.43	2.5	2.033(L)
	2.062(W)	2.068(L)				
	2.111(W)	2.143(W)				
Mg(ben) with H_2O 2[a]	2.031(L)	2.033(L)	-4.48	0.60	3.4	2.033(L)
	2.062(W)	2.068(L)				
	2.111(W)	2.143(W)				
Mg(sal)	2.025(L)	2.025(L)	-4.60	0.85	18.8	2.025(L)
	2.042(W)	2.042(W)				
	2.115(W)	2.115(W)				
Mg(pams)	1.998(W)	1.998(W)	-7.58	0.50	1.7	1.998(W)
	2.098(L)	2.098(L)				
	2.149(W)	2.149(W)				
Mg(*p*NO_2) site 1	2.046(W)	2.046(W)	3.66	0.70	7.0	2.122(W)
	2.056(W)	2.056(W)				
	2.122(W)	2.122(W)				
Mg(*p*NO_2) site 2	2.043(W)	2.047(W)	2.58	0.82	7.9	2.147(W)
	2.057(W)	2.072(W)				
	2.111(W)	2.147(W)				
Mg(*p*NO_2) site 3	2.044(W)	2.044(W)	1.95	0.74	13.7	2.101(W)
	2.053(W)	2.053(W)				
	2.101(W)	2.101(W)				

[a] This nomenclature refers to a calculation which has been performed with the first (1) or second (2) orientation of the disordered water molecule present in the lattice.

Our GIPAW DFT computations suggest that the value of $C_Q(^{25}Mg)$ is positive when 'MgO_6' octahedra are present in the form of $[Mg(H_2O)_6]^{2+}$ clusters. In order to evaluate the validity of this hypothesis, we have performed GIPAW DFT computations on a family of inorganic magnesium compounds that contain $[Mg(H_2O)_6]^{2+}$ units; these are $MgCl_2{\cdot}6H_2O$,[62] $MgSO_4{\cdot}11H_2O$,[63] $Mg(NH_4)_2(SO_4)_2{\cdot}6H_2O$,[64] and $Mg(NO_3)_2{\cdot}6H_2O$.[65] Reported in Table 4.5 are their respective $C_Q(^{25}Mg)$ values along with the orientation of V_{33} with respect to the longest or shortest Mg–O bond length. It is clear that first, there are changes in the sign of C_Q depending on the compound and that secondly, V_{33} is not clearly oriented along any Mg–O bond compared to the results from the Mg aryl carboxylates. The latter statement is significant because this provides insight as to why the $C_Q(^{25}Mg)$ values and the longitudinal strain are not as well correlated for inorganic solids[26,32] compared to near-octahedral organic magnesium complexes (see Figure 4.6). This may be caused by the presence of smaller/harder ions in closer proximity to the Mg^{2+} centres in inorganic solids resulting in stronger EFGs stemming from presence of anions in the 2nd or 3rd coordination sphere of Mg^{2+}. As for the benzoates and salicylates in this study for example, the orientations of the EFG tensors are dictated solely by the first coordination sphere possibly because the organic anions are much larger and they diffuse their negative charge through resonance effects. Therefore, geometrical considerations (e.g., longitudinal strain) are enough to explain the breadth in the $C_Q(^{25}Mg)$ values experimentally observed for all of the organic magnesium complexes currently characterized by ^{25}Mg SSNMR.

Table 4.5: Mg–O Distances, Calculated EFG Tensor Parameters, and the Orientation of V_{33} With Respect to a Unique Mg–O bond for Salts Containing $[Mg(H_2O)_6]^{2+}$ Units.

compound	$d_{Mg\text{-}O}$ /Å (L=ligand, W=water)		$C_Q(^{25}Mg)$ /MHz	η_Q	$\angle V_{33}$-Mg-O /°	V_{33} along
$MgSO_4 \cdot 11H_2O$ site 1	2.038(W)	2.038(W)	2.07	0.70	31.4	2.070(W)
	2.063(W)	2.063(W)				
	2.070(W)	2.070(W)				
$MgSO_4 \cdot 11H_2O$ site 2	2.051(W)	2.051(W)	1.20	0.22	40.9	2.070(W)
	2.055(W)	2.055(W)				
	2.070(W)	2.070(W)				
$Mg(NH_4)_2(SO_4)_2 \cdot 6H_2O$	2.051(W)	2.051(W)	-2.76	0.87	23.6	2.051(W)
	2.073(W)	2.073(W)				
	2.083(W)	2.083(W)				
$MgCl_2 \cdot 6H_2O$	2.057(W)	2.057(W)	0.88	0.02	39.2	2.057(W)
	2.062(W)	2.062(W)				
	2.062(W)	2.062(W)				
$MgNO_3 \cdot 6H_2O$	2.053(W)	2.053(W)	-2.06	0.30	22.8	2.053(W)
	2.061(W)	2.061(W)				
	2.063(W)	2.063(W)				

4.4 Conclusions

As part of this Chapter, a series of six magnesium aryl carboxylates that feature Mg^{2+} in organic coordination environments was synthesized. These have been characterized by multinuclear (^{13}C and ^{25}Mg) solid-state NMR spectroscopy. It has been demonstrated that the ^{13}C carbonyl resonances are sensitive to the binding mode of the ligand to the Mg dication as characterized by a difference of ~8 ppm between unbound (–O–C–O–) and bridging (Mg–O–C–O–Mg) carboxylate moieties. The use of an ultrahigh-field magnet (B_0 = 21.1 T) was highly advantageous in order to obtain high-quality natural abundance ^{25}Mg NMR spectra. ^{25}Mg isotropic chemical shifts were shown to be sensitive to the type of framework of the solid rather than only the hydration state of Mg^{2+} as previously suggested. Lower chemical shifts are observed for the compounds present in 1D chains or 2D sheets,

whereas higher chemical shifts are observed for the compounds that crystallize with Mg^{2+} as part of an isolated molecule. A good correlation has been observed between the ^{25}Mg quadrupolar coupling constant and the longitudinal strain of the octahedron formed by the six oxygen atoms present in the first coordination sphere of Mg^{2+} for the compounds in the present study and all other organic Mg-containing compounds for which ^{25}Mg solid-state NMR data already exist. These relationships between the crystal structures and the NMR parameters hold promise for ^{25}Mg solid-state NMR as a tool for refining and optimizing more complex structures such as MOFs. In Mg(ben) for example, the ^{25}Mg NMR data were not consistent with the previously reported structure and a new crystal structure was determined for this compound. GIPAW DFT calculations have also allowed us to visualize the EFG tensor principal components with respect to the molecular structure. We found that the largest component, V_{33}, is oriented along the pseudo-unique Mg–O bond in the MgO_6 coordination octahedron. This has provided reasoning for the observed relationship between the $C_Q(^{25}Mg)$ values and the longitudinal strain for Mg^{2+} in organic coordination environments compared to the situation for inorganic magnesium compounds.

4.5 References for Chapter 4

1. Babu, C. S.; Dudev, T.; Lim, C. *J. Am. Chem. Soc.* **2013**, *135*, 6541.
2. Lim, D.-W.; Yoon, J. W.; Ryu, K. Y.; Suh, M. P. *Angew. Chem. Int. Ed.* **2012**, *51*, 9814.
3. Glover, T. G.; Peterson, G. W.; Schindler, B. J.; Britt, D.; Yaghi, O. *Chem. Eng. Sci.* **2011**, *66*, 163.
4. Kong, X.; Scott, E.; Ding, W.; Mason, J. A.; Long, J. R.; Reimer, J. A. *J. Am. Chem. Soc.* **2012**, *134*, 14341.
5. Lin, L.-C.; Kim, J.; Kong, X.; Scott, E.; McDonald, T. M.; Long, J. R.; Reimer, J. A.; Smit, B. *Angew. Chem. Int. Ed.* **2013**, *52*, 4410.
6. Huang, Y.-L.; Gong, Y.-N.; Jiang, L.; Lu, T.-B. *Chem. Commun.* **2013**, *49*, 1753.
7. Miehé-Brendlé, J.; Tuilier, M.-H.; Marichal, C.; Gallego, J.-C.; Reinholdt, M. *Eur. J. Inorg. Chem.* **2010**, 5587.
8. Wasylishen, R. E.; Ashbrook, S. E.; Wimperis, S. (eds) NMR of Quadrupolar Nuclei in Solid Materials, Wiley: Chichester UK, **2012**.
9. Fernandez, C.; Pruski, M. *Top. Curr. Chem.* **2012**, *306*, 119.
10. Ashbrook, S. E.; Duer, M. J. *Concepts Magn. Reson. Part A* **2006**, *28*, 183.
11. Harris, R. K.; Wasylishen, R. E.; Duer, M. J. (eds.) NMR Crystallography, Wiley: Chichester UK, **2009**.
12. Perras, F. A.; Bryce, D. L. *J. Phys. Chem. C* **2012**, *116*, 19472.
13. Santos, S. M.; Rocha, J.; Mafra, L. *Cryst. Growth. Des.* **2013**, *13*, 2390.

14. Pawlak, T.; Jaworska, M.; Potrzebowski, M. J. *Phys. Chem. Chem. Phys.* **2013**, *15*, 3137.

15. Brouwer, D. H.; Cadars, S.; Eckert, J.; Liu, Z.; Terasaki, O.; Chmelka, B. F. *J. Am. Chem. Soc.* **2013**, *135*, 5641.

16. Macholl, S.; Börner, F.; Buntkowsky, G. *Chem. Eur. J.* **2004**, *10*, 4808.

17. Elena, B.; Emsley, L. *J. Am. Chem. Soc.* **2005**, *127*, 9140.

18. Elena, B.; Pintacuda, G.; Mifsud, N.; Emsley, L. *J. Am. Chem. Soc.* **2006**, *128*, 9555.

19. Pickard, C. J.; Salager, E.; Pintacuda, G.; Elena, B.; Emsley, L. *J. Am. Chem. Soc.* **2007**, *129*, 8932.

20. Dutour, J.; Guillou, N.; Huguenard, C; Taulelle, F.; Mellot-Draznieks, C.; Férey, G. Chiolite, A. *Solid State Sci.* **2004**, *6*, 1059.

21. Bouchevreau, B.; Martineau, C.; Mellot-Draznieks, C.; Tuel, A.; Suchomel, M. R.; Trébosc, J.; Lafon, O.; Amoureux, J.-P.; Taulelle, F. *Chem. Eur. J.* **2013**, *19*, 5009.

22. Brouwer, D. H. *J. Am. Chem. Soc.* **2008**, *130*, 6306.

23. Brouwer, D. H.; Enright, G. D. *J. Am. Chem. Soc.* **2008**, *130*, 3095.

24. Brouwer, D. H. *J. Magn. Reson.* **2008**, *194*, 136.

25. Freitas, J. C. C.; Smith, M. E. *Annu. Rep. Nucl. Magn. Reson. Spectrosc*. **2012**, *75*, 25.

26. Laurencin, D.; Gervais, C.; Stork, H.; Krämer, S.; Massiot, D.; Fayon, F. *J. Phys. Chem. C* **2012**, *116*, 19984.

27. Sham, S.; Wu, G. *Inorg. Chem.* **2000**, *39*, 4.

28. Wu, G.; Wong, A.; Wang, S. *Can. J. Chem.* **2003**, *81*, 275.

29. Wong, A.; Ida, R.; Mo, X.; Gan, Z.; Poh, J.; Wu, G. *J. Phys. Chem. A* **2006**, *110*, 10084.

30. Lipton, A. S.; Heck, R. W.; Primak, S.; McNeill, D. R.; Wilson III, D. M.; Ellis, P. D. *J. Am. Chem. Soc.* **2008**, *130*, 9332.

31. Freitas, J. C. C.; Wong, A.; Smith, M. E. *Magn. Reson. Chem.* **2009**, *47*, 9.

32. Cahill, L. S.; Hanna, J. V.; Wong, A.; Freitas, J. C. C.; Yates, J. R.; Harris, R. K.; Smith, M. E. *Chem. Eur. J.* **2009**, *15*, 9785.

33. Pallister, P. J.; Moudrakovski, I. L.; Ripmeester, J. A. *Phys. Chem. Chem. Phys.* **2009**, *11*, 11487.

34. Arlin, J.-B.; Florence, A. J.; Johnston, A.; Kennedy, A. R.; Miller, G. J.; Patterson, K. *Cryst. Growth Des*. **2011**, *11*, 1318.

35. Zhang, Z.; Zhao, Y.; Gong, Q.; Li, Z.; Li, J. *Chem. Commun*. **2013**, *49*, 653.

36. Xu, J.; Terskikh, V. V.; Huang, Y. *J. Phys. Chem. Lett.* **2013**, *4*, 7.

37. Xu, J.; Terskikh, V. V.; Huang, Y. *Chem. Eur. J.* **2013**, *19*, 4432.

38. Bonhomme, C.; Gervais, C.; Babonneau, F.; Coelho, C.; Pourpoint, F.; Azaïs, T.; Ashbrook, S. E.; Griffin, J. M.; Yates, J. R.; Mauri, F.; Pickard, C. J. *Chem. Rev.* **2012**, *112*, 5733.

39. APEX Software Suite v.2010. Madison, WI: Bruker AXS **2005**.

40. Blessing, R. *Acta Cryst. A* **1995**, *51*, 33.

41. Sheldrick, G. M. *Acta Cryst. A* **2008**, *64*, 112

42. Opella, S. J.; Frey, M. H. *J. Am. Chem. Soc.* **1979**, *101*, 5854.

43. Eichele, K.; Wasylishen, R. E. *WSOLIDS NMR Simulation Software Version 1.17.30*, Universitat Tübingen, Tübingen (Germany), **2001**.

44. Bak, M.; Rasmussen, J. T.; Nielsen, N. C. *J. Magn. Reson.* **2000**, *147*, 296.

45. Massiot, D.; Fayon, F.; Capron, M.; King, I.; Le Calvé, S.; Alonso, B.; Durand, J.-O.; Bujoli, B.; Gan, Z.; Hoatson, G. *Magn. Reson. Chem.* **2002**, *40*, 70.

46. Segall, M. D.; Lindan, P. J. D.; Probert, M. J.; Pickard, C. J.; Hasnip, P. J.; Clark, S. J.; Payne, M. C *J. Phys. Condens. Matter* **2002**, *14*, 2717.

47. Cole, L. B.; Holt, E. M. *Inorg. Chim. Acta* **1989**, *160*, 195.

48. Drake, S. R.; Sanderson, K. D.; Hursthouse, M. B.; Malik, K. M. A *Inorg. Chem*. **1993**, *32*, 1041.

49. Felmy, A. R.; Qafoku, O.; Arey, B. W.; Hu, J. Z.; Hu, M.; Schaef, H. T.; Ilton,; E. S.; Hess, N. J.; Pearce, C. I.; Feng, J.; Rosso, K. M. *Geochim. Cosmochim. Acta* **2012**, *91*, 271.

50. Hopkinson, L.; Rutt, K.; Cressey, G. *J. Geol.* **2008**, *116*, 387-400.

51. Patra, A.; Sen, T. K.; Bhattacharyya, R.; Mandal, S. K.; Bera, M. *RSC Adv.* **2012**, *2*, 1774.

52. Ye, B.-H.; Li, X.-Y.; Williams, I. D.; Chen, X.-M. *Inorg. Chem.* **2002**, *41*, 6426.

53. Ghose, S.; Tsang, T. *Am. Mineral.* **1973**, *58*, 748.

54. Rossano, S.; Mauri, F.; Pickard, C. J.; Farnan, I. *J. Phys. Chem. B* **2005**, *109*, 7245.

55. Widdifield, C. M.; Bryce, D. L. *Phys. Chem. Chem. Phys.* **2009**, *11*, 7120.

56. O'Dell, L. A.; Moudrakovski, I. L. *Chem. Phys. Lett.* **2013**, *565*, 56.

57. Johnston, K. E.; Mitchell, M. R.; Blanc, F.; Lightfoot, P.; Ashbrook, S. E. *J. Phys. Chem. C* **2013**, *117*, 2252.

58. Burgess, K. M. N.; Korobkov, I.; Bryce, D. L. *Chem. Eur. J.* **2012**, *18*, 5748.

59. Widdifield, C. M.; Bryce, D. L. *J. Phys. Chem. A* **2010**, *114*, 10810.

60. Bryce, D. L.; Bultz, E. B.; Aebi, D. *J. Am. Chem. Soc.* **2008**, *130*, 9282.

61. Zhu, J.; Lin, Z.; Yan, Z.; Huang, Y. *Chem. Phys. Lett.* **2008**, *461*, 260.

62. Agron, P. A.; Busing, W. R. *Acta Crystallogr. C* **1985**, *41*, 8.

63. Geneceli, F. E.; Lutz, M.; Spek, A. L.; Witkamp, G.-J. *Cryst. Growth Des.* **2007**, *7*, 2460.

64. Margulis, T. N.; Templeton, D. H. *Z. Krist.* **1962**, *117*, 344.

65. Braibanti, A.; Tiripicchio, A.; Lanfredi, A. M. M.; Bigoli, F. *Acta Crystallogr. B* **1969**, *25*, 354.

5 Calcium and Strontium Carboxylate Complexes Characterized by ^{43}Ca and ^{87}Sr SSNMR Spectroscopy

In the previous Chapter was presented the ^{25}Mg SSNMR investigation of Mg^{2+} coordinated to organic ligands such as benzoate and salicylate. In all cases, the first coordination sphere about Mg^{2+} was occupied solely by oxygen atoms. In this Chapter, the same ligands are chelated to Ca^{2+} and Sr^{2+} ions, however a new type of coordination to the metal via the nitrogen atom in the pams ligand is observed. One focus herein will be on the correlation between the SSNMR parameters and the coordination of the amine functionality to the alkaline-earth metal.

5.1 Introduction

The divalent calcium and strontium cations (Ca^{2+} and Sr^{2+}) have large abundances in Earth's crust and play important roles in many areas of chemistry, biochemistry, and materials science. For example, both cations are often present in the active sites associated with many biochemical processes including those in oxygen-evolving complexes such as photosystem II[1,2,3] and metalloproteins.[4,5] The alkaline-earth metal cations also play key roles in tunable fluorescent indicators,[6] ion sensing,[7] macrocyclic ion receptors,[8] and MOFs for selective CO_2 and N_2 adsorption.[9,10,11] Various groups have discussed the economic

benefit of Ca^{2+} and Sr^{2+} over transition metals as catalysts for C–C or C–N bond formation,[12,13] often with chiral nitrogen-binding ligands.[14,15] The potential applications of calcium Grignard reagents[16] and allylcalcium complexes[17,18] are also currently under investigation.

Despite this plethora of applications, alkaline-earth metal SSNMR is still a rather underdeveloped field specifically when attempting to relate certain NMR signatures to the structure or activity of a metal complex. In organic molecular environments, an increased dilution factor for Ca^{2+} and Sr^{2+} ions compared to some inorganic materials may hamper the acquisition of NMR spectra in a reasonable amount of time. Three recent reviews on alkaline-earth metal SSNMR[19,20,21] have aided in identifying the major pitfalls encountered when performing calcium and strontium NMR experiments. As summarized in Chapter 1,[22] both NMR active nuclei (^{43}Ca and ^{87}Sr) have very low Larmor frequencies compared to ^{13}C. The main challenge in ^{43}Ca NMR spectroscopy is its natural abundance of 0.14 % (compared to 7.02 % for ^{87}Sr), which is one of the smallest of all NMR-active nuclides in the periodic table. The primary difficulty with ^{87}Sr NMR spectroscopy stems from its large quadrupole moment of 305 mbarn, whereas the currently accepted Q value for ^{43}Ca is much smaller (–40.8 mbarn).[23] The very low receptivity of each of these nuclides means that it is often impractical to record NMR spectra in a reasonable amount of time at standard magnetic field strengths.

Advancements in NMR technologies have resulted in the emergence of ultrahigh-field magnets and thus an increase in the amenability to exotic low-γ nuclei such as ^{43}Ca and ^{87}Sr to NMR experiments. An array of studies are available in which Ca^{2+} ions present in biological materials have been probed by ^{43}Ca MAS NMR. These include materials

containing alkyl/aryl boronate[24,25] and phosphonate ligands,[26] kidney stones[27] and calcium oxalate salts,[28] and other various organic ligands.[29] One impressive study from Laurencin *et al*. on calcium benzoate trihydrate (referred to in this work as Ca(ben)) employed ^{43}Ca isotopic labeling and experiments probing heteronuclear correlations such as transfer of population double resonance (TRAPDOR) between ^{43}Ca and ^{13}C nuclei.[30] Successful studies on other biologically relevant systems such as phosphates[31] and hydroxyapatite[32,33] have paved the way for the study of more challenging samples like bones, teeth,[34] and cement.[35] The ^{87}Sr nucleus, however, has not been studied as extensively due to its larger quadrupole moment. The most recent study by Bonhomme *et al*.[36] employs WURST pulses coupled with QCPMG acquisition and ^{87}Sr isotopic labeling at high magnetic field strengths in order to characterize Sr^{2+} environments in Sr-doped Ca-silicate based bioglasses. In addition, the authors examined a number of organic and inorganic crystalline strontium phases.

Studies to date involving ^{43}Ca and ^{87}Sr SSNMR have focused mainly on oxygen coordination environments.[20] For example, researchers have correlated the average Ca–O distance of the first coordination sphere to the ^{43}Ca isotropic chemical shift, δ_{iso}.[37,38] There is, however, a relative dearth in studies involving coordination of Ca^{2+} and Sr^{2+} to other atoms, namely nitrogen. Amino acids have been shown previously to bind to Ca^{2+} via their nitrogen atoms,[39,40,41] and so it is important to study such environments if we are to understand how ^{43}Ca and ^{87}Sr NMR spectroscopy can be useful in characterizing metalloproteins, which are constituted mainly of nitrogen-containing amino acids. For this thesis Chapter, we have prepared a series of Ca^{2+} and Sr^{2+} complexes containing various aryl and carboxylate ligands, such as those illustrated in Figure 4.1 of Chapter 4 with the addition of the ethylenediaminetetracetate (EDTA) ligand (see Figure 5.1). The pams and EDTA

ligands bind to the metal centers *via* their nitrogen atoms. ^{43}Ca and ^{87}Sr SSNMR experiments under stationary and/or MAS conditions are used in an attempt to correlate the presence of coordinated nitrogen atoms to changes in the alkaline-earth metal NMR parameters. We note that ^{25}Mg SSNMR has been used previously to examine Mg^{2+} centers featuring nitrogen coordination, e.g., in porphyrins[42] and Mg_3N_2,[43] although these studies did not specifically investigate the role of nitrogen on the alkaline earth metal NMR parameters.

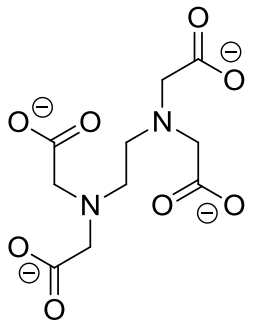

EDTA

Figure 5.1: The ethylenediaminetetracetate (EDTA). The structures of the other ligands considered in this chapter can be found in Figure 4.1.

We also corroborate our experimental findings with GIPAW DFT calculations of the NMR parameters. This combined experimental-theoretical approach in NMR has found widespread usage especially in the field of alkaline-earth metal SSNMR due to the difficulties outlined above in interpreting NMR spectra of low-γ nuclei.[20] Because of the large dataset of calcium compounds characterized by ^{43}Ca SSNMR in this study, in addition to currently available ^{43}Ca quadrupolar coupling constants, we are able to establish a meaningful correlation between the calculated and experimental $C_Q(^{43}Ca)$ values.

5.2 Experimental Details

5.2.1 Sample Preparation and Synthesis

Commercially available starting materials were used for the syntheses presented in this work. *p*-Fluorobenzoic acid (*p*F, ≥ 98.0%), *p*-chlorobenzoic acid (*p*Cl, ≥ 99.0%), *p*-nitrobenzoic acid (*p*NO_2, ≥ 98.0%), sodium benzoate (Na(ben), ≥ 99.5%), sodium salicylate (Na(sal), ≥ 99.5%), sodium *p*-aminosalicylate (Na(pams), ≥ 97.0%), ethylenediaminetetracetic acid (H_4EDTA, ≥ 98.5%), calcium carbonate ($CaCO_3$, ≥ 99.0%), strontium carbonate ($SrCO_3$, ≥ 98.0%), calcium chloride ($CaCl_2$), strontium chloride ($SrCl_2$, ≥ 96.0%), and calcium acetate ($Ca(OAc)_2 \cdot H_2O$, ≥ 99.0%) were all purchased from Sigma-Aldrich and used without further purification.

The abbreviations AE(ligand), where AE = Ca or Sr and the ligands are presented in Figures 4.1 and 5.1, are used for conciseness. Several of the samples are hydrates and the actual molecular formulas for each alkaline-earth metal complex are provided in Table 5.1. Ca(*p*F), Ca(*p*Cl), Sr(*p*Cl), and Sr(*p*NO_2) were synthesized using a previously reported method by Arlin *et al*.,[44] wherein a 1:1 stoichiometric amount of substituted benzoic acid (1 g) and metal carbonate were dissolved in 20 mL of distilled water. The solution was stirred overnight and the residual solids were filtered over a pad of celite. The collected mother liquor was slowly evaporated at room temperature over several days or weeks to yield the appropriate crystalline salt.

Table 5.1: Table of abbreviations for the alkaline-earth metal compounds studied in this chapter.

compound abbreviation	molecular formula
Ca(ben)	$\{[Ca(ben)(H_2O)_3](ben)\}_n$
Ca(*p*F)	$\{[Ca(pF)(H_2O)_3](pF)\}_n$
Ca(*p*Cl)	$\{[Ca(pCl)(H_2O)_3](pCl)\}_n$
Ca(sal)	$[Ca(sal)_2(H_2O)_2]_n$
Ca(pams)	$[Ca_2(pams)_4(H_2O)]_n$
Ca(pams)(OAc)	$\{[Ca(pams)(OAc)(H_2O)](H_2O)\}_n$
Ca_2(EDTA)·$7H_2O$	$\{[Ca(CaEDTA)(H_2O)_3](H_2O)_4\}_n$
Sr(ben)	$[Sr_2(ben)_4(H_2O)_2]_n$
Sr(*p*Cl)	$\{(Sr(pCl)(H_2O)_4](pCl)\}_n$
Sr(sal)	$[Sr(sal)_2(H_2O)_2]_n$
Sr(*p*NO_2)	$[Sr(pNO_2)(H_2O)_7](pNO_2)(H_2O)_2$
Sr(pams)	$[Sr_2(pams)_4(H_2O)]_n$

Natural isotopic abundance samples of Ca(sal), Ca(pams), Sr(ben), Sr(sal), and Sr(pams) were prepared[44] by dissolving the appropriate amount of sodium salt (1 g) and alkaline-earth metal chloride in a 1:1 stoichiometric ratio in a minimum amount of distilled water. The mixture was stirred for several minutes and filtered over cotton. The resulting solution was slowly evaporated at room temperature until the appearance of transparent crystals. Isotopically enriched ^{43}Ca(pams) was synthesized in a similar way as described above using $^{43}CaCl_2$ (50 mg) and 2.05 equivalents of Na(pams), which were dissolved in a minimum amount of H_2O. In order to synthesize $^{43}CaCl_2$, a ^{43}Ca-labeled polymer chelate (donated by an industrial collaborator) was stirred in a 1 M HCl solution. The non-dissolved polymer was filtered away and, upon solvent evaporation, a yellow oil was obtained. 25 mg of this oil along with 25 mg of natural abundance $CaCl_2$ was used in the synthesis. We estimate the enrichment level of ^{43}Ca to be 4 % based on comparison with NMR experiments performed at natural abundance for Ca(pams).

The Ca(pams)(OAc) analogue was synthesized in a similar way as Ca(pams), with $Ca(OAc)_2 \cdot H_2O$ as a source of calcium and 2 equivalents of Na(pams) (1 g).[45] $Ca_2(EDTA) \cdot 7H_2O$ was synthesized according to a literature procedure.[46] The phase purity of all synthesized alkaline-earth metal carboxylates was verified by comparing experimental PXRD patterns to those simulated with the available crystal structures (see Figures 4.2 and 4.3 for Ca and Sr compounds, respectively).

In the case of Ca(*p*NO_2), multiple attempts were made to synthesize this compound however experimental PXRD was not consistent with that of the reported single crystal structure and so this compound was omitted from the series.

5.2.2 Solid-State NMR Experiments

Solid-state NMR experiments were performed on all calcium and strontium samples at the National Ultrahigh-Field NMR Facility for Solids in Ottawa using a 21.1 T magnet (Bruker AVANCE II, $\nu_L(^1H)$ = 900.13 MHz, $\nu_L(^{43}Ca)$ = 60.6 MHz, $\nu_L(^{87}Sr)$ = 39.0 MHz). All ^{43}Ca NMR experiments at natural abundance were performed with a Bruker 7 mm MAS low-frequency double-resonance (HX) probe using a single pulse MAS experiment. In the case of ^{43}Ca(pams), a Bruker 4 mm MAS low-frequency double-resonance (HX) probe was used for one-pulse experiments under both MAS and stationary conditions. CW ^1H decoupling was used in certain cases. Experiments for strontium samples were performed using a home-built 7 mm low-frequency double-resonance (HX) probe and the WURST–QCPMG pulse sequence with ^1H decoupling. For Sr(pams), it was necessary to perform a Solomon echo experiment in order to observe a broader Sr^{2+} resonance due to its short spin–spin relaxation time constant, T_2. In this case, multiple pieces were acquired with

varying transmitter offset frequencies using the VOCS method.[47] These experiments were acquired using a modified Bruker broadband single channel probe. Chemical shifts were referenced to 0.00 ppm with a 1.0 M aqueous solution of $CaCl_2$[20] or $SrCl_2$. The CT-selective $\pi/2$ pulse lengths were those of the standard scaled by a factor of $1/(I + 1/2) = 1/4$ for ^{43}Ca and 1/5 for ^{87}Sr. Selective $\pi/4$ pulses were used in certain cases for natural abundance ^{43}Ca NMR experiments due to the uncertainty in the longitudinal relaxation time constant, T_1. In the case of $Ca_2(EDTA)\cdot 7H_2O$, the pulse length was calibrated directly on the sample.

Additional experiments were performed either at 9.4 T (Bruker AVANCE III, $\nu_L(^1H)$ = 400.13 MHz, $\nu_L(^{43}Ca)$ = 26.9 MHz) with a Bruker 7 mm MAS low-frequency double-resonance (HX) probe or at 11.75 T (Bruker AVANCE, $\nu_L(^1H)$ = 500.13 MHz, $\nu_L(^{43}Ca)$ = 33.7 MHz) with a Bruker 4 mm MAS low-frequency double-resonance (HX) probe. In all cases, single-pulse experiments were used. The chemical shift referencing and pulse calibrations were carried out analogously to the procedure described above. Specific experimental details pertaining to each compound in this work may be found in Appendix A5.1 and A5.2 in Appendix A.

5.2.3 Spectral Processing and Simulations

All spectra were recorded and processed using the Bruker TopSpin software (ver. 3.0). Most ^{43}Ca NMR spectra were left-shifted a small number of data points to remove signal due to probe ringing. The first echoes in all ^{87}Sr WURST–QCPMG experiments were removed also due to probe ringing and spectra were analyzed in magnitude mode in the frequency domain. All individual pieces in the Solomon echo spectra of Sr(pams) are presented in magnitude mode and co-added in the frequency domain to yield the full

spectrum. ^{43}Ca and ^{87}Sr spectra were simulated using the WSolids1 program (ver. 1.20.15).[48] Graphics were prepared with the aid of DMFit (ver. 2011).[49]

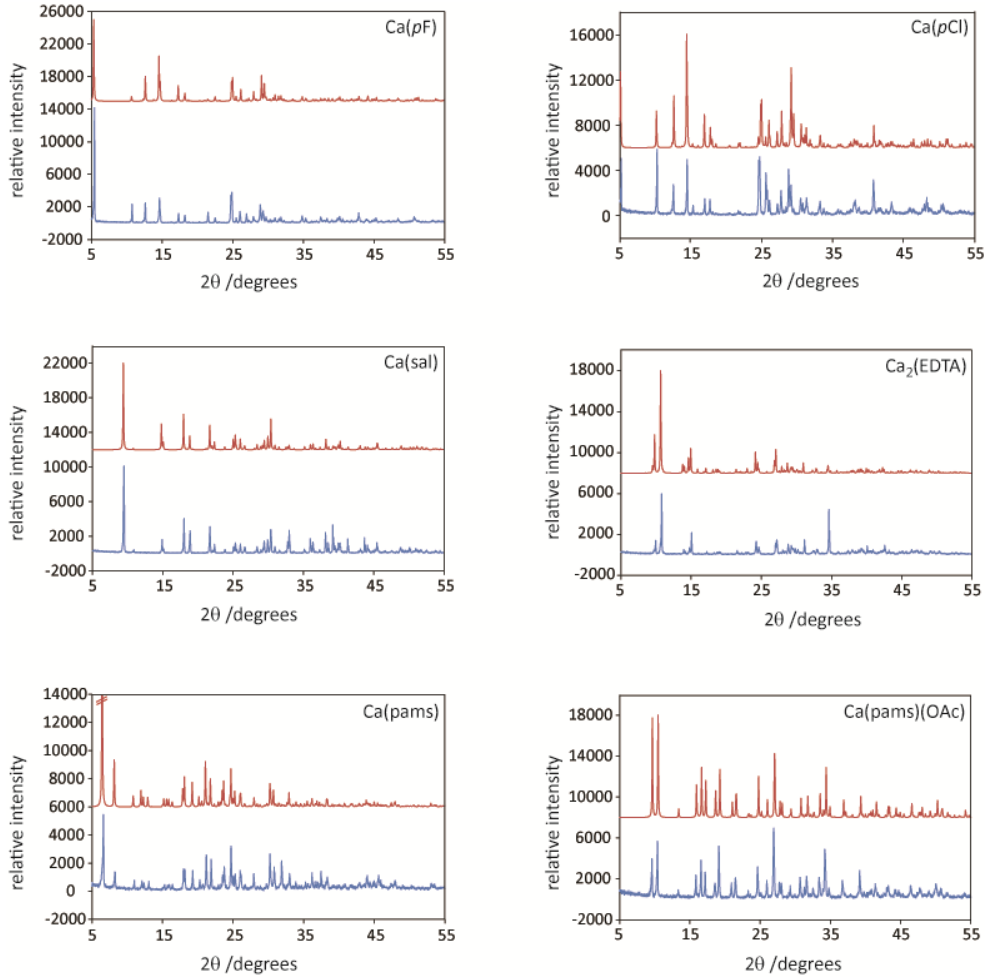

Figure 5.2: Experimental powder X-ray diffraction patterns for all calcium compounds (experimental traces are in blue) along with simulations in red based on the existing X-ray crystal structure data (see main text for appropriate references). All experiments were carried out using a Rigaku Ultima IV instrument with 2θ ranging between 5 and 55° in increments of 0.02° at a rate of 2° per minute. Simulations were generated using the Mercury software available from the Cambridge Crystallographic Data Centre.

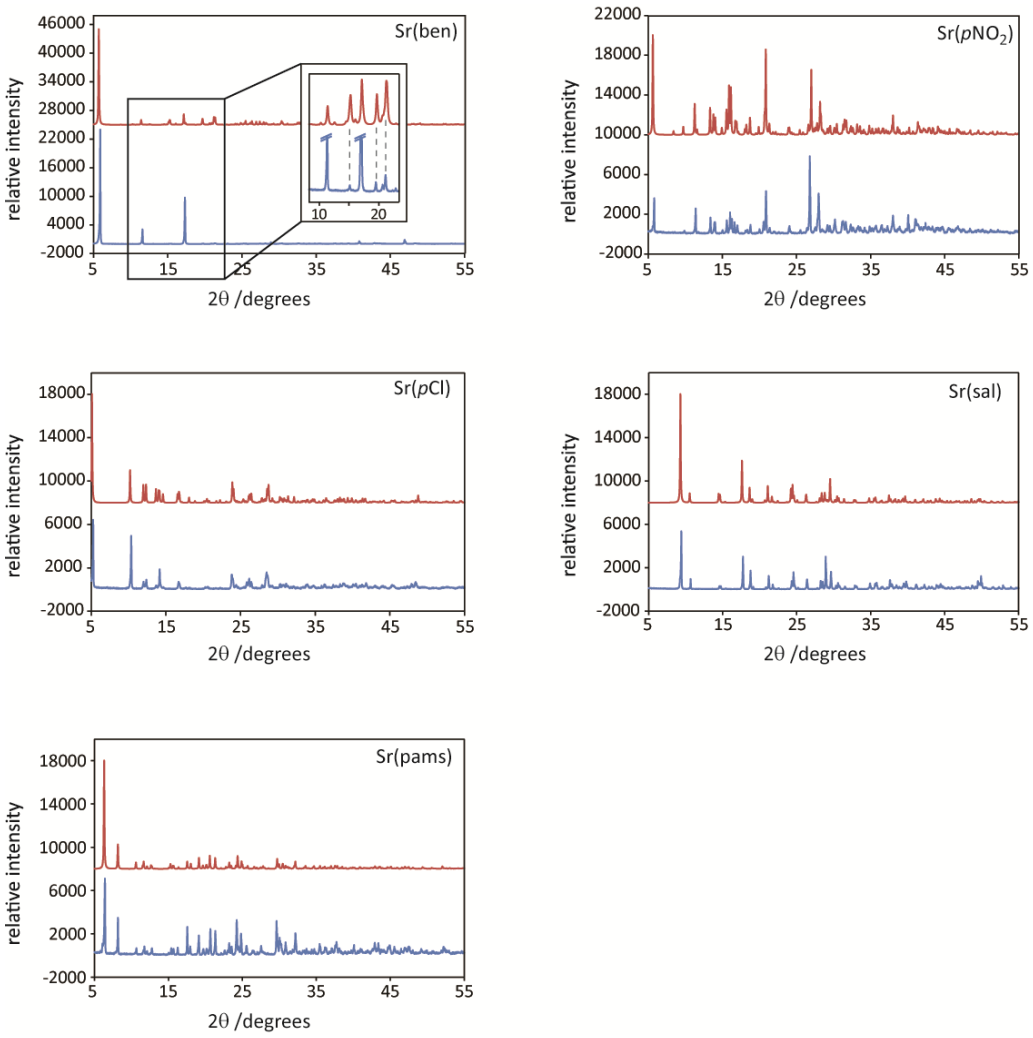

Figure 5.3: Experimental powder X-ray diffraction patterns for all strontium compounds (experimental traces are in blue) along with simulations in red based on the existing X-ray crystal structure data (see main text for appropriate references). All experiments were carried out using a Rigaku Ultima IV instrument with 2θ ranging between 5 and 55° in increments of 0.02° at a rate of 2° per minute. Simulations were generated using the Mercury software available from the Cambridge Crystallographic Data Centre. For Sr(ben), some peaks are particularly weak in intensity, presumably due to preferential alignment of the crystallites. An inset shows the presence of diagnostic peaks.

5.2.4 Computational Details

GIPAW DFT calculations were performed using ver. 4.1 of the CASTEP-NMR code (Accelrys Inc., San Diego, CA) as implemented in the Materials Studio (Accelrys Inc.) software package (ver. 3.2). The available single crystal X-ray structure crystallographic information files (.cif) for each compound were used as input structures. The structures of Ca(*p*Cl), Ca(pams), Sr(ben), Sr(*p*Cl), Sr(*p*NO_2), and Sr(pams) are all from ref. 44; those of Ca(sal) and Sr(sal) were reported by Debuyst et al.[50]; the structures of Ca(*p*F)[51] and Ca(ben)[52] were previously reported. The structure of Ca_2(EDTA)·$7H_2O$ can be found in ref. 46; some water molecules present in the lattice (i.e., not bound to Ca^{2+}) were assumed to have full occupancy for the calculations as these are not expected to affect greatly the calculated ^{43}Ca NMR parameters. Our structure for Ca(pams)(OAc), which has similar unit cell parameters to a previously reported one,[45] was used for the calculations. The *Pnma* space group for Ca(pams)(OAc) has a mirror plane bisecting the aryl ring, which creates disorder in the positioning of the hydroxyl group on the pams ligand. The disorder was removed manually and a modified .cif file was used for the calculations (see Appendix B5 for the modified .cif). The structures for Ca(D-gluconate)·$5H_2O$ and Ca(C_2O_4)·$3H_2O$ are taken from references [53] and [54], respectively. The PBE XC functional under GGA was used in all cases. On-the-fly generated pseudopotentials were employed for all atoms. All hydrogen atom positions were optimized prior to performing the NMR calculations. Many structures required a "coarse" setting for kinetic energy cut-off values and *k*-point grid due to large unit cell volumes. Specific considerations for each calculation are found in Appendix A5.3 in Appendix A.

For non-periodic DFT calculations, an isolated molecular model for Ca(pams) was built where both Ca^{2+} sites are present and benzoate ligands were converted to formate ligands. The nitrogen atom bound to calcium was hydrogen capped to make an ammonia ligand. A depiction of this model is found in Figure 5.8. The Gaussian '09 software package was used for the DFT computations on the Ca(pams) model using the B3LYP hybrid functional and the 6–31+G* basis set on all atoms. Hydrogen positions were optimized prior to NMR calculations. Multiple NMR calculations were performed where the Ca–N distance was varied between 2.50 Å and 2.90 Å in 0.05 Å increments. The EFGShield program was used in order to extract NMR parameters from the Gaussian '09 and CASTEP-NMR output files.

5.3 Results and Discussion

5.3.1 ^{43}Ca SSNMR Spectroscopy of Calcium Aryl Carboxylates

In Table 5.2 are presented the experimental and GIPAW DFT calculated ^{43}Ca EFG tensor and isotropic chemical shift parameters for all of the calcium carboxylate compounds considered in this work. Due to the absence of a discernible line shape at the higher magnetic field, some spectra (i.e., those for Ca(pams)(OAc) and $Ca_2(EDTA)\cdot 7H_2O$) were acquired at two magnetic field strengths. As for Ca(*p*Cl) and Ca(*p*F), both structures pack similarly to Ca(ben), which has already recently been extensively studied by ^{43}Ca SSNMR.[30] It is therefore not surprising that these three compounds exhibit similar experimental and calculated EFG tensor parameters (see Figure 5.4 for the NMR spectra). Inspection of all

data in Table 5.2 shows that both the $|C_Q(^{43}Ca)|$ values (ranging from ~0.7 MHz in site 2 of $Ca_2(EDTA)\cdot 7H_2O$ to 2.60 MHz in site 2 of Ca(pams)) and δ_{iso} values (a total range of 22 ppm) change considerably depending on the nature of the carboxylate ligand bound to Ca^{2+}. This observation is supported by GIPAW DFT calculations (*vide infra*). Some specific insights obtained when relating the ^{43}Ca NMR parameters of the calcium carboxylates to their respective crystal structures are outlined below.

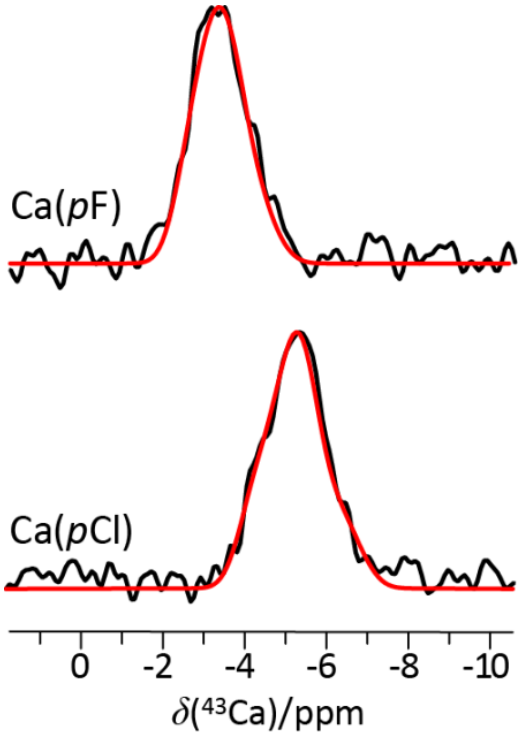

Figure 5.4: Natural abundance ^{43}Ca solid-state NMR spectra (in black) for Ca(*p*Cl) and Ca(*p*F) recorded at B_0 = 21.1 T under MAS conditions (ν_{rot} = 5 kHz). Analytical simulations (see Table 1) are in red.

Table 5.2: Experimental and Calculated ^{43}Ca NMR Parameters for Organic Calcium Complexes[a]

compound	site	$\lvert C_Q(^{43}Ca)\rvert$ /MHz	η_Q	δ_{iso} /ppm[c]	Ω /ppm	κ
Ca(ben)[b]		**1.10(0.05)**	**0.7(0.1)**	**-2.5(0.2)**	**15(1)**	**0.75(0.10)**
		1.12	*0.68*	*-7*	*38*	*0.59*
Ca(*p*F)		**1.2(0.1)**	**0.6(0.2)**	**-2.3(0.2)**	**-**	**-**
		0.94	*0.75*	*-4.9*	*37*	*0.53*
Ca(*p*Cl)		**1.3(0.1)**	**0.75(0.10)**	**-3.5(0.5)**	**-**	**-**
		0.95	*0.85*	*-6.3*	*39*	*0.61*
Ca(sal)		**1.55(0.10)**	**0.50(0.10)**	**-4.0(0.5)**	**-**	**-**
		1.58	*0.13*	*-5.9*	*42*	*-0.21*
Ca(pams)	**1**	**1.63(0.03)**	**0.35(0.05)**	**-3.2(0.5)**	**30(5)**	**-1.0(0.1)**
	1	*1.61*	*0.48*	*-6.0*	*37*	*-0.65*
	2[d]	**2.60(0.05)**	**0.60(0.03)**	**-5.5(0.5)**	**65(5)**	**0.6(0.1)**
	2	*2.37*	*0.64*	*-6.8*	*70*	*0.52*
Ca(pams)(OAc)		**1.15(0.05)**	**0.7(0.1)**	**5.4(0.2)**	**-**	**-**
		1.24	*0.39*	*5.8*	*27*	*0.36*
Ca_2(EDTA)·$7H_2O$	**1**[e]	**P_Q = 0.8(0.2)**		**6.1(0.8)**	**-**	**-**
	1	*0.97*	*0.31*	*3.4*	*34*	*-0.24*
	2[e]	**P_Q = 0.7(0.3)**		**15.1(0.4)**	**-**	**-**
	2	*0.99*	*0.75*	*15.7*	*18*	*-0.20*

[a] Errors are given in parentheses. Experimental ^{43}Ca NMR parameters are in boldface and GIPAW DFT calculated results are italicized.

[b] Experimental ^{43}Ca NMR parameters are from ref. 30. Calculations were performed as part of this work.

[c] The calculated σ_{iso} values were converted to chemical shifts using the relationship found in ref. 56 (i.e., $\delta_{iso} = -0.8032\sigma_{iso} + 901.6$ ppm).

[d] For this site, it was possible to determine the Euler angles which dictate the relative orientation of the EFG and CS tensor principal axis systems (α, β, γ = 210(20), 20(10), 110(10)°). For site 1 and other compounds, these angles were set to (α, β, γ = 0, 0, 0°) as the simulated line shape was not sensitive the values used.

[e] Due to the absence of discernible line shapes, P_Q and δ_{iso} parameters were calculated using the method described in ref. 20. An error of 1 ppm was used for both sites at 21.1 T and errors of 2 and 3 ppm (widths at approximately 90% peak height) were used for sites 1 and 2 respectively at 9.4 T. Standard deviations as a result of these errors are in parentheses.

In Figure 5.5b is shown the natural abundance ^{43}Ca MAS NMR spectrum for Ca(sal) at 21.1 T. Also depicted in this figure is the immediate coordination environment of each Ca^{2+} ion from the reported single crystal X-ray structure.[50] The ^{43}Ca NMR spectrum for

Ca(sal) is characterized by a single resonance, consistent with one crystallographic Ca site, with a $|C_Q(^{43}Ca)|$ value of 1.55 MHz. This resonance is very similar in shape to the more intense signal in the natural abundance ^{43}Ca spectrum of Ca(pams) shown in Figure 5.5a. A qualitative comparison between the first coordination spheres about both Ca sites in Ca(pams) to that of Ca(sal) can be made: site 1 in Ca(pams) is very similar to Ca(sal) (i.e., both are 8-coordinate with oxygen atoms which form a distorted square face bicapped trigonal prism geometry about Ca^{2+}). It is also possible to observe a second broader resonance at natural abundance for Ca(pams) after quite a long experiment time of nearly 42 hours (indicated by a dashed rectangle in Figure 5.5a). At this point, it was possible to assign this broader resonance to Ca site 2 in Ca(pams), which contains a nitrogen atom in its first coordination sphere. Since ^{43}Ca SSNMR has not been used previously in order to characterize Ca environments where nitrogen binding is present, we sought to isotopically label this sample (see Experimental Details) to both accurately and precisely measure the EFG and CS tensor parameters for both Ca sites in Ca(pams) and relate these values to the calcium environments. Both MAS and stationary NMR spectra acquired at 21.1 T, along with a MAS spectrum at 11.75 T, are presented in Figure 5.6. From the MAS spectra, it is clear that two crystallographically unique sites are present in the structure in a 1:1 ratio with differing $|C_Q(^{43}Ca)|$ values of 1.63 and 2.60 MHz for sites 1 and 2, respectively. Both sites, however, have very similar experimental and calculated δ_{iso} values. It was also possible, in light of the GIPAW DFT calculations, to extract the CS tensor spans, Ω, for both Ca sites in ^{43}Ca(pams). Very few ^{43}Ca SSNMR studies have reported chemical shift tensor parameters to date.[19,20,21] Widdifield *et al*.[55] have reported a Ω value of 31 ppm for anhydrous $CaCl_2$ whereas very distinct chemical shift tensor parameters have been found for the three different

anhydrous polymorphs of $CaCO_3$.[56] Site 2 in Ca(pams) (with N-coordination) exhibits one of the largest known Ω values of 65 ppm, whereas site 1 has a value of 30 ppm. It is therefore clear that N-binding ligands can significantly alter both the ^{43}Ca EFG and the CS tensor parameters relative to the case where only oxygen atoms interact with the Ca^{2+} cation.

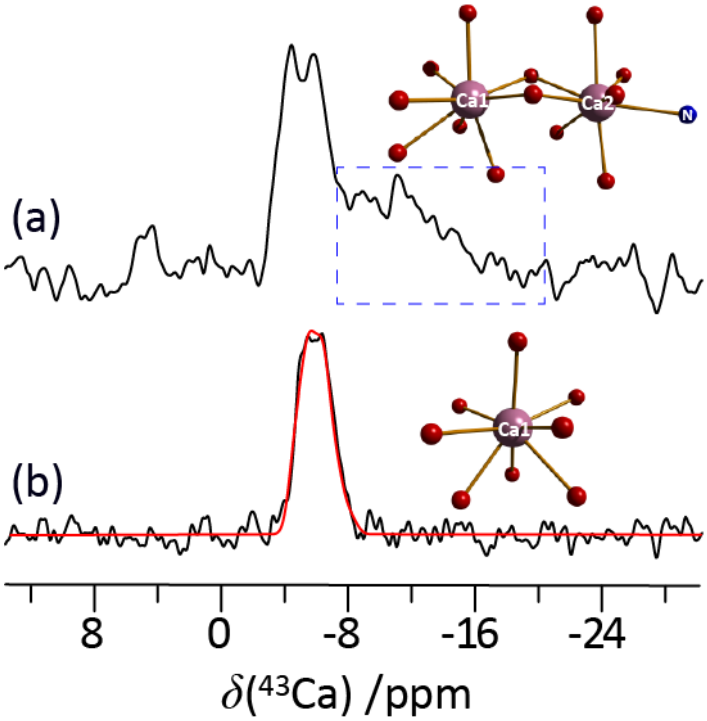

Figure 5.5: Natural abundance ^{43}Ca solid-state NMR spectra (in black) for Ca(sal) (b) and Ca(pams) (a) recorded at B_0 = 21.1 T under MAS conditions (ν_{rot} = 5 kHz). A dashed blue rectangle highlights a second broader ^{43}Ca resonance. In red is the analytical simulation for Ca(sal) in (b). The immediate coordination environment surrounding the Ca^{2+} sites in both compounds is also depicted. Calcium atoms are pink, oxygen atoms are red, and nitrogen atoms are blue.

5.3.2 N-atom Coordination to Ca^{2+}

In order to further investigate how N-coordination may affect the ^{43}Ca NMR parameters more generally, we have synthesized a different Ca complex with the pams ligand using $Ca(OAc)_2 \cdot H_2O$ as a source of Ca^{2+} ions. Ca(pams)(OAc) has one crystallographically unique Ca site which is 8-coordinate, including one N atom (see Figure 5.7a), like site 2 in Ca(pams). The OAc^- counter anions are also present in the lattice. Natural abundance ^{43}Ca MAS spectra acquired at 9.4 and 21.1 T confirm the presence of one Ca site (see Figures 5.7b and 5.7c respectively). Interestingly, a large decrease in the $|C_Q(^{43}Ca)|$ value (to 1.15 MHz) and an increase by approximately 10 ppm in the δ_{iso} value (5.4 ppm) are observed compared to site 2 in Ca(pams). Again, GIPAW DFT calculations (see Table 5.2) reproduce these experimental changes.

The EDTA ligand is known for its binding of various cations including alkaline-earth metals. In the case of Ca^{2+} chelation, the crystal structure of the $Ca_2(EDTA) \cdot 7H_2O$ complex has two distinct Ca sites, where site 1 is fully coordinated by oxygen atoms and site 2 contains two nitrogen atoms in its first coordination sphere (see Figure 5.7d). The natural abundance ^{43}Ca MAS NMR spectrum was acquired at 21.1 T in a relatively short amount of experimental time (4 hours) and has two featureless peaks that are clearly separated by approximately 10 ppm (see Figure 5.7f). Thus, only the quadrupolar product, $|P_Q(^{43}Ca)|$ (i.e., $P_Q = C_Q(1 + (\eta_Q)^2/3)^{1/2}$), and the δ_{iso} values could be quantified even after acquiring a MAS spectrum at 9.4 T (see Figure 5.7e). The NMR parameters are reported in Table 5.2 and a significant difference in δ_{iso} values between both Ca sites (6.1 and 15.1 ppm for sites 1 and 2 respectively) is observed and reproduced with GIPAW DFT calculations. It was also

possible to assign both resonances to the crystal structure on the basis of chemical shifts; site 2, which contains Ca–N bonds, corresponds to the more deshielded resonance.

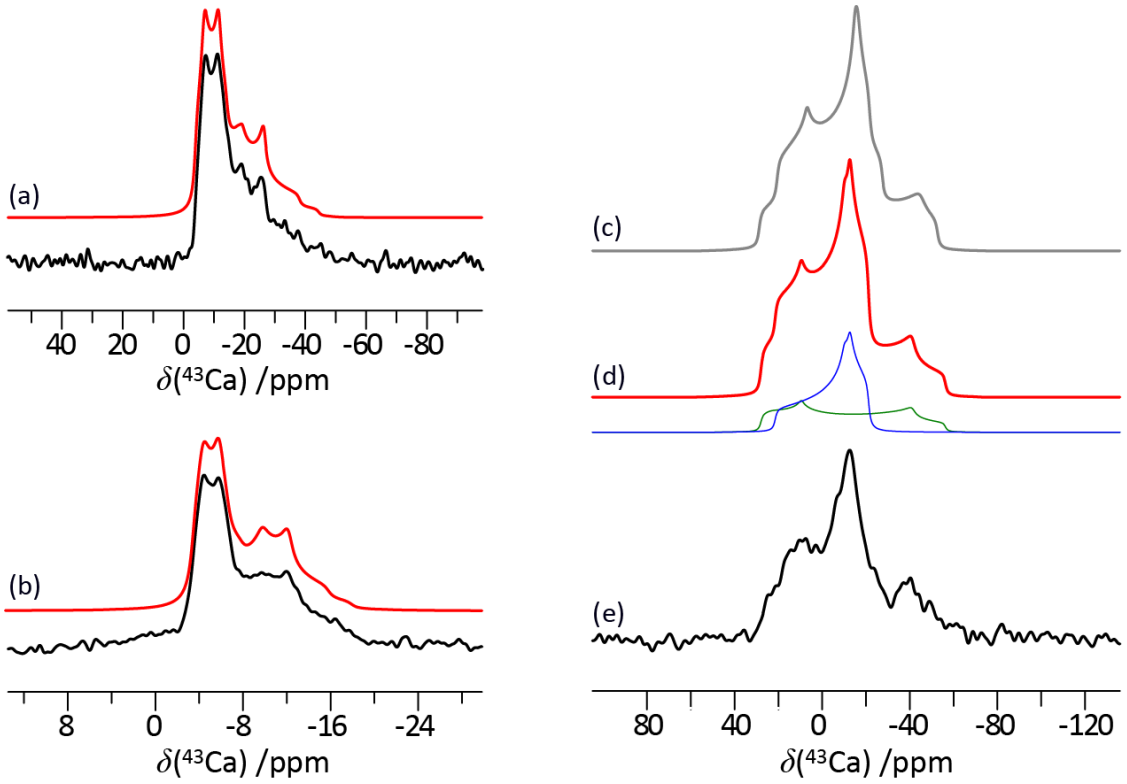

Figure 5.6: Experimental ^{43}Ca solid-state NMR experiments on isotopically enriched (~4%) ^{43}Ca(pams) acquired at B_0 = 21.1 T (b) and 11.75 T (a) under MAS conditions (ν_{rot} = 10 kHz) using single pulse experiments. Their respective analytical simulations are in red. In (e) is the ^{43}Ca NMR spectrum of the same sample acquired under stationary conditions with ^{1}H decoupling at B_0 = 21.1 T. The analytical simulation for the stationary NMR experiment is in (d) and a deconvolution is shown in blue and green for sites 1 and 2 respectively. The number of parameters required for the simulations in (d) was reduced as the quadrupolar parameters and δ_{iso} were constrained to values obtained from MAS experiments. In (c) is the line shape predicted from GIPAW DFT calculations.

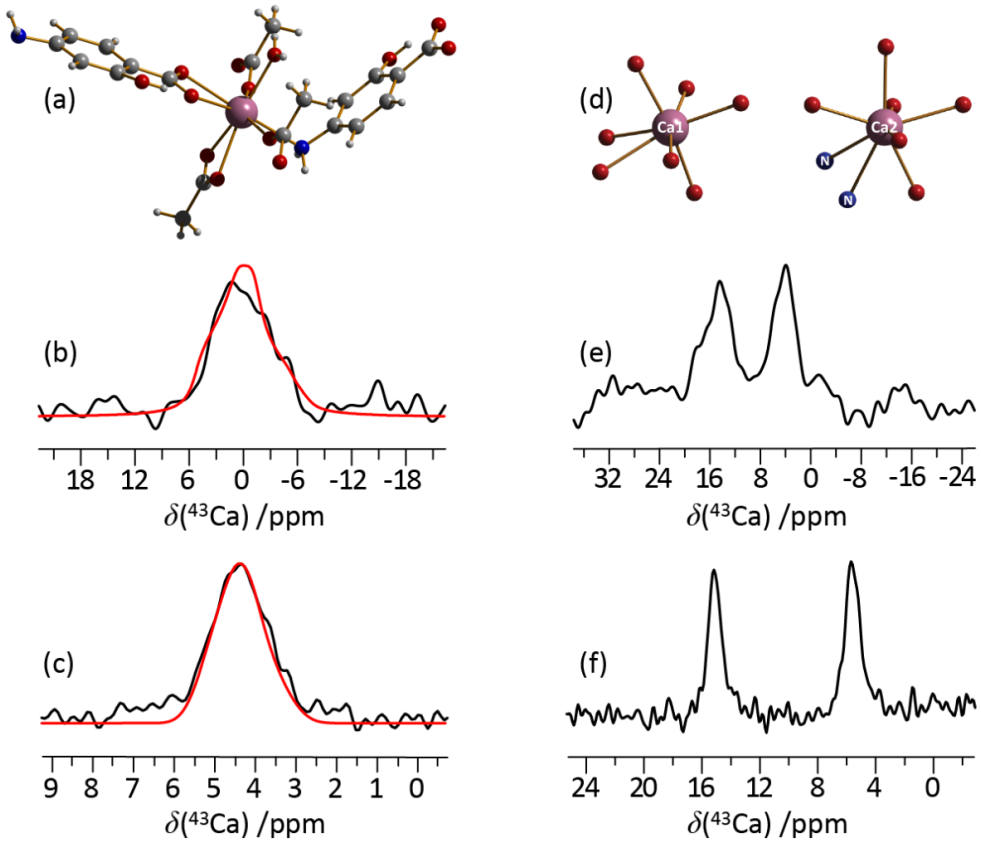

Figure 5.7: Natural abundance ^{43}Ca solid-state NMR spectra recorded at B_0 = 9.4 (b and e) and 21.1 T (c and f) under MAS conditions (ν_{rot} = 5 kHz) for Ca(pams)(OAc) [left] and $Ca_2(EDTA)\cdot 7H_2O$ [right] respectively. Analytical simulations are in red. The structure of Ca(pams)(OAc) is depicted in (a), where a *p*-aminosalicylate ligand is bound to Ca *via* its nitrogen atom. The immediate coordination environment surrounding both Ca^{2+} sites in $Ca_2(EDTA)\cdot 7H_2O$ is in (d). The two distinct Ca sites are clearly resolved for $Ca_2(EDTA)\cdot 7H_2O$. Calcium atoms are pink, oxygen atoms are red, and nitrogen atoms are blue.

It is not immediately clear how the ^{43}Ca δ_{iso} values are systematically affected by nitrogen coordination. In Ca(pams), the Ca^{2+} site with a nitrogen ligand is shielded by 2.3 ppm relative to the site which is fully coordinated by oxygen atoms, while in $Ca_2(EDTA)\cdot 7H_2O$, a deshielding of 10.2 ppm is observed for the site with two nitrogen ligands compared to the site which is fully coordinated by oxygen atoms. We were curious to see how changes in the Ca–N distance may affect the Ca NMR parameters, as Ca(pams) (d_{Ca-N} = 2.7085 Å) and Ca(pams)(OAc) (d_{Ca-N} = 2.5813 Å) have δ_{iso} values of −5.5 and +5.4 ppm, respectively. Such a large difference in chemical shifts cannot be entirely accounted for by the change in the average Ca–O bond lengths for the two compounds (~0.03 Å) and the slope of −154 ppm/Å from model calculations on calcium organic compounds.[38] An isolated molecular model of Ca(pams) was built (see Figure 5.8a) and, after geometry optimization of the hydrogen atom positions, the Ca–N distance, d_{Ca-N}, was varied systematically from 2.50 to 2.90 Å (this is a representative range for Ca–N bond lengths in other similar complexes[39,57,58]) and the changes in the calculated NMR parameters were monitored. In Figure 5.8b is shown how the individual principal components of the ^{43}Ca CS tensor are affected by changing d_{Ca-N}. Firstly, it is evident that a large decrease in δ_{33} is observed compared to the changes in δ_{11} and δ_{22}. This in turn decreases the value of δ_{iso} as the Ca–N bond length is increased. This demonstrates the sensitivity of ^{43}Ca NMR towards small structural differences within the first coordination sphere of Ca^{2+} specifically when nitrogen atoms are involved in metal binding. While the ^{43}Ca chemical shift cannot be easily used to determine the number of nitrogen atoms in the first coordination sphere, it does appear to be diagnostic of the calcium-nitrogen distance. To compare the effect on the computed ^{43}Ca chemical shift of changing a single Ca–O distance vs a single Ca–N distance,

the ammonia ligand in the model shown in Figure 5.8b was replaced by a water molecule and the Ca–O distance was systematically varied over a range of typical values (2.30 to 2.70 Å). The ^{43}Ca chemical shift was found to be approximately equally sensitive to the varied distance for N-binding (-36 ppm/Å) and O-binding (-29 ppm/Å).

Table 5.3: Additional Experimental and GIPAW DFT Calculated $|C_Q(^{43}Ca)|$ Values used in Figure 5.9.

compound	exp. $\|C_Q(^{43}Ca)\|$ /MHz	reference[a]	calc. $\|C_Q(^{43}Ca)\|$ /MHz[b]	reference[a]
$Ca(OH)_2$	2.49(0.02)	35	2.29	56
$CaCl_2$	0.95(0.20)	55	1.07	55
$CaCO_3$ (aragonite)	0.259(0.003)	59	0.35	56
$CaCO_3$ (calcite)	1.39(0.10)	56	1.60	56
$Ca_{10}(PO_4)_6(OH)_2$–site 1	2.6(0.4)	32	2.00	31
$Ca_{10}(PO_4)_6(OH)_2$–site 2	2.4(0.1)	33	2.02	31
β–C_2S–site 1	2.41(0.2)	35	2.28	35
β–C_2S–site 2	2.98(0.2)	35	3.06	35
$Ca(HCOO)_2$	1.24(0.05)	29	1.35	56
Ca(D-gluconate)·$5H_2O$	1.25(0.1)	29	1.26	this work
$Ca(C_2O_4)\cdot 3H_2O$[c]	1.55(0.1)	29	0.57[c]	this work
$Ca(C_2O_4)\cdot H_2O$–site 1	1.5(0.2)	28	1.34	28
$Ca(C_2O_4)\cdot H_2O$–site 2	1.6(0.2)	28	1.60	28

[a] These are cross-references to the main text.

[b] These calculated values are scaled with the updated nuclear electric quadrupole moment for ^{43}Ca of –44.4 mbarn. This is why the values differ from the values reported in the references listed. Heavy atoms are fixed to the experimental values in all calculations; hydrogen atom positions are optimized in the case of single-crystal X-ray structures.

[c] This compound was identified as a major outlier and is not shown in Figure 6. This could be due to a poor structure; its optimization is beyond the scope of this work.

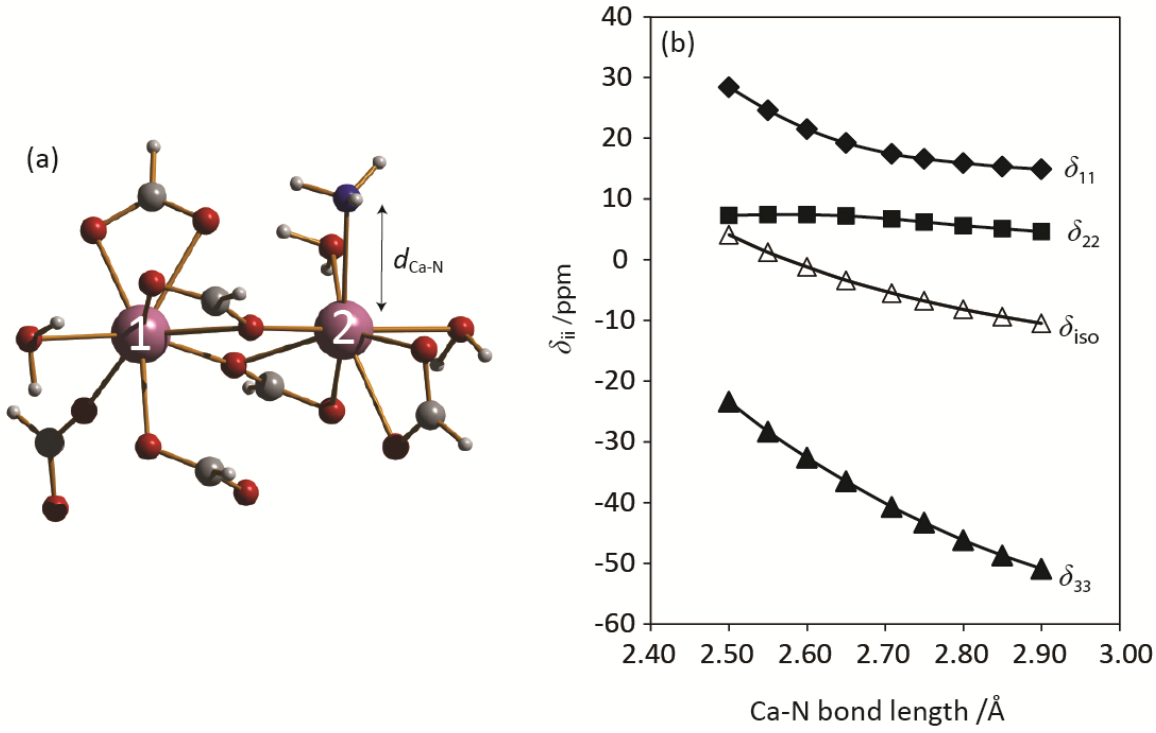

Figure 5.8: Calculated principal components of the ^{43}Ca chemical shift tensor as a function of the Ca–N distance (B3LYP/6–31+G*) (part (b)). A model system (part (a)) was built from the available crystal structure of Ca(pams) wherein both Ca sites are present and coordinated by water, formate, and ammonia ligands. All chemical shifts are relative to a calculation on the original structure of Ca(pams). An approximate range of 10 ppm for δ_{iso} is observed for a range of Ca–N distances between 2.50 and 2.90 Å. δ_{iso} changes by about -36 ppm/Å over this range. When visualizing the principal tensor components with respect to the molecular frame, δ_{33} is observed to be nearly perpendicular to the Ca–N bond vector, which explains the larger change in the value of δ_{33}.

5.3.3 A New Quadrupole Moment for ^{43}Ca

As summarized in a recent review by Moudrakovski,[21] reliable $|C_Q(^{43}Ca)|$ values are scarce and many studies report only P_Q rather than C_Q values. Given the accurate characterization of the ^{43}Ca EFG tensor parameters in a larger dataset of compounds as part of this work, a plot of the GIPAW DFT calculated $|C_Q(^{43}Ca)|$ values versus the experimentally determined values yields a useful correlation (Figure 5.9). This plot includes only reliable experimental $|C_Q(^{43}Ca)|$ values reported to date from the current and previous studies, which are summarized in Table 5.3.[24,29,30,31,32,33,35,55,56,59,25] Furthermore, only data for compounds with high-quality structures from single-crystal X-ray or neutron diffraction are included. A rather good correlation is observed (R^2 = 0.910), but GIPAW DFT calculations seem to consistently underestimate the experimental values. Recently, a new value of Q for ^{43}Ca of –44.4 mbarn[60] has been proposed by combining the measured electric quadrupole hyperfine-structure constant and relativistic coupled-cluster calculations. One plot was generated using each Q value (only the graph where Q = –44.4 mbarn is shown in Figure 5.9). The slopes of the linear regressions are 0.861 and 0.937 for Q = –40.8 and –44.4 mbarn, respectively (recall, $C_Q = eV_{33}Q/h$). It is therefore recommended to use the updated quadrupole moment of –44.4 mbarn when performing calculations in order to improve the accuracy of the predicted ^{43}Ca EFG tensor parameters. This analysis will serve as a useful tool in future studies including those involving crystal structure refinements.

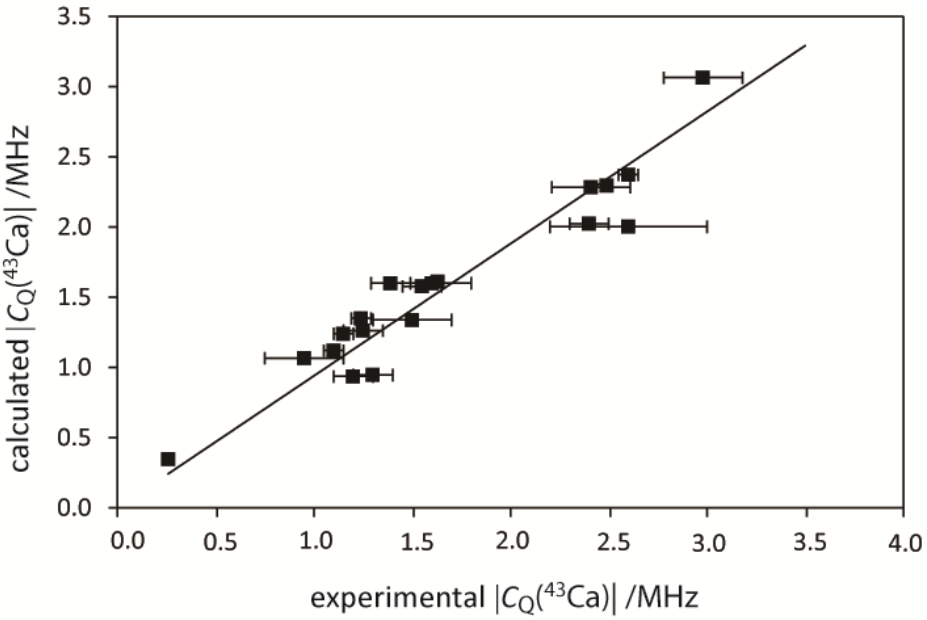

Figure 5.9: GIPAW DFT computed $|C_Q(^{43}Ca)|$ values versus the experimental values from this work and previously characterized Ca environments for which reliable ^{43}Ca SSNMR data are available (see main text for relevant references). Two plots were generated wherein the ^{43}Ca quadrupole moment is –40.8 mbarn ($|C_Q(^{43}Ca, \text{calc.})| = 0.861|C_Q(^{43}Ca, \text{exp.})|$, R^2 = 0.910) or –44.4 mbarn ($|C_Q(^{43}Ca, \text{calc.})| = 0.937|C_Q(^{43}Ca, \text{exp.})|$, $R^2 = 0.910$). Only the latter of the linear regressions is shown above for clarity. In both cases, the (0,0) data point was included in the linear regression.

5.3.4 ^{87}Sr WURST–QCPMG NMR of Strontium Aryl Carboxylates

Given the structural similarities between some calcium and strontium complexes, as well as the dearth of ^{87}Sr NMR information for strontium complexes bearing organic ligands, we next extended our work to the study of analogous strontium aryl carboxylate complexes. In total, ^{87}Sr SSNMR spectra were recorded for five strontium compounds. Spectra for

Sr(ben), Sr(sal), Sr(*p*Cl), and Sr(*p*NO_2), along with their respective analytical simulations, are shown in Figure 5.10. The experimental ^{87}Sr EFG tensor parameters and chemical shifts are reported in Table 5.4. We note that in all analytical simulations of ^{87}Sr NMR spectra, chemical shift anisotropy was not considered due to the dominance of the QI. All spectra illustrated in Figure 5.10 were acquired using the WURST–QCPMG method at a magnetic field strength of 21.1 T. WURST pulses provided uniform and broadband excitation of the entire CT line shape in one transmitter offset setting (in our spectra, some line shapes spanned over 150 kHz at 21.1 T). The very low receptivity of the ^{87}Sr nucleus prompted us to use the QCPMG method. Due to increased quadrupolar broadening of the CT line shape and the low resonance frequency, experiments at lower magnetic fields strengths (such as 9.4 T) were not feasible. The $|C_Q(^{87}Sr)|$ values, which range from 11.7 MHz for Sr(*p*NO_2) to 33.8 MHz for site 2 in Sr(pams), were found to be particularly sensitive to the local Sr^{2+} environment. Isotropic chemical shifts could not be measured as precisely as in our ^{43}Ca experiments given the acquisition method and the ^{87}Sr spectral breadth. The experimental errors in the analytical simulations for δ_{iso} range from 20 to 50 ppm, which represents 10 to 25 % of the total range (i.e., 200 ppm, see Table 5.4) of chemical shifts characterized as part of this work. Therefore, the establishment of meaningful correlations between δ_{iso} and the Sr^{2+} coordination environment is not feasible.

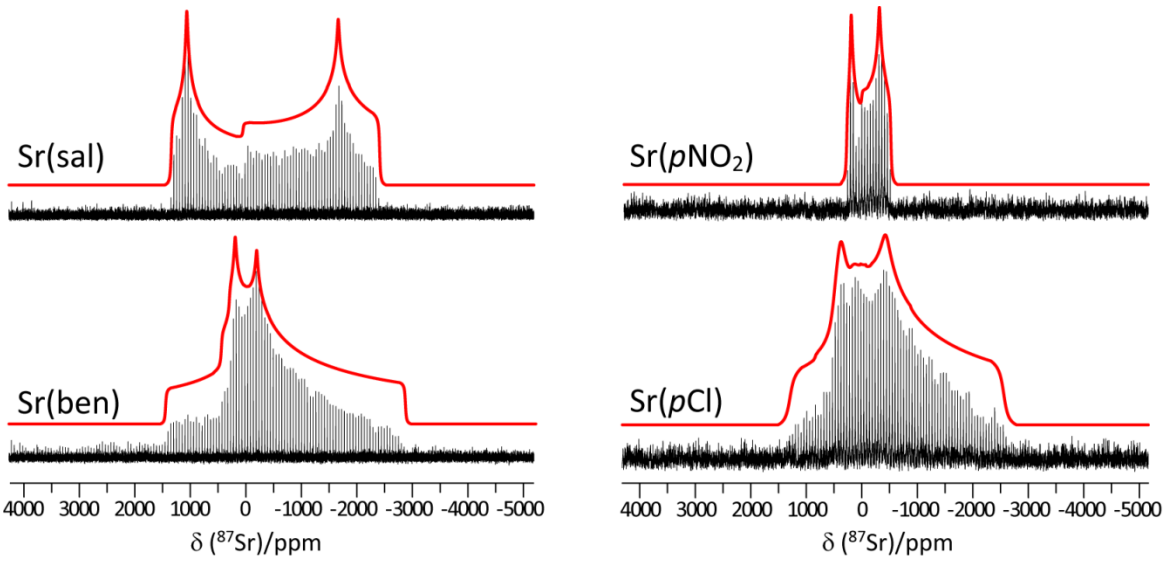

Figure 5.10: Experimental ^{87}Sr NMR spectra acquired at 21.1 T under stationary conditions using the WURST–QCPMG pulse sequence. Spikelet separations are 2 kHz for all samples. Partially excited satellite transitions are visible beyond the high-frequency discontinuity in the spectrum of Sr(ben). Red traces represent analytical simulations and NMR parameters are summarized in Table 5.4. Chemical shift anisotropy was not included in the simulations.

Table 5.4: Experimental and Calculated ^{87}Sr NMR Parameters for Strontium Aryl Carboxylates [a]

compound	space group	site	$\lvert C_Q(^{87}Sr)\rvert$ /MHz	η_Q	δ_{iso} /ppm[b]
Sr(ben)	$C2/c$		**22.5(0.5)**	**0.87(0.02)**	**0(50)**
		1	*20.7*	*0.76*	*-52*
		2	*20.8*	*0.84*	*-58*
Sr(*p*Cl)	$P\bar{1}$		**22.2(0.2)**	**0.71(0.02)**	**0(50)**
			22.3	*0.69*	*-65*
Sr(sal)	$P2_1$		**26.1(0.3)**	**0.18(0.03)**	**30(20)**
			32.2	*0.45*	*-25*
Sr(*p*NO_2)	$P2_1/c$		**11.70(0.3)**	**0.25(0.05)**	**10(20)**
			15.3	*0.31*	*-30*
Sr(pams)	$P2_1/n$	**1**	**22.0(0.5)**	**0.92(0.02)**	**-50(30)**
		1	*22.0*	*0.86*	*-5*
		2	**33.8(0.3)**	**0.85(0.03)**	**150(50)**
		2	*35.1*	*0.65*	*-30*

[a] Errors are given in parentheses. Experimental ^{87}Sr NMR parameters are in boldface and GIPAW DFT calculated results are italicized.

[b] The calculated σ_{iso} values were converted to chemical shifts using the relationship found in ref. 36 (i.e., $\delta_{iso} = -0.8750\sigma_{iso} + 2574$ ppm).

The WURST–QCPMG ^{87}Sr NMR spectrum of Sr(ben) shows one discernible Sr site characterized by a $\lvert C_Q(^{87}Sr)\rvert$ value of 22.5(0.5) MHz and an asymmetry parameter, η_Q, of 0.87. However, according to the X-ray crystal structure reported in the literature,[44] two distinct strontium sites are expected. GIPAW DFT calculations on this structure reveal very similar EFG tensor parameters for both sites, with $\lvert C_Q(^{87}Sr)\rvert$ values of 20.7 and 20.8 MHz and η_Q values of 0.76 and 0.84, for strontium sites 1 and 2, respectively. Structurally, both sites have nearly identical oxygen coordination environments but are mirror images of one another (see Figure 5.11). The ^{87}Sr NMR spectrum for Sr(ben) demonstrates one of the limitations of the WURST–QCPMG method in resolving sites which have very similar quadrupolar and chemical shift parameters. Sr(sal) ($P2_1$ space group) is characterized by a

larger $|C_Q(^{87}Sr)|$ value of 26.1 MHz compared to Sr(*p*Cl) (*P*1 space group) and Sr(ben) (*C*2/*c* space group) with $|C_Q(^{87}Sr)|$ values of 22.2 and 22.5 MHz, respectively. Qualitative inspection of the coordination geometry about Sr^{2+} in each of the three compounds does not reveal any obvious reason for the moderate variability in the ^{87}Sr quadrupolar coupling constants; indeed it has been shown recently that geometrical considerations about the immediate coordination sphere of Sr^{2+} alone do not fully account for changes in the value of $C_Q(^{87}Sr)$.[36] However, GIPAW DFT calculations prove to predict quite accurately these changes in the EFG tensor parameters (see Table 5.4).

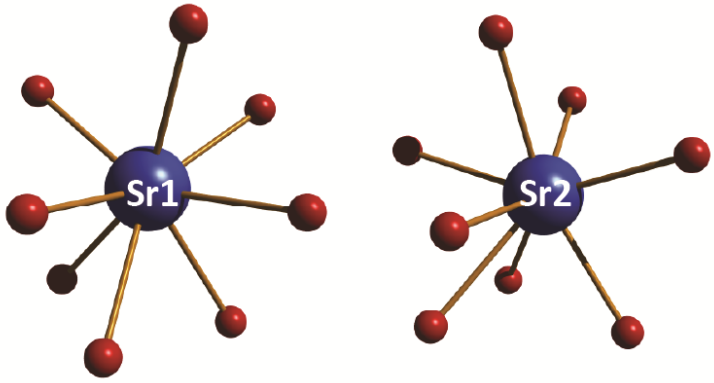

Figure 5.11: Representation of both crystallographically unique Sr sites in Sr(ben). Both sites are 8-coordinate with oxygen atoms (in red). The coordination polyhedra are quite similar for both sites and they appear to be approximate mirror images of each other.

The spectrum of Sr(*p*NO_2) is shown in Figure 5.10 and has the narrowest ^{87}Sr line shape considered in this work. It is characterized by a much smaller $|C_Q(^{87}Sr)|$ value of 11.7 MHz and hence fewer spikelets define the CT line shape. GIPAW DFT calculations also predict a lowering of the $|C_Q(^{87}Sr)|$ value for Sr(*p*NO_2) relative to the compounds discussed

above, but the calculations overestimate the experimental datum by several MHz (Table 5.4). This overestimation might be due to the presence of a larger number of coordinated water molecules (i.e., 7 in this case) about the Sr^{2+} cation compared to the other compounds considered in this work. Dynamics of coordinated water molecules are not accounted for in our calculations (performed at 0 K). Recall that water dynamics affected the quadrupolar parameters for Mg(*p*NO_2) in Chapter 4. More interestingly, Sr(*p*NO_2) is 9-fold coordinated with oxygen atoms whereas Sr(ben), Sr(sal), Sr(*p*Cl), and site 1 of Sr(pams) are all coordinated to 8 oxygen atoms. A lower value of $|C_Q(^{87}Sr)|$ for Sr(*p*NO_2) is consistent with a few previously characterized 9-oxygen coordinated strontium sites such as those in $SrCO_3$ ($|C_Q(^{87}Sr)|$ = 8.91 MHz)[61] and a micaceous mineral ($|C_Q(^{87}Sr)|$ = 9.02 MHz).[62] However, the previously studied strontium malonate[36] is 9-coordinate[63] and has a larger $|C_Q(^{87}Sr)|$ value of 31.5 MHz. Both oxygen coordination polyhedra surrounding Sr(*p*NO_2) and strontium malonate are monocapped square antiprisms. The latter complex has, qualitatively, a much larger degree of distortion, which explains the large difference between the $|C_Q(^{87}Sr)|$ values.

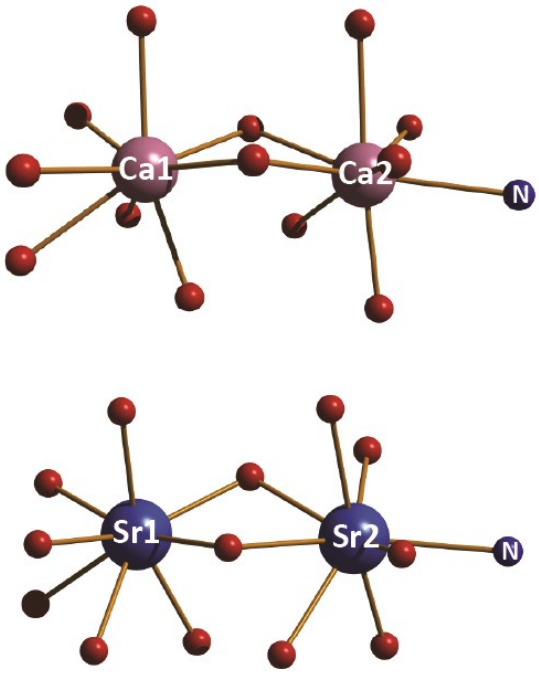

Figure 5.12: Immediate cation coordination environments in Ca(pams) (top) and Sr(pams) (bottom). Both compounds crystallize in the same space group, $P2_1/n$, and have similar differences in their EFG tensor parameters when comparing site 1 with site 2 (see main text). Oxygen atoms are in red.

5.3.5 Sr(pams): N-Coordination to Sr^{2+}

The final Sr compound in our series, Sr(pams), has a molecular and crystal structure that resembles closely its calcium analogue, Ca(pams) (see Figure 5.12 for a comparison). Both structures crystallize in the $P2_1/n$ space group and have two crystallographically unique metal cation sites. As is the case for Ca(pams), site 1 in Sr(pams) is fully coordinated by oxygen atoms and site 2 has seven oxygen atoms and 1 nitrogen atom in the first coordination sphere. Our first attempt at acquiring this ^{87}Sr spectrum was in the same manner as for the other Sr compounds in this study. The ^{87}Sr WURST–QCPMG spectrum is

shown in Figure 5.13b and resembles quite closely the spectrum observed for Sr(ben) with an asymmetry parameter near unity and a $|C_Q(^{87}Sr)|$ value of ~22 MHz. The observation of a single Sr site is in disagreement with the reported crystal structure, which has two crystallographically unique Sr^{2+} cations. Furthermore, unlike for Sr(ben), the GIPAW DFT calculations predict substantially different $|C_Q(^{87}Sr)|$ values for Sr(pams); these are 22.0 and 35.1 MHz for sites 1 and 2 respectively (see Figure 5.13a for a simulation based on the calculated NMR parameters). The larger $|C_Q(^{87}Sr)|$ value is in agreement with what is observed for Ca(pams) where site 2, which contains the alkaline-earth metal-bound nitrogen atom, is characterized by a C_Q value about 1.5 times larger than that for site 1. We were unable to observe the second broader site in the ^{87}Sr NMR spectrum even when stepping the transmitter offset frequency in the WURST–QCPMG experiment. The reason for this is likely a smaller T_2 value for site 2. Instead, a solid echo experiment was successfully used to acquire the spectrum of both strontium sites (see Figure 5.13c). For this spectrum, multiple transmitter offset settings were required in order to obtain the full CT line shape, with a spectral breadth of nearly 400 kHz. The singularities in this spectrum confirm the presence of a second Sr site with a larger $|C_Q(^{87}Sr)|$ value of 33.8 MHz. The observation of this broader site is in agreement with the GIPAW DFT calculations and thus the larger C_Q value can be attributed to the presence of a nitrogen atom coordinated to Sr^{2+} as was shown for the Ca(pams) analogue. As shown with this example, care must be taken when performing WURST–QCPMG experiments on Sr samples as T_2 values may affect our ability to observe Sr^{2+} in certain chemical environments.

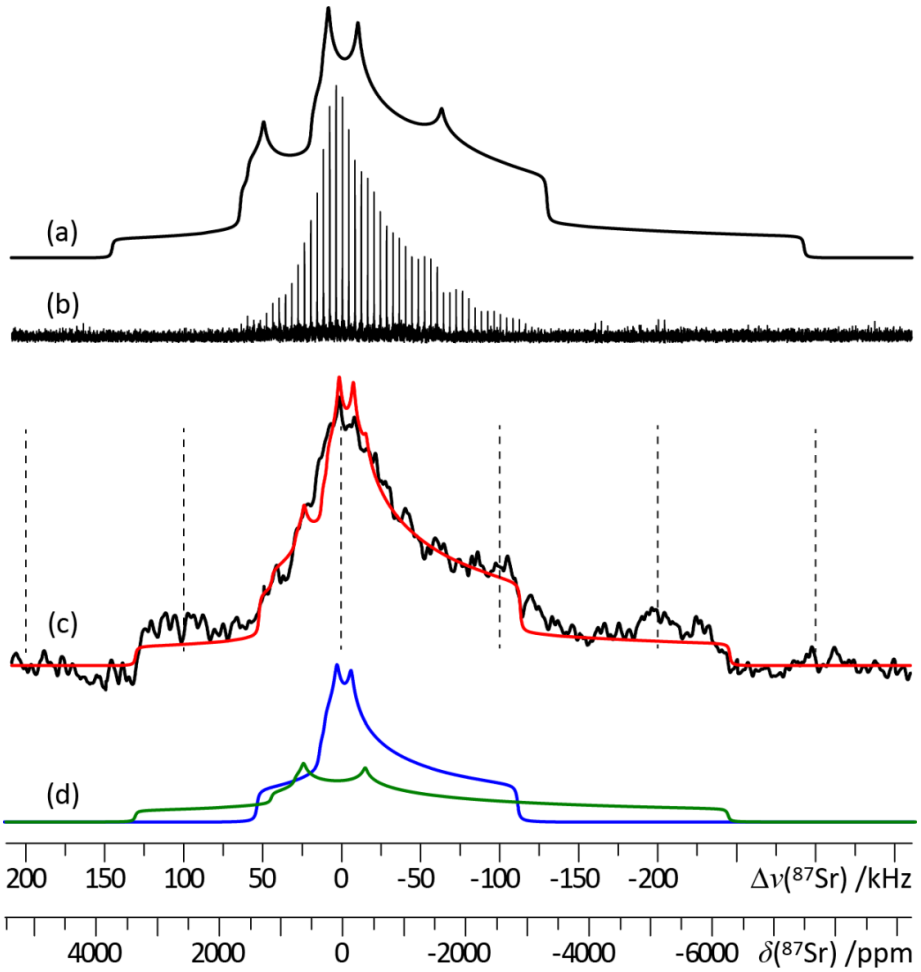

Figure 5.13: Experimental ^{87}Sr WURST–QCPMG NMR spectrum of Sr(pams) acquired at 21.1 T (b) and simulation of the GIPAW DFT calculated ^{87}Sr NMR spectrum under stationary conditions (a). Only the NMR parameters for the narrower Sr line shape can be estimated using this method. A stepped solid echo experiment was performed at 21.1 T (c, black trace) and a simulation with two strontium sites in a 1:1 ratio is shown in red. The deconvolution of the simulation from (c) is depicted in (d) where site 1 is in blue and site 2 is in green. Dashed lines indicate transmitter offset frequency settings for VOCS data acquisition.

5.4 Conclusions

In summary, this Chapter contains a ^{43}Ca and ^{87}Sr SSNMR study on the Ca^{2+} and Sr^{2+} cations present in various organic molecular environments which may serve as models for metal organic frameworks, metal ion receptors, and biological systems. The benzoate, salicylate, and ethylenediaminetetracetate (EDTA) ligands employed in this study allow for a variety of coordination motifs to be probed by alkaline-earth metal solid-state NMR spectroscopy including nitrogen binding to the metal centers. It was shown with the examples of Ca(pams), its derivative, Ca(pams)(OAc), and Sr(pams) that both the electric field gradient and chemical shift tensors are sensitive to the presence of alkaline earth metal-nitrogen interactions. For example, DFT computations on a model for Ca(pams) demonstrated a reciprocal correlation between the calcium chemical shift and the Ca–N bond length which is consistent with the trend observed experimentally for Ca(pams) and Ca(pams)(OAc). It was also possible to fully characterize the ^{43}Ca chemical shift tensors of both crystallographically unique sites in Ca(pams) with the aid of ^{43}Ca isotopic labeling. A structural assignment could be made with the aid of GIPAW DFT computations that predicted larger CSA and $|C_Q(^{43}Ca)|$ values for the Ca^{2+} interacting with a nitrogen atom in its first coordination sphere.

Many previous studies have been unsuccessful in fully characterizing accurate ^{43}Ca EFG tensor parameter (i.e., by only reporting P_Q values for example), thus prohibiting until now the establishment of a meaningful correlation between DFT calculated and experimental $|C_Q(^{43}Ca)|$ values for future crystal structure refinement purposes. This study has also allowed for the accurate characterization of both the ^{43}Ca quadrupolar coupling constants and

asymmetry parameters. The best agreement was observed between the GIPAW DFT calculated $|C_Q(^{43}Ca)|$ values and experiment when using the newly proposed quadrupole moment for ^{43}Ca, $Q = -44.4$ mbarn, suggesting that this value be used in such studies going forward.

Finally, ^{87}Sr WURST–QCPMG NMR was used to characterize a series of analogous organic strontium complexes. It was found that, in general, for ^{87}Sr NMR, the EFG tensor is the most sensitive parameter to minute structural changes as was evidenced by both Sr(*p*Cl) and Sr(sal). This is consistent with the recent findings of Bonhomme *et al*.[36] In the case of Sr(*p*NO_2), the smaller $|C_Q(^{87}Sr)|$ value was attributed to a more symmetric 9-oxygen coordinate monocapped square antiprism geometry. As for Sr(pams), changes in the ^{87}Sr NMR acquisition method allowed us to observe the second broader NMR line shape associated with the nitrogen-binding Sr site. Good agreement between experiment and GIPAW DFT calculations was also noted for ^{87}Sr NMR parameters. This contribution has allowed for a deeper understanding of how subtle structural changes about alkaline-earth metal cations are manifested in their NMR parameters, and may find use in future studies involving these essential elements which play key roles in metalloproteins and more affordable alkaline-earth metal catalysts, to name but a few applications.

5.5 Reference for Chapter 5

1. Gatt, P.; Petrie, S.; Stranger, R.; Pace, R. J. *Angew. Chem. Int. Ed.* **2012**, *51*, 12025.
2. Tsui, E. Y.; Tran, R.; Yano, J.; Agapie, T. *Nature Chem.* **2013**, *5*, 293.
3. Park, Y. J.; Cook, S. A.; Sickerman, N. S.; Sano, Y.; Ziller, J. W.; Borovik, A. S. *Chem. Sci.* **2013**, *4*, 717.
4. Babu, C. S.; Dudev, T.; Lim, C. *J. Am. Chem. Soc.* **2013**, *135*, 6541.
5. Hoi, H.; Matsuda, T.; Nagai, T.; Campbell, R. E. *J. Am. Chem. Soc.* **2013**, *135*, 46.
6. Collot, M. Loukou, C.; Yakovlev, A. V.; Wilms, C. D.; Li, D.; Evrard, A.; Zamaleeva, A.; Bourdieu, L.; Léger, J.-F.; Ropert, N.; Eilers, J.; Oheim, M.; Feltz, A.; Mallet, J.-M. *J. Am. Chem. Soc.* **2012**, *134*, 14923.
7. Bar-Shir, A.; Gilad, A. A.; Chan, K. W. Y.; Liu, G.; van Zijl, P. C. M.; Bulte, J. W. M.; McMahon, M. T. *J. Am. Chem. Soc.* **2013**, *135*, 12164.
8. Sleem, H. F.; Dawe, L. N.; Georghiou P. E. *New J. Chem.* **2012**, *36*, 2451.
9. Banerjee, D.; Zhang, Z.; Plonka, A. M.; Li, J.; Parise, J. B. *Cryst. Growth Des.* **2012**, *12*, 2162.
10. Zhang, X.; Huang, Y.-Y.; Zhang, M.-J.; Zhang, J.; Yao, Y.-G. *Cryst. Growth Des.* **2012**, *12*, 3231.
11. Yeh, C.-T.; Lin, W.-C.; Lo, S.-H.; Kao, C.-C.; Lin, C.-H.; Yang, C.-C. *CrystEngComm* **2012**, *14*, 1219.
12. Begouin, J.-M.; Niggemann, M. *Chem. Eur. J.* **2013**, *19*, 8030.
13. Brinkmann, C.; Barrett, A. G. M.; Hill, M. S.; Procopiou, P. *J. Am. Chem. Soc.* **2012**, *134*, 2193.

14. Tsubogo, T.; Yamashita, Y.; Kobayashi, S. *Chem. Eur. J.* **2012**, *18*, 13624.

15. Kobayashi, S.; Yamashita, Y. *Acc. Chem. Res.* **2011**, *44*, 58.

16. Köler, M.; Langer, J.; Fischer, R.; Görls, H.; Westerhausen, M. *Chem. Eur. J.* **2013**, *19*, 10497.

17. Jochmann, Ph.; Dols, T. S.; Spanio, T. P.; Perrin, L.; Maron, L.; Okuda, J. *Angew. Chem. Int. Ed.* **2009**, *48*, 5715.

18. Jochmann, P.; Maslek, S.; Spanio, T. P.; Okuda, J. *Organometallics* **2011**, *30*, 1991.

19. Bryce, D. L. *Dalton Trans.* **2010**, *39*, 8593.

20. Laurencin, D.; Smith, M. E. *Prog. Nucl. Magn. Reson. Spectrosc.* **2013**, *68*, 1.

21. Moudrakovski, I. L. *Ann. Rep. NMR Spectrosc.* **2013**, *79*, 129.

22. Harris, R. K.; Becher, E. D.; Cabral de Menezes, S. M.; Goodfellow, R.; Branger, P. *Pure Appl. Chem.* **2001**, *73*, 1795.

23. Pyykkö, P. *Mol. Phys.* **2008**, *106*, 1965.

24. Reinholdt, M.; Croissant, J.; Di Carlo, L.; Granier, D.; Gaveau, P.; Bégu, S.; Devoisselle, J.-M.; Mutin, P. H.; Smith, M. E.; Bonhomme, C.; Gervais, C.; van der Lee, A.; Laurencin, D. *Inorg. Chem.* **2011**, *50*, 7802.

25. Sene, S.; Reinholdt, M.; Renaudin, G.; Berthomieu, D.; Zicovich-Wilson, C. M.; Gervais, C.; Gaveau, P.; Bonhomme, C.; Filinchuk, Y.; Smith, M. E.; Nedelec, J.-M.; Bégu, S.; Mutin, P. H.; Laurencin, D. *Chem. Eur. J.* **2013**, *19*, 880.

26. Sene, S.; Bouchevreau, B.; Martineau, C.; Gervais C.; Bonhomme, C.; Gaveau P.; Mauri, F.; Bégu, S.; Mutin, P. H.; Smith, M. E.; Laurencin, D. *CrystEngComm* **2013**, *15*, 8763.

27. Bowers, G. M.; Kirkpatrick, R. J. *Cryst. Growth Des.* **2011**, *11*, 5188.

28. Colas, H.; Bonhomme-Coury, L.; Giogo, C. C.; Tielens, F.; Babonneau, G.; Gervais, C.; Bazin D.; Laurencin D.; Smith, M. E.; Hanna, J. V.; Daudon, M.; Bonhomme, C. *CrystEngComm* **2013**, *15*, 8840.

29. Wong, A.; Howes, A. P.; Dupree, R.; Smith, M. E. *Chem. Phys. Lett.* **2006**, *427*, 201.

30. Laurencin, D.; Gervais, C.; Wong, A.; Coelho, C.; Mauri, F.; Massiot, D.; Smith, M. E.; Bonhomme, C. *J. Am. Chem. Soc.* **2009**, *131*, 13430.

31. Gervais, C. Laurencin, D.; Wong, A.; Pourpoint, F.; Labram J.; Woodward, B.; Howes, A. P.; Pike K. J.; Dupree, R.; Mauri, F.; Bonhomme, C.; Smith, M. E. *Chem. Phys. Lett.* **2008**, *464*, 42.

32. Laurencin, D.; Wong, A.; Dupree, R.; Smith, M. E. *Magn. Reson. Chem.* **2008**, *46*, 347.

33. Wong, A.; Laurencin, D.; Dupree, R.; Smith, M. E. *Solid State Nucl. Magn. Reson.* **2009**, *35*, 32.

34. Laurencin, D.; Wong, A.; Chrzanowski, W.; Knowles, J. C.; Qiu, D.; Pickup D. M.; Newport, R. J.; Gan, Z.; Duer, M. J.; Smith, M. E. *Phys. Chem. Chem. Phys.* **2010**, *12*, 1081.

35. Moudrakovski, I. L.; Alizadeh, R.; Beaudoin, J. J. *Phys. Chem. Chem. Phys.* **2010**, *12*, 6961.

36. Bonhomme, C.; Gervais, C.; Folliet, N.; Pourpoint, F.; Diogo, C. C.; Lao, J.; Jallot, E.; Lacroix, J.; Nedelec, J.-M.; Iuga, D.; Hanna, J. V.; Smith, M. E.; Xiang, Y.; Du, J.; Laurencin, D. *J. Am. Chem. Soc.* **2012**, *134*, 12611.

37. Dupree, R.; Howes, A. P.; Kohn, S. C. *Chem. Phys. Lett.* **1997**, *276*, 399.

38. Wong, A.; Laurencin, D.; Wu, G.; Dupree, R.; Smith, M. E. *J. Phys. Chem. A* **2008**, *112*, 9807.

39. Fox, S.; Büsching, I.; Barklage, W.; Strasdeit, H. *Inorg. Chem.* **2007**, *46*, 818.

40. Kim, E. E.; Sicignano, A.; Eriks, K. *J. Am. Chem. Soc.* **1985**, *107*, 6042.

41. Schmidbaur, H.; Bach, I.; Wilkinson, D. L.; Müller, G. *Chem. Ber.* **1989**, *122*, 1439.

42. Wu, G.; Wong, A.; Wang, S. *Can. J. Chem.* **2003**, *81*, 275.

43. Pallister, P. J.; Moudrakovski, I. L.; Ripmeester, J. A. *Phys. Chem. Chem. Phys.* **2009**, *11*, 11487.

44. Arlin, J.-B.; Florence, A. J.; Johnston, A.; Kennedy, A. R.; Miller, G. J.; Patterson, K. *Cryst. Growth Des.* **2011**, *11*, 1318.

45. Cole, L. B.; Holt, E. M. *Inorg. Chim. Acta* **1989**, *160*, 195.

46. Barnett, B. L.; Uchtman, V. A. *Inorg. Chem.* **1979**, *18*, 2674.

47. Massiot, D.; Farnan, I.; Gautier, N.; Trumeau, D.; Trokiner, A.; Coutures, J. P. *Solid State Nucl. Magn. Reson. Spectrosc.* **1995**, *4*, 241.

48. Eichele, K.; Wasylishen, R. E. WSOLIDS NMR Simulation Software Version 1.17.30, Universität Tübingen, Tübingen, Germany, **2001**.

49. Massiot, D.; Fayon, F.; Capron, M.; King, I.; Le Calvé, S.; Alonso, B.; Durand, J.-O.; Bujoli, B.; Gan, Z.; Hoatson, G. *Magn. Reson. Chem.* **2002**, *40*, 70.

50. Debuyst, R.; Dejehet, F.; Dekandelaer, M.-C.; Declercq J.-P.; Germain, G.; van Meerssche, M. *J. Chim. Phys. Phys.-Chim. Biol.* **1979**, *76*, 1117.

51. Karipides, A.; McKinney, C.; Peiffer, K. *Acta Crystallogr., Sect. C: Cryst. Struct. Commun.* **1988**, *44*, 46.

52. Senkovska, I.; Thewalt, U. *Acta Crystallogr., Sect. C: Cryst. Struct. Commun.* **2005**, *61*, m448.

53. Wieczorek, M. W.; Blaszczyk, J.; Krol, B. W. *Acta Crystallogr., Sect. C* **1996**, *52*, 1193.

54. Deganello, S.; Kampf, A. R.; Moore, P. B. *Am. Mineral.* **1981**, *66*, 859.

55. Widdifield, C. M.; Bryce, D. L. *Can. J. Chem.* **2011**, *89*, 754.

56. Bryce, D. L.; Bultz, E. B.; Aebi, D. *J. Am. Chem. Soc.* **2008**, *130*, 9282.

57. Deng, Z.-P.; Kang, W.; Zhu, Z.-B.; Huo, L.-H.; Zhao, H.; Gao, S. *Dalton Trans.* **2012**, *41*, 8354.

58. Plonka, A. M.; Banerjee, D.; Parise, J. B. *Cryst. Growth Des.* **2012**, *12*, 2460–2467.

59. Huang, Y.-C.; Mou, Y.; Tsai, T. W.-T.; Wu, Y.-J.; Lee, H.-K.; Huang, S.-J.; Chan, J. C. C. *J. Phys. Chem. B* **2012**, *116*, 14295.

60. Sahoo, B. K. *Phys. Rev. A* **2009**, *80*, 012515.

61. Bowers, G. M.; Lipton, A. S.; Mueller, K. T. *Solid State Nucl. Magn. Reson*. **2006**, *29*, 95.

62. Bowers, G. M.; Ravella, R.; Komarneni, S.; Mueller, K. T. *J. Phys. Chem. B* **2006**, *110*, 7159.

63. Briggman, B.; Oskarson, Å. *Acta Crystallogr., Sect. B: Struct. Sci.* **1977**, *33*, 1900.

6 A ^{43}Ca SSNMR Perspective on the Multiple Structures of the Vaterite Polymorph of $CaCO_3$

One of the highlights in Chapter 5 was the improved correlation between the GIPAW DFT calculated and experimental $|C_Q(^{43}Ca)|$ values when the newly reported quadrupole moment for ^{43}Ca is used ($Q(^{43}Ca) = -44.4$ mbarn). In this Chapter, that correlation is used as a calibration curve in order to compare GIPAW DFT calculations of the multiple proposed structures of the vaterite polymorph of $CaCO_3$ to the experimental ^{43}Ca SSNMR NMR spectra of the sample.

6.1 Introduction

The crystalline phases of calcium carbonate ($CaCO_3$) are important biomaterials and minerals which have been identified in various living organisms and in the Earth's crust.[1,2,3] Much recent research has focused on amorphous forms of $CaCO_3$ and their transformation to one or many of the three polymorphs of this material: calcite, aragonite, and vaterite.[4,5,6,7,8] Despite these studies, the crystal structure of the vaterite polymorph still remains puzzling in part due to challenges in growing suitably large single crystals for accurate diffraction experiments. It is of great importance to fully characterize vaterite to better study the various

crystallization mechanisms of amorphous $CaCO_3$ as well as measure its role in biological systems. Recently, Pokroy and co-workers[9] characterized vaterite as having at mixture of least two interspersed structures. The major structure is proposed to exhibit hexagonal symmetry consistent with the original single crystal X-ray structure reported by Kahmi,[10,11] whereas a minor structure with unknown structural symmetry is suggested to also be present. In addition, many research groups have proposed various alternate structural models for vaterite via a range of characterization methods including PXRD,[12] Raman spectroscopy,[13] and *ab initio* calculations.[14] Shown in Figure 6.1 is a chart of the proposed vaterite structures available in the literature. They are organized in such a way so as to identify the parent vaterite structures along with some newly proposed models from Demichelis *et al*. by DFT computations.[15,16] Given the great interest in this field of research and the many hypothesized structures, we submit that ^{43}Ca NMR experiments should provide unique information for the determination of the crystal structure of vaterite.

It is well understood that, even with the very low natural abundance of ^{43}Ca (see Table 1.1 for nuclear properties), calcium NMR observables such as the C_Q and the δ_{iso} are very sensitive to subtle differences about the Ca^{2+} centres in crystal structures.[17,18,19] It was recently shown By the Bryce group using natural abundance ^{43}Ca SSNMR experiments that it was possible to distinguish between three polymorphs of $CaCO_3$ via ^{43}Ca SSNMR at multiple magnetic field strengths under MAS conditions.[20] The work presented in Chapter 5[21] as well as that of other groups,[22,23,24] show that GIPAW DFT calculations accurately reproduce experimental $|C_Q(^{43}Ca)|$ values, especially when using the recently updated quadrupole moment for ^{43}Ca of –44.4 mbarn.[21,25]

In this Chapter, NMR crystallography will be used in order to evaluate the validity of each of the vaterite structures in Figure 6.1 as possible models in representing this $CaCO_3$ polymorph. NMR crystallography is a growing field wherein SSNMR observables alongside DFT *ab initio* computations, molecular mechanics, crystal structure prediction, or powder diffraction experiments are used in combination to elucidate the crystal structure of a given sample.[26,27,28,29,30,31,32] Its application in SSNMR has begun to find widespread use specifically for polycrystalline samples that do not readily form single crystals suitable for X-ray analysis.[33,34,35] Firstly, we will employ the established correlation curve for $|C_Q(^{43}Ca)|$, from Chapter 5,[21] in order to appropriately scale the GIPAW DFT calculated quadrupolar parameters obtained from calculations performed on all the proposed structures in Figure 6.1. Secondly, these values are used to analytically predict the ^{43}Ca NMR spectra corresponding to each structural model, which are subsequently compared with newly acquired ^{43}Ca SSNMR data on ^{43}Ca isotopically-enriched vaterite. We note here that many structural models for vaterite reported to date, particularly those predicted by DFT, contain multiple crystallographically unique Ca sites. We employ a range of techniques including ^{43}Ca MAS, DOR and MQMAS NMR experiments at magnetic field strengths of 9.4 and 21.1 T in attempts to resolve various possible Ca sites. Finally, we assess the differences in the simulated ^{43}Ca NMR spectra with respect to experiment and attempt to identify the structure that is most consistent with all of the available ^{43}Ca SSNMR data and powder XRD.

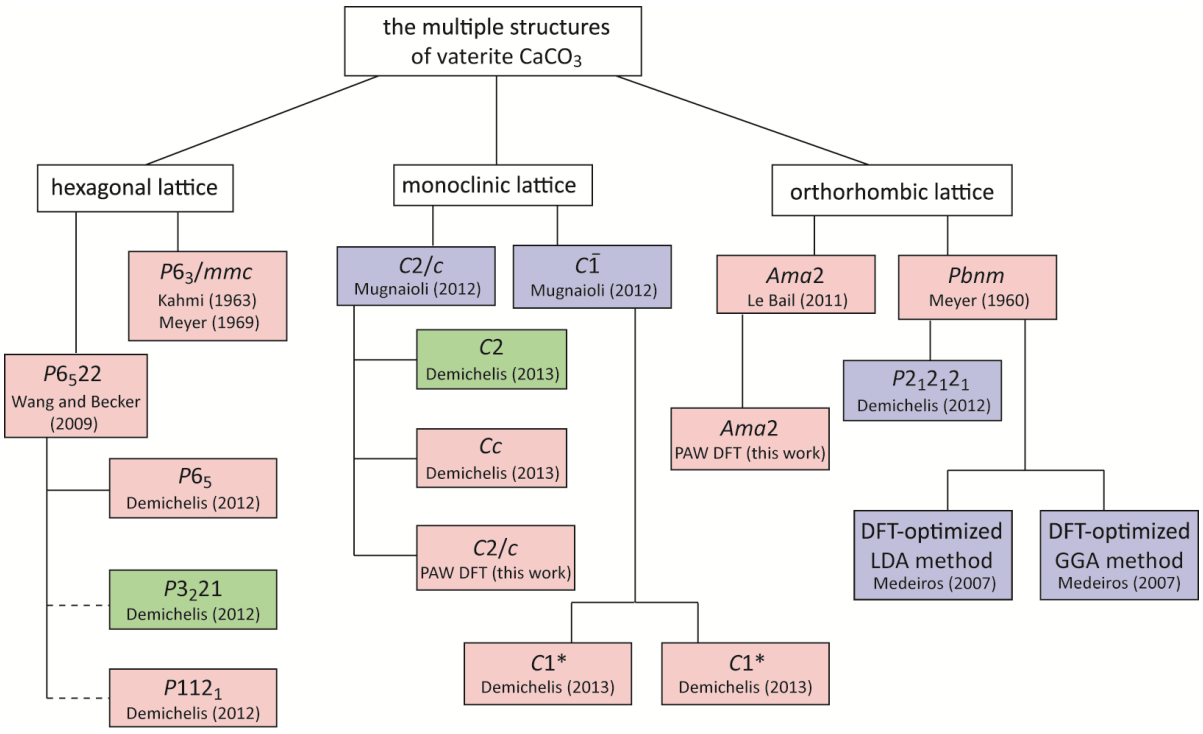

Figure 6.1: Chart summarizing the multiple proposed structures for the vaterite polymorph of $CaCO_3$. Models are based on hexagonal, monoclinic, or orthorhombic lattices. We indicate as well that many DFT structures are optimized from diffraction structures. Note that the $P3_221$ and $P112_1$ DFT structures, while not hexagonal, were optimized from a parent hexagonal structure. An asterisk (*) denotes that two different optimized structures were proposed with the same $C1$ space group. These structures are referred to as $C1$_1 and $C1$_2 in the main text. Structures highlighted in blue are eliminated by comparing simulations of PXRD diffractograms to experiment. Rose colored structures are eliminated based on disagreement with experimental ^{43}Ca SSNMR experiments reported herein. Vaterite models in best agreement with both ^{43}Ca SSNMR and PXRD data are in green

6.2 Experimental Details

6.2.1 Preparation of a ^{43}Ca Isotopically-Enriched Sample of Vaterite

The vaterite polymorph of $CaCO_3$ was synthesized according to a previously reported literature procedure[36] wherein 6.11 g of glycine (Sigma-Aldrich) were dissolved in 100 mL of distilled water. 10 mL of a 0.5 M aqueous solution of Na_2CO_3 (Sigma-Aldrich) were added drop wise over 5 minutes and the resulting solution was stirred for 20 minutes. A $*CaCl_2$ solution was prepared by dissolving 0.17 g of ^{43}Ca isotopically enriched $*CaCl_2$ (see ref. 21 for more details) and 0.38 g of natural abundance $CaCl_2$ (Sigma-Aldrich) for a total of 0.55 g in 10 mL of distilled water. The resulting solution of $*CaCl_2$ was added drop wise over a 10 minute period to the Na_2CO_3/glycine mixture. After one hour of stirring, the vaterite $*CaCO_3$ precipitate was filtered and dried under vacuum (0.237 g, 47 % yield). We estimate the level of ^{43}Ca isotopic enrichment of the final product to be 5%.

6.2.2 Powder X-Ray Diffraction

PXRD experiments on the powdered ^{43}Ca isotopically-enriched vaterite sample were carried out on a Rigaku Ultima IV instrument with Cu Kα_1 radiation (λ = 1.54060 Å) and 2θ ranging between 10 and 70° at a rate of 0.5° per minute and an increment of 0.02°. Simulations of the powder patterns from the available crystal structures of vaterite were generated with the Mercury software (v. 3.1) available from the Cambridge Crystallographic Data Centre.

6.2.3 ^{43}Ca Solid-State NMR Experiments

In all cases at B_0 = 9.4 T (Bruker AVANCE III, $\nu(^{43}\text{Ca})$ = 26.929 MHz), pulse calibrations were initially performed on a 2 M solution of Na_2MoO_4 ($\nu(^{95}\text{Mo})$ = 26.076 MHz, i.e., a frequency close to that of ^{43}Ca). A ^{43}Ca MAS NMR (ν_{rot} = 5 kHz) experiment was performed using a Bruker 7 mm HX MAS probe and a single pulse experiment. The selective $\pi/2$ pulse length used was 6 μs and the ^{43}Ca chemical shifts were referenced to a 1.5 M aqueous solution of $CaCl_2$ at 0.0 ppm. A total of 94480 scans were acquired with a recycle delay of 2 s. For the ^{43}Ca DOR NMR experiment, a Bruker HP WB 73A DOR probe was used with 4.3 mm inner and 14 mm outer rotor diameters, respectively. The outer rotor spinning was set to 700 Hz while the inner rotor spinning (~3 kHz) could be monitored using an oscilloscope. A CT-selective 100 μs $\pi/2$ pulse was used along with a 15 s recycle delay and a total of 1200 scans. DFS (sweeping from 250 to 40 kHz over a period of 2 ms) was also employed to polarize the CT prior to the $\pi/2$ observe pulse.

Experiments at B_0 = 21.1 T (Bruker AVANCE II, $\nu(^{43}\text{Ca})$ = 60.579 MHz) used a Bruker 7 mm low-gamma single channel probe equipped with a Hall sensor. All chemical shifts were referenced to a 2 M aqueous solution of $CaCl_2$ at 0.0 ppm. For the ^{43}Ca MAS NMR single pulse experiment (ν_{rot} = 8 kHz), a 2 μs pulse was used along with a recycle delay of 5 s for a total of 3072 scans. A static experiment was also performed under the same conditions with a total of 15360 transients. The standard ^{43}Ca 3QMAS experiment was acquired using the 3-pulse z-filtered experiment[37]. The excitation, conversion, and detection pulse lengths of 7.0, 2.8, and 9.0 μs were optimized on the vaterite sample. A recycle delay of 3 s was used and a total of 456 scans were acquired for each of the 48 slices with a t_1

increment of 125 μs for a total experiment time of 18 hours. The States method was used to obtain purely absorptive 2D peak shapes.[38]

6.2.4 GIPAW DFT Calculations on the Proposed Vaterite Structures

All GIPAW DFT computations were performed using the CASTEP-NMR program (v. 4.4). Input files for the calculations were generated in Materials Studio (v. 3.2, Accelrys) by importing the available crystal structure files of the various models for vaterite. In most cases, a E_{cut} value of 610 eV and a "fine" setting for the *k*-point grids were used. On-the-fly generated ultrasoft pseudopotentials were used for all atoms. The PBE XC functional was employed under GGA for all calculations.[39] In the case of the $P6_3/mmc$ structure, disorder of the carbonate ions is present. There are two equivalent carbonate ions per unit cell and only two relative orientations are possible. Only the orientation which yields the closest value of $|C_Q(^{43}Ca)|$ to experiment is presented in this work. Geometry optimizations were performed on Mugnaioli's $C2/c$ and Le Bail's $Ama2$ structures. Within the Materials Studio program, both structures were assigned the $P1$ space group so that the geometry optimization would not be restricted by crystal symmetry. In Table A6.1 of Appendix A are tabulated the resulting Ca–O bond distances and angles. In other cases in the literature, as indicated in Figure 6.1, some vaterite models were originally proposed from DFT optimization. GIPAW DFT calculations performed on the $P112_1$ structure yielded unreasonable estimations for $|C_Q(^{43}Ca)|$ (values of up to 11.18 MHz) and for δ_{iso} (values ranging from 46.9 to 1449.9 ppm) and was thus excluded from further investigation as a possible structure for vaterite. The EFG and chemical shift tensor parameters were parsed from the output files using an updated version of EFGShield. The calculated $|C_Q(^{43}Ca)|$ values were scaled in order to compare to

the experimentally observed value by using a calibration curve discussed in Chapter 5 (i.e., $|C_Q(^{43}Ca,exp.)| = 1.067|C_Q(^{43}Ca,calc.)|$) which accounts both for systematic error in the calculations and for the recently revised quadrupole moment for ^{43}Ca of –44.4 mbarn. The RMSD for calculated $|C_Q(^{43}Ca)|$ vs experimental values using this equation is 0.2 MHz as assessed in Chapter 5 for a series of well-characterized crystalline compounds. The calculated ^{43}Ca δ_{iso} values were determined using the relationship given by Moudrakovski *et al.*[24] for GIPAW DFT calculated σ_{iso} values as a function of experimental δ_{iso} values (i.e., $\delta_{iso,exp.} = -0.8434\sigma_{iso,calc.} + 952.3$ ppm). Predicted δ_{iso} values of the compounds included in this calibration have a RMSD of 5.0 ppm.

6.3 Results

6.3.1 Powder X-Ray Experiments

Using a literature procedure[36] it was possible to synthesize vaterite $CaCO_3$ using ^{43}Ca isotopically-enriched $CaCl_2$ as a calcium source. The experimental PXRD pattern is shown in Figure 6.2 and is consistent with previously reported PXRD patterns from both synthetic and natural sources of vaterite.[40] A PXRD experiment performed 2 months after the original synthesis (see Figure 6.2) shows that vaterite seems to be stable over that period of time; it is certainly clear that there is no transformation to the more stable crystalline aragonite or calcite polymorphs. Simulated diffractograms generated from the crystallographic information files for many of the proposed structures (Figure 6.1) match the experimental diffractogram very closely. However, due to the presence of additional reflections in the

PXRD simulations, it is immediately possible to rule out certain orthorhombic structures: the GGA and LDA structures of Medeiros *et al*.[41] and the $P2_12_12_1$ structure of Demichelis *et al*.[15] (see Figure 6.2). Even after acquiring the 20 to 30 degrees region of the PXRD pattern for a longer period, the expected low intensity peaks for an orthorhombic lattice are not observed (see Figure 6.3). Both of the monoclinic $C2/c$ and $C\bar{1}$ structures of Mugnaioli *et al*.[42] determined from precession electron diffraction experiments can be eliminated as well on the basis of the simulated PXRD patterns shown in Figure 6.2. In the case of the $C\bar{1}$ structure, none of the diffraction peaks are superimposable with respect to experiment. These same monoclinic structures have already been somewhat dismissed by Demichelis *et al*.[16] as possible stable structures for vaterite as these were identified using DFT as transition state structures. As for the monoclinic $C2$ structure, there are indeed additional reflections in the simulation near 35 and 45 degrees; however, the peaks in the experimental PXRD powder pattern are broad and we are reluctant to unambiguously eliminate this structure solely on the basis of PXRD alone.

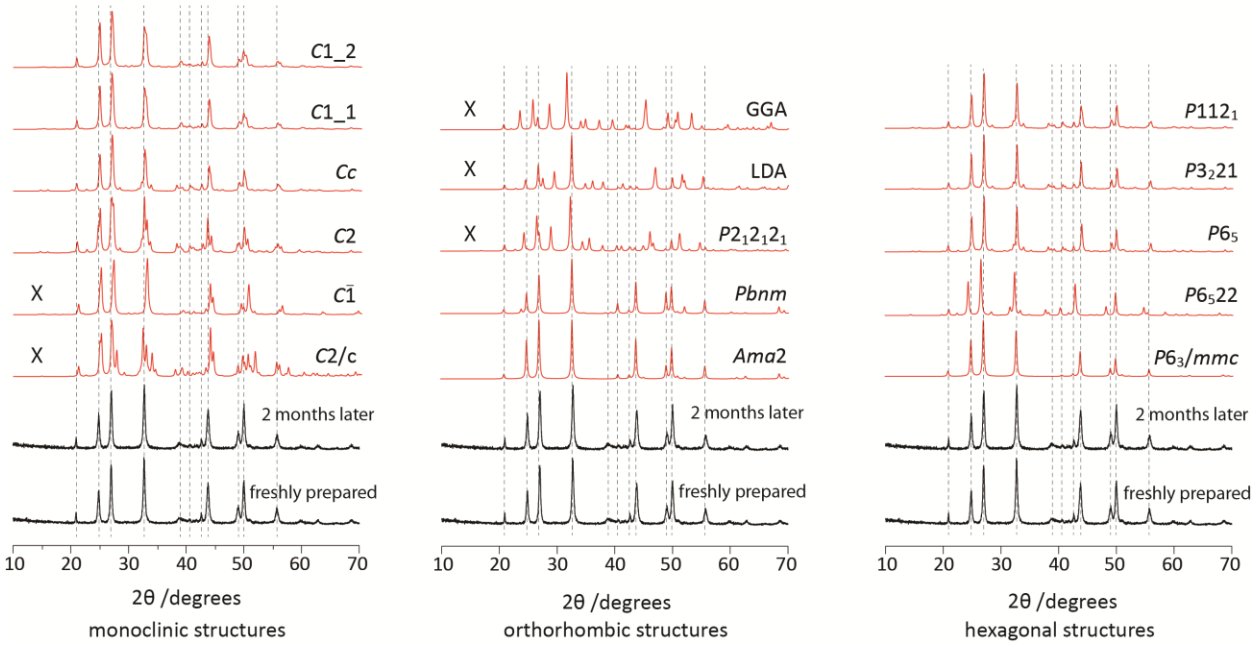

Figure 6.2: Powder X-ray diffractograms for a ^{43}Ca isotopically-enriched sample of vaterite (bottom traces). Over a period of over two months, the sample is stable as both experimental powder patterns in black are identical and no peaks are observed that would indicate the presence of calcite or aragonite. Also shown are powder X-ray diffraction simulations from all crystal structure models for vaterite. Simulations in red were generated using the Mercury software. Dashed lines are used as guides to the eye. Simulations showing an "X" represent candidate structures that have been eliminated based on their disagreement with the experimental PXRD pattern.

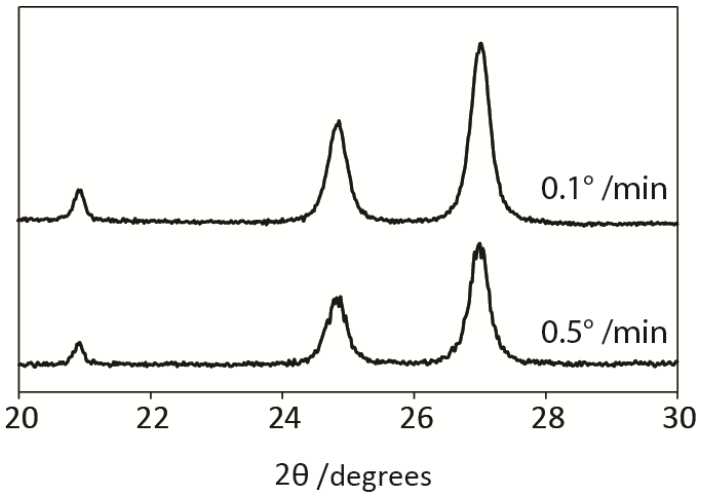

Figure 6.3: A comparison between the original PXRD data acquired with a collection rate of 0.5° per minute versus a diffractogram acquired at 0.1° per minute. If the structure of vaterite was of one of the orthorhombic symmetries, low intensity peaks should be present near 22 and 28 degrees. See the Experimental Details section for experimental details on PXRD experiments.

The simulations of the PXRD patterns for the hexagonal structures may also be found in Figure 6.2. It is clear that it is not possible to distinguish between the proposed hexagonal structures by PXRD alone. In this work, we show that ^{43}Ca SSNMR, specifically under DOR conditions, allows for the differentiation between the proposed hexagonal structures (*vide infra*). Although it is possible to remove some structural models by PXRD, many monoclinic and orthorhombic candidate structures still remain plausible candidates. In general, we will present ^{43}Ca SSNMR simulations of calculated NMR parameters on all of the structures considered in Figure 6.1 regardless of whether or not they were eliminated by disagreement with PXRD in attempts to find the most plausible structural model for vaterite that is in best agreement simultaneously with both characterization methods.

6.3.2 ^{43}Ca Solid-State NMR Experiments

In order to differentiate between the remaining structures in Figure 6.1, we have performed new ^{43}Ca SSNMR experiments on the ^{43}Ca-enriched vaterite sample. Reliable chemical shift and quadrupolar coupling constant scales for ^{43}Ca will allow for a meaningful comparison between experimental and computed data. In Figure 6.4 are presented ^{43}Ca MAS NMR spectra acquired at 9.4 and 21.1 T. With experiments at both magnetic fields, it was possible to simulate both MAS spectra with one unique calcium site; C_Q and η_Q values are 3.2(0.2) MHz and 0.4(0.1) respectively, and an updated δ_{iso} value of 15(2) ppm is observed. The quadrupolar parameters, while more accurate and precise here, are within experimental error of the previous ^{43}Ca NMR study on natural abundance vaterite.[20] The chemical shift, however, differs significantly from previous experiments[20] since it is now commonly understood that the $CaCl_2$(aq) ^{43}Ca chemical shift depends highly on its concentration.[18,19,43] In addition, we also show a ^{43}Ca NMR experiment performed under stationary conditions in Figure 6.4, from which it is possible to extract the chemical shift tensor parameters of Ω and κ of 60(10) ppm and -0.1(0.1) respectively. Once again, these values for the chemical shift tensor parameters are within the experimental errors of the previous investigation by Bryce *et al.*[20] (see Table 6.1). DOR and MQMAS experiments were also carried out at 9.4 and 21.1 T, respectively, in attempts to observe multiple crystallographically unique Ca sites, which would be consistent with the notion of multiple $CaCO_3$ phases within the vaterite polymorph as suggested by the experiments and structures reported by Kabalah-Amitai,[9] Wang,[14] Demichelis,[15,16] and Mugnaioli.[42] The DOR spectrum in Figure 6.5a reveals a unique and relatively broad resonance centered at –22(1) ppm. The full width at half maximum (FWHM) of 280 Hz for vaterite is large in comparison to the values observed for a range of

highly crystalline compounds such as anhydrous *$Ca(NO_3)_2$ (FWHM = 12 Hz; manuscript in preparation). Note that the position of the peak in the DOR spectrum, δ_{DOR}, is equal to $\delta_{iso} - \delta_{QIS}$, where δ_{QIS} is the quadrupole induced shift (for a spin 7/2 nucleus like ^{43}Ca, $\delta_{QIS} = (1/392)[C_Q^2(1 + \eta_Q^2/3)]/\nu_L^2$). As for the MQMAS experiment in Figure 6.5b, it is clear that only one unique calcium site is present in the structure but with a slight distribution of both the chemical shifts and C_Q values, consistent with the broadened resonance in the ^{43}Ca DOR NMR spectrum. It is possible to select one-dimensional slices of the rows in the MQMAS spectrum to show that the FWHM ranges between 630 and 740 Hz, a variation of just over 100 Hz, which is within the FWHM value observed in the ^{43}Ca DOR spectrum. This observation further suggests the presence of a slight distribution of quadrupolar and chemical shift parameters. We note here that the ^{43}Ca DOR NMR spectrum was acquired in 5 h at 9.4 T, whereas the MQMAS spectrum required 18 hours of experiment time at 21.1 T. Therefore ^{43}Ca DOR NMR experiments hold much promise for future high-resolution ^{43}Ca SSNMR experiments.

Table 6.1: ^{43}Ca solid-state NMR parameters for vaterite as part of the current work. Error bars are in parentheses.

NMR parameter	vaterite $CaCO_3$ (current work)
$\lvert C_Q(^{43}Ca)\rvert$ / MHz	3.2(0.2)
η_Q	0.4(0.1)
δ_{iso} / ppm	15(2)
Ω / ppm	60(10)
κ	–0.1(0.1)
$\alpha/\beta/\gamma$/deg.	30(10)/0(5)/30(10)

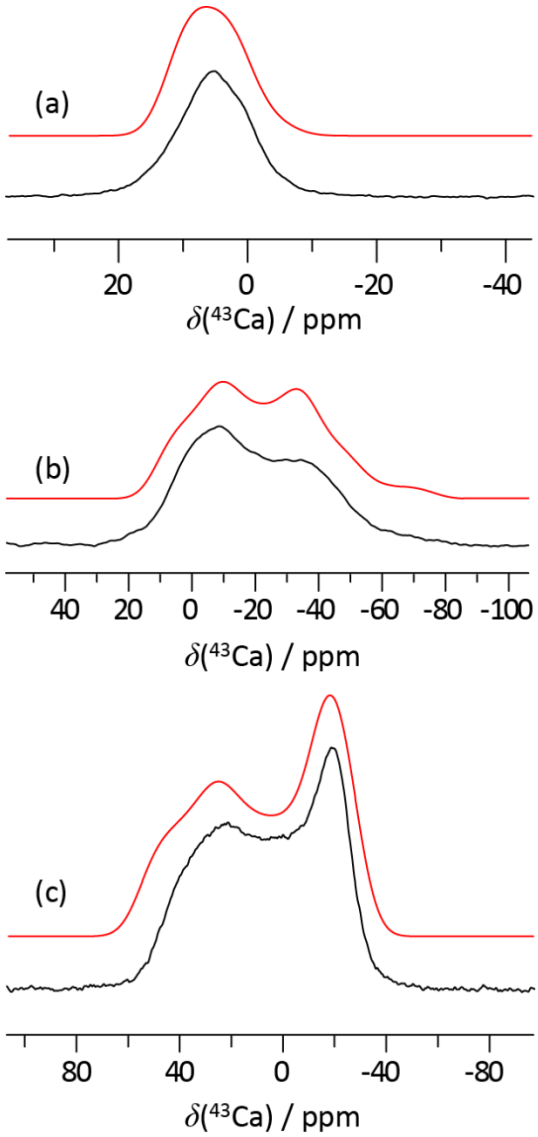

Figure 6.4: ^{43}Ca MAS NMR spectra acquired at 21.1 T (a) and at 9.4 T (b) with spinning frequencies of 8 and 5 kHz, respectively, using single pulse experiments. A ^{43}Ca NMR spectrum was also acquired under stationary conditions at 21.1 T (c) using a single pulse experiment. All WSolids analytical simulations are in red and experimental data are in black. Note that the simulations do not explicitly account for distributions in the NMR parameters, except in the form of apodization. 30, 50, and 50 Hz of apodization were applied for spectra presented in (a), (b), and (c), respectively.

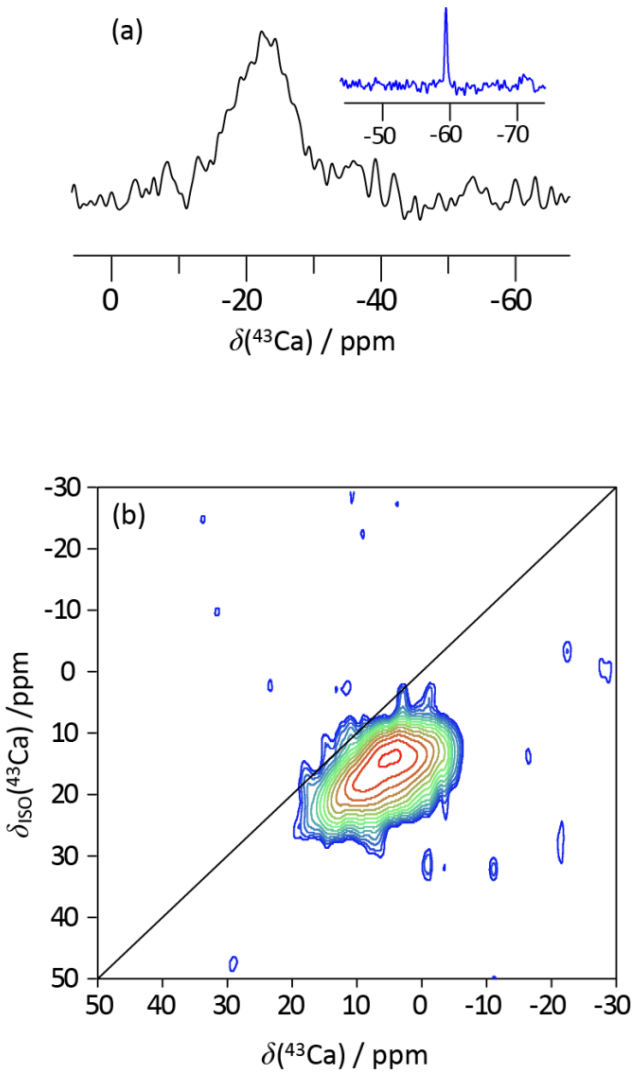

Figure 6.5: High-resolution ^{43}Ca solid-state NMR experiments performed on an isotopically-enriched vaterite sample. A DOR spectrum is shown in (a) and was acquired at 9.4 T using a single pulse experiment with DFS signal enhancement. For comparison of line widths, a ^{43}Ca DOR spectrum acquired for an isotopically-enriched sample of anhydrous *$Ca(NO_3)_2$ is shown as a blue inset (FWHM 12 Hz; preliminary data). 20 Hz of apodization was applied to the ^{43}Ca DOR spectrum. A ^{43}Ca MQMAS spectrum at 21.1 T is presented in (b). In both experiments it is not possible to resolve multiple Ca sites in vaterite. 100 Hz of apodization was applied in each dimension of the ^{43}Ca MQMAS spectrum.

6.3.3 The Monoclinic Models for Vaterite

All of the GIPAW DFT calculated NMR parameters pertinent to our discussion for the monoclinic structures can be found in Table 6.2. Although already eliminated on the basis of the PXRD data, calculations on the *C*2/*c* and $C\bar{1}$ structures reported by Mugnaioli *et al.*[42] have some large predicted $|C_Q(^{43}Ca)|$ values (i.e., 8.10 MHz for site 1 in the *C*2/*c* structure and 13.95 MHz for site 18 in the $C\bar{1}$ structure!), which provides further evidence for their dismissal as plausible vaterite structures. Such large values for $|C_Q|$ have never been observed experimentally for ^{43}Ca, with some of the largest being approximately 4 MHz.[18] We note that it was not possible to calculate chemical shift values for the $C\bar{1}$ structure due to its large unit cell volume of 2165 Å^3. Even low energy cut-off values failed to yield an appropriate level of energy convergence with our available infrastructure. The elimination of these two structures is consistent with our interpretation from the PXRD diffractograms (*vide supra*). Demichelis *et al.*[16] postulated that the *C*2/*c* structures and the $C\bar{1}$ structures are in fact transition state structures from vibrational energy calculations, which might account for our unreasonably large calculated values for $|C_Q(^{43}Ca)|$. The same authors proposed four more stable monoclinic structures after some rotations of the carbonate anions in the lattice (i.e., the *C*2, *Cc*, and two slightly different *C*1 structures). In addition to these structures, we have performed a geometry optimization of Mugnaioli's *C*2/*c* structure within CASTEP.

The analytical simulations of the ^{43}Ca DOR NMR spectra at 9.4 T as well as the MAS NMR line shapes at 9.4 and 21.1 T for the proposed monoclinic structures are presented in Figure 6.6 and superimposed over the experimental spectra discussed above. From the DOR NMR spectrum alone it is possible eliminate both *C*1 structures given the large number of

distinct resonances observed. As for the *Cc* and geometry optimized *C*2/*c* structures, both have δ_{DOR} values at nearly –40 ppm which is inconsistent with the experimental δ_{DOR} of –22(1) ppm. For Ca site 2 in the PAW DFT-optimized *C*2/*c* structure, for example, a δ_{iso} value of 35.5 ppm is calculated, a 20.5 ppm difference from experiment. Calculated chemical shift values are typically within 5 ppm from experiment (RMSD) using the GIPAW DFT method (*vide supra*). We observe that the *C*2 structure produces the best agreement with the DOR NMR spectrum at 9.4 T. As for the MAS spectrum at 9.4 T, the simulation of the *C*2 structure is also in good agreement with experiment whereas that of the MAS NMR spectrum at 21.1 T has additional low-intensity features at higher frequencies. These features arise from site 3 in the simulation with near axial symmetry in the calculated ^{43}Ca EFG tensor. Therefore, from the simulations of the MAS and DOR spectra, it would appear that the best model as far as monoclinic structures are concerned must be the *C*2 model, which is a DFT-optimized structure derived from the *C*2/*c* structure experimentally established by Mugnaioli *et al*. (see Figure 6.1).

Table 6.2: Calculated ^{43}Ca NMR Parameters for Monoclinic Vaterite Structures.

site	$\lvert C_Q(^{43}Ca)\rvert$ /MHz	calibrated $\lvert C_Q(^{43}Ca)\rvert$ /MHz	$\lvert \Delta C_Q\rvert$ /MHz	η_Q	δ_{iso} /ppm	$\lvert \Delta\delta_{iso}\rvert$ /ppm	δ_{DOR} /ppm
*C*2/*c*							
Ca1	7.59	8.10	4.90	0.42	41.7	26.7	-202.8
Ca2	7.59	8.10	4.90	0.42	41.7	26.7	-202.8
Ca3	4.15	4.43	1.23	0.77	29.8	14.8	-52.6
*C*2/*c* geometry optimization (PAW DFT)							
Ca1	3.67	3.92	0.72	0.55	21.2	6.2	-38.2
Ca2	2.69	2.87	0.33	0.80	35.5	20.5	0.3
Ca3	3.67	3.92	0.72	0.55	21.2	6.2	-38.2
$C\bar{1}$							
Ca1	3.47	3.70	0.50	0.48	-	-	-
Ca2	3.47	3.70	0.50	0.48	-	-	-
Ca3	3.52	3.75	0.55	0.80	-	-	-
Ca4	3.52	3.75	0.55	0.80	-	-	-
Ca5	4.71	5.03	1.83	0.41	-	-	-
Ca6	4.71	5.03	1.83	0.41	-	-	-
Ca7	4.87	5.20	2.00	0.83	-	-	-
Ca8	4.87	5.20	2.00	0.83	-	-	-
Ca9	5.07	5.41	2.21	0.28	-	-	-
Ca10	5.07	5.41	2.21	0.23	-	-	-
Ca11	5.30	5.66	2.46	0.35	-	-	-
Ca12	5.63	6.01	2.81	0.08	-	-	-
Ca13	5.63	6.01	2.81	0.08	-	-	-
Ca14	6.27	6.69	3.49	0.32	-	-	-
Ca15	6.27	6.69	3.49	0.32	-	-	-
Ca16	7.87	8.40	5.20	0.24	-	-	-
Ca17	7.87	8.40	5.20	0.24	-	-	-
Ca18	13.08	13.95	10.75	0.14	-	-	-
*C*2							
Ca1	2.85	3.04	0.16	0.24	13.0	2.0	-20.2
Ca2	2.82	3.00	0.20	0.40	8.9	6.1	-24.6
Ca3	3.53	3.77	0.57	0.08	29.0	14.0	-21.1
Cc							
Ca1	3.39	3.62	0.42	0.49	15.3	0.3	-34.4
Ca2	3.31	3.54	0.34	0.24	2.3	12.7	-42.5
Ca3	3.18	3.40	0.20	0.45	30.7	15.7	-12.6

site	$\lvert C_Q(^{43}Ca)\rvert$ /MHz	calibrated $\lvert C_Q(^{43}Ca)\rvert$ /MHz	$\lvert\Delta C_Q\rvert$ /MHz	η_Q	δ_{iso} /ppm	$\lvert\Delta\delta_{iso}\rvert$ /ppm	δ_{DOR} /ppm
*C*1_1							
Ca1	3.60	3.84	0.64	0.28	17.9	2.9	-35.4
Ca2	3.89	4.15	0.95	0.22	24.6	9.6	-37.0
Ca3	3.59	3.83	0.63	0.25	21.0	6.0	-31.7
Ca4	2.92	3.11	0.09	0.50	21.1	6.1	-15.8
Ca5	3.41	3.64	0.44	0.28	18.1	3.1	-29.6
Ca6	3.37	3.60	0.40	0.39	4.7	10.3	-43.2
Ca7	2.70	2.88	0.32	0.23	13.2	1.8	-16.5
Ca8	3.53	3.76	0.56	0.66	14.0	1.0	-43.0
Ca9	2.64	2.82	0.38	0.24	12.9	2.1	-15.6
Ca10	3.43	3.66	0.46	0.51	15.6	0.6	-35.6
Ca11	3.72	3.97	0.77	0.21	28.6	13.6	-27.7
Ca12	3.13	3.34	0.14	0.73	12.9	2.1	-33.4
Ca13	3.13	3.34	0.14	0.40	11.3	3.7	-30.1
Ca14	2.94	3.14	0.06	0.74	14.8	0.2	-26.3
Ca15	3.89	4.15	0.95	0.25	22.7	7.7	-39.1
Ca16	3.44	3.67	0.47	0.27	18.4	3.4	-30.1
Ca17	2.72	2.90	0.30	0.34	11.5	3.5	-19.2
Ca18	2.88	3.07	0.13	0.29	13.1	1.9	-21.0
*C*1_2							
Ca1	3.62	3.86	0.66	0.28	18.2	3.2	-35.7
Ca2	3.78	4.03	0.83	0.24	22.2	7.2	-36.0
Ca3	3.25	3.47	0.27	0.30	18.1	3.1	-25.5
Ca4	2.99	3.19	0.01	0.32	26.2	11.2	-10.8
Ca5	3.87	4.13	0.93	0.06	18.6	3.6	-41.3
Ca6	3.09	3.29	0.09	0.11	3.2	11.8	-35.1
Ca7	3.42	3.65	0.45	0.45	15.3	0.3	-34.7
Ca8	2.60	2.77	0.43	0.56	12.1	2.9	-17.7
Ca9	2.62	2.79	0.41	0.44	13.0	2.0	-16.1
Ca10	3.52	3.75	0.55	0.35	15.1	0.1	-36.5
Ca11	3.43	3.66	0.46	0.52	15.8	0.8	-35.4
Ca12	3.94	4.20	1.00	0.29	25.8	10.8	-38.0
Ca13	2.95	3.15	0.05	0.85	13.6	1.4	-29.6
Ca14	3.07	3.28	0.08	0.43	14.0	1.0	-26.0
Ca15	3.49	3.72	0.52	0.29	18.3	3.3	-31.8
Ca16	3.79	4.05	0.85	0.27	21.2	6.2	-37.7
Ca17	2.94	3.13	0.07	0.43	12.0	3.0	-24.7
Ca18	3.19	3.40	0.20	0.37	13.5	1.5	-29.0

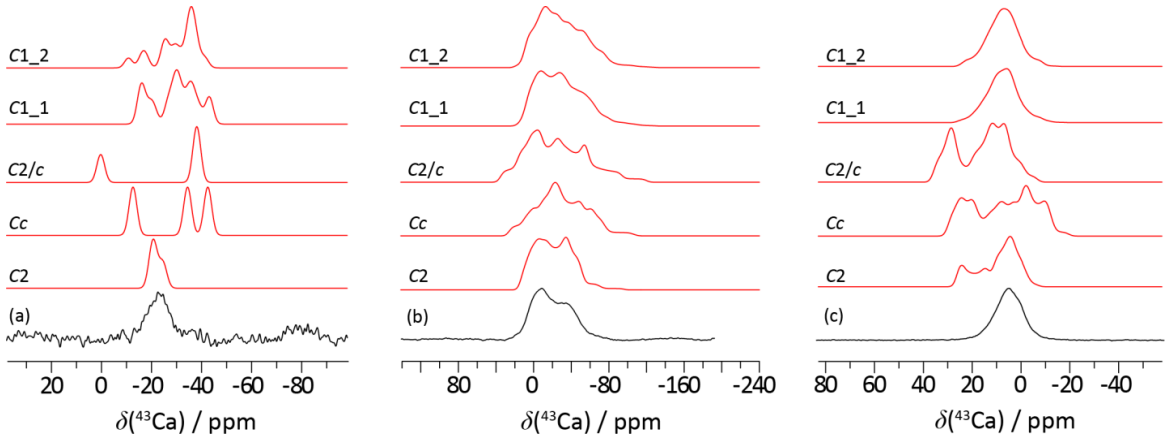

Figure 6.6: ^{43}Ca NMR line shape simulations for the monoclinic models for vaterite under MAS conditions at 9.4 (b) and 21.1 T (c) and DOR conditions at 9.4 T (a). All experimental spectra in black were acquired for the ^{43}Ca isotopically-enriched vaterite sample. All simulations are in red and were generated in WSolids from the calculated NMR parameters reported in Table 6.2. The *C*2/*c* simulation is based on the geometry-optimized structure determined in this work.

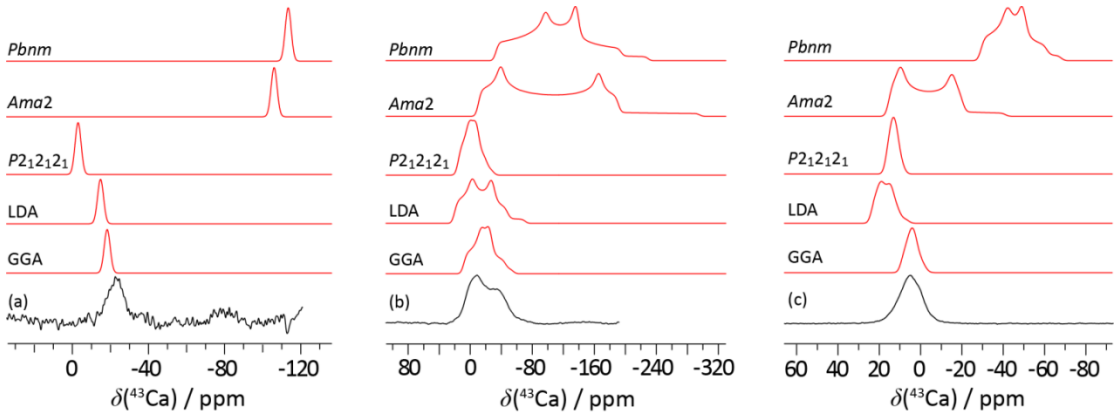

Figure 6.7: ^{43}Ca NMR line shape simulations for the orthorhombic models for vaterite under MAS at 9.4 (b) and 21.1 T (c) and DOR conditions at 9.4 T (a). All experimental spectra in black were acquired for the ^{43}Ca isotopically enriched vaterite sample. All simulations are in

red and were generated in WSolids from the calculated NMR parameters reported in Table 6.3.

6.3.4 The Orthorhombic Models for Vaterite

The GIPAW DFT-calculated ^{43}Ca NMR parameters for the orthorhombic structures are reported in Table 6.3 and their respective analytical simulations for the 9.4 T MAS and DOR NMR spectra and 21.1 T MAS NMR spectra are displayed in Figure 6.7. It is immediately possible to eliminate on the basis of their δ_{DOR} values the original *Pbnm* structure from Meyer in 1959,[44] the recently proposed *Ama*2 model from Le Bail *et al.*,[12] as well as its geometry optimized structure (PAW DFT) as possible candidates for the structure of vaterite due to their unreasonable δ_{DOR} values of −113.4, −128.1, and −106.0 ppm respectively. These large values are again manifested in rather broad MAS line shapes predicted at 9.4 and 21.1 T.

Table 6.3: Calculated ^{43}Ca NMR Parameters for Orthorhombic Vaterite Structures.

site	$\lvert C_Q(^{43}Ca)\rvert$ /MHz	calibrated $\lvert C_Q(^{43}Ca)\rvert$ /MHz	$\lvert \Delta C_Q\rvert$ /MHz	η_Q	δ_{iso} /ppm	$\lvert \Delta\delta_{iso}\rvert$ /ppm	δ_{DOR} /ppm
*Ama*2							
Ca1	6.02	6.43	3.23	0.19	19.0	4.0	-128.1
Ama2 geometry optimization (CASTEP)							
Ca1	5.62	6.00	2.80	0.16	21.7	6.7	-106.0
Pbnm							
Ca1	4.36	4.65	1.45	0.59	-28.4	43.4	-113.4
Pbnm (LDA geometry optimization)							
Ca1	3.05	3.25	0.05	0.43	24.6	9.6	-14.8
Pbnm (GGA geometry optimization)							
Ca1	2.47	2.63	0.57	0.65	9.5	5.5	-18.3
$P2_12_12_1$							
Ca1	2.11	2.25	0.95	0.57	16.8	1.8	-3.0

Since Meyer's publication on the *Pbnm* structure,[44] Medeiros *et al*.[41] have proposed the LDA and GGA structures from PAW DFT geometry optimizations and Demichelis *et al*.[15] proposed the $P2_12_12_1$ space group again from calculations. Although the $P2_12_12_1$ structure has a δ_{DOR} value of -3 ppm, calculations on the GGA and LDA structures yield δ_{DOR} values that are relatively close to experiment (within 4 and 7 ppm respectively from experiment, see Table 6.3). In the case of the GGA structure, an underestimation of the $|C_Q(^{43}Ca)|$ value is observed (2.63 MHz). We also caution however, that additional reflections are observed in the simulated PXRD diffractograms of these structures (see Figure 6.2). At this point, we cannot conclusively at this point assign a candidate DFT-derived orthorhombic structure stemming from Meyer's original *Pbnm* structure that adequately represents vaterite $CaCO_3$.

6.3.5 The Hexagonal Models for Vaterite

Currently, a hexagonal lattice is esteemed by different authors to best represent the crystal structure of vaterite.[9,16,45] This point is supported by a simple inspection of the simulated PXRD diffractograms in Figure 6.2 which are most consistent with the experimental pattern. Our PXRD experiments cannot differentiate between the various hexagonal structures summarized in Figure 6.1 due to the broad nature of the peaks in the experimental diffractograms. (Note that the $P3_221$ and $P112_1$ DFT structures, while not hexagonal, were optimized from a parent hexagonal structure and we include the discussion of these structures here.) In Figure 6.8 are shown the analytical simulations from the GIPAW DFT calculations of the ^{43}Ca DOR and MAS NMR spectra at 9.4 T and the ^{43}Ca

MAS spectrum at 21.1 T. The NMR parameters are tabulated in Table 6.4. Demichelis *et al.*[16] concluded that the $P6_522$ structure, reported originally by Wang and Becker,[14] is a transition state structure. Upon rotations of the carbonate anions, Demichelis *et al.*[16] proposed three other structures: $P6_5$, $P3_221$ (or its stereoisomer structure $P3_121$), and $P112_1$. Both the $P6_5$ and the $P3_221$ structures yield reasonable possibilities for the structure of vaterite when observing only the ^{43}Ca MAS spectra at both 9.4 and 21.1 T. However, all three structures do not reproduce a single broadened resonance observed in the experimental ^{43}Ca DOR spectrum at –22 ppm. In fact, some calcium sites in these structures have calculated δ_{DOR} values down to –49.0, which is notably far from the experimental value. Among these structures, the $P3_221$ (or $P3_121$) structures are in best agreement with the ^{43}Ca SSNMR experiments given that an overestimation of the $|C_Q(^{43}Ca)|$ values by only 0.4 MHz is observed in some Ca sites in these structures (recall, the RMSD for calculated vs. experimental $|C_Q(^{43}Ca)|$ values for an independent series of well-characterized crystalline compounds is 0.2 MHz). Furthermore, the computed δ_{iso} values of between 13.0 and 19.1 ppm for the three crystallographically distinct calcium sites in each of the $P3_221$ and $P3_121$ structures are not unreasonable estimations given that GIPAW DFT calculated values for this parameter are accurate with a RMSD of 5.0 ppm for ^{43}Ca.[24] We emphasize here that ^{43}Ca EFG tensor and chemical shift calculations, especially in the context of the ^{43}Ca DOR NMR simulations, offer a unique test for the validity of a proposed crystal structure for vaterite and calcium-containing materials in general.

\

Table 6.4: Calculated ^{43}Ca NMR Parameters for Hexagonal Vaterite Structures.

site	$\lvert C_Q(^{43}Ca)\rvert$ /MHz	calibrated $\lvert C_Q(^{43}Ca)\rvert$ /MHz	$\lvert \Delta C_Q\rvert$ /MHz	η_Q	δ_{iso} /ppm	$\lvert \Delta\delta_{iso}\rvert$ /ppm	δ_{DOR} /ppm
$P6_3/mmc$							
Ca1	4.73	5.05	1.85	0.56	11.7	3.3	-87.4
$P6_522$							
Ca1	2.58	2.75	0.45	0.78	10.0	5.0	-22.1
Ca2	3.33	3.56	0.36	0.34	17.1	2.1	-29.1
Ca3	3.07	3.27	0.07	0.38	-1.4	16.4	-40.9
$P6_5$							
Ca1	2.96	3.16	0.04	0.70	15.5	0.5	-25.3
Ca2	3.98	4.25	1.05	0.38	17.6	2.6	-49.0
Ca3	3.43	3.66	0.46	0.30	15.3	0.3	-33.4
$P3_221$							
Ca1	3.48	3.71	0.51	0.49	18.2	3.2	-34.1
Ca2	3.50	3.74	0.54	0.39	18.9	3.9	-32.7
Ca3	2.87	3.07	0.13	0.27	13.1	1.9	-20.8
$P3_121$							
Ca1	3.48	3.72	0.52	0.39	19.1	4.1	-32.0
Ca2	2.82	3.01	0.19	0.27	13.0	2.0	-19.7
Ca3	3.45	3.68	0.48	0.49	18.4	3.4	-33.1

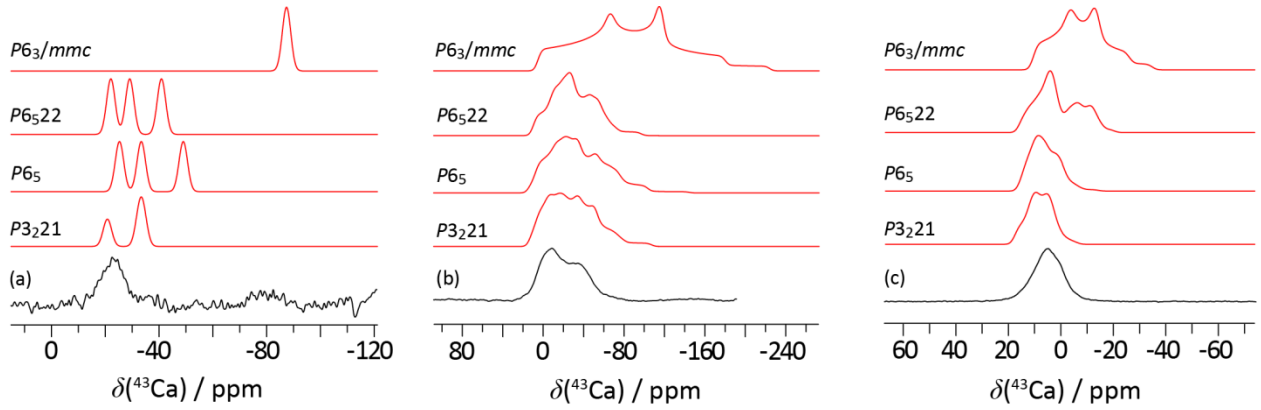

Figure 6.8: ^{43}Ca NMR line shape simulations for the hexagonal models for vaterite under MAS at 9.4 (b) and 21.1 T (c) and DOR conditions at 9.4 T (a). All experimental spectra in

black were acquired for the ^{43}Ca isotopically enriched vaterite sample. All simulations are in red and were generated in WSolids from the calculated NMR parameters reported in Table 6.4.

The final structure in this discussion is Kahmi's 1963 model[10] for vaterite, which crystallizes in the $P6_3/mmc$ space group. In their recent work on a natural sample of vaterite using high-resolution synchrotron powder diffraction and high-resolution transmission electron microscopy, Pokroy and coworkers[9] concluded that vaterite may be comprised of two substructures: a major structure most likely best described with the $P6_3/mmc$ model and a minor unknown structure. When performing GIPAW DFT calculations on the $P6_3/mmc$ model, a large overestimation in the value of $|C_Q(^{43}Ca)|$ (a calibrated value of 5.05 MHz, a 1.85 MHz error with respect to experiment) is observed, resulting in a δ_{DOR} value of −87.4 ppm, which is not consistent with the new experimental data reported presently. This was somewhat surprising given that in previous ^{43}Ca MAS NMR experiments, the $P6_3/mmc$ model was deemed to be more accurate in describing vaterite than the orthorhombic *Pbnm* space group.[20] However, the previous natural abundance ^{43}Ca NMR experiments were referenced to a saturated $CaCl_2$ solution rather than a dilute solution. Thus, a new experimental ^{43}Ca δ_{iso} value for vaterite of 15(2) is reported herein compared to the previous report of −3(1) ppm, an 18 ppm difference. We do note that a closer value of 12.6 ppm was estimated previously when factoring in an error caused by chemical shift referencing.[17,18] It is emphasized here that the calculated ^{43}Ca δ_{iso} values for the $P6_3/mmc$ and the *Pbnm* models are 11.7 and −28.4 ppm, respectively, and so the former hexagonal model is still more representative of vaterite than the orthorhombic model, which is in agreement with our previous results. Due to a relatively large difference between the calculated and

experimental $|C_Q(^{43}Ca)|$ value (ΔC_Q = 1.85 MHz), however, the $P6_3/mmc$ model is not the best suited to describe the major structure of vaterite.

6.3.6 The Most Likely Candidate Structures

If the major component of vaterite is comprised of a hexagonal lattice, as emphasized by Pokroy and coworkers,[9] the $P3_221$ or $P3_121$ structures (which are optimized from a hexagonal starting point) result in computed NMR parameters which are in better agreement with our experimental ^{43}Ca NMR results than does the $P6_3/mmc$ model. We cannot, however, rule out the possibility of a monoclinic lattice to describe vaterite especially when comparing the simulation of the ^{43}Ca DOR spectrum for the $C2$ structure (see Figure 6.6). In their paper describing a possible interplay between a major hexagonal lattice and a minor structure for vaterite, Pokroy and coworkers[9] assess the possibility that Mugnaioli's monoclinic structures were acquired at lower resolution than that obtainable by aberration-corrected high-resolution transmission electron microscopy (HRTEM). Therefore, a lower symmetry space group such as $C2/c$, the parent structure of the $C2$ model, could incorporate a superposition of both the major and minor structures for vaterite thus providing a more accurate model for vaterite in terms of experiment and computation of ^{43}Ca DOR and multiple field MAS experiments.

In Figure 6.9 is shown a bar chart summarizing the calculated $|C_Q(^{43}Ca)|$ and δ_{iso} values for the five vaterite structure models that most accurately reproduce the ^{43}Ca NMR parameters (excluding those eliminated by PXRD (blue boxes in Figure 6.1); note that there are three non-equivalent calcium sites in each model). In general, it is clear that no model perfectly reproduces both the $|C_Q(^{43}Ca)|$ and δ_{iso} values within the limits of their respective

RMSD values (indicated by the dashed lines and grey shading). It is clear, however, that the $P3_221$ (or $P3_121$, see Table 6.4) are the most accurate structures given that all three chemical shift values are within the RMSD of 5 ppm and two of the quadrupolar coupling constants are only slightly overestimated with respect to the RMSD of 0.2 MHz.

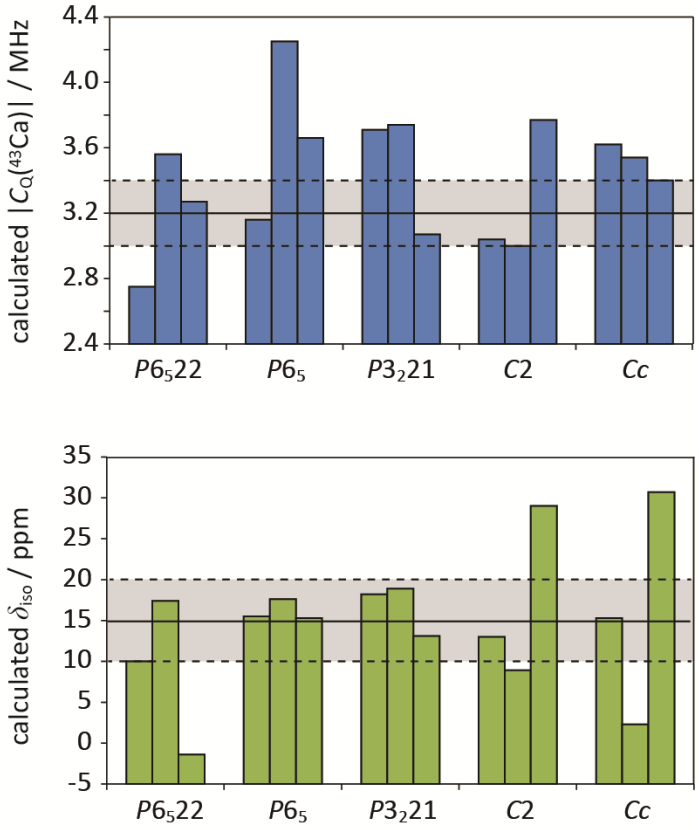

Figure 6.9: Bar charts of the GIPAW DFT calculated $|C_Q(^{43}Ca)|$ and δ_{iso} values for the structural models that best represent vaterite in this study. There are three bars per space group representing the three unique Ca sites in each of the models. A solid black line indicates the experimental values observed for the synthetic isotopically-enriched vaterite sample in this work. Dashed lines indicate the RMSD limits for the GIPAW DFT calculated vs. experimental $|C_Q(^{43}Ca)|$ and δ_{iso} values of 0.2 MHz and 5.0 ppm respectively, on the basis

of an extensive data set reported for a range of well-characterized crystalline calcium compounds in Chapter 5 and in ref. 24.

In the case of the *C*2 structure, a modest overestimation in the $|C_Q(^{43}Ca)|$ value for one of the calcium sites ($|\Delta C_Q|$ = 0.57 MHz) combined with a rather large error in δ_{iso} of 14.0 ppm demonstrates how the $P3_221$ structure could be favored, although, once again a qualitative assessment of the NMR spectra shows that a more accurate line shape is observed in the ^{43}Ca DOR spectrum for the *C*2 model.

6.4 Conclusions

A combination of (i) newly proposed DFT and XRD-based structural models for vaterite, (ii) a more accurate ^{43}Ca chemical shift scale, (iii) the calibration curve relating experimental and GIPAW DFT calculated ^{43}Ca quadrupolar coupling constants from Chapter 5, and (iv) new high-resolution ^{43}Ca SSNMR experiments using MQMAS and DOR methods, have enabled a detailed reassessment and quantification of the agreement between ^{43}Ca SSNMR data and the various proposed structures of vaterite. The data suggest that vaterite contains one crystallographically unique calcium site with a distribution in both the ^{43}Ca quadrupolar parameters and chemical shifts, given the rather broad nature of the single resonance obtained with DOR and MQMAS NMR. Due to the relatively small quadrupole moment for ^{43}Ca, DOR NMR experiments on the ^{43}Ca nucleus may offer a high degree of resolution and hold promise in future studies on calcium-containing materials.

The following conclusions are reached regarding the structural models for vaterite:

- some models including the DFT-predicted GGA, LDA, and $P2_12_12_1$ as well as the monoclinic $C2/c$ and $C\bar{1}$ structures are inconsistent with the PXRD data (blue shading in Figure 6.1);
- many recently proposed structures are ruled out as accurate models due to large discrepancies between their calculated and the experimental δ_{DOR} shifts and unreasonably large calculated $|C_Q(^{43}Ca)|$ values (i.e., the orthorhombic *Ama*2 and *Pbnm* structures and the hexagonal $P6_3/mmc$ structure; see rose shading in Figure 6.1);
- the $P3_221$ model (or its stereoisomeric $P3_121$ structure) and the monoclinic $C2$ model provide the best simultaneous agreement between the experimental and calculated NMR data, and the experimental and simulated PXRD data (green shading in Figure 6.1). The unit cells of both structures are presented in Figure A6.1

Interestingly, none of the 18 structures provide perfect agreement between experimental and simulated data to within the established RMSD values for the various NMR parameters, suggesting that the data reported herein will remain valuable for the cross-validation of further proposals for the true structure of vaterite.

6.5 References for Chapter 6

1. Frenzel, M.; Harper, E. M. *J. Struct. Biol.* **2011**, *174*, 321.
2. Qiao, L.; Feng, Q.-L.; Li, Z. *Cryst. Growth Des.* **2007**, *7*, 275.
3. Lowenstam, H. A.; Abbott, D. P. *Science* **1975**, *188*, 363.
4. Ihli, J.; Wong, W. C.; Noel, E. H.; Kim, Y.-Y.; Kulak, A. N.; Christenson, H. K.; Duer, M. J.; Meldrum, F. C. *Nat. Commun.* **2014**, *5*, 3169.
5. Noel, E. H.; Kim, Y.-Y.; Charnock, J. M.; Meldrum, F. C. *CrystEngComm* **2013**, *15*, 697.
6. Cartwright, J. H. E.; Checa, A. G.; Gale, J. D.; Gebauer, D.; Sainz-Díaz, C. I. *Angew. Chem. Int. Ed.* **2012**, *51*, 11960.
7. Rodriguez-Blanco, J. D.; Shaw, S.; Benning, L. G. *Nanoscale* **2011**, *3*, 265.
8. Huang, Y.-C.; Mou, Y.; Wen-Tin, T.; Wu, Y.-J.; Lee, H.-K.; Huang, S.-J.; Chan, J. C. C. *J. Phys. Chem. B* **2012**, *116*, 14295.
9. Kabalah-Amitai, L.; Mayzel, B.; Kauffmann, Y.; Fitch, A. N.; Bloch, L.; Gilbert, P. U. P. A.; Pokroy, B. *Science* **2013**, *340*, 454.
10. Kahmi, S. R. *Acta Cryst.* **1963**, *16*, 770.
11. Meyer, V. H. J. *Z. Kristallogr.* **1969**, *128*, 183.
12. Le Bail, A.; Ouhenia, S.; Chateigner, D. *Powder Diffr.* **2011**, *26*, 16.
13. Wehrmeister, U.; Soldati, A. L.; Jacob, D. E.; Häger, T.; Hofmeister, W. *J. Raman Spectrosc.* **2010**, *41*, 193.
14. Wang, J.; Becker, U. *Am. Mineral.* **2009**, *94*, 380.
15. Demichelis, R.; Raiteri, P.; Gale, J. D.; Dovesi, R. *CrystEngComm* **2012**, *14*, 44.

16. Demichelis, R.; Raiteri, P.; Gale, J. D.; Dovesi, R. *Cryst. Growth Des.* **2013**, *13*, 2247.

17. Moudrakovski, I. L. *Ann. Rep. NMR Spectrosc.* **2013**, *79*, 129.

18. Laurencin, D.; Smith, M. E. *Prog. Nucl. Magn. Reson. Spectrosc.* **2013**, *68*, 1.

19. Bryce, D. L. *Dalton Trans.* **2010**, *39*, 8593.

20. Bryce, D. L.; Bultz, E. B.; Aebi, D. *J. Am. Chem. Soc.* **2008**, *130*, 9282.

21. Burgess, K. M. N.; Xu, Y.; Leclerc, M. C.; Bryce, D. L. *Inorg. Chem.* **2014**, *53*, 552.

22. Colas, H.; Bonhomme-Coury, L.; Diogo, C. C.; Tielens, F.; Babonneau, F.; Gervais, C.; Bazin, D.; Laurencin, D.; Smith, M. E.; Hanna, J. V.; Daudon, M.; Bonhomme, C.; *CrystEngComm* **2013**, *15*, 8840.

23. Laurencin, D.; Gervais, C.; Wong, A.; Coelho, C.; Mauri, F.; Massiot, D.; Smith, M. E.; Bonhomme, C. *J. Am. Chem. Soc.* **2009**, *131*, 13430.

24. Moudrakovski, I. L.; Alizadeh, R.; Beaudoin, J. J. *Phys. Chem. Chem. Phys.* **2010**, *12*, 6961.

25. Sahoo, B. K. *Phys. Rev. A* **2009**, *80*, 012515.

26. Baias, M.; Dumez, J.-N.; Svensson, P. H.; Schantz, S.; Day, G. M.; Emsley, L. *J. Am. Chem. Soc.* **2013**, *135*, 17501.

27. Martineau, C.; Senker, J.; Taulelle, F. *Ann. Rep. NMR Spectrosc.* **2014**, *82*, 1–57.

28. Bouchevreau, B.; Martineau, C.; Mellot-Draznieks, C.; Tuel, A.; Suchomel, M. R.; Trébosc, J.; Lafon, O.; Amoureux, J.-P.; Taulelle, F. *Chem. Mater.* **2013**, *25*, 2227.

29. Seymour, V. R.; Eschenroeder, E. C. V.; Castro, M.; Wright, P. A.; Ashbrook, S. E. *CrystEngComm* **2013**, *15*, 8668.

30. Dudenko, D. V.; Yates, J. R.; Harris, K. D. M.; Brown, S. P. *CrystEngComm* **2013**, *15*, 8797.

31. Harris, R. K.; Wasylishen, R. E.; Duer, M. J. NMR Crystallography, John Wiley & Sons Ltd, Chichester UK, **2009**.

32. Widdifield, C. M.; Bryce, D. L. *Phys. Chem. Chem. Phys.* **2009**, *11*, 7120.

33. Brower, D. H.; Cadars, S.; Eckert, J.; Liu, Z.; Terasaki, O.; Chmelka, B. F. *J. Am. Chem. Soc.* **2013**, *135*, 5641.

34. Sene, S.; Reinholdt, M.; Renaudin, G.; Berthomieu, D.; Zicovich-Wilson, C. M.; Gervais, C.; Gaveau, P.; Bonhomme, C.; Filinchuk, Y.; Smith, M. E.; Nedelec, J.-M.; Bégu, S.; Mutin, P. H.; Laurencin, D. *Chem. Eur. J.* **2013**, *19*, 880.

35. Perras, F. A.; Bryce, D. L. *J. Phys. Chem. C* **2012**, *116*, 19472.

36. Shivkumara, C.; Singh, P.; Gupta, A.; Hegde, M. S. *Mater. Res. Bull.* **2006**, *41*, 1455.

37. Amoureux, J.-P.; Fernandez, C.; Steuernagel, S. *J. Magn. Reson., Ser. A* **1986**, *123*, 116.

38. States, D. J.; Haberkorn, R. A.; Ruben, D. J. *J. Magn. Reson.* **1982**, *48*, 286.

39. Perdew, J. P.; Burke, K.; Ernzerhof, M. *Phys. Rev. Lett.* **1996**, *77*, 3865.

40. Spann, N.; Harper, E. M.; Aldridge, D. C. *Naturwissenschaften* **2010**, *97*, 743.

41. Medeiros, S. K.; Albuquerque, E. L.; Maia Jr., F. F.; Caetano, E. W. S.; Freire, V. N. *Chem. Phys. Lett.* **2007**, *435*, 59.

42. Mugnaioli, E.; Andrusenko, I.; Schüler, R.; Loges, N.; Dinnebier, R. E.; Panthöfer, M.; Tremel, W.; Kolb, U. *Angew. Chem. Int. Ed.* **2012**, *51*, 7041.

43. Gervais, C.; Laurencin, D.; Wong, A.; Pourpoint, F.; Labram, J.; Woodward, B.; Howes, A. P.; Pike, K. J.; Dupree, R.; Mauri, F.; Bonhomme, C.; Smith, M. E. *Chem. Phys. Lett.* **2008**, *464*, 42.

44. Meyer, H.-J. *Angew. Chem.* **1959**, *71*, 678.

45. Wang, H.; Han, Y.; Li, J. *Cryst. Growth. Des.* **2013**, *13*, 1820.

7 General Conclusions and Outlook

In terms of the various research projects undertaken as reported in this dissertation, it is clear that SSNMR of exotic quadrupolar nuclei has the potential in providing a rich landscape of structural and chemical information on the studied systems and has been shown to be an extremely powerful technique in corroborating or refuting XRD data. As was discussed in Chapters 3, 4, and 5, the studies involved the synthesis of some systematic series of compounds that could be characterized by either $^{79/81}$Br or alkaline-earth metal (^{25}Mg, ^{43}Ca, and ^{87}Sr) SSNMR. In those Chapters, the exotic quadrupolar nucleus was in an organic coordination environment, resulting in a smaller concentration of the nuclei of interest compared to inorganic systems, which have been most of the focus in the recent literature. In the case of ^{43}Ca experiments, it was sometimes necessary to isotopically enrich the sample in order to gain meaningful insight from the NMR experiments. In future studies involving ^{43}Ca, a low level of isotopic enrichment (perhaps 10%) will go a long way in obtaining usable NMR spectra for applications in structural characterization and refinement. Given the challenges associated with each of these exotic quadrupolar nuclei, it was still nonetheless possible to extract both reliable CS and EFG tensor information in the various systems considered in this dissertation and to then interpret their relationship with the solid-state structures. All of the work presented herein was made possible by the availability of both high-resolution quadrupolar NMR techniques (i.e., MAS, DOR, and MQMAS) as well as

modern ultra-wideline NMR techniques such as the VOCS method and the WURST-QCPMG sequence. NONE of the conclusions presented in the individual Chapters of this dissertation could have been attainable had it not been for access to an ultrahigh-field NMR facility such as the 21.1 T instrument in Ottawa!

7.1 The CS Tensor of Exotic Quadrupolar Nuclei as a Probe for Molecular Structure

It was found in the cases of Ca(pams) and Ca(pams)(OAc), for example, that N-coordination, more specifically the Ca–N distance from the crystal structure, could be correlated to the ^{43}Ca δ_{iso}. Furthermore, one major conclusion from the application of $^{79/81}$Br SSNMR on the characterization of EFG and CS tensors in TPP bromides was that the CS tensor was intimately related to the structure of the phosphonium halides via a correlation between the $^{79/81}$Br CSA and a change in the shortest Br–P distance. Hence, the CS tensor can indeed provide structural information in organic ionic systems.

Given the promise of $^{79/81}$Br SSNMR as a probe for structure, this study could be moved to the next level by attempting to identify correlations between $^{79/81}$Br EFG and CS tensors and the strength or geometry of the anion-π interaction, another organic coordination environment.[1] Such applications are currently emerging for a similar non-covalent interaction known as halogen bonding.[2,3] Although a meaningful correlation between the $^{79/81}$Br CS tensor and the molecular structure of TPP bromides was established experimentally and verified theoretically with GIPAW DFT calculations, quantitative reproducibility of the CS tensor parameters from the calculations was not observed. In fact,

the calculated CS tensor spans were more than double the experimental values. There are multiple reasons for this apparent overestimation including the fact that an absolute shielding constant for bromine has not been identified experimentally. Therefore, calculated CS tensor values for bromine rely currently on the performance of the calculations on a reference solid such as KBr. Another reason for such an overestimation in the calculations of $^{79/81}$Br CS tensor parameters could be in the exclusion of relativistic effects in the GIPAW DFT program used. Currently, the CASTEP program does not incorporate relativistic effects under ZORA. There was an attempt at accounting for relativity using the ADF program but cluster-based modeling was found not to be accurate in representing organic ionic solids. It would be useful to perform DFT calculations that incorporate both the periodic boundary conditions of GIPAW DFT and the relativistic effects under ZORA in order to quantitatively reproduce $^{79/81}$Br CS tensor information looking forward. Such calculations will aid immensely in the identification of new correlations between CS and molecular structure such as in anion-π systems.

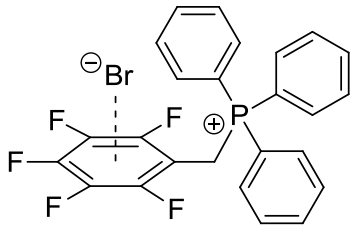

Figure 7.1: An anion-π interaction between the Br^- and a perfluorinated benzene ring.

Another avenue currently being investigated for SSNMR of exotic quadrupolar nuclei is on the ^{59}Co (I = 7/2) study of some Co(I) catalysts such as the one presented in Figure 1.1 of this thesis. In some preliminary ^{59}Co SSNMR spectra, a significant amount of broadening

from CSA (on the order of thousands of ppm) has been observed and we are currently attempting to identify the structure-activity relationship between the CS tensor and the catalysts. With the advancing technology of superconducting high field magnets, it is only a matter of time before experiments performed at B_0 = 21.1 T might become routine. If one day, a 2 GHz magnet ($\nu_L(^1H)$ = 2000 MHz) were to become available (and this is not unfeasible as there are currently 1.2 GHz magnets being manufactured), NMR spectra of nuclei such as $^{79/81}Br$ and ^{59}Co could become CSA dominated rather than quadrupole dominated allowing for the precise measurement of the CS tensor in exotic qudrupolar nuclei and subsequent correlation to structure. This could also be applied to the case of ^{25}Mg for example, where CSA was not discernable in the organic ionic compounds studied as part of this dissertation. With "ultra"ultrahigh-field experiments, it is even conceivable to observe small effects on stationary SSNMR spectra caused by the dipolar interaction, which is a direct distance measurement probe in solids.

7.2 Application of Exotic Quadrupolar Nuclei to NMR Crystallography

A second objective for this thesis was to apply bromine and alkaline-earth metal SSNMR to NMR crystallography applications. It was shown in Chapters 3 and 4 that $^{79/81}Br$ and ^{25}Mg SSNMR forced the re-investigation of the structure of anhydrous PPh_4Br as well as Mg(ben) respectively. Both of these examples show how quadrupolar SSNMR experiments can be used to corroborate or even refine a crystal structure. Moreover, it was shown in Chapter 4, that the distribution in Mg–O bond lengths of the immediate coordination sphere about Mg^{2+}, measured by the longitudinal strain, could be correlated to the ^{25}Mg EFG tensor,

thus intimately relating the long range ordering of an ionic organic solid with ^{25}Mg SSNMR. As an example, this type of correlation could be used in the future when answering questions about the immediate Mg^{2+}-coordination environment in gas-adsorbed MOFs, which are normally weak in crystallinity.

One of the most significant results from the research presented in this dissertation was in the observation of a correlation between GIPAW DFT calculated and accurately measured experimental $|C_Q(^{43}Ca)|$ values. This plot allowed for the conclusion that the newly reported value for the ^{43}Ca quadrupole moment, –44.4 mbarn, should be used in future studies involving ^{43}Ca SSNMR experiments. As an example for the applicability of this correlation curve presented in Chapter 5, an NMR crystallography approach was used in Chapter 6 in order to identify the structural model most consistent with the ^{43}Ca SSNMR data for the vaterite polymorph of $CaCO_3$. In that study, it was possible to narrow the possible number of vaterite structures from 18 to 2, thus inching us closer to the identification of the true structure of vaterite. Over the course of the redaction of this thesis, an independent, but conceptually similar, study emerged in the literature corroborating the findings written in Chapter 6. In fact, the authors use a completely different spectroscopic tool, Raman spectroscopy, and compared their experimental spectrum for vaterite to DFT simulated Raman spectra. The very satisfying result came when Demichelis and co-workers[4] identified the $C2$ and $P3_221$ structures as the most probable structures of vaterite, in exact agreement with the conclusions from Chapter 6. It is clear that more work is necessary in order to fully characterize the complex vaterite system.

Thankfully, there are two other NMR-active nuclei comprising vaterite, ^{13}C and the quadrupolar ^{17}O nucleus (I = 5/2), which has an even lower natural abundance than ^{43}Ca

(0.038% for ^{17}O). An enriched ^{17}O vaterite sample has been successfully synthesized and MQMAS and DOR experiments are currently underway. Preliminary results suggest that multiple ^{17}O sites are present in the vaterite sample. The application of ^{13}C–^{17}O heteronuclear correlation experiments may also provide further insight. The combination of both the ^{43}Ca and ^{17}O data will surely be extremely useful in identifying constraints for solving the structure of vaterite. Since vaterite is not the most stable polymorph of calcium carbonate, it is possible that the crystal structure itself is a dynamic one (i.e., containing multiple interchangeable substructures). If this is the case, one could envisage coupling both molecular dynamics simulations within the GIPAW DFT calculations, where NMR parameters could by calculated "on-the-fly" as the structure is evolving.

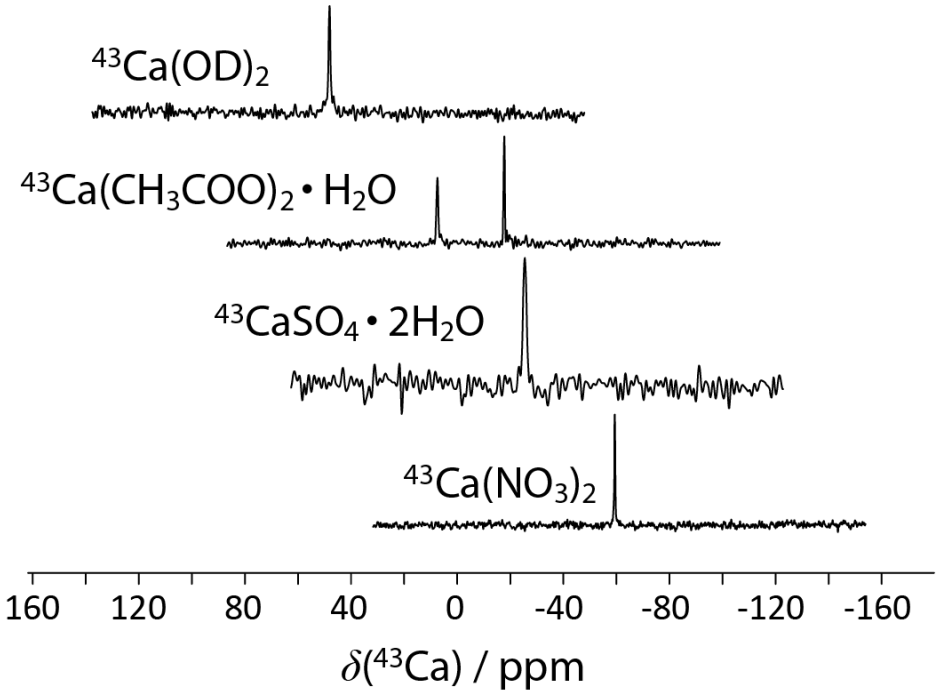

Figure 7.2: ^{43}Ca DOR NMR spectra acquired on some ^{43}Ca-enriched calcium salts. DOR provides impeccable resolution (solution-like) for ^{43}Ca NMR experiments. Experiments were performed at B_0 = 9.4 T with DFS signal enhancement.

The methodology that holds much promise for future studies involving calcium-containing materials is indeed the DOR technique. As shown, in Figure 7.2, it is possible to differentiate between multiple crystalline calcium compounds using ^{43}Ca DOR when ^{43}Ca-enriched samples are available. In fact, every compound has a different δ_{DOR} value. Unfortunately, the technology surrounding the DOR method is quite underdeveloped and it is still far from a routine experiment. MQMAS on the other hand could be used but the 2D experiments would be too insensitive for calcium-containing materials applications. It would be useful to perform ^{43}Ca DOR experiments on non-labeled samples since synthetic isotopic enrichment protocols can only go so far in the preparation of challenging samples such as vaterite. Therefore, it will be exciting to see, in the coming years, advancements in probe technologies as well as the emergence of ever higher magnetic field strengths, which can greatly increase the sensitivity of low-γ nuclei such as the alkaline-earth metals.

7.3 References for Chapter 7

1. Albrecht, M.; Müller, M.; Mergel, O.; Rissanen, K.; Valkonen, A. *Chem. Eur. J.* **2010**, *16*, 5062.
2. Attrell, R. J.; Widdifield, C. M.; Korobkov, I.; Bryce, D. L. *Cryst. Growth Des.* **2012**, *12*, 1641.
3. Viger-Gravel, J.; Leclerc, S.; Korobkov, I.; Bryce, D. L. *J. Am. Chem. Soc.* **2014**, *136*, 6929.
4. De La Pierre, M.; Demichelis, R.; Wehrmeister, U.; Jacob D. E.; Paolo, R.; Gale, J. D.; Orlando, R. *J. Phys. Chem. C* **2014**, *118*, 27493.

List of Publications

9. Damir Safin, Rebecca J. Holmberg, Kevin M. N. Burgess, Koen Robeyns, David L. Bryce & Muralee Murugesu, **Designing a Novel Hybrid Material Constructed from $Hg(SCN)_2$ and 2,4,6-Tris(2-Pyrimidyl)-1,3,5-Triazine (TPymT): First Example of Coordination of TPymT in a 2,2'-Bipyridine-like Mode**, *Eur. J. Inorg. Chem.* **2014**, DOI: 10.1002/ejic.201402832.

8. Kevin M. N. Burgess & David L. Bryce, **On the Crystal Structure of the Vaterite Polymorph of $CaCO_3$. A Calcium-43 Solid-State NMR and Computational Assessment,** *Solid State Nucl. Magn. Reson.* **2014**, DOI: 10.1016/j.ssnmr.2014.08.003.

7. Damir Safin, Kevin M. N. Burgess, Ilia Korobkov, David L. Bryce & Muralee Murugesu, **Renaissance of the Coordination Chemistry of 2-4-6(tris(2-pyrimidyl)-1,3,5(triazine) (TPymT). Part II: New Insights into the Reaction of TPymT with $Pb(NO_3)_2$**, *CrystEngComm* **2014**, *16*, 3466–3469.

6. Kevin M. N. Burgess, Yang Xu, Matthew C. Leclerc & David L. Bryce, **Alkaline-Earth Metal Carboxylates Characterized by ^{43}Ca and ^{87}Sr Solid-State NMR: Impact of Metal-Amine Bonding**, *Inorg. Chem.* **2014**, *53*, 552–561.

5. Kevin M. N. Burgess, Yang Xu, Matthew C. Leclerc & David L. Bryce, **Insight into Magnesium Coordination Environments in Benzoate and Salicylate Complexes through ^{25}Mg Solid-State NMR Spectroscopy**, *J. Phys. Chem. A* **2013**, *117*, 6561–6570.

4. Frédéric A. Perras, Jasimine Viger-Gravel, Kevin M. N. Burgess & David L. Bryce, **Signal Enhancement in Solid-State NMR of Quadrupolar Nuclei**, *Solid State Nucl. Magn. Reson.* **2013**, *51-52,* 1–15.

3. Kevin M. N. Burgess, Frédéric A. Perras, Aurore Lebrun, Elisabeth Messner-Henning, Ilia Korobkov & David L. Bryce, **Sodium-23 Solid-State Nuclear Magnetic Resonance of Commercial Sodium Naproxen and its Solvates**, *J. Pharm. Sci.* **2012**, *101*, 2930–2940.

2. Kevin M. N. Burgess, Ilia Korobkov & David L. Bryce, **A Combined Solid-State NMR and X-ray Crystallography Study of the Bromide Anion Environments in Triphenylphosphonium Bromides**, *Chem. Eur. J.* **2012**, *18,* 5748–5758.

1. David R. Stuart, Mégan Bertrand-Laperle, Kevin M. N. Burgess & Keith Fagnou, **Indole Synthesis via Rhodium Catalyzed Oxidative Coupling of Acetanilides and Internal Alkynes**, *J. Am. Chem. Soc.* **2008**, *130* (49), 16474–16475.

Appendix A – Additional Experimental Parameters

Chapter 3 Appendices

Table A3.1: Detailed $^{79/81}$Br and $^{35/37}$Cl SSNMR acquisition parameters.

B_0 /T	^{A}Z	window /kHz	points	$\pi/2$ /μs	scans	recycle delay /s	$\tau_1;\tau_2$ /μs	details
				$BuPPh_3Br$				
9.4	^{79}Br	1 000	2 048	1.6	118 961	0.5	60;10	static; solid echo; 1 piece
9.4	^{81}Br	1 000	2 048	1.0	113 155	0.5	60;10	static; solid echo; 1 piece
11.75	^{79}Br	1 000	4 096	2.1	20 480	0.2	30;20	static; solid echo; 1 piece
11.75	^{81}Br	1 000	4 096	1.5	20 480	0.2	30;20	static; solid echo; 1 piece
21.1	^{79}Br	500	1 024	2.0	7 200	0.5	28;0	static; solid echo; 1 piece
21.1	^{81}Br	500	1 024	1.0	4 800	0.5	29;0	static; solid echo; 1 piece
21.1	^{81}Br	250	1 024	1.0	5 800	0.5	31;0	MAS(ν_{rot} = 31.25 kHz); solid echo
				$PrPPh_3Br$				
9.4	^{79}Br	1 000	2 048	1.6	340 424	0.2	60;10	static; solid echo; 1 piece
9.4	^{81}Br	1 000	2 048	1.3	304 729	0.2	60;10	static; solid echo; 1 piece
11.75	^{79}Br	1 000	4 096	2.2	43 081	0.2	30;20	static; solid echo; 1 piece
11.75	^{81}Br	1 000	4 096	1.6	42 787	0.2	30;20	static; solid echo; 1 piece
21.1	^{81}Br	500	1 024	1.0	5 800	0.5	29;0	static; solid echo; 1 piece
21.1	^{81}Br	250	1 024	1.0	6 900	0.5	31;0	MAS(ν_{rot} = 31.25 kHz); solid echo

Table A3.1 continued

B_0 /T	^{A}Z	window /kHz	points	π/2 /μs	scans	recycle delay /s	$\tau_1;\tau_2$ /μs	details
				$EtPPh_3Br$				
9.4	^{79}Br	1 000	2 048	1.5	304 000	0.2	60;10	static; solid echo; 2 pieces; offset = 100 kHz
9.4	^{81}Br	1 000	2 048	1.3	307 200	0.2	60;10	static; solid echo; 2 pieces; offset = 100 kHz
11.75	^{79}Br	1 000	4 096	2.2	240 640	0.2	30;20	static; solid echo; 3 pieces; offset = 150 kHz
11.75	^{81}Br	1 000	4 096	1.6	40 960	0.2	30;20	static; solid echo; 1 piece
21.1	^{81}Br	500	1 024	1.0	9 600	0.5	29;0	static; solid echo; 1 piece
21.1	^{81}Br	500	2 048	1.0	114 360	0.5	31;0	MAS(ν_{rot} = 62.5 kHz); solid echo
				$MePPh_3Br$				
9.4	^{79}Br	1 000	2 048	1.5	267 891	0.2	60;10	static; solid echo; 1 piece
9.4	^{81}Br	1 000	2 048	1.3	107 315	0.2	60;10	static; solid echo; 1 piece
11.75	^{79}Br	1 000	4 096	2.2	97 280	0.2	30;20	static; solid echo; 1 piece
11.75	^{81}Br	1 000	4 096	1.6	51 200	0.2	30;20	static; solid echo; 1 piece
21.1	^{81}Br	500	1 024	1.0	4 000	0.5	29;0	static; solid echo; 1 piece
21.1	^{81}Br	250	1 024	1.0	6 400	0.5	31;0	MAS(ν_{rot} = 31.25 kHz); solid echo
				$HPPh_3Br$				
11.75	^{79}Br	1 000	4 096	2.0	8 192	0.5	28;0	static; solid echo; 3 pieces; offset = 150 kHz
11.75	^{81}Br	500	2 048	2.0	15 301	0.5	28;0	static; solid echo; 1 piece
21.1	^{81}Br	1 000	2 048	1.0	8 192	1.0	29;0	static; solid echo; 1 piece
21.1	^{81}Br	250	2 048	1.0	27 400	0.5	31;0	MAS(ν_{rot} = 62.5 kHz); solid echo

Table A3.1 continued

B_0 /T	^{A}Z	window /kHz	points	π/2 /μs	scans	recycle delay /s	$\tau_1;\tau_2$ /μs	details
				$C_5H_9PPh_3Br$				
11.75	^{79}Br	1 000	2 048	2.0	16 384	0.5	28;0	static; solid echo; 3 pieces; offset = 150 kHz
11.75	^{81}Br	500	2 048	2.0	49 152	0.5	28;0	static; solid echo; 1 piece
21.1	^{81}Br	500	1 024	1.0	7 800	0.5	29;0	static; solid echo; 1 piece
21.1	^{81}Br	500	2 048	1.0	36 800	0.5	21;0	MAS(ν_{rot} = 62.5 kHz); solid echo
				PPh_4Br				
21.1	^{81}Br	250	2 048	1.0	122 880	0.5	31;0	MAS(ν_{rot} = 62.5 kHz); solid echo
				$BuPPh_3Cl$				
9.4	^{35}Cl	100	1 988	5.0	27 688	2.0	120;0	MAS(ν_{rot} = 8 kHz); solid echo
9.4	^{37}Cl	100	1 988	5.0	29 696	2.0	120;0	MAS(ν_{rot} = 8 kHz); solid echo
21.1	^{35}Cl	50	4 096	4.0	1 024	2.0	196;0	MAS(ν_{rot} = 5 kHz); solid echo

Table A3.2: Energy cut-offs and *k*-point grids for GIPAW DFT calculations on phosphonium bromides.

compound	E_{cut} (eV)	*k*-point grid
$BuPPh_3Br$	390	2x2x1
$PrPPh_3Br$	390	2x3x1
$EtPPh_3Br$	390	2x2x1
$MePPh_3Br$	390	3x1x2
$C_5H_9PPh_3Br$	390	2x2x3
$HPPh_3$	390	2x2x2
PPh_4Br	390	3x3x2
$BuPPh_3Cl$	390	2x3x1
$BuPPh_3Br$ (no Br)	390	2x2x1
$BuPPh_3Cl$ (no Cl)	390	2x3x1
$BuPPh_3Br$ (Br–P stretch)	390	2x2x1
KBr	220	4x4x4

Table A3.3: Summary of ADF Calculations on an HBr[a] and a $BuPPh_3Br$[b] Model.

	bromine (HBr)			**bromine ($BuPPh_3Br$)**			**phosphorus ($BuPPh_3Br$)**		
relativity	none	scalar	spin-orbit	none	scalar	spin-orbit	none	scalar	spin-orbit
σ_{iso}	2574.48	2531.97	2744.77	2356.95	2278.096	2493.00	272.729	269.810	281.323
σ_{iso}[d]	-	-	-	2407.43	2342.958	2555.69	267.298	263.777	275.06
σ_{11}	2298.55	2237.52	2484.96	1947.15	1826.085	2076.112	251.146	246.685	259.166
σ_{11}[d]	-	-	-	2108.79	2016.581	2254.144	245.735	242.371	253.885
σ_{22}	2298.55	2237.52	2484.96	2508.95	2453.993	2654.877	274.096	270.923	283.465
σ_{22}[d]	-	-	-	2471.93	2420.042	2626.042	267.310	263.482	274.151
σ_{33}	3126.32	3120.88	3264.38	2614.74	2554.211	2748.011	292.944	291.822	301.339
σ_{33}[d]	-	-	-	2641.57	2592.253	2786.879	288.848	285.477	297.135
Ω	827.768	883.36	779.42	667.58	728.126	671.899	41.798	45.137	42.173
Ω[d]	-	-	-	532.78	575.672	532.735	43.113	43.106	43.25

[a] The HBr model consisted of one H and one Br atom separated by 1.414 Å.
[b] The $BuPPh_3Br$ model consisted of on phosphonium cation and one Br anion from the reported crystal structure.
[c] All calculations were performed in the Amsterdam Density Functional (ADF) program using the QZ4P basis set on all atoms, the BP86 functional, and scalar or spin-orbit relativistic effects were accounted for using the ZORA.
[d] Results of the same ADF calculations when the hydrogen positions of the $BuPPh_3Br$ model are optimized beforehand with the Gaussian '09 software (B3LYP/6-31G* on all atoms).

Chapter 4 Appendices

Table A4.1: Experimental ^{25}Mg Solid-State NMR Conditions for Mg Aryl Carboxylates.

B_0 /T	window /kHz	points	π/2 /μs	scans	recycle delay /s	$\tau_1;\tau_2$ /μs	details
Mg(*p*F)							
9.4	1000	3960	10	20480	5	100;0	7 mm static; Hahn-echo; DFS; ^{1}H dec.
21.1	100	4 096	3	26624	2	116;0	7 mm static; solid echo; ^{1}H dec.
21.1	100	4 096	3	16640	2	122;0	4 mm MAS (ν_{rot} = 8 kHz); solid echo; ^{1}H dec.
Mg(*p*Cl)							
9.4	1000	3960	10	118902	2	45;0	7 mm static; Hahn-echo; DFS; ^{1}H dec.
21.1	100	3960	3	31040	2	114.5;0	7 mm static; Hahn-echo; ^{1}H dec.
21.1	100	3960	3	5120	2	94.5;0	4 mm MAS (ν_{rot} = 10 kHz); Hahn-echo; ^{1}H dec.
Mg(ben)							
9.4	1000	4096	10	164352	2	45;0	7 mm static; Hahn-echo; ^{1}H dec.
21.1	100	4096	3	28288	2	116;0	7 mm static; solid echo; ^{1}H dec.
21.1	100	3960	5	10720	2	117.5;0	7 mm MAS (ν_{rot} = 8 kHz); Hahn-echo
Mg(sal)							
9.4	1000	97524	10	33792	5		7 mm static; QCPMG (1 kHz spikelet sep., 48 echoes); DFS; VOCS (o1 = –4, –20, and 12 kHz); ^{1}H dec.
21.1	100	4096	3	12320	5	116;0	7 mm static; solid echo; ^{1}H dec.
21.1	100	4096	3	4096	5	120.5	4 mm MAS (ν_{rot} = 10 kHz); Hahn-echo; ^{1}H dec.

Table A4.1 continued

B_0 /T	window /kHz	points	π/2 /μs	scans	recycle delay /s	$\tau_1;\tau_2$ /μs	details
Mg(pams)							
9.4	1000	3960	10	261120	2	45;0	7 mm static; Hahn-echo; DFS; VOCS (o1 = –50, –20, and 10 kHz); ^{1}H dec.
21.1	100	3960	3	25600	2	114.5;0	7 mm static; Hahn-echo; ^{1}H dec.
21.1	100	3960	3	25600	2	74.5;0	4 mm MAS (ν_{rot} = 12.5 kHz); Hahn-echo; ^{1}H dec.
Mg(*p*NO_2)							
9.4	250	3960	10	178240	2	90;0	7 mm static; solid echo; ^{1}H dec.
9.4	250	3960	8	51215	2	192;0	7 mm MAS (ν_{rot} = 5 kHz); solid echo; ^{1}H dec.
21.1	100	3960	3	9216	2	114.5;0	7 mm static; Hahn-echo; ^{1}H dec.
21.1	100	3960	5	13072	2	117.5;0	7 mm MAS (ν_{rot} = 8 kHz); Hahn-echo

Table A4.2: Computational Details[a] for Mg Aryl Carboxylates and Inorganic Mg Compounds Containing $[Mg(H_2O)_6]^{2+}$ Units

compound	E_{cut} (eV)	*k*-point grid
Mg(*p*F)	610	3×4×2
Mg(*p*Cl) – 1[a]	400	1×1×2
Mg(*p*Cl) – 2[a]	400	1×1×2
Mg(ben) – 1[a]	400	3×3×3
Mg(ben) – 2[a]	400	3×3×3
Mg(sal)	610	4×5×1
Mg(pams)	610	3×2×4
Mg(*p*NO_2)	400	1×1×1
$MgSO_4 \cdot 11H_2O$	610	4×4×1
$Mg(NH_4)_2(SO_4)_2 \cdot 6H_2O$	610	3×2×4
$MgCl_2 \cdot 6H_2O$	610	4×4×4
$MgNO_3 \cdot 6H_2O$	610	4×2×4

[b]This nomenclature refers to a calculation which has been performed with the first (1) or second (2) orientation of the disordered water molecule present in the lattice.

Chapter 5 Appendices

Table A5.1: Experimental Solid-State NMR Conditions for ^{43}Ca.

B_0 /T	window /kHz	points	π/2 /μs	scans	recycle delay /s	details
			Ca(*p*F)			
21.1	20	2 048	1.5	37 888	2	7 mm MAS (ν_{rot} = 5 kHz); single pulse; selective 45° pulse
9.4	10	1 024	3	79400	3	7 mm MAS (ν_{rot} = 5 kHz); single pulse; selective 90° pulse
			Ca(*p*Cl)			
21.1	20	2 048	1.5	41 984	2	7 mm MAS (ν_{rot} = 5 kHz); single pulse; selective 45° pulse
9.4	10	1 024	3	87800	3	7 mm MAS (ν_{rot} = 5 kHz); single pulse; selective 90° pulse
			Ca(sal)			
21.1	20	2 048	1.5	35 840	2	7 mm MAS (ν_{rot} = 5 kHz); single pulse; selective 45° pulse
9.4	10	1 024	3	83825	3	7 mm MAS (ν_{rot} = 5 kHz); single pulse; selective 90° pulse
			Ca(pams)			
21.1	20	2 048	1.5	77 128	2	7 mm MAS (ν_{rot} = 5 kHz); single pulse; selective 45° pulse
21.1	20	2 048	2	10 880	2	4 mm MAS (ν_{rot} = 8 kHz); single pulse; ^{43}Ca enriched sample
21.1	50	1 912	2	28 672	2	4 mm stationary sample; single pulse with ^{1}H dec.; ^{43}Ca enriched sample
11.8	20	2 048	2	72 040	2	4 mm MAS (ν_{rot} = 8 kHz); single pulse; ^{43}Ca enriched sample
			Ca(pams)(OAc)			
21.1	20	2 048	1.5	40 960	2	7 mm MAS (ν_{rot} = 5 kHz); single pulse; selective 45° pulse
9.4	20	888	5.3	78 208	3	7 mm MAS (ν_{rot} = 5 kHz); single pulse with ^{1}H dec.
			$Ca_2(EDTA)\cdot 7H_2O$			
21.1	25	2 048	3.3	4 800	2	7 mm MAS (ν_{rot} = 5 kHz); single pulse with ^{1}H dec.; π/2 optimized on sample (twice the selective π/2)
9.4	20	888	10.5	82 904	3	7 mm MAS (ν_{rot} = 5 kHz); single pulse with ^{1}H dec.; pulse is twice that of selective π/2

Table A5.2. Experimental Solid-State NMR Conditions for ^{87}Sr.

B_0 /T	window /kHz	points	π/2 /μs	scans	recycle delay /s	details
			Sr(*p*Cl)			
21.1	1 000	64 064	n/a	53 248	1	7 mm stationary; WURST-QCPMG; 50 μs pulse; 2 kHz spikelet separation; ^{1}H dec.
			Sr(ben)			
21.1	1 000	64 064	n/a	73 728	1	7 mm stationary; WURST-QCPMG; 50 μs pulse; 2 kHz spikelet separation; ^{1}H dec.
			Sr(sal)			
21.1	1 000	64 064	n/a	53 248	1	7 mm stationary; WURST-QCPMG; 50 μs pulse; 2 kHz spikelet separation; ^{1}H dec.
			Sr(*p*NO$_2$)			
21.1	1 000	64 064	n/a	77 824	1	7 mm stationary; WURST-QCPMG; 50 μs pulse; 2 kHz spikelet separation; ^{1}H dec.
			Sr(pams)			
21.1	1 000	32 040	n/a	57 344	1	7 mm stationary; WURST-QCPMG; 25 μs pulse; 4 kHz spikelet separation; ^{1}H dec.
21.1	500	2 048	2	602 112	1	7 mm stationary; solid echo; 38 μs interpulse delay; 7 pieces with transmitter frequencies of -300, -200, -100, 0, 100, 200, and 300 kHz

Table A5.3: GIPAW DFT Computational Details for Ca and Sr Carboxylates.

compound	E_{cut} (eV)	*k*-point grid
Ca(*p*F)	450	2×1×2
Ca(*p*Cl)	450	2×1×2
Ca(ben)	450	2×1×2
Ca(sal)	450	2×2×2
Ca(pams)	450	1×2×1
Ca(pams)(OAc)	450	1×2×2
Ca_2(EDTA)·7H_2O	450	1×1×2
Ca(D-gluconate)	610	4×4×2
$Ca(C_2O_4)·3H_2O$	610	4×3×5
Sr(ben)	450	1×2×1
Sr(sal)	450	2×2×2
Sr(pCl)	450	2×2×1
Sr(*p*NO_2)	450	2×1×1
Sr(pams)	450	1×2×1

Chapter 6 Appendices

Table A6.1: Table of Ca–O distances and angles for the *C*2/*c* and *Ama*2 geometry optimized structures. Note that unit cell dimensions and angles of the original structures were not optimized here.

site	atom 1	atom 2	distance /Å	atom 1	atom 2	atom 3	angle 1,2,3 /deg.
*C*2/*c* site 1	Ca1	O12	2.293	O5	Ca1	O12	146.20
	Ca1	O5	2.318	O17	Ca1	O12	134.94
	Ca1	O17	2.320	O13	Ca1	O12	76.98
	Ca1	O13	2.346	O11	Ca1	O12	79.85
	Ca1	O11	2.388	O2	Ca1	O12	95.88
	Ca1	O2	2.411	O10	Ca1	O12	52.11
	Ca1	O10	2.698	O17	Ca1	O5	78.60
				O13	Ca1	O5	70.42
				O11	Ca1	O5	88.11
				O2	Ca1	O5	91.56
				O10	Ca1	O5	157.79
				O13	Ca1	O17	147.55
				O11	Ca1	O17	104.58
				O2	Ca1	O17	83.66
				O10	Ca1	O17	86.46
*C*2/*c* site 2	Ca5	O4	2.283	O12	Ca5	O4	180.00
	Ca5	O12	2.283	O14	Ca5	O4	94.55
	Ca5	O14	2.355	O6	Ca5	O4	85.45
	Ca5	O6	2.355	O15	Ca5	O4	94.50
	Ca5	O15	2.360	O7	Ca5	O4	85.50
	Ca5	O7	2.360	O14	Ca5	O12	85.45
				O6	Ca5	O12	94.55
				O15	Ca5	O12	85.50
				O7	Ca5	O12	94.50
				O6	Ca5	O14	179.99
				O15	Ca5	O14	99.78
				O7	Ca5	O14	80.22
				O15	Ca5	O6	80.22
				O7	Ca5	O6	99.78
				O7	Ca5	O15	180.00

Table A6.1 continued

site	atom 1	atom 2	distance /Å	atom 1	atom 2	atom 3	angle 1,2,3 /deg.
*Ama*2	Ca1	O5	2.257	O6	Ca1	O5	143.26
	Ca1	O6	2.257	O1	Ca1	O5	77.27
	Ca1	O1	2.415	O2	Ca1	O5	133.46
	Ca1	O2	2.415	O1	Ca1	O5	74.36
	Ca1	O1	2.495	O2	Ca1	O5	101.56
	Ca1	O2	2.495	O1	Ca1	O5	49.88
	Ca1	O1	2.846	O2	Ca1	O5	97.26
	Ca1	O2	2.846	O1	Ca1	O6	133.46
				O2	Ca1	O6	77.27
				O1	Ca1	O6	101.56
				O2	Ca1	O6	74.36
				O1	Ca1	O6	97.26
				O2	Ca1	O6	49.88
				O2	Ca1	O1	84.25
				O1	Ca1	O1	114.55
				O2	Ca1	O1	75.37
				O1	Ca1	O1	103.18
				O2	Ca1	O1	172.58
				O1	Ca1	O2	75.37
				O2	Ca1	O2	114.55
				O1	Ca1	O2	172.58
				O2	Ca1	O2	103.18
				O2	Ca1	O1	167.39
				O1	Ca1	O1	101.14
				O2	Ca1	O1	68.05
				O1	Ca1	O2	68.05
				O2	Ca1	O2	101.14
				O2	Ca1	O1	69.40

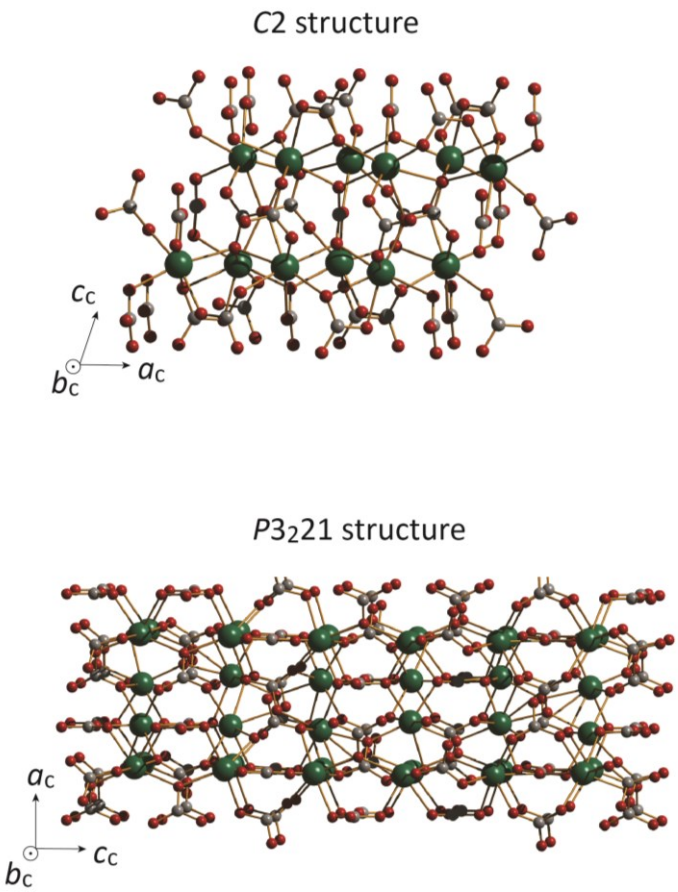

Figure A6.1: Molecular picture of the two most plausible vaterite structural models. Carbon atoms are grey, oxygen atoms are red, and calcium atoms are green.

Appendix B – Crystallographic Information Files

Chapter 3 Structures

$C_5H_9PPh_3Br$

```
data_db049a
_symmetry_cell_setting          orthorhombic
_symmetry_space_group_name_H-M   'P n m a'
_symmetry_Int_Tables_number      62
loop_
_symmetry_equiv_pos_site_id
_symmetry_equiv_pos_as_xyz
1 x,y,z
2 1/2-x,-y,1/2+z
3 -x,1/2+y,-z
4 1/2+x,1/2-y,1/2-z
5 -x,-y,-z
6 1/2+x,y,1/2-z
7 x,1/2-y,z
8 1/2-x,1/2+y,1/2+z
_cell_length_a                 15.958(2)
_cell_length_b                 13.259(2)
_cell_length_c                 9.2250(14)
_cell_angle_alpha               90.00
_cell_angle_beta                90.00
_cell_angle_gamma                 90.00
_cell_volume                   1951.89
loop_
_atom_site_label
_atom_site_type_symbol
_atom_site_fract_x
_atom_site_fract_y
_atom_site_fract_z
```

		x/a_c	y/b_c	z/c_c
Br1	Br	0.376862(12)	0.25	0.52159(2)
P1	P	0.55384(3)	0.25	0.90877(4)
C1	C	0.59905(8)	0.14040(9)	0.82618(13)
C2	C	0.55490(8)	0.08336(10)	0.72506(13)
H2A	H	0.4989	0.1007	0.7004
C3	C	0.59361(10)	0.00068(10)	0.66043(15)
H3A	H	0.5634	-0.0396	0.5931
C4	C	0.67539(10)	-0.02305(11)	0.69363(16)
H4A	H	0.7014	-0.0797	0.6493
C5	C	0.71990(10)	0.03531(12)	0.79133(17)
H5A	H	0.7767	0.0194	0.8123
C6	C	0.68205(8)	0.11665(10)	0.85857(15)
H6A	H	0.7125	0.1562	0.9265
C7	C	0.58012(11)	0.25	1.09737(18)
C8	C	0.58615(9)	0.15917(10)	1.17214(14)
H8A	H	0.5827	0.0969	1.1214
C9	C	0.59727(9)	0.16010(13)	1.32125(15)
H9A	H	0.6013	0.0983	1.3729
C10	C	0.60251(13)	0.25	1.3944(2)
H10A	H	0.6098	0.25	1.4966
C11	C	0.44203(10)	0.25	0.88740(19)
H11A	H	0.4301	0.248	0.781
C12	C	0.3994(6)	0.1533(10)	0.9576(15)
H12A	H	0.3792	0.106	0.8823
H12B	H	0.4386	0.1175	1.0231
C13	C	0.3247(3)	0.2017(4)	1.0437(5)
H13A	H	0.2744	0.1581	1.0381
H13B	H	0.3399	0.2108	1.147
C14	C	0.3080(2)	0.3026(3)	0.9731(4)
H14A	H	0.2767	0.3484	1.0383
H14B	H	0.277	0.295	0.8807
C15	C	0.3958(8)	0.3384(12)	0.9485(17)
H15A	H	0.3965	0.3956	0.8795
H15B	H	0.4215	0.3605	1.0408
C1	C	0.59905(8)	0.35960(9)	0.82618(13)
C2	C	0.55490(8)	0.41664(10)	0.72506(13)
H2A	H	0.4989	0.3993	0.7004
C3	C	0.59361(10)	0.49932(10)	0.66043(15)
H3A	H	0.5634	0.5396	0.5931
C4	C	0.67539(10)	0.52305(11)	0.69363(16)
H4A	H	0.7014	0.5797	0.6493
C5	C	0.71990(10)	0.46469(12)	0.79133(17)

H5A	H	0.7767	0.4806	0.8123
C6	C	0.68205(8)	0.38335(10)	0.85857(15)
H6A	H	0.7125	0.3438	0.9265
C8	C	0.58615(9)	0.34083(10)	1.17214(14)
H8A	H	0.5827	0.4031	1.1214
C9	C	0.59727(9)	0.33990(13)	1.32125(15)
H9A	H	0.6013	0.4017	1.3729
H11A	H	0.4301	0.252	0.781
C12	C	0.3994(6)	0.3467(10)	0.9576(15)
H12A	H	0.3792	0.394	0.8823
H12B	H	0.4386	0.3825	1.0231
C13	C	0.3247(3)	0.2983(4)	1.0437(5)
H13A	H	0.2744	0.3419	1.0381
H13B	H	0.3399	0.2892	1.147
C14	C	0.3080(2)	0.1974(3)	0.9731(4)
H14A	H	0.2767	0.1516	1.0383
H14B	H	0.277	0.205	0.8807
C15	C	0.3958(8)	0.1616(12)	0.9485(17)
H15A	H	0.3965	0.1044	0.8795
H15B	H	0.4215	0.1395	1.0408

$EtPPh_3Br$

```
data_db034
_symmetry_cell_setting          monoclinic
_symmetry_space_group_name_H-M   'C 2/c'
_symmetry_Int_Tables_number      15
loop_
_symmetry_equiv_pos_site_id
_symmetry_equiv_pos_as_xyz
1 x,y,z
2 -x,y,1/2-z
3 1/2+x,1/2+y,z
4 1/2-x,1/2+y,1/2-z
5 -x,-y,-z
6 x,-y,1/2+z
7 1/2-x,1/2-y,-z
8 1/2+x,1/2-y,1/2+z
_cell_length_a                 14.2027(2)
_cell_length_b                 12.5625(2)
_cell_length_c                 19.7600(3)
_cell_angle_alpha               90.00
_cell_angle_beta                92.9910(10)
_cell_angle_gamma               90.00
_cell_volume                   3520.8
loop_
_atom_site_label
_atom_site_type_symbol
_atom_site_fract_x
_atom_site_fract_y
_atom_site_fract_z
```

		x/a_c	y/b_c	z/c_c
Br1	Br	0.247318(8)	0.738313(10)	0.177859(6)
P1	P	0.275007(18)	0.11275(2)	0.127713(13)
C1	C	0.32059(7)	0.04591(9)	0.05617(5)
C2	C	0.29643(9)	-0.06021(10)	0.04378(6)
H2A	H	0.2621	-0.099	0.0756
C3	C	0.32300(10)	-0.10848(11)	-0.01535(6)
H3A	H	0.3053	-0.1802	-0.0246
C4	C	0.37503(9)	-0.05297(11)	-0.06090(6)
H4A	H	0.3923	-0.0865	-0.1015
C5	C	0.40184(9)	0.05031(11)	-0.04772(6)
H5A	H	0.4395	0.0871	-0.0784
C6	C	0.37396(8)	0.10111(10)	0.01044(6)
H6A	H	0.3912	0.1731	0.019
C7	C	0.34057(8)	0.23378(9)	0.14145(6)
C8	C	0.43826(9)	0.22814(11)	0.15372(7)
H8A	H	0.4688	0.1609	0.1553
C9	C	0.49045(9)	0.32018(12)	0.16357(7)
H9A	H	0.5568	0.3162	0.1722
C10	C	0.44593(10)	0.41796(11)	0.16081(7)
H10A	H	0.482	0.4811	0.1676
C11	C	0.34958(9)	0.42495(10)	0.14829(7)
H11A	H	0.3197	0.4926	0.1461
C12	C	0.29640(8)	0.33257(10)	0.13883(6)
H12A	H	0.23	0.337	0.1306
C13	C	0.15241(7)	0.14236(9)	0.10917(5)
C14	C	0.09987(8)	0.18566(10)	0.16054(6)
H14A	H	0.1291	0.2007	0.2038
C15	C	0.00452(8)	0.20631(11)	0.14740(7)
H15A	H	-0.0316	0.2362	0.1818
C16	C	-0.03824(8)	0.18365(11)	0.08446(7)
H16A	H	-0.1036	0.1975	0.0761
C17	C	0.01348(9)	0.14107(12)	0.03384(7)
H17A	H	-0.0163	0.1259	-0.0092
C18	C	0.10926(8)	0.12025(10)	0.04577(6)
H18A	H	0.145	0.0912	0.0109
C19	C	0.27931(8)	0.02670(10)	0.20051(6)
H19A	H	0.2466	0.0627	0.2372
H19B	H	0.2434	-0.0388	0.1886
C20	C	0.37717(10)	-0.00554(13)	0.22810(7)
H20A	H	0.3716	-0.0522	0.2674
H20B	H	0.4131	0.0582	0.2417
H20C	H	0.4099	-0.0435	0.1929

$MePPh_3Br$

```
data_db038
_symmetry_cell_setting          monoclinic
_symmetry_space_group_name_H-M   'P 21/n'
_symmetry_Int_Tables_number      14
loop_
_symmetry_equiv_pos_site_id
_symmetry_equiv_pos_as_xyz
1 x,y,z
2 1/2-x,1/2+y,1/2-z
3 -x,-y,-z
4 1/2+x,1/2-y,1/2+z
_cell_length_a                 9.0887(2)
_cell_length_b                 18.6129(4)
_cell_length_c                 10.5950(2)
_cell_angle_alpha               90.00
_cell_angle_beta                108.0300(10)
_cell_angle_gamma                90.00
_cell_volume                   1704.31
loop_
_atom_site_label
_atom_site_type_symbol
_atom_site_fract_x
_atom_site_fract_y
_atom_site_fract_z
```

		x/a_c	y/b_c	z/c_c
Br1	Br	0.847466(16)	0.179817(7)	0.262612(13)
P1	P	0.58880(3)	0.104205(16)	0.83844(3)
C1	C	0.42777(14)	0.07888(7)	0.69803(12)
C2	C	0.34242(16)	0.13436(8)	0.62042(14)
H2A	H	0.3743	0.1829	0.6388
C3	C	0.21044(18)	0.11809(9)	0.51617(16)
H3A	H	0.1521	0.1556	0.4628
C4	C	0.16364(17)	0.04742(9)	0.48982(15)
H4A	H	0.0741	0.0365	0.4176
C5	C	0.24664(17)	-0.00737(8)	0.56811(15)
H5A	H	0.2128	-0.0557	0.5506
C6	C	0.37959(16)	0.00786(7)	0.67252(14)
H6A	H	0.437	-0.0299	0.7259
C7	C	0.71161(14)	0.16512(7)	0.78636(12)
C8	C	0.73067(19)	0.15802(9)	0.66190(15)
H8A	H	0.6702	0.1243	0.6001
C9	C	0.8391(2)	0.20067(11)	0.62797(18)
H9A	H	0.8529	0.1961	0.5431
C10	C	0.9261(2)	0.24961(9)	0.71875(17)
H10A	H	1.0012	0.2781	0.6963
C11	C	0.90541(18)	0.25755(8)	0.84105(16)
H11A	H	0.9646	0.2921	0.9018
C12	C	0.79813(16)	0.21529(7)	0.87639(14)
H12A	H	0.7841	0.2206	0.9611
C13	C	0.70059(14)	0.02652(7)	0.90958(13)
C14	C	0.74754(18)	-0.02118(9)	0.82727(17)
H14A	H	0.7165	-0.0137	0.734
C15	C	0.8400(2)	-0.07956(9)	0.8833(2)
H15A	H	0.8722	-0.1124	0.8284
C16	C	0.88493(18)	-0.08979(9)	1.0188(2)
H16A	H	0.9471	-0.1301	1.0564
C17	C	0.84097(18)	-0.04234(9)	1.10054(18)
H17A	H	0.8739	-0.0498	1.1938
C18	C	0.74838(16)	0.01648(8)	1.04645(14)
H18A	H	0.7181	0.0494	1.1023
C19	C	0.51740(15)	0.14777(7)	0.95763(13)
H19A	H	0.6045	0.1618	1.0346
H19B	H	0.4497	0.1148	0.9861
H19C	H	0.4587	0.1906	0.9177

PPh_4Br

```
data_db037
_symmetry_cell_setting          triclinic
_symmetry_space_group_name_H-M   'P -1'
_symmetry_Int_Tables_number      2
loop_
_symmetry_equiv_pos_site_id
_symmetry_equiv_pos_as_xyz
1 x,y,z
2 -x,-y,-z
_cell_length_a                 9.3969(8)
_cell_length_b                 10.2884(9)
_cell_length_c                 11.2664(10)
_cell_angle_alpha               75.619(4)
_cell_angle_beta                71.910(4)
_cell_angle_gamma                  78.421(4)
_cell_volume                   993.865
loop_
_atom_site_label
_atom_site_type_symbol
_atom_site_fract_x
_atom_site_fract_y
_atom_site_fract_z
```

		x/a_c	y/b_c	z/c_c
Br1	Br	0.5	0.5	0.5
Br2	Br	0.5	0.5	0
P1	P	0.0624	0.1606	0.1997
C1	C	0.1024(1)	0.2470(1)	0.3036(1)
C2	C	0.0184(2)	0.2364(1)	0.4311(1)
H2A	H	-0.0645	0.1859	0.4638
C3	C	0.0569(2)	0.3000(2)	0.5096(1)
H3A	H	-0.0011	0.2942	0.596
C4	C	0.1787(2)	0.3718(2)	0.4634(1)
H4A	H	0.2047	0.4144	0.518
C5	C	0.2626(1)	0.3817(1)	0.3375(1)
H5A	H	0.3463	0.4313	0.3058
C6	C	0.2252(1)	0.3195(1)	0.2575(1)
H6A	H	0.2833	0.3264	0.171
C7	C	-0.1253(1)	0.1149(1)	0.2646(1)
C8	C	-0.2445(1)	0.2089(1)	0.3137(1)
H8A	H	-0.2254	0.294	0.3196
C9	C	-0.3909(2)	0.1777(2)	0.3538(2)
H9A	H	-0.4725	0.2408	0.3885
C10	C	-0.4178(2)	0.0547(2)	0.3433(2)
H10A	H	-0.5186	0.0343	0.3694
C11	C	-0.3009(2)	-0.0389(2)	0.2955(2)
H11A	H	-0.3211	-0.1234	0.2893
C12	C	-0.1530(2)	-0.0099(1)	0.2563(1)
H12A	H	-0.0718	-0.0747	0.2242
C13	C	0.1953(1)	0.0099(1)	0.1885(1)
C14	C	0.2444(1)	-0.0577(1)	0.2956(1)
H14A	H	0.2166	-0.0184	0.3688
C15	C	0.3340(1)	-0.1826(1)	0.2945(1)
H15A	H	0.3665	-0.2299	0.3674
C16	C	0.3757(2)	-0.2378(1)	0.1861(2)
H16A	H	0.436	-0.3238	0.1857
C17	C	0.3307(2)	-0.1693(2)	0.0787(2)
H17A	H	0.3622	-0.2073	0.0045
C18	C	0.2397(2)	-0.0453(1)	0.0794(1)
H18A	H	0.2079	0.0017	0.0061
C19	C	0.0743(1)	0.2626(1)	0.0432(1)
C20	C	0.2135(1)	0.2918(1)	-0.0409(1)
H20A	H	0.3041	0.2573	-0.0164
C21	C	0.2185(2)	0.3718(2)	-0.1611(1)
H21A	H	0.3126	0.3935	-0.2185
C22	C	0.0869(2)	0.4196(1)	-0.1970(1)

H22A	H	0.0911	0.4731	-0.2796
C23	C	-0.0500(2)	0.3908(1)	-0.1143(1)
H23A	H	-0.1399	0.4246	-0.1401
C24	C	-0.0582(1)	0.3124(1)	0.0068(1)
H24A	H	-0.1532	0.2931	0.0641

$PPh_4Br \cdot H_2O$

```
data_db031
_symmetry_cell_setting          triclinic
_symmetry_space_group_name_H-M   'P -1'
_symmetry_Int_Tables_number      2
loop_
_symmetry_equiv_pos_site_id
_symmetry_equiv_pos_as_xyz
1 x,y,z
2 -x,-y,-z
_cell_length_a                 9.954(3)
_cell_length_b                 10.573(4)
_cell_length_c                 10.647(3)
_cell_angle_alpha               77.282(16)
_cell_angle_beta                83.514(16)
_cell_angle_gamma                  71.942(17)
_cell_volume                   1037.99
loop_
_atom_site_label
_atom_site_type_symbol
_atom_site_fract_x
_atom_site_fract_y
_atom_site_fract_z
```

		x/a_c	y/b_c	z/c_c
Br1	Br	0.559540(19)	0.756526(17)	0.122010(14)
P1	P	0.06265(4)	0.76283(4)	0.34249(3)
C13	C	-0.10556(17)	0.78155(15)	0.42886(13)
C21	C	0.3057(2)	0.7718(2)	0.61711(18)
H21A	H	0.3228	0.8375	0.6562
C1	C	0.06205(17)	0.92064(15)	0.23763(13)
C7	C	0.10295(17)	0.63294(15)	0.24778(13)
C6	C	-0.0642(2)	1.01273(16)	0.19543(14)
H6A	H	-0.1516	0.9968	0.2283
C24	C	0.25678(19)	0.57807(18)	0.50511(16)
H24A	H	0.2402	0.5115	0.4668
C14	C	-0.11722(19)	0.79161(18)	0.55874(14)
H14A	H	-0.0347	0.7797	0.6023
C4	C	0.0650(2)	1.15016(18)	0.05627(15)
H4A	H	0.0657	1.2291	-0.0067
C19	C	0.19442(17)	0.71497(16)	0.45821(13)
C20	C	0.21979(19)	0.81264(19)	0.51335(16)
H20A	H	0.1785	0.9064	0.4801
C15	C	-0.2475(2)	0.8186(2)	0.62394(15)
H15A	H	-0.2545	0.8257	0.712
C2	C	0.19083(19)	0.94310(17)	0.18972(14)
H2A	H	0.2775	0.8799	0.2196
C12	C	0.0127(2)	0.55637(17)	0.24618(15)
H12A	H	-0.0726	0.569	0.2983
C8	C	0.2295(2)	0.61216(18)	0.17307(15)
H8A	H	0.2915	0.6643	0.1745
C3	C	0.1909(2)	1.05853(19)	0.09821(15)
H3A	H	0.2779	1.0745	0.0643
C11	C	0.0488(2)	0.46068(19)	0.16712(18)
H11A	H	-0.0132	0.4088	0.1643
C5	C	-0.0625(2)	1.12861(17)	0.10468(16)
H5A	H	-0.1488	1.1931	0.0759
C17	C	-0.3570(2)	0.82303(19)	0.43342(16)
H17A	H	-0.4398	0.8325	0.3914
C9	C	0.2642(2)	0.51450(18)	0.09649(16)
H9A	H	0.351	0.4989	0.0465
C16	C	-0.3671(2)	0.8352(2)	0.56200(17)
H16A	H	-0.4569	0.855	0.6068
C10	C	0.1736(2)	0.44063(19)	0.09296(18)
H10A	H	0.197	0.3754	0.0392
C23	C	0.3431(2)	0.5397(2)	0.60800(18)
H23A	H	0.3868	0.4462	0.6406

C18	C	-0.22742(18)	0.79731(17)	0.36690(14)
H18A	H	-0.2212	0.7903	0.2789
C22	C	0.3661(2)	0.6364(3)	0.66344(18)
H22A	H	0.4247	0.609	0.7349
O1	O	0.43162(17)	0.92594(16)	0.83093(12)
H1A	H	0.42936(18)	0.9988(17)	0.8417(3)
H1B	H	0.4500(5)	0.8851(10)	0.8970(16)

$BuPPh_3Cl$

```
data_db040
_symmetry_cell_setting          monoclinic
_symmetry_space_group_name_H-M   'P 21/c'
_symmetry_Int_Tables_number      14
loop_
_symmetry_equiv_pos_site_id
_symmetry_equiv_pos_as_xyz
1 x,y,z
2 -x,1/2+y,1/2-z
3 -x,-y,-z
4 x,1/2-y,1/2+z
_cell_length_a                 11.1419(3)
_cell_length_b                 9.9882(3)
_cell_length_c                 17.2512(5)
_cell_angle_alpha               90.00
_cell_angle_beta                103.4600(10)
_cell_angle_gamma                90.00
_cell_volume                   1867.11
loop_
_atom_site_label
_atom_site_type_symbol
_atom_site_fract_x
_atom_site_fract_y
_atom_site_fract_z
```

		x/a_c	y/b_c	z/c_c
P1	P	0.76952(2)	0.20337(2)	0.041341(14)
C1	C	0.90241(9)	0.13624(10)	0.11002(6)
C2	C	0.91882(10)	-0.00106(11)	0.12152(6)
H2A	H	0.8598	-0.0622	0.0925
C3	C	1.02307(11)	-0.04781(13)	0.17622(7)
H3A	H	1.0354	-0.1414	0.1843
C4	C	1.10846(11)	0.04139(15)	0.21873(7)
H4A	H	1.1794	0.0084	0.2555
C5	C	1.09195(11)	0.17786(15)	0.20841(7)
H5A	H	1.1509	0.2384	0.2381
C6	C	0.98830(10)	0.22588(12)	0.15420(7)
H6A	H	0.9758	0.3196	0.1472
C7	C	0.81626(10)	0.29967(10)	-0.03467(6)
C8	C	0.72317(11)	0.35591(13)	-0.09460(7)
H8A	H	0.639	0.3446	-0.0933
C9	C	0.75419(12)	0.42827(13)	-0.15594(7)
H9A	H	0.6914	0.4686	-0.1959
C10	C	0.87675(12)	0.44135(12)	-0.15865(7)
H10A	H	0.8977	0.4891	-0.2012
C11	C	0.96894(12)	0.38541(13)	-0.09985(8)
H11A	H	1.0528	0.3953	-0.1022
C12	C	0.93944(10)	0.31460(12)	-0.03722(7)
H12A	H	1.0029	0.2768	0.0034
C13	C	0.69137(9)	0.31079(10)	0.09730(6)
C14	C	0.65076(10)	0.25279(11)	0.16069(6)
H14A	H	0.6641	0.1603	0.1724
C15	C	0.59072(10)	0.33200(13)	0.20615(7)
H15A	H	0.5619	0.2934	0.2488
C16	C	0.57289(10)	0.46746(12)	0.18935(7)
H16A	H	0.5323	0.5211	0.2209
C17	C	0.61358(11)	0.52529(12)	0.12707(7)
H17A	H	0.6011	0.6181	0.1162
C18	C	0.67279(10)	0.44686(11)	0.08049(7)
H18A	H	0.7004	0.4859	0.0375
C19	C	0.67049(9)	0.07026(10)	-0.00626(6)
H19A	H	0.6594	0.0048	0.0346
H19B	H	0.5884	0.1076	-0.0315
C20	C	0.72274(10)	-0.00259(11)	-0.07013(6)
H20A	H	0.7198	0.0584	-0.1158
H20B	H	0.8102	-0.0262	-0.0474
C21	C	0.65009(11)	-0.12966(11)	-0.09960(7)
H21A	H	0.5609	-0.1084	-0.1121

H21B	H	0.6712	-0.1591	-0.1496
C22	C	0.67450(13)	-0.24448(13)	-0.04016(8)
H22A	H	0.6253	-0.3224	-0.0629
H22B	H	0.6516	-0.2173	0.009
H22C	H	0.7623	-0.2677	-0.0283
Cl1	Cl	0.37565(3)	0.12066(3)	0.835367(16)

Chapter 4 Structures

B4.1: Mg(ben)

```
data_db105
_symmetry_cell_setting          monoclinic
_symmetry_space_group_name_H-M   'C 2/c'
_symmetry_Int_Tables_number      15
loop_
_symmetry_equiv_pos_site_id
_symmetry_equiv_pos_as_xyz
1 x,y,z
2 -x,y,1/2-z
3 1/2+x,1/2+y,z
4 1/2-x,1/2+y,1/2-z
5 -x,-y,-z
6 x,-y,1/2+z
7 1/2-x,1/2-y,-z
8 1/2+x,1/2-y,1/2+z
_cell_length_a                 35.226(4)
_cell_length_b                 10.4274(10)
_cell_length_c                 8.9061(9)
_cell_angle_alpha               90.00
_cell_angle_beta                97.477(8)
_cell_angle_gamma               90.00
_cell_volume                   3243.53
loop_
_atom_site_label
_atom_site_type_symbol
_atom_site_fract_x
_atom_site_fract_y
_atom_site_fract_z
```

		x/a_c	y/b_c	z/c_c
Mg1	Mg	0.30486(3)	0.41480(11)	0.02461(11)
O1	O	0.34705(7)	0.3747(2)	0.1964(2)
O2	O	0.33887(7)	0.5150(3)	0.3764(3)
O3	O	0.30841(7)	0.2338(2)	-0.0674(3)
O4	O	0.31099(9)	0.0367(3)	0.0265(4)
O5	O	0.26542(7)	0.3464(2)	0.1703(2)
H5B	H	0.2384	0.3372	0.1443
H5C	H	0.2763	0.2694	0.2286
O6	O	0.25658(7)	0.4473(3)	-0.1279(3)
H6B	H	0.2613	0.5262	-0.1767
H6C	H	0.2288	0.4408	-0.1134
O7	O	0.29963(9)	0.6043(3)	0.1026(3)
H7B	H	0.3109	0.6111	0.2058
H7C	H	0.299	0.6906	0.0521
C1	C	0.35834(10)	0.4320(3)	0.3178(4)
C2	C	0.39793(11)	0.4019(4)	0.3941(4)
C3	C	0.41442(11)	0.4722(4)	0.5182(4)
H3A	H	0.3999	0.5371	0.5596
C4	C	0.45152(12)	0.4489(5)	0.5819(5)
H4A	H	0.4625	0.4976	0.6667
C5	C	0.47282(13)	0.3541(5)	0.5223(5)
H5A	H	0.4985	0.3384	0.5658
C6	C	0.45683(13)	0.2834(5)	0.4009(5)
H6A	H	0.4715	0.2181	0.361
C7	C	0.41959(12)	0.3059(4)	0.3355(4)
H7A	H	0.4088	0.2563	0.2512
C8	C	0.32670(11)	0.1314(4)	-0.0241(4)
C9	C	0.36863(11)	0.1238(4)	-0.0352(4)
C10	C	0.38600(12)	0.2084(4)	-0.1268(5)
H10A	H	0.3712	0.273	-0.1825
C11	C	0.42466(13)	0.1980(5)	-0.1360(6)
H11A	H	0.4363	0.2549	-0.1998
C12	C	0.44662(13)	0.1066(5)	-0.0546(6)
H12A	H	0.4733	0.1013	-0.0608
C13	C	0.42971(14)	0.0227(5)	0.0363(6)
H13A	H	0.4448	-0.0405	0.093
C14	C	0.39064(11)	0.0302(3)	0.0453(4)
H14A	H	0.379	-0.0289	0.1066
Mg1	Mg	0.30486(3)	0.58520(11)	0.52461(11)
O2	O	0.33887(7)	0.4850(3)	-0.1236(3)
O8	O	0.31446(11)	0.8002(3)	0.9052(4)
H8A	H	0.3047	0.873	0.953

H8B	H	0.3423	0.8126	0.8952
O9	O	0.28157(18)	0.8050(5)	0.9233(6)
H9A	H	0.3014	0.8674	0.9436
H9B	H	0.2558	0.8476	0.9117

modified .cif for Ca(pams)(OAc) calculations

```
data_db112a
_symmetry_cell_setting          orthorhombic
_symmetry_space_group_name_H-M   'P 1'
_symmetry_Int_Tables_number      1
loop_
_symmetry_equiv_pos_site_id
_symmetry_equiv_pos_as_xyz
1 x,y,z
_cell_length_a                  18.2851(11)
_cell_length_b                  6.8377(4)
_cell_length_c                  9.5084(6)
_cell_angle_alpha                 90.00
_cell_angle_beta                 90.00
_cell_angle_gamma                   90.00
_cell_volume                    1188.82
loop_
_atom_site_label
_atom_site_type_symbol
_atom_site_fract_x
_atom_site_fract_y
_atom_site_fract_z
```

		x/a_c	y/b_c	z/c_c
Ca1	Ca	0.019776	0.249999	0.39398
Ca2	Ca	0.480225	0.749999	0.89398
Ca3	Ca	0.519776	0.249999	0.10602
Ca4	Ca	0.980225	0.749999	0.60602
O5	O	0.924195	0.090516	0.2415
O6	O	0.575805	0.909484	0.7415
O7	O	0.424195	0.409484	0.2585
O8	O	0.075805	0.590516	0.7585
O9	O	0.075805	0.909484	0.7585
O10	O	0.424195	0.090516	0.2585
O11	O	0.575805	0.590516	0.7415
O12	O	0.924195	0.409484	0.2415
O13	O	0.828186	0.607178	0.0854
H14	H	0.867371	0.5979	0.1309
O15	O	0.94751	0.089477	0.586
O16	O	0.55249	0.910523	0.086
O17	O	0.44751	0.410523	0.914
O18	O	0.05249	0.589477	0.414
O19	O	0.05249	0.910523	0.414
O20	O	0.44751	0.089477	0.914
O21	O	0.55249	0.589477	0.086
O22	O	0.94751	0.410523	0.586
O23	O	0.09967	0.249999	0.1963
O24	O	0.40033	0.749999	0.6963
O25	O	0.59967	0.249999	0.3037
O26	O	0.90033	0.749999	0.8037
H27	H	0.423279	0.819214	0.6176
H28	H	0.11029	0.114929	0.1685
H29	H	0.61029	0.385071	0.3315
H30	H	0.88971	0.885071	0.8315
H31	H	0.61029	0.114929	0.3315
H32	H	0.38971	0.614929	0.6685
H33	H	0.11029	0.385071	0.1685
O34	O	0.476196	0.620972	0.4735
O35	O	0.523804	0.120972	0.5265
H36	H	0.020508	0.509399	0.0091
H37	H	0.479492	0.490601	0.5091
H38	H	0.479492	0.009399	0.5091
H39	H	0.020508	0.990601	0.0091
H40	H	0.424072	0.667175	0.4752
H41	H	0.575928	0.167175	0.5248
N42	N	0.877624	0.749999	0.4196

N43	N	0.122376	0.249999	0.5804
H44	H	0.882508	0.858825	0.3634
H45	H	0.117493	0.358825	0.6366
H46	H	0.117493	0.141175	0.6366
H47	H	0.882508	0.641175	0.3634
C48	C	0.894226	0.249999	0.2076
C49	C	0.605774	0.749999	0.7076
C50	C	0.394226	0.249999	0.2924
C51	C	0.105774	0.749999	0.7924
C52	C	0.825317	0.249999	0.1269
C53	C	0.674683	0.749999	0.6269
C54	C	0.325317	0.249999	0.3731
C55	C	0.174683	0.749999	0.8731
C56	C	0.791687	0.074097	0.0868
C57	C	0.708313	0.925903	0.5868
C58	C	0.291687	0.425903	0.4132
C59	C	0.208313	0.574097	0.9132
C60	C	0.208313	0.925903	0.9132
C61	C	0.291687	0.074097	0.4132
C62	C	0.708313	0.574097	0.5868
C63	C	0.791687	0.425903	0.0868
H64	H	0.314209	0.54712	0.3906
C65	C	0.725586	0.075928	0.0143
C66	C	0.774414	0.924072	0.5143
C67	C	0.225586	0.424072	0.4857
C68	C	0.274414	0.575928	0.9857
C69	C	0.274414	0.924072	0.9857
C70	C	0.225586	0.075928	0.4857
C71	C	0.774414	0.575928	0.5143
C72	C	0.725586	0.424072	0.0143
H73	H	0.20343	0.544312	0.5121
H74	H	0.79657	0.455688	0.4879
C75	C	0.808106	0.749999	0.4801
C76	C	0.191894	0.249999	0.5199
C77	C	0.92688	0.249999	0.6381
C78	C	0.57312	0.749999	0.1381
C79	C	0.42688	0.249999	0.8619
C80	C	0.07312	0.749999	0.3619
C81	C	0.876587	0.249999	0.7628
C82	C	0.623413	0.749999	0.2628
C83	C	0.376587	0.249999	0.7372
C84	C	0.123413	0.749999	0.2372
H85	H	0.862122	0.384583	0.7847

H86	H	0.362122	0.115417	0.7153
H87	H	0.137878	0.615417	0.2153
H88	H	0.637878	0.884583	0.2847
H89	H	0.901794	0.19281	0.8439
H90	H	0.401794	0.30719	0.6561
H91	H	0.098206	0.80719	0.1561
H92	H	0.598206	0.69281	0.3439
H93	H	0.832886	0.172485	0.741101
H94	H	0.332886	0.327515	0.758899
H95	H	0.167114	0.827515	0.258899
H96	H	0.667114	0.672485	0.241101
O97	O	0.0238	0.379	-0.0265
O98	O	-0.0238	0.879	0.0265
H99	H	-0.0759	0.832801	0.0248
H100	H	0.0759	0.332801	-0.0248
H101	H	0.8897	0.6149	0.8315
O102	O	0.6718	0.3928	0.5854
H103	H	0.6326	0.4021	0.6309
H104	H	0.6858	1.047101	0.6094
O105	O	0.3282	-0.1072	0.4146
H106	H	0.3674	-0.0979	0.3691
H107	H	0.2966	0.4557	1.0121
C108	C	0.3081	0.749999	1.0199
N109	N	0.3776	0.749999	1.080399
H110	H	0.3825	0.6412	1.1366
H111	H	0.3825	0.8588	1.1366
H112	H	0.2966	1.0443	1.0121
H113	H	0.1858	0.452899	0.8906
O114	O	0.1718	1.1072	0.9146
H115	H	0.1326	1.0979	0.8691
H116	H	0.7034	0.5443	-0.0121
C117	C	0.6919	0.249999	-0.0199
H118	H	0.7034	-0.0443	-0.0121
N119	N	0.6224	0.249999	-0.0804
H120	H	0.6175	0.1412	-0.1366
H121	H	0.6175	0.3588	-0.1366
H122	H	0.8142	-0.0471	0.1094
H123	H	0.2034	-0.0443	0.5121
H124	H	0.7966	1.0443	0.4879